UNIVERSITY OF COPENHAGEN
FACULTY OF SCIENCE

Unconventional Superconductivity and Altermagnetism

Mercè Roig Server

Niels Bohr Institute
University of Copenhagen

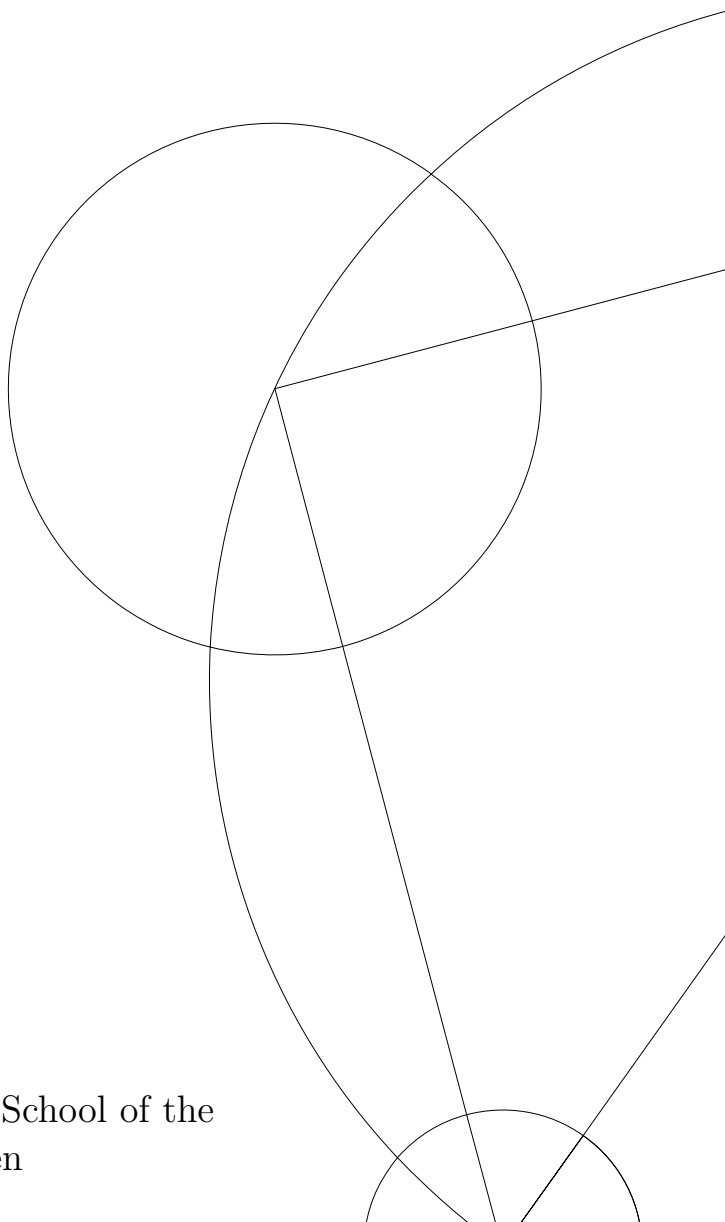

PhD Thesis

Supervisor: Brian Møller Andersen

Date: 31/08/2024

This thesis has been submitted to the PhD School of the Faculty of Science, University of Copenhagen

Unconventional Superconductivity and Altermagnetism
Mercè Roig Server

PhD Thesis

Condensed Matter Theory
Niels Bohr Institute
University of Copenhagen

Supervisor:
Prof. Brian Møller Andersen

Assessment committee:
Prof. Jens Paaske
Prof. Roser Valentí
Prof. Maxim Khodas

Abstract

Superconductivity and magnetism are fascinating fields in condensed matter physics giving rise to exotic and puzzling phases of matter. In this thesis we explore three different topics: in the first part of the thesis we investigate unconventional superconductivity in a one-band Hubbard model within the spin-fluctuation approach. We construct phase diagrams examining the role of on-site and extended Coulomb interactions on the preferred superconducting state. In addition, we study the transitions between different symmetries and find that spin-singlet orders generate a coexistence region breaking time-reversal symmetry. Then, we focus on multiorbital systems, which offer a new route to generate superconductivity based on a direct attraction due to a large Hund's exchange. We compare this mechanism to the spin-fluctuation mediated pairing by examining two distinct multiorbital models. We find that, when the bands exhibit significant nesting, the spin-fluctuation mechanism dominates, which is relevant for systems like Sr_2RuO_4.

The second part of the thesis explores the superconducting diode effect, which exists in systems where both inversion and time-reversal symmetries are broken. In usual diode setups, time-reversal symmetry is broken by applying an in-plane magnetic field. However, we show that out-of-plane magnetization gradients also induce the diode effect, generating comparable efficiencies. Moreover, we also propose alternative device designs based on out-of-plane magnetization gradients, emphasizing the importance of an optimized gradient profile, which may significantly enhance the diode efficiency.

In the last part of the thesis, we focus on altermagnetism, a new class of magnetic order distinct from conventional ferromagnetism and antiferromagnetism. We construct minimal models for altermagnetism based on symmetry arguments, and reveal the mechanisms stabilizing this phase by examining the analytic expressions for the susceptibility. Additionally, we apply the model to relevant altermagnetic material candidates, including RuO_2, MnF_2, $FeSb_2$, κ-Cl, CrSb and MnTe, and find that it gives rise to a large Berry curvature linear in the spin-orbit coupling. Finally, we derive the Landau free energy expansion and the analytic expressions for the coefficients from the minimal model, investigating the interplay between the magnetization and the altermagnetic order parameter at domain walls and in the presence of spin-orbit coupling.

Resumé

Superledning og magnetisme er fascinerende fænomener i faststoffysik, der giver anledning til eksotiske og gådefulde faser. Denne afhandling er delt i tre: i den første del studerer vi ukonventionel superledning i Hubbard-modellen ved brug af spin-fluktuationsmetoden. Vi konstruerer fasediagrammer for at undersøge den lokale og den langtrækkende Coulomb-interaktions rolle for den foretrukne superledende tilstand. Derudover undersøger vi overgangene mellem forskellige superledende faser og finder, at spin-singlet tilstande foretrækker en speciel form for sameksistens hvor tidsomvendingssymmetrien er brudt. Herefter fokuserer vi på multiorbitale systemer, som giver en ny vej til at opnå superledning baseret på en direkte tiltrækning på grund af stor Hund's udveksling. Vi sammenligner denne mekanisme med den spin-fluktuations-medierede kobling ved at undersøge to forskellige multiorbitale modeller. Vi finder, at når båndene udviser betydelig "nesting", dominerer spin-fluktuations mekanismen, hvilket er relevant for systemer som Sr_2RuO_4.

Anden del af afhandlingen studerer den superledende diodeeffekt, som eksisterer i systemer, hvor både inversions- og tidsomvendingssymmetrier brydes. I sædvanlige diode-opsætninger brydes tidsomvendingssymmetrien ved at påføre et magnetfelt i planet. Imidlertid viser vi, at magnetiseringsgradienter uden for planet også inducerer diodeeffekten, hvilket genererer sammenlignelige diodeeffektiviteter. Desuden foreslår vi også alternative diode designs baseret på magnetiseringsgradienter uden for planet, hvilket understreger vigtigheden af en optimeret gradientprofil, som kan forbedre diodeeffektiviteten betydeligt.

I den sidste del af afhandlingen fokuserer vi på altermagnetisme, en ny klasse af magnetisk orden, der adskiller sig fra konventionel ferromagnetisme og antiferromagnetisme. Vi konstruerer minimale modeller for altermagnetisme baseret på symmetriargumenter og afslører mekanismerne, der stabiliserer denne fase ved at undersøge de analytiske udtryk for susceptibiliteten. Derudover anvender vi modellen på altermagnetiske materialekandidater, herunder RuO_2, MnF_2, $FeSb_2$, κ-Cl, CrSb og MnTe, og finder ud af at spin-bane koblingen giver anledning til en stor Berry-krumning lineær i spin-bane koblingen. Endelig udleder vi funktionalen for den fri energi og finder analytiske udtryk for koefficienterne fra den minimale model, og vi undersøger samspillet mellem magnetisering og altermagnetiske ordensparametre ved domænevægge samt i tilfælde med spin-bane kobling.

Acknowledgments

First of all, I would like to thank my supervisor, Brian M. Andersen, for the guidance and encouragement over the past few years and for giving me the opportunity to pursue my PhD in Copenhagen. These years have been invaluable for both my academic and personal growth. Your ambition and enthusiasm for the research projects have made this thesis possible and inspired me to continue in this field.

I am also indebted with Clara N. Breiø, Morten H. Christensen, Peter J. Hirschfeld, Panagiotis Kotetes, Andreas Kreisel and Astrid T. Rømer for enlightening and stimulating discussions, and to Morten for helping me with the Danish translation of the abstract. I would also like to thank the CMT group and in particular my officemates Clara N. Breiø, Cecilie Hermansen and Ida E. Nielsen for creating a great work environment and for the (never enough) Danish lessons.

I would like to express my sincere gratitude to Daniel F. Agterberg for hosting me during three months at the University of Wisconsin - Milwaukee for my external stay. I would also like to thank Danylo Radevych, Tatsuya Shishidou, Shuntaro Sumita, Kate Valerius, Michael Weinert and Yue Yu for providing a welcoming work environment during those three months. I have benefited immensely from discussions with Daniel and Yue, and I look forward to keep learning and collaborating together in the next chapter of my academic career.

I would like to extend my thanks to my closest friends from Barcelona, in particular to Griselda Ballester, Marta Carrizo, Raúl Morral, Carla Muñoz, Carlos Ruiz, Alba Torras and Santiago Vallés for the emotional support during my PhD and the many fun video calls. Thank you for preserving our friendship despite the distance; it means a lot to me.

I would also like to express my appreciation to my family, especially my mother, father and brother, for their love and encouragement. I would not have achieved this without your invaluable support. My sincere thanks go to my mom for her unwavering faith in me and confidence in my abilities. Your kindness in ensuring that we always had the best Spanish ham in Copenhagen was immensely appreciated after long days of work.

Finally, my deepest gratitude goes to my fiancé, Roger Morales, for his constant support over the past three years, the patience with our many physics discussions and his unwavering confidence in my potential, especially during times of self-doubt. I would also like to extend special thanks for your meticulous and thorough proofreading of this thesis. Thank you for uplifting me during challenging times and for celebrating our achievements together.

List of publications

This thesis is based on the following manuscripts and published papers, as indicated in each Chapter:

[1] M. Roig, A.T. Rømer, P.J. Hirschfeld and B.M. Andersen
Revisiting superconductivity in the extended one-band Hubbard model: Pairing via spin and charge fluctuations, *Phys. Rev. B* **106**, 214530 (2022).

[2] M. Roig, A.T. Rømer, A. Kreisel, P.J. Hirschfeld and B.M. Andersen
Superconductivity in multiorbital systems with repulsive interactions: Hund's pairing versus spin-fluctuation pairing, *Phys. Rev. B* **106**, L100501 (2022).

[3] M. Roig, P. Kotetes and B.M. Andersen
Superconducting diodes from magnetization gradients, *Phys. Rev. B* **109**, 144503 (2024).

[4] M. Roig, A. Kreisel, Y. Yu, B.M. Andersen and D.F. Agterberg
Minimal Models for Altermagnetism, arXiv:2402.15616.

[5] M. Roig, A. Kreisel, Y. Yu, B.M. Andersen and D.F. Agterberg
Landau theory of altermagnetism from microscopic models, in preparation (2024).

During the PhD, I also contributed to the following works, which are not included in this thesis:

[6] H.S. Røising, G. Wagner, M. Roig, A.T. Rømer and B.M. Andersen
Heat capacity double transitions in time-reversal symmetry broken superconductors, *Phys. Rev. B* **106**, 174518 (2022).

[7] C.N. Breiø, A. Kreisel, M. Roig, P.J. Hirschfeld and B.M. Andersen
Time-reversal symmetry breaking from lattice dislocations in superconductors, *Phys. Rev. B* **109**, 014505 (2024).

[8] Y. Yu, H.-G. Suh, M. Roig and D.F. Agterberg
Altermagnetism from coincident Van Hove singularities: application to κ-Cl, arXiv:2402.05180.

Contents

Introduction

Strongly correlated electron systems are an intriguing and stimulating research area in constant evolution, driven by both theoretical and experimental puzzles. An outstanding example is superconductivity, which is a fascinating phase of matter that occurs at low temperatures, where a phase transition takes place and electrons form bound states that significantly alter the properties of the system. This phenomenon was successfully explained for the first time in 1957 by the theory of Bardeen, Cooper and Schrieffer [9], attributing it to the exchange of phonons between electrons.

It was not until 1979, when superconductivity in $CeCu_2Si_2$ was discovered [10], that the first unconventional superconductor was experimentally identified. In this case, the mechanism behind superconductivity was not attributed to electron-phonon coupling, but instead should be due to a different origin. In particular, a possible mechanism could be the exchange of spin fluctuations, as a consequence of a nearby magnetic instability. A few years later, unconventional superconductivity was also discovered in the cuprate family, where a notably high-temperature superconducting phase was observed for the first time [11].

Another remarkable example of an unconventional superconductor is Sr_2RuO_4. Superconductivity in this material was discovered in 1994 with a critical temperature around 1.5 K [12]. Despite being considered an ideal candidate to understand unconventional superconductivity, after more than two decades of research describing the superconducting state in this material still remains an open problem in condensed matter physics [13]. The main theoretical challenge is to propose a consistent explanation in agreement with all experimental results, and elucidate the apparently contradicting observations [14].

Notably, realistic theoretical models for Sr_2RuO_4 must include three orbitals contributing to the superconducting state, as well as the effect of spin-orbit coupling [15, 16]. Regarding the pairing mechanism, since spin-fluctuations have been reported on this material [17], a reasonable suggestion is that they could mediate superconductivity. In this direction, assuming a spin-fluctuation mediated pairing interaction, Refs. [18,19] investigated the resulting superconducting state for Sr_2RuO_4, pointing out the role of the longer-range Coulomb repulsion to find a solution in agreement with most experimental observations. Motivated by these works, in the first part of the thesis we explore the role of longer-range Coulomb interactions in the preferred symmetry of the superconducting state for a one-band model, by obtaining the phase diagrams within the spin-fluctuation approach.

However, in multiorbital systems there is another route to mediate superconductivity, which is based on the direct attraction obtained from the bare interactions when the Hund's exchange is sufficiently larger. This has also been proposed as the pairing mechanism to describe the superconducting state in Sr_2RuO_4 [20,21]. Therefore, it is crucial to examine the spin-fluctuation mediated pairing and the direct attraction induced from the bare interactions to determine which pairing mechanisms dominates. With this purpose, in this thesis we compare the two mechanisms on equal footing for different multiorbital systems, by investigating the generated superconducting state in both cases and the corresponding critical temperatures.

Recently, another phenomenon characteristic of superconductors has attracted a lot of interest: the superconducting diode effect, which exists in device junctions when both time-reversal and inversion symmetries are broken [22]. The semiconductor diodes (p-n junctions) are widely used nowadays, and they are the basis of many electronic compounds such as signal rectifiers and photosensors. In the superconducting analogue of the diode effect, the critical supercurrents are different along opposite directions, giving rise to a non-dissipative effect. Consequently, achieving higher efficiencies for the superconducting diode effect could broaden and improve the current applications of the p-n junctions.

In the usual superconducting diode setups, time-reversal symmetry is broken through an applied in-plane magnetic field [22]. The starting point for our work is based on the previous analysis of Ref. [23], suggesting that out-of-plane magnetization gradients may also generate the diode effect. Regarding the origin of the superconducting diode effect, our particular focus in this thesis is due to the finite center-of-mass momentum of the Cooper pairs in the superconducting state, exhibiting what is known as the helical phase [24,25], which generates a preferred direction in the system and allows for nonreciprocal currents. Notably, magnetization gradients offer a new route to design devices exhibiting the diode effect, but optimizing the magnetization profile is an important task to achieve higher efficiencies.

Finally, we also investigate another relevant phenomenon in condensed matter physics, the emergent field of altermagnetism, which has recently been recognized as a new class of magnetic order [26, 27]. This unique state differs from both conventional ferromagnets and antiferromagnets. In particular, it exhibits a vanishing net magnetization, like antiferromagnets, but shows time-reversal symmetry breaking and a spin-split band structure, similar to ferromagnets. These exceptional properties make altermagnets ideal candidates for spintronic applications, as they are not sensitive to external magnetic field perturbations.

Therefore, it is important to understand the mechanisms stabilizing this phase over conventional ferromagnetism and antiferromagnetism. With this purpose, in this thesis we identify realistic minimal models that can be used to describe altermagnetic material candidates, which also provide a platform to perform analytic calculations for the Berry curvature and investigate the anomalous Hall response. In addition, since altermagnets feature net magnetization, it is a difficult task to manipulate domain walls by an external field. The minimal models also provide a setup to derive the Landau free energy expansion and investigate the magnetization induced at domain walls and due to the effect of spin-orbit coupling, in order to make predictions relevant for experimental observations.

Thesis outline

This thesis focuses on the fields of superconductivity and magnetism and has three distinct parts:

I Superconductivity from the Hubbard model

In the first part of the thesis, we explore unconventional superconductivity emerging from the Hubbard model. First, in Chapter 1 we focus on a one-band model to derive the pairing interaction from the spin-fluctuations mechanism, implementing on-site and extended Coulomb interactions. We analyze in detail the symmetries of the order parameter and the regions of coexistence between different symmetries. In Chapter 2, we focus on multiorbital systems and compare on equal footing two mechanisms inducing superconductivity: spin fluctuations and a direct attraction induced at the bare level when the Hund's exchange is sufficiently large. We examine the superconducting state in two different models: a two-orbital model describing iron-based superconductors and a three-orbital model relevant for Sr_2RuO_4.

II Superconducting diode effect

The second part of the thesis focuses on the superconducting diode effect for a Rashba superconductor that arises both in the presence of an in-plane field and a uniform out-of-plane magnetization gradient. In Chapter 3, we demonstrate that both configurations stabilize the helical phase as the preferred ground state, and compare the efficiencies obtained for the diode effect. In addition, we explore alternative configurations based on out-of-plane magnetization gradients, and compare the associated efficiencies.

III Altermagnetism

In the last part of the thesis, we first construct in Chapter 4 general minimal models for altermagnetism based on symmetry arguments, including the form of the spin-orbit coupling. The minimal models allow us to examine the mechanisms stabilizing the altermagnetic phase and derive analytic expressions for the Berry curvature. Moreover, we apply the models to relevant altermagnetic material candidates, including RuO_2, MnF_2, $FeSb_2$, κ-Cl, MnTe and CrSb. Finally, in Chapter 5 we use the previous minimal models to derive the form of the Landau free energy for altermagnetism, investigating the induced magnetization at domain walls. In addition, we analyze the role of spin-orbit coupling in both the orientation of the moments and the coupling between the magnetization and the altermagnetic order parameter.

Part I

Superconductivity from the Hubbard model

Chapter 1

Superconductivity in the extended one-band Hubbard model

Info: *Part of the content and figures of this Chapter have been published together with A.T. Rømer, P.J. Hirschfeld and B.M. Andersen in Ref.* [1]*, available at Phys. Rev. B* **106**, 214530 (2022).

1.1 Introduction

The theory of Bardeen, Cooper and Schrieffer (BCS) successfully described conventional superconductivity for the first time in 1957 [9]. In BCS theory, electrons attract each other through an effective interaction mediated by phonons, combining into bound states known as the Cooper pairs. The BCS Hamiltonian,

$$H = \sum_{\mathbf{k},\sigma} \xi_{\mathbf{k}} c^{\dagger}_{\mathbf{k}\sigma} c_{\mathbf{k}\sigma} + \sum_{\mathbf{k},\mathbf{k}'} V(\mathbf{k},\mathbf{k}') c^{\dagger}_{\mathbf{k}\uparrow} c_{-\mathbf{k}\downarrow} c_{-\mathbf{k}'\downarrow} c_{\mathbf{k}'\uparrow}, \tag{1.1}$$

provides a framework for describing the superconducting state, where $c^{\dagger}_{\mathbf{k}\sigma}$ ($c_{\mathbf{k}\sigma}$) is the creation (annihilation) operator for an electron with momentum $\mathbf{k}$ and spin σ, $\xi_{\mathbf{k}}$ denotes the dispersion, which depends on the specific model, and $V(\mathbf{k},\mathbf{k}')$ corresponds to the interaction. By diagonalizing this Hamiltonian, a self-consistent equation for the superconducting order parameter $\Delta_{\mathbf{k}}$ can be found within the mean-field approach,

$$\Delta_{\mathbf{k}} = -\sum_{\mathbf{k}'} V(\mathbf{k},\mathbf{k}') \frac{\Delta_{\mathbf{k}'}}{2E_{\mathbf{k}'}} \tanh \frac{E_{\mathbf{k}'}}{2k_B T}, \tag{1.2}$$

where $E_{\mathbf{k}}$ are the eigenvalues of the Hamiltonian and $k_B T$ denotes the temperature (in energy units). According to BCS theory, there is an effective attraction between electrons in a small window given by electron-phonon interactions, where $V(\mathbf{k},\mathbf{k}') = g < 0$. Since this cancels the minus sign on the right-hand side of Eq. (1.2), this leads to a solution for the superconducting gap, which has the same sign over the Fermi surface. This corresponds to an on-site attraction between electrons in real space, giving rise to conventional s-wave superconductivity.

In strongly correlated electron systems, the Coulomb interaction dominates over the attractive electron-phonon coupling. Hence, if $V(\mathbf{k},\mathbf{k}') = U > 0$, in principle there is no solution for the gap from Eq. (1.2). In these systems, phonons cannot mediate the attractive interaction between electrons, and the natural explanation for the pairing mechanism was the electron-electron interaction itself, leading to unconventional superconductivity. This idea was proposed in 1965 by Kohn and Luttinger [28], where they introduced a new mechanism for the pairing based on the screening of the bare Coulomb repulsion, corresponding to bubble diagrams. This gives rise to Friedel oscillations, such that Cooper pairs of higher angular momentum can take advantage of the attractive part of these oscillations. As a consequence, for these unconventional superconducting states, even though there is a repulsive interaction, a solution of Eq. (1.2) can be found if the gap changes sign for some momentum $\mathbf{q}$, $\Delta_{\mathbf{k}} = -\Delta_{\mathbf{k}+\mathbf{q}}$. This results in a nodal gap structure with different symmetries, as will be discussed in this Chapter. For instance, the superconducting symmetries include $d_{x^2-y^2}$, which has nodes along $k_x = \pm k_y$; d_{xy}, with nodes along $k_x = 0$ and $k_y = 0$; and g-wave, which has a more complex nodal structure. In addition to the screening effect, it was pointed out in Ref. [28] that exchange diagrams, which can be drawn as ladder diagrams, also play an important role in the effective interaction. Consequently, we will include both type of diagrams in our effective interaction in Sec. 1.2.

A year after the work of Kohn and Luttinger, Berk and Schrieffer analyzed the exchange of spin fluctuations in ^{3}He [29], obtaining more realistic critical temperatures compared to Ref. [28]. The idea is that spins can yield an effective interaction between electrons, thus referred to as spin-fluctuation pairing. In particular, in the random-phase approximation (RPA), the screening of the bare electron-electron interaction is accounted for by summing the contribution of bubble and ladder diagrams to all orders, with the spin susceptibility in a one-band model given by

$$\chi_{\mathrm{RPA}}(\mathbf{q},\omega) = \frac{\chi_0(\mathbf{q},\omega)}{1 - U\chi_0(\mathbf{q},\omega)}, \tag{1.3}$$

where $\chi_0(\mathbf{q},\omega)$ is the bare susceptibility evaluated at momentum $\mathbf{q}$ and frequency ω (the specific form will be given in Sec. 1.2). The assumption that these diagrams give rise to the dominant contribution relies on Stoner's criteria for the onset of magnetic order, which corresponds to $1 = U\,\mathrm{Re}\{\chi_0(\mathbf{q},0)\}$, giving rise to a divergent RPA susceptibility at zero energy [30]. The key point is that these fluctuations are strong close to a magnetic ordering and, as a consequence, can also give rise to superconductivity. We consider that at low temperatures pairing occurs in the vicinity of the Fermi surface, i.e., we focus on the static pairing interaction ($\omega = 0$) throughout this thesis.

To investigate unconventional superconductivity arising from repulsive interactions, a common approach is to use the one-band two-dimensional Hubbard model on a square lattice,

$$H = -t \sum_{\langle \mathbf{i},\mathbf{j}\rangle,\sigma} (c^\dagger_{\mathbf{i}\sigma} c_{\mathbf{j}\sigma} + \mathrm{h.c.}) - \mu \sum_{\mathbf{i}} c^\dagger_{\mathbf{i}\sigma} c_{\mathbf{i}\sigma} + U \sum_{\mathbf{i}} n_{\mathbf{i}\uparrow} n_{\mathbf{i}\downarrow}, \tag{1.4}$$

where t corresponds to the nearest-neighbor hopping, $\langle \mathbf{i},\mathbf{j}\rangle$ denotes the sum over nearest neighbors, μ is the chemical potential and U is the on-site Coulomb repulsion. In this equation, $c^\dagger_{\mathbf{i}\sigma}$ ($c_{\mathbf{i}\sigma}$) refers to the creation (annihilation) operator for an electron at site $\mathbf{i}$ with spin σ, where $\mathbf{i}$

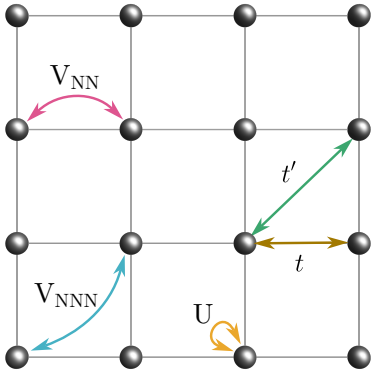

Figure 1.1: Illustration of the two-dimensional extended Hubbard model on the square lattice. We include on-site (U), nearest-neighbor (V_{NN}) and next-nearest neighbor (V_{NNN}) Coulomb interactions, while t and t' denote the nearest neighbor and next-nearest neighbor hoppings.

is the shorthand notation for $\mathbf{R_i}$ denoting the coordinates on a two-dimensional square lattice (with lattice constant $a = 1$).

This model has already been addressed by many theoretical works [28, 31–61], including exact methods on small systems, weak-coupling approaches and spin-fluctuation pairing obtained within RPA. These approaches in general find that the superconducting gap has $d_{x^2-y^2}$ symmetry close to half filling, considering nearest-neighbor hopping and a smaller next-nearest neighbor hopping, which becomes a model relevant for cuprates. Away from half filling, different superconducting gap symmetries are present, which also depend on the coupling strength. In particular, Ref. [50] constructed the phase diagram of the leading superconducting instabilities from an RPA spin-fluctuation approach, including on-site repulsion for a different range of interactions and band structures, by varying the next-nearest neighbor hopping. Even though spin-fluctuation-mediated pairing does not include self-energy corrections, recent studies reported that it yields comparable results to other approaches [52, 57].

However, the previous works focused only on the case of on-site Coulomb repulsion, but longer-range Coulomb interactions can also be important and give rise to different superconducting gap symmetries. When additional interactions between different sites of the lattice are included in Eq. (1.4), this leads to the extended Hubbard model, with the hoppings and interactions illustrated in Fig. 1.1. This model has also been addressed by different techniques [62–73]. In particular, previous works found that the $d_{x^2-y^2}$ symmetry is robust for a small nearest-neighbor Coulomb repulsion [63, 67, 70, 73]. Triplet superconductivity has also been found as the hole doping is increased from half filling, although further away the d_{xy} solution dominates [62]. In the weak-coupling limit, the gap with g-wave symmetry has been proposed as the leading solution around half filling [66], in contrast to previous works [64].

Moreover, longer-range Coulomb interactions should modify the phase boundaries as well as the gap structure, since higher harmonics are favored due to the repulsion on the closest sites, giving rise to a more complex nodal structure. Different superconducting symmetries may coexist close to the phase transition, as we will explore in Sec. 1.8, finding that it is possible to

form time-reversal symmetry breaking combinations of the two superconducting symmetries.

In particular, this is relevant for the material Sr_2RuO_4, where an RPA spin-fluctuation approach predicted a time-reversal symmetry breaking degeneracy between two superconducting instabilities with different symmetries [18, 74], in agreement with muon spin rotation and polar Kerr effect measurements [75, 76]. However, recent experimental observations have pointed out that the gap could have d_{xy} symmetry [77, 78]. From the spin-fluctuation approach, the role of the nearest-neighbor Coulomb repulsion is crucial, as it favors d_{xy} against $d_{x^2-y^2}$ superconductivity [19].

There is another motivation to investigate the impact of nearest-neighbor interactions. Reference [79] recently studied the doped cuprate material $Ba_{2-x}Sr_xCuO_{3+\delta}$ using angle-resolved photoemission spectroscopy (ARPES). Surprisingly, by analyzing the spinon and holon branches, they revealed a strong nearest-neighbor attraction from the coupling to phonons [80]. This effect could have an important role in high-temperature superconductors. Due to the structural and chemical similarities between one-dimensional and two-dimensional cuprate materials, this motivates studying in detail the effect of nearest-neighbor attraction on superconductivity [81–85].

In this Chapter, we present a detailed analysis of the effect of longer-range interactions on the superconducting instabilities within the RPA spin-fluctuation approach, considering a one-band two-dimensional Hubbard model. First, in Sec. 1.2 we focus on the case of repulsive on-site, nearest-neighbor and next-nearest-neighbor interactions and derive the effective interaction from spin-fluctuation mediated pairing. With this interaction, we solve for the leading superconducting symmetries using the linearized gap equation and self-consistent approaches, as explained in Secs. 1.3 and 1.4, respectively, analyzing in detail the gap symmetries in Sec. 1.4. We discuss the effect of longer-range Coulomb repulsion on the pairing by Fourier transforming it to real space in Sec. 1.5. Then, in Sec 1.6 we map out the phase diagram, and we analyze the gap structure in momentum space in Sec. 1.7. In order to study the different phase transitions, in Sec. 1.8 we examine the coexistence regions between different symmetries. Next, motivated by Ref. [79], in Sec. 1.9 we consider only the on-site Coulomb repulsion and additionally introduce a nearest-neighbor attraction to study the leading superconducting symmetries. Finally, in Sec. 1.10 we present the conclusions of this Chapter.

1.2 Derivation of the effective interaction

In this section, we derive the effective interaction within the RPA approximation including bubble and ladder diagrams [86, 87]. First, we include only on-site Coulomb interactions and derive the effective interaction generalizing the formalism to include spin dependence, which will also be useful in Chapter 2. Next, we turn to the discussion of the extended Hubbard model including longer-range interactions, and derive the expression for the pairing in this case.

1.2.1 On-site Coulomb repulsion

We start from the Hamiltonian including only bare repulsive interactions, and then we generalize the interaction term to include the screening due to higher-order processes within RPA.

Therefore, we focus on the one-band two-dimensional Hubbard model on a square lattice,

$$H = -t \sum_{\langle \mathbf{i},\mathbf{j}\rangle,\sigma} (c^\dagger_{\mathbf{i}\sigma} c_{\mathbf{j}\sigma} + \text{h.c.}) - t' \sum_{\langle\langle \mathbf{i},\mathbf{j}\rangle\rangle,\sigma} (c^\dagger_{\mathbf{i}\sigma} c_{\mathbf{j}\sigma} + \text{h.c.}) - \mu \sum_{\mathbf{i},\sigma} n_{\mathbf{i}\sigma} + H_{\text{int}}, \tag{1.5}$$

including nearest-neighbors (NN) hopping t and next-nearest-neighbors (NNN) hopping t' (see Fig. 1.1), with $n_{\mathbf{i}\sigma} = c^\dagger_{\mathbf{i}\sigma} c_{\mathbf{i}\sigma}$. In this Chapter, we set $t = 1$ for the energy scale and we choose to fix the filling $\langle n \rangle = \frac{1}{N} \sum_{\mathbf{k},\sigma} \left\langle c^\dagger_{\mathbf{k}\sigma} c_{\mathbf{k}\sigma} \right\rangle$ and adjust the chemical potential correspondingly, with N denoting the number of $\mathbf{k}$-points.

Considering only on-site Coulomb interaction U, the interaction term in the Hamiltonian is given by

$$H_{\text{int}} = \frac{U}{2} \sum_{\mathbf{i},\sigma} n_{\mathbf{i}\sigma} n_{\mathbf{i}\bar{\sigma}}. \tag{1.6}$$

We can Fourier transform the Hamiltonian to momentum space,

$$H = \sum_{\mathbf{k},\sigma} \xi_{\mathbf{k}} c^\dagger_{\mathbf{k}\sigma} c_{\mathbf{k}\sigma} + H_{\text{int}}, \tag{1.7}$$

where the dispersion corresponds to $\xi_{\mathbf{k}} = -2t(\cos k_x + \cos k_y) - 4t' \cos k_x \cos k_y - \mu$, and the interacting part of the Hamiltonian considering zero center-of-mass momenta for the Cooper pairs corresponds to

$$H_{\text{int}} = \frac{U}{2} \sum_{\mathbf{k},\mathbf{k}',\sigma} c^\dagger_{\mathbf{k}\sigma} c^\dagger_{-\mathbf{k}\bar{\sigma}} c_{-\mathbf{k}'\bar{\sigma}} c_{\mathbf{k}'\sigma}. \tag{1.8}$$

Since it will be convenient when introducing longer-range Coulomb interactions, we rewrite this Hamiltonian in the general form

$$H_{\text{int}} = \sum_{\mathbf{k},\mathbf{k}',\sigma_i} [U]^{\sigma_1\sigma_2}_{\sigma_3\sigma_4} c^\dagger_{\mathbf{k}\sigma_1} c^\dagger_{-\mathbf{k}\sigma_3} c_{-\mathbf{k}'\sigma_2} c_{\mathbf{k}'\sigma_4}, \tag{1.9}$$

with the bare interaction

$$\begin{aligned} [U]^{\sigma\,\bar{\sigma}}_{\bar{\sigma}\,\sigma} &= U, \\ [U]^{\sigma\,\sigma}_{\bar{\sigma}\,\bar{\sigma}} &= -U. \end{aligned} \tag{1.10}$$

This relation can be verified by anticommuting the fermionic operators in Eq. (1.9). The notation introduced above is also useful to generalize the interactions to a multiorbital case, as we will see in Chapter 2.

Let us now introduce the form for the general interaction including bare elements and higher-order diagrams,

$$H_{\text{int}} = \sum_{\mathbf{k},\mathbf{k}',\sigma_i} [V(\mathbf{k},\mathbf{k}')]^{\sigma_1\sigma_2}_{\sigma_3\sigma_4} c^\dagger_{\mathbf{k}\sigma_1} c^\dagger_{-\mathbf{k}\sigma_3} c_{-\mathbf{k}'\sigma_2} c_{\mathbf{k}'\sigma_4}, \tag{1.11}$$

where the pairing interaction corresponds to $[V(\mathbf{k},\mathbf{k}')]^{\sigma_1\sigma_2}_{\sigma_3\sigma_4} = [U]^{\sigma_1\sigma_2}_{\sigma_3\sigma_4} + [V_{\text{eff}}(\mathbf{k},\mathbf{k}')]^{\sigma_1\sigma_2}_{\sigma_3\sigma_4}$. Thus, the bare interaction gives the first-order correction to the effective interaction, and higher-order terms are obtained by summing bubble and ladder diagrams to all orders in U. The effective interaction diagram is shown in Fig. 1.2(a), while the bare interaction corresponds to Fig. 1.2(b). Since in this case we consider only on-site Coulomb repulsion, the range of the

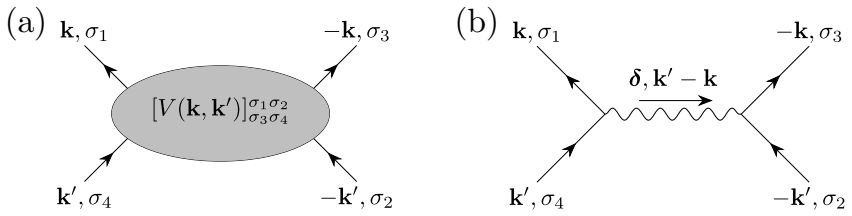

Figure 1.2: (a) Effective pairing interaction labeled by the four electronic spin indices σ_i, including the bare interaction and the contribution to all orders in U from bubble and ladder diagrams. (b) Bare interaction diagram with $\boldsymbol{\delta}$ denoting the real space vector labelling the range of the bare Coulomb interaction.

interaction corresponds to $\boldsymbol{\delta} = \mathbf{0}$. However, the $\boldsymbol{\delta}$-vector will become important in the presence of longer-range interactions, as we will discuss in the following subsection.

We begin by deriving the effective interaction from bubble diagrams. The second-order diagram is shown in Fig. 1.3(a), and can be written as

$$-[V^{(2)}_{\text{bub}}(\mathbf{k}, \mathbf{k}')]^{\sigma_1\sigma_2}_{\sigma_3\sigma_4} = -\frac{1}{N\beta}[U]^{\sigma_1 s_2}_{s_1\sigma_4} \sum_{\mathbf{p}, ip_n} G_{s_3 s_2}(\mathbf{p}, ip_n) G_{s_1 s_4}(\mathbf{p} - (\mathbf{k} - \mathbf{k}'), ip_n - (ik_n - ik_n'))[U]^{s_3\sigma_2}_{\sigma_3 s_4}, \tag{1.12}$$

where $i\omega_n$, ik_n and ik_n' denote the Matsubara frequencies and the minus sign is due to the fermion loop. In this expression, summation over repeated indices s_i is implicit. We introduce the bare susceptibility as

$$\begin{aligned}[\chi_0(\mathbf{q}, i\omega_n)]^{s_1 s_2}_{s_3 s_4} &= \frac{1}{N}\int_0^\beta d\tau e^{i\omega_n \tau} \sum_{\mathbf{k}, \mathbf{k}'} \langle T_\tau c^\dagger_{\mathbf{k}-\mathbf{q} s_1}(\tau) c_{\mathbf{k} s_2}(\tau) c^\dagger_{\mathbf{k}'+\mathbf{q} s_3}(0) c_{\mathbf{k}' s_4}(0)\rangle_0 \\ &= -\frac{1}{N\beta}\sum_{\mathbf{p}, ip_n} G_{s_3 s_2}(\mathbf{p}, ip_n) G_{s_1 s_4}(\mathbf{p} - \mathbf{q}, ip_n - i\omega_n),\end{aligned} \tag{1.13}$$

where T_τ is the time-ordered operator for the imaginary time τ. To obtain the second line we have used Wick's theorem,

$$\langle T_\tau c^\dagger_{\mathbf{k}-\mathbf{q} s_1}(\tau) c_{\mathbf{k} s_2}(\tau) c^\dagger_{\mathbf{k}'+\mathbf{q} s_3}(0) c_{\mathbf{k}' s_4}(0)\rangle_0 = -\langle T_\tau c_{\mathbf{k} s_2}(\tau) c^\dagger_{\mathbf{k}'+\mathbf{q} s_3}(0)\rangle_0 \langle T_\tau c_{\mathbf{k}' s_4}(0) c^\dagger_{\mathbf{k}-\mathbf{q} s_1}(\tau)\rangle_0, \tag{1.14}$$

and we have expressed this in terms of the Green's function, $G_{s_3 s_2} = \langle T_\tau c_{\mathbf{k} s_2}(\tau) c^\dagger_{\mathbf{k} s_3}(0)\rangle_0$, Fourier transforming from imaginary time τ to the Matsubara frequency space $i\omega_n$. In the absence of spin-orbit coupling, $s_3 = s_2$ and $s_1 = s_4$, and $G_{\sigma\sigma}(\mathbf{p}) = \frac{1}{i\omega_n - \xi_{\mathbf{p}}}$. Thus, performing the sum over the fermionic Matsubara frequency ip_n, the spin-matrix elements for the susceptibility at momentum $\mathbf{q}$ and bosonic Matsubara frequency $i\omega_n$ are simply given by

$$[\chi_0(\mathbf{q}, i\omega_n)]^{\sigma\sigma'}_{\sigma'\sigma} = \frac{1}{N}\sum_{\mathbf{p}} \frac{f(\xi_{\mathbf{p}}) - f(\xi_{\mathbf{p}-\mathbf{q}})}{i\omega_n + \xi_{\mathbf{p}-\mathbf{q}} - \xi_{\mathbf{p}}}, \tag{1.15}$$

with the only non-zero elements corresponding to $\sigma = \sigma'$ and $\sigma = -\sigma'$. In the following, we will omit the Matsubara frequency dependence in the susceptibility for ease of notation, recalling from Sec. 1.1 that we consider here that pairing occurs close to the Fermi level, and thus we

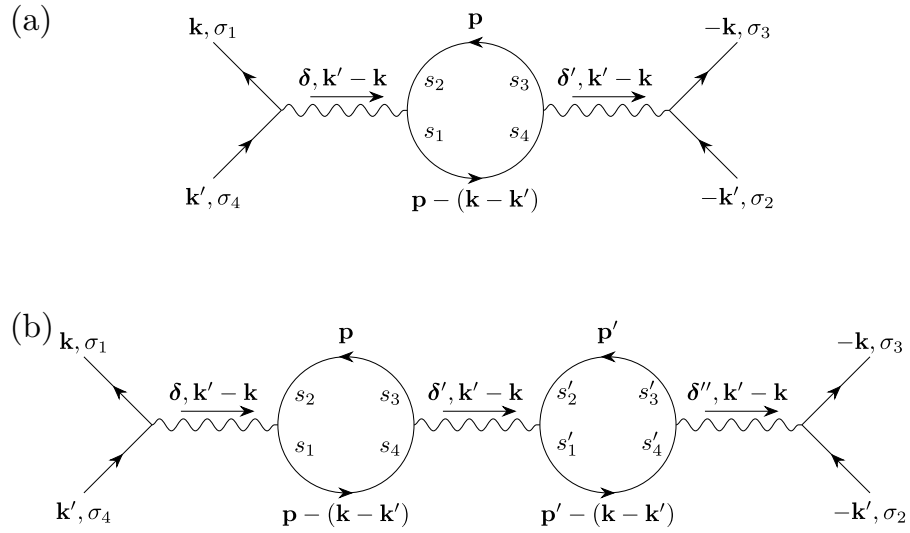

Figure 1.3: (a) Second- and (b) third-order bubble diagrams. Each interaction line carries the four spin indices, with $\boldsymbol{\delta}$ denoting the real-space vector labelling the range of the bare Coulomb interaction.

take $\omega = 0$ (after performing the analytic continuation $i\omega_n \to \omega + i\eta$, with η being a small parameter). Using the symmetry of the interaction Hamiltonian in Eq. (1.10), the second-order bubble diagram is given by

$$-[V^{(2)}_{\text{bub}}(\mathbf{k},\mathbf{k}')]^{\sigma_1\sigma_2}_{\sigma_3\sigma_4} = [U]^{\sigma_1\sigma_4}_{s_1s_2}[\chi_0(\mathbf{k}-\mathbf{k}')]^{s_1s_2}_{s_3s_4}[U]^{s_3s_4}_{\sigma_3\sigma_2} = [U\chi_0(\mathbf{k}-\mathbf{k}')U]^{\sigma_1\sigma_4}_{\sigma_3\sigma_2}. \tag{1.16}$$

The spin indices are combined to construct the matrix elements as $A_{\sigma_1+\sigma_2 D,\sigma_3+\sigma_4 D} = [A]^{\sigma_1\sigma_2}_{\sigma_3\sigma_4}$, with $A = \{U, \chi_0\}$ and $D = 2$ in our case since there are only two possibilities for spin, $\sigma_i = \{0, 1\}$. The third-order bubble diagram is shown in Fig. 1.3(b), and similarly to the previous case, it can be written as

$$\begin{aligned} -[V^{(3)}_{\text{bub}}(\mathbf{k},\mathbf{k}')]^{\sigma_1\sigma_2}_{\sigma_3\sigma_4} &= (-1)^2[U]^{\sigma_1 s_2}_{s_1\sigma_4}[\chi_0(\mathbf{k}-\mathbf{k}')]^{s_1s_2}_{s_3s_4}[U]^{s_3s'_2}_{s'_3s_4}[\chi_0(\mathbf{k}-\mathbf{k}')]^{s'_1s'_2}_{s'_3s'_4}[U]^{s'_3\sigma_2}_{\sigma_3 s'_4} \\ &= -[U\chi_0(\mathbf{k}-\mathbf{k}')U\chi_0(\mathbf{k}-\mathbf{k}')U]^{\sigma_1\sigma_4}_{\sigma_3\sigma_2}. \end{aligned} \tag{1.17}$$

Following our convention in Eq. (1.10) and in order to agree with the form of the effective pairing in Refs. [1, 18], we have to reverse all signs for the bare interaction U.[1] Therefore, the contribution from bubble diagrams to all orders corresponds to

$$[V_{\text{bub}}(\mathbf{k},\mathbf{k}')]^{\sigma_1\sigma_2}_{\sigma_3\sigma_4} = -[U(\mathbb{1} - \chi_0(\mathbf{k}-\mathbf{k}')U)^{-1}\chi_0(\mathbf{k}-\mathbf{k}')U]^{\sigma_1\sigma_4}_{\sigma_3\sigma_2}. \tag{1.18}$$

Next, we focus on the ladder diagrams. The second-order diagram is shown in Fig. 1.4(a) and is given by

$$-[V^{(2)}_{\text{lad}}(\mathbf{k},\mathbf{k}')]^{\sigma_1\sigma_2}_{\sigma_3\sigma_4} = -[U]^{\sigma_1\sigma_2}_{s_4s_1}[\chi_0(\mathbf{k}+\mathbf{k}')]^{s_4s_1}_{s_2s_3}[U]^{s_2s_3}_{\sigma_3\sigma_4} = -[U\chi_0(\mathbf{k}+\mathbf{k}')U]^{\sigma_1\sigma_2}_{\sigma_3\sigma_4}. \tag{1.19}$$

[1] Alternatively, one may proceed by summing all orders with the current sign, so that to all orders we would instead obtain $-[U(\mathbb{1} + \chi_0(\mathbf{k}-\mathbf{k}')U)^{-1}\chi_0(\mathbf{k}-\mathbf{k}')U]^{\sigma_1\sigma_4}_{\sigma_3\sigma_2}$. However, in this formulation the divergence of the susceptibility is hidden in the orbital indices, but as it was shown in Ref. [88], in the one-band model we recover the usual Stoner criteria for the spin susceptibility.

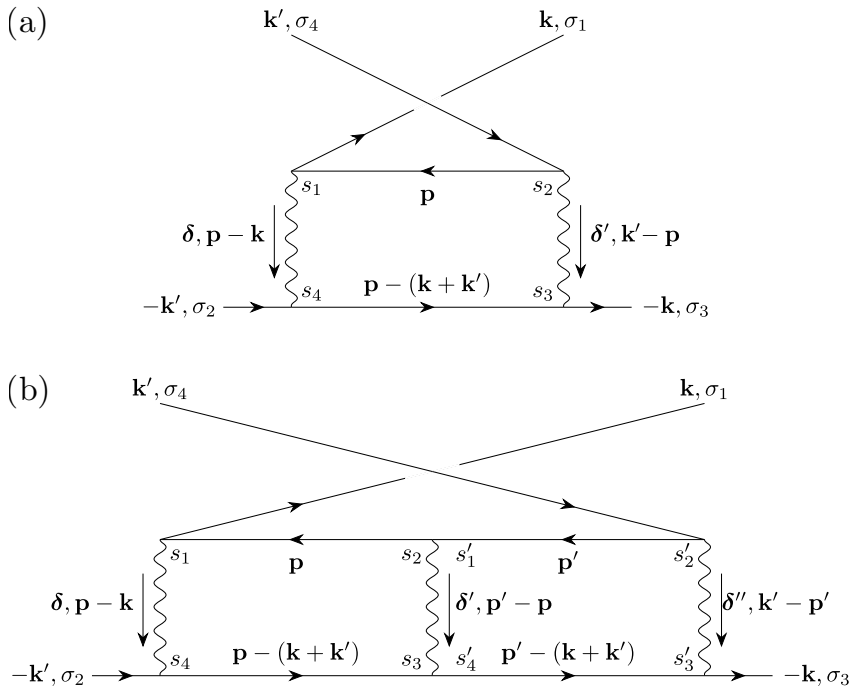

Figure 1.4: (a) Second- and (b) third-order ladder diagrams. Each interaction line carries the four spin indices, with $\boldsymbol{\delta}$ denoting the real-space vector labelling the range of the bare Coulomb interaction. In this case, the interaction line depends on the internal momentum $\mathbf{p}$ of the fermion propagators.

In this case, since there is no fermion loop we do not obtain an extra minus sign. The third-order ladder diagram is displayed in Fig. 1.4(b), and corresponds to

$$\begin{aligned} -[V^{(3)}_{\text{lad}}(\mathbf{k},\mathbf{k}')]^{\sigma_1\sigma_2}_{\sigma_3\sigma_4} &= [U]^{\sigma_1\sigma_2}_{s_4 s_1}[\chi_0(\mathbf{k}+\mathbf{k}')]^{s_4 s_1}_{s_2 s_3}[U]^{s_2 s_3}_{s_4' s_1'}[\chi_0(\mathbf{k}+\mathbf{k}')]^{s_4' s_1'}_{s_2' s_3'}[U]^{s_2' s_3'}_{\sigma_3\sigma_4} \\ &= [U\chi_0(\mathbf{k}+\mathbf{k}')U\chi_0(\mathbf{k}+\mathbf{k}')U]^{\sigma_1\sigma_2}_{\sigma_3\sigma_4}. \end{aligned} \tag{1.20}$$

Thus, reversing again the signs from the bare interactions, the contribution from ladder diagrams to all orders can be written as

$$[V_{\text{lad}}(\mathbf{k},\mathbf{k}')]^{\sigma_1\sigma_2}_{\sigma_3\sigma_4} = [U(\mathbb{1} - \chi_0(\mathbf{k}+\mathbf{k}')U)^{-1}\chi_0(\mathbf{k}+\mathbf{k}')U]^{\sigma_1\sigma_2}_{\sigma_3\sigma_4}. \tag{1.21}$$

Finally, the pairing interaction including the bare interactions and the contribution from bubble and ladder diagrams to all orders is given by

$$\begin{aligned} [V(\mathbf{k},\mathbf{k}')]^{\sigma_1\sigma_2}_{\sigma_3\sigma_4} = \quad & [U]^{\sigma_1\sigma_2}_{\sigma_3\sigma_4} - [U(\mathbb{1} - \chi_0(\mathbf{k}-\mathbf{k}')U)^{-1}\chi_0(\mathbf{k}-\mathbf{k}')U]^{\sigma_1\sigma_4}_{\sigma_3\sigma_2} \\ & + [U(\mathbb{1} - \chi_0(\mathbf{k}+\mathbf{k}')U)^{-1}\chi_0(\mathbf{k}+\mathbf{k}')U]^{\sigma_1\sigma_2}_{\sigma_3\sigma_4}. \end{aligned} \tag{1.22}$$

This form of the interaction satisfies the symmetries imposed by the interacting Hamiltonian in Eq. (1.11) obtained by anticommuting the fermionic operators,

$$[V(\mathbf{k},\mathbf{k}')]^{\sigma_1\sigma_2}_{\sigma_3\sigma_4} = -[V(\mathbf{k},-\mathbf{k}')]^{\sigma_1\sigma_4}_{\sigma_3\sigma_2}. \tag{1.23}$$

1.2.2 Longer-range Coulomb interaction

In the extended Hubbard model, the interaction Hamiltonian including bare longer-range Coulomb interactions is

$$H_{\text{int}} = \frac{1}{2}\sum_{\mathbf{i},\boldsymbol{\delta},\sigma,\sigma'} V_0(\boldsymbol{\delta}) n_{\mathbf{i}\sigma} n_{\mathbf{i}+\boldsymbol{\delta},\sigma'}, \tag{1.24}$$

with $V_0(\boldsymbol{\delta}=\mathbf{0}) = U$ for the on-site Coulomb interaction, $V_0(\boldsymbol{\delta}) = V_{\text{NN}}$ for nearest-neighbors at $\boldsymbol{\delta} = \{\pm\hat{\mathbf{x}}, \pm\hat{\mathbf{y}}\}$, and $V_0(\boldsymbol{\delta}) = V_{\text{NNN}}$ for next-nearest-neighbors at $\boldsymbol{\delta} = \{\pm(\hat{\mathbf{x}} \pm \hat{\mathbf{y}})\}$. In momentum space, this is now given by

$$H_{\text{int}} = \frac{1}{2}\sum_{\mathbf{k},\mathbf{k}',\sigma,\sigma'} V_0(\mathbf{k},\mathbf{k}') c^\dagger_{\mathbf{k}\sigma} c^\dagger_{-\mathbf{k}\sigma'} c_{-\mathbf{k}'\sigma'} c_{\mathbf{k}'\sigma}, \tag{1.25}$$

where $V_0(\mathbf{k},\mathbf{k}') = \sum_{\boldsymbol{\delta}} V_0(\boldsymbol{\delta}) e^{-i\boldsymbol{\delta}\cdot(\mathbf{k}-\mathbf{k}')}$ is the Fourier transform of the real-space interaction. In the case of NN and NNN interactions,

$$\sum_{\boldsymbol{\delta}=\{\pm\hat{\mathbf{x}},\pm\hat{\mathbf{y}}\}} V_{\text{NN}} e^{-i\boldsymbol{\delta}\cdot(\mathbf{k}-\mathbf{k}')} = 2V_{\text{NN}}\big\{\cos\big(k_x - k'_x\big) + \cos\big(k_y - k'_y\big)\big\}, \tag{1.26}$$

$$\sum_{\boldsymbol{\delta}=\{\pm(\hat{\mathbf{x}}\pm\hat{\mathbf{y}})\}} V_{\text{NNN}} e^{-i\boldsymbol{\delta}\cdot(\mathbf{k}-\mathbf{k}')} = 4V_{\text{NNN}} \cos\big(k_x - k'_x\big)\cos\big(k_y - k'_y\big). \tag{1.27}$$

With the aim of including higher-order interactions, we can use the general notation with spin indices in the pairing, so that the Hamiltonian can be written as

$$H_{\text{int}} = \sum_{\mathbf{k},\mathbf{k}',\sigma_i} [V(\mathbf{k},\mathbf{k}')]^{\sigma_1\sigma_2}_{\sigma_3\sigma_4} c^\dagger_{\mathbf{k}\sigma_1} c^\dagger_{-\mathbf{k}\sigma_3} c_{-\mathbf{k}'\sigma_2} c_{\mathbf{k}'\sigma_4}, \tag{1.28}$$

where now the pairing interaction includes both bare and effective interactions from bubble and ladder diagrams, $[V(\mathbf{k},\mathbf{k}')]^{\sigma_1\sigma_2}_{\sigma_3\sigma_4} = [V_0(\mathbf{k},\mathbf{k}')]^{\sigma_1\sigma_2}_{\sigma_3\sigma_4} + [V_{\text{eff}}(\mathbf{k},\mathbf{k}')]^{\sigma_1\sigma_2}_{\sigma_3\sigma_4}$. As opposed to the previous subsection where we included only on-site bare interactions, $[V_0(\mathbf{k},\mathbf{k}')]^{\sigma_1\sigma_2}_{\sigma_3\sigma_4}$ is now $\mathbf{k}$-dependent (see Eqs. (1.26)-(1.27)). The non-zero elements of the bare interaction correspond to

$$[V_0(\mathbf{k},\mathbf{k}')]^{\sigma,\sigma'}_{\sigma'\sigma} = U\delta_{\sigma\bar{\sigma}'} + 2V_{\text{NN}}[\cos\big(k_x - k'_x\big) + \cos\big(k_y - k'_y\big)] + 4V_{\text{NNN}}[\cos\big(k_x - k'_x\big)\cos\big(k_y - k'_y\big)], \tag{1.29}$$

and by the symmetries of the Hamiltonian in Eq. (1.28), $[V_0(\mathbf{k},\mathbf{k}')]^{\sigma,\sigma}_{\sigma'\sigma'} = -[V_0(\mathbf{k},-\mathbf{k}')]^{\sigma,\sigma'}_{\sigma'\sigma}$. The diagram corresponding to the bare interactions is shown in Fig. 1.2(b), where $\boldsymbol{\delta}$ is the vector labelling the range of the Coulomb interaction.

Focusing first on the bubble diagrams, as seen in Fig. 1.3, the sum over $\boldsymbol{\delta}$ can be done independently of the sum over the internal momentum $\mathbf{p}$. As a consequence, summing up bubble diagrams to all orders can be performed using the same procedure as for on-site interactions, obtaining

$$[V_{\text{bub}}(\mathbf{k},\mathbf{k}')]^{\sigma_1\sigma_2}_{\sigma_3\sigma_4} = -[V_0(\mathbf{k},\mathbf{k}')(\mathbb{1} - \chi_0(\mathbf{k}-\mathbf{k}')V_0(\mathbf{k}-\mathbf{k}'))^{-1}\chi_0(\mathbf{k}-\mathbf{k}')V_0(\mathbf{k},\mathbf{k}')]^{\sigma_1\sigma_4}_{\sigma_3\sigma_2}. \tag{1.30}$$

In contrast, for the ladder diagrams shown in Fig. 1.4, the interaction line depends both on the range of the Coulomb interaction and on the internal momentum $\mathbf{p}$. Therefore, the effective

interaction from the second-order ladder diagram shown in Fig. 1.4(a) yields

$$-[V^{(2)}_{\text{lad}}(\mathbf{k},\mathbf{k}')]^{\sigma_1\sigma_2}_{\sigma_3\sigma_4} = -\sum_{\boldsymbol{\delta},\boldsymbol{\delta}'} e^{-i\boldsymbol{\delta}\cdot\mathbf{k}} e^{i\boldsymbol{\delta}'\cdot\mathbf{k}'} [V_0(\boldsymbol{\delta})]^{\sigma_1\sigma_2}_{s_4s_1} \underbrace{\frac{1}{N\beta}\sum_{\mathbf{p}} e^{i\mathbf{p}\cdot(\boldsymbol{\delta}-\boldsymbol{\delta}')} G_{s_1s_2}(\mathbf{p}) G_{s_3s_4}(\mathbf{p}-(\mathbf{k}+\mathbf{k}'))}_{[\chi_0(\mathbf{k}+\mathbf{k}',\boldsymbol{\delta},\boldsymbol{\delta}')]^{s_4s_1}_{s_2s_3}} [V_0(\boldsymbol{\delta}')]^{s_2s_3}_{\sigma_3\sigma_4}, \tag{1.31}$$

where we have introduced the generalized susceptibility at zero energy [89, 90]

$$\chi_0(\mathbf{q},\boldsymbol{\delta},\boldsymbol{\delta}') = \frac{1}{N}\sum_{\mathbf{p}} e^{i\mathbf{p}\cdot(\boldsymbol{\delta}-\boldsymbol{\delta}')} \frac{f(\xi_{\mathbf{p}}) - f(\xi_{\mathbf{p}-\mathbf{q}})}{\xi_{\mathbf{p}-\mathbf{q}} - \xi_{\mathbf{p}}}. \tag{1.32}$$

The spin-matrix elements are again given by $[\chi_0(\mathbf{q},\boldsymbol{\delta},\boldsymbol{\delta}')]^{\sigma,\sigma'}_{\sigma'\sigma} = \chi_0(\mathbf{q},\boldsymbol{\delta},\boldsymbol{\delta}')$, with the only non-zero elements corresponding to $\sigma = \sigma'$ and $\sigma = -\sigma'$. Therefore, in the case of NN interactions, to perform the sum over $\boldsymbol{\delta},\boldsymbol{\delta}'$ in Eq. (1.31) we account for the extra dependence on these two spatial vectors by uplifting the susceptibility matrix to be of dimension $2^2\cdot 5\times 2^2\cdot 5$,

$$\begin{pmatrix}
[\chi(\mathbf{q},\mathbf{0},\mathbf{0})]^{\sigma_1\sigma_2}_{\sigma_3\sigma_4} & [\chi(\mathbf{q},\mathbf{0},\hat{\mathbf{x}})]^{\sigma_1\sigma_2}_{\sigma_3\sigma_4} & [\chi(\mathbf{q},\mathbf{0},-\hat{\mathbf{x}})]^{\sigma_1\sigma_2}_{\sigma_3\sigma_4} & [\chi(\mathbf{q},\mathbf{0},\hat{\mathbf{y}})]^{\sigma_1\sigma_2}_{\sigma_3\sigma_4} & [\chi(\mathbf{q},\mathbf{0},-\hat{\mathbf{y}})]^{\sigma_1\sigma_2}_{\sigma_3\sigma_4} \\
[\chi(\mathbf{q},\hat{\mathbf{x}},\mathbf{0})]^{\sigma_1\sigma_2}_{\sigma_3\sigma_4} & [\chi(\mathbf{q},\hat{\mathbf{x}},\hat{\mathbf{x}})]^{\sigma_1\sigma_2}_{\sigma_3\sigma_4} & [\chi(\mathbf{q},\hat{\mathbf{x}},-\hat{\mathbf{x}})]^{\sigma_1\sigma_2}_{\sigma_3\sigma_4} & [\chi(\mathbf{q},\hat{\mathbf{x}},\hat{\mathbf{y}})]^{\sigma_1\sigma_2}_{\sigma_3\sigma_4} & [\chi(\mathbf{q},\hat{\mathbf{x}},-\hat{\mathbf{y}})]^{\sigma_1\sigma_2}_{\sigma_3\sigma_4} \\
[\chi(\mathbf{q},-\hat{\mathbf{x}},\mathbf{0})]^{\sigma_1\sigma_2}_{\sigma_3\sigma_4} & [\chi(\mathbf{q},-\hat{\mathbf{x}},\hat{\mathbf{x}})]^{\sigma_1\sigma_2}_{\sigma_3\sigma_4} & [\chi(\mathbf{q},-\hat{\mathbf{x}},-\hat{\mathbf{x}})]^{\sigma_1\sigma_2}_{\sigma_3\sigma_4} & [\chi(\mathbf{q},-\hat{\mathbf{x}},\hat{\mathbf{y}})]^{\sigma_1\sigma_2}_{\sigma_3\sigma_4} & [\chi(\mathbf{q},-\hat{\mathbf{x}},-\hat{\mathbf{y}})]^{\sigma_1\sigma_2}_{\sigma_3\sigma_4} \\
[\chi(\mathbf{q},\hat{\mathbf{y}},\mathbf{0})]^{\sigma_1\sigma_2}_{\sigma_3\sigma_4} & [\chi(\mathbf{q},\hat{\mathbf{y}},\hat{\mathbf{x}})]^{\sigma_1\sigma_2}_{\sigma_3\sigma_4} & [\chi(\mathbf{q},\hat{\mathbf{y}},-\hat{\mathbf{x}})]^{\sigma_1\sigma_2}_{\sigma_3\sigma_4} & [\chi(\mathbf{q},\hat{\mathbf{y}},\hat{\mathbf{y}})]^{\sigma_1\sigma_2}_{\sigma_3\sigma_4} & [\chi(\mathbf{q},\hat{\mathbf{y}},-\hat{\mathbf{y}})]^{\sigma_1\sigma_2}_{\sigma_3\sigma_4} \\
[\chi(\mathbf{q},-\hat{\mathbf{y}},\mathbf{0})]^{\sigma_1\sigma_2}_{\sigma_3\sigma_4} & [\chi(\mathbf{q},-\hat{\mathbf{y}},\hat{\mathbf{x}})]^{\sigma_1\sigma_2}_{\sigma_3\sigma_4} & [\chi(\mathbf{q},-\hat{\mathbf{y}},-\hat{\mathbf{x}})]^{\sigma_1\sigma_2}_{\sigma_3\sigma_4} & [\chi(\mathbf{q},-\hat{\mathbf{y}},\hat{\mathbf{y}})]^{\sigma_1\sigma_2}_{\sigma_3\sigma_4} & [\chi(\mathbf{q},-\hat{\mathbf{y}},-\hat{\mathbf{y}})]^{\sigma_1\sigma_2}_{\sigma_3\sigma_4}
\end{pmatrix}, \tag{1.33}$$

where each entry is a 4×4 matrix including spin space,

$$[\chi(\mathbf{q},\boldsymbol{\delta},\boldsymbol{\delta})]^{\sigma_1\sigma_2}_{\sigma_3\sigma_4} = \begin{pmatrix}
[\chi(\mathbf{q},\boldsymbol{\delta},\boldsymbol{\delta}')]^{\uparrow\uparrow}_{\uparrow\uparrow} & [\chi(\mathbf{q},\boldsymbol{\delta},\boldsymbol{\delta}')]^{\uparrow\uparrow}_{\uparrow\downarrow} & [\chi(\mathbf{q},\boldsymbol{\delta},\boldsymbol{\delta}')]^{\uparrow\uparrow}_{\downarrow\uparrow} & [\chi(\mathbf{q},\boldsymbol{\delta},\boldsymbol{\delta}')]^{\uparrow\uparrow}_{\downarrow\downarrow} \\
[\chi(\mathbf{q},\boldsymbol{\delta},\boldsymbol{\delta}')]^{\uparrow\downarrow}_{\uparrow\uparrow} & [\chi(\mathbf{q},\boldsymbol{\delta},\boldsymbol{\delta}')]^{\uparrow\downarrow}_{\uparrow\downarrow} & [\chi(\mathbf{q},\boldsymbol{\delta},\boldsymbol{\delta}')]^{\uparrow\downarrow}_{\downarrow\uparrow} & [\chi(\mathbf{q},\boldsymbol{\delta},\boldsymbol{\delta}')]^{\uparrow\downarrow}_{\downarrow\downarrow} \\
[\chi(\mathbf{q},\boldsymbol{\delta},\boldsymbol{\delta}')]^{\downarrow\uparrow}_{\uparrow\uparrow} & [\chi(\mathbf{q},\boldsymbol{\delta},\boldsymbol{\delta}')]^{\downarrow\uparrow}_{\uparrow\downarrow} & [\chi(\mathbf{q},\boldsymbol{\delta},\boldsymbol{\delta}')]^{\downarrow\uparrow}_{\downarrow\uparrow} & [\chi(\mathbf{q},\boldsymbol{\delta},\boldsymbol{\delta}')]^{\downarrow\uparrow}_{\downarrow\downarrow} \\
[\chi(\mathbf{q},\boldsymbol{\delta},\boldsymbol{\delta}')]^{\downarrow\downarrow}_{\uparrow\uparrow} & [\chi(\mathbf{q},\boldsymbol{\delta},\boldsymbol{\delta}')]^{\downarrow\downarrow}_{\uparrow\downarrow} & [\chi(\mathbf{q},\boldsymbol{\delta},\boldsymbol{\delta}')]^{\downarrow\downarrow}_{\downarrow\uparrow} & [\chi(\mathbf{q},\boldsymbol{\delta},\boldsymbol{\delta}')]^{\downarrow\downarrow}_{\downarrow\downarrow}
\end{pmatrix}. \tag{1.34}$$

The effective bare interaction entering in Eq. (1.31) also gets an additional dependence on the interaction range $\boldsymbol{\delta}$,

$$\begin{pmatrix}
[U]^{\sigma_1\sigma_2}_{\sigma_3\sigma_4} & 0 & 0 & 0 & 0 \\
0 & [V_0(\boldsymbol{\delta})]^{\sigma_1\sigma_2}_{\sigma_3\sigma_4} & 0 & 0 & 0 \\
0 & 0 & [V_0(\boldsymbol{\delta})]^{\sigma_1\sigma_2}_{\sigma_3\sigma_4} & 0 & 0 \\
0 & 0 & 0 & [V_0(\boldsymbol{\delta})]^{\sigma_1\sigma_2}_{\sigma_3\sigma_4} & 0 \\
0 & 0 & 0 & 0 & [V_0(\boldsymbol{\delta})]^{\sigma_1\sigma_2}_{\sigma_3\sigma_4}
\end{pmatrix}, \tag{1.35}$$

where again each entry is 4×4 in spin space and the only non-zero elements for the interaction are $[V_0(\boldsymbol{\delta})]^{\sigma\bar{\sigma}}_{\bar{\sigma}\sigma} = V_{\text{NN}}$. When additionally including NNN interactions, the susceptibility and the bare interaction matrices become $2^2\cdot 9\times 2^2\cdot 9$. Thus, the second-order contribution from ladder diagrams can generally be written as

$$\begin{aligned}
-[V^{(2)}_{\text{lad}}(\mathbf{k},\mathbf{k}')]^{\sigma_1\sigma_2}_{\sigma_3\sigma_4} &= -\sum_{\boldsymbol{\delta},\boldsymbol{\delta}'} e^{-i\boldsymbol{\delta}\cdot\mathbf{k}} e^{i\boldsymbol{\delta}'\cdot\mathbf{k}'} [V_0(\boldsymbol{\delta})]^{\sigma_1\sigma_2}_{s_4s_1} [\chi_0(\mathbf{k}+\mathbf{k}',\boldsymbol{\delta},\boldsymbol{\delta}')]^{s_4s_1}_{s_2s_3} [V_0(\boldsymbol{\delta}')]^{s_2s_3}_{\sigma_3\sigma_4} \\
&= -\sum_{\boldsymbol{\delta},\boldsymbol{\delta}'} e^{-i\boldsymbol{\delta}\cdot\mathbf{k}} e^{i\boldsymbol{\delta}'\cdot\mathbf{k}'} [V_0(\boldsymbol{\delta})\chi_0(\mathbf{k}+\mathbf{k}',\boldsymbol{\delta},\boldsymbol{\delta}')V_0(\boldsymbol{\delta}')]^{\sigma_1\sigma_2}_{\sigma_3\sigma_4}.
\end{aligned} \tag{1.36}$$

Similarly, the third-order ladder diagram in Fig. 1.4(b) can be evaluated as

$$-[V^{(3)}_{\text{lad}}(\mathbf{k},\mathbf{k}')]^{\sigma_1\sigma_2}_{\sigma_3\sigma_4} = \frac{1}{(N\beta)^2}\sum_{\boldsymbol{\delta},\boldsymbol{\delta}',\boldsymbol{\delta}''}\sum_{\mathbf{p},\mathbf{p}'}[V_0(\boldsymbol{\delta})]^{\sigma_1\sigma_2}_{s_4s_1}e^{i\boldsymbol{\delta}\cdot(\mathbf{p}-\mathbf{k})}G_{s_1s_2}(\mathbf{p})G_{s_3s_4}(\mathbf{p}-(\mathbf{k}+\mathbf{k}'))[V_0(\boldsymbol{\delta}')]^{s_2s_3}_{s_4's_1'} \\ \times e^{i\boldsymbol{\delta}'\cdot(\mathbf{p}'-\mathbf{p})}G_{s_1's_2'}(\mathbf{p}')G_{s_3's_4'}(\mathbf{p}'-(\mathbf{k}+\mathbf{k}'))[V_0(\boldsymbol{\delta}'')]^{s_2's_3'}_{\sigma_3\sigma_4}e^{i\boldsymbol{\delta}''\cdot(\mathbf{k}'-\mathbf{p})}. \tag{1.37}$$

Introducing the generalized susceptibility of Eq. (1.32),

$$-[V^{(3)}_{\text{lad}}(\mathbf{k},\mathbf{k}')]^{\sigma_1\sigma_2}_{\sigma_3\sigma_4} = e^{-i\boldsymbol{\delta}\cdot\mathbf{k}}e^{i\boldsymbol{\delta}''\cdot\mathbf{k}'}[V_0(\boldsymbol{\delta})\chi_0(\mathbf{k}+\mathbf{k}',\boldsymbol{\delta},\boldsymbol{\delta}')V_0(\boldsymbol{\delta}')\chi_0(\mathbf{k}+\mathbf{k}',\boldsymbol{\delta}',\boldsymbol{\delta}'')V_0(\boldsymbol{\delta}'')]^{\sigma_1\sigma_2}_{\sigma_3\sigma_4}. \tag{1.38}$$

Therefore, we can sum up all ladder diagrams to infinite order,

$$[V_{\text{lad}}(\mathbf{k},\mathbf{k}')]^{\sigma_1\sigma_2}_{\sigma_3\sigma_4} = \sum_{\boldsymbol{\delta},\boldsymbol{\delta}'}e^{-i\boldsymbol{\delta}\cdot\mathbf{k}}e^{i\boldsymbol{\delta}'\cdot\mathbf{k}'}[V_0(\boldsymbol{\delta})(\mathbb{1}-\chi_0(\mathbf{k}+\mathbf{k}',\boldsymbol{\delta},\boldsymbol{\delta}'')V_0(\boldsymbol{\delta}''))^{-1}\chi_0(\mathbf{k}+\mathbf{k}',\boldsymbol{\delta},\boldsymbol{\delta}')V_0(\boldsymbol{\delta}')]^{\sigma_1\sigma_2}_{\sigma_3\sigma_4}, \tag{1.39}$$

where summation over the longer-range vector $\boldsymbol{\delta}''$ is implicit.

1.2.3 Effective interaction within the RPA approximation

Finally, generalizing the notation we obtain the effective interaction including the bare term and the contribution from bubble and ladder diagrams,

$$[V_{\text{eff}}(\mathbf{k},\mathbf{k}')]^{\sigma_1\sigma_2}_{\sigma_3\sigma_4} = \sum_{\boldsymbol{\delta},\boldsymbol{\delta}'}e^{-i\boldsymbol{\delta}\cdot\mathbf{k}}e^{i\boldsymbol{\delta}'\cdot\mathbf{k}'}[W(\mathbf{k},-\mathbf{k}',\boldsymbol{\delta})\chi_{\text{RPA}}(\mathbf{k}+\mathbf{k}',\boldsymbol{\delta},\boldsymbol{\delta}')W(\mathbf{k},-\mathbf{k}',\boldsymbol{\delta}')]^{\sigma_1\sigma_2}_{\sigma_3\sigma_4} \\ - e^{-i\boldsymbol{\delta}\cdot\mathbf{k}}e^{-i\boldsymbol{\delta}'\cdot\mathbf{k}'}[W(\mathbf{k},\mathbf{k}',\boldsymbol{\delta})\chi_{\text{RPA}}(\mathbf{k}-\mathbf{k}',\boldsymbol{\delta},\boldsymbol{\delta}')W(\mathbf{k},\mathbf{k}',\boldsymbol{\delta}')]^{\sigma_1\sigma_4}_{\sigma_3\sigma_2}, \tag{1.40}$$

where we have correctly symmetrized the effective interaction to satisfy Eq. (1.23). Here, we have introduced bare interaction matrices $[W(\mathbf{k}+\mathbf{k}',\boldsymbol{\delta})]^{\sigma_1\sigma_4}_{\sigma_3\sigma_2}$ to include both the contribution from bubble and ladder diagrams, which are given by

$$[W(\mathbf{k},\mathbf{k}',\boldsymbol{\delta}=\mathbf{0})]^{\sigma\sigma}_{\sigma'\sigma'} = -U\delta_{\sigma\bar{\sigma}'} - 2V_{\text{NN}}[\cos(k_x-k_x')+\cos(k_y-k_y')] \\ - 4V_{\text{NNN}}\cos(k_x-k_x')\cos(k_y-k_y'), \tag{1.41}$$
$$[W(\mathbf{k},\mathbf{k}',\boldsymbol{\delta}=\mathbf{0})]^{\sigma\bar{\sigma}}_{\bar{\sigma}\sigma} = U, \quad [W(\mathbf{k},\mathbf{k}',\boldsymbol{\delta}\neq\mathbf{0})]^{\sigma\bar{\sigma}}_{\bar{\sigma}\sigma} = V(\boldsymbol{\delta}), \quad [W(\mathbf{k},\mathbf{k}',\boldsymbol{\delta}\neq\mathbf{0})]^{\sigma\sigma}_{\sigma\sigma} = V(\boldsymbol{\delta}).$$

In the effective pairing in Eq. (1.40), the RPA susceptibility is obtained from

$$[\chi_{\text{RPA}}(\mathbf{q},\boldsymbol{\delta},\boldsymbol{\delta}')]^{\sigma_1\sigma_2}_{\sigma_3\sigma_4} = [(\mathbb{1}-\chi_0(\mathbf{q},\boldsymbol{\delta},\boldsymbol{\delta}'')W(\mathbf{q},\boldsymbol{\delta}''))^{-1}\chi_0(\mathbf{q},\boldsymbol{\delta},\boldsymbol{\delta}')]^{\sigma_1\sigma_2}_{\sigma_3\sigma_4}, \tag{1.42}$$

with the generalized susceptibility introduced in Eq. (1.32). In the following results, we calculate the RPA susceptibility at temperature $k_BT = 0.015$ and zero energy ($\omega = 0$).

To conclude with this section, we have derived the effective interaction within RPA including on-site and longer-range Coulomb interactions, which we will use throughout this Chapter to generate the pairing and solve for the superconducting gap. However, it is also worth introducing two quantities relevant for experimental probes: the physical spin and charge susceptibilities. In particular, the differential cross section measured in neutron scattering is proportional to

the spin susceptibility, while similarly the charge susceptibility can be related to resonant X-ray scattering measurements [91,92]. In our formalism, they can be calculated as

$$\chi_{\rm sp}^{\alpha\beta}(\mathbf{q}) = \frac{1}{N}\int_0^\beta d\tau e^{i\omega_n\tau}\langle T_\tau S^\alpha_{-\mathbf{q}}(\tau)S^\beta_{\mathbf{q}}(,0)\rangle = \frac{1}{4}\sum_{\{\sigma_i\}}\sigma^\alpha_{\sigma_1,\sigma_2}\sigma^\beta_{\sigma_3,\sigma_4}[\chi_{\rm RPA}(\mathbf{q},\boldsymbol{\delta}=\mathbf{0},\boldsymbol{\delta}'=\mathbf{0})]^{\sigma_1\sigma_2}_{\sigma_3\sigma_4},$$
$$\chi_{\rm ch}(\mathbf{q}) = \frac{1}{N}\int_0^\beta d\tau e^{i\omega_n\tau}\langle T_\tau n_{-\mathbf{q}}(\tau)n_{\mathbf{q}}(0)\rangle = \frac{1}{4}\sum_{\sigma_1,\sigma_2}[\chi_{\rm RPA}(\mathbf{q},\boldsymbol{\delta}=\mathbf{0},\boldsymbol{\delta}'=\mathbf{0})]^{\sigma_1\sigma_1}_{\sigma_2\sigma_2}, \tag{1.43}$$

where we have introduced the charge density, $n_{\mathbf{q}}(\tau) = \sum_{\mathbf{k},s_1} c^\dagger_{s_1}(\mathbf{k}+\mathbf{q},\tau)c_{s_1}(\mathbf{q},\tau)$, and the spin operator, $S^\alpha_{\mathbf{q}}(\tau) = \frac{1}{2}\sum_{\mathbf{k},s_1,s_2} c^\dagger_{s_1}(\mathbf{k}+\mathbf{q},\tau)\sigma^\alpha_{s_1s_2}c_{s_2}(\mathbf{k},\tau)$, with s_1, s_2 denoting spin indices and σ^α corresponding to the three Pauli matrices. Since we do not include spin-orbit coupling nor magnetic order, $\chi^{xx}_{\rm sp}(\mathbf{q}) = \chi^{yy}_{\rm sp}(\mathbf{q}) = \chi^{zz}_{\rm sp}(\mathbf{q})$ [18,93], but this will not be the case in Chapter 2. We will use these expressions to calculate and visualize the structure of the spin and charge susceptibilities in Fig. 1.9.

1.3 Linearized gap equation

In order to obtain the leading superconducting instability, we first derive the superconducting gap equation starting from the BCS Hamiltonian,

$$H = \sum_{\mathbf{k},\sigma}\xi_{\mathbf{k}}c^\dagger_{\mathbf{k}\sigma}c_{\mathbf{k}\sigma} + \frac{1}{2}\sum_{\mathbf{k},\mathbf{k}',\sigma}[V(\mathbf{k},\mathbf{k}')]^{\sigma\bar\sigma}_{\bar\sigma\sigma}c^\dagger_{\mathbf{k}\sigma}c^\dagger_{-\mathbf{k}\bar\sigma}c_{-\mathbf{k}'\bar\sigma}c_{\mathbf{k}'\sigma}. \tag{1.44}$$

Using the mean-field approximation in the Cooper channel, the Hamiltonian is reduced to

$$H = \sum_{\mathbf{k},\sigma}\xi_{\mathbf{k}}c^\dagger_{\mathbf{k}\sigma}c_{\mathbf{k}\sigma} + \sum_{\mathbf{k},\sigma}([\Delta_{\mathbf{k}}]^\sigma_{\bar\sigma}c^\dagger_{\mathbf{k}\sigma}c^\dagger_{-\mathbf{k}\bar\sigma} + ([\Delta_{\mathbf{k}}]^\sigma_{\bar\sigma})^* c_{-\mathbf{k}\bar\sigma}c_{\mathbf{k}\sigma}), \tag{1.45}$$

with the superconducting order parameter given by

$$\begin{aligned}[\Delta_{\mathbf{k}}]^\sigma_{\bar\sigma} &= \sum_{\mathbf{k}'}([V(\mathbf{k},\mathbf{k}')]^{\sigma\bar\sigma}_{\bar\sigma\sigma} + [V(\mathbf{k},\mathbf{k}')]^{\sigma\sigma}_{\bar\sigma\bar\sigma})\langle c_{-\mathbf{k}'\bar\sigma}c_{\mathbf{k}'\sigma}\rangle \\ &= \frac{1}{2}\sum_{\mathbf{k}'}\left\{\Gamma^s_{\mathbf{k},\mathbf{k}'}\left(\langle c_{-\mathbf{k}'\bar\sigma}c_{\mathbf{k}'\sigma}\rangle - \langle c_{-\mathbf{k}'\sigma}c_{\mathbf{k}'\bar\sigma}\rangle\right) + \Gamma^t_{\mathbf{k},\mathbf{k}'}\left(\langle c_{-\mathbf{k}'\bar\sigma}c_{\mathbf{k}'\sigma}\rangle + \langle c_{-\mathbf{k}'\sigma}c_{\mathbf{k}'\bar\sigma}\rangle\right)\right\},\end{aligned} \tag{1.46}$$

where we have projected the interaction in the singlet (s) and triplet (t) channels,

$$\Gamma^{s/t}_{\mathbf{k},\mathbf{k}'} = [V_0(\mathbf{k},\mathbf{k}') + V_{\rm eff}(\mathbf{k},\mathbf{k}')]^{\sigma\bar\sigma}_{\bar\sigma\sigma} \mp [V_0(\mathbf{k},\mathbf{k}') + V_{\rm eff}(\mathbf{k},\mathbf{k}')]^{\sigma\sigma}_{\bar\sigma\bar\sigma}. \tag{1.47}$$

The one-band model can easily be solved analytically by introducing the Bogoliubov transformation that diagonalizes the Hamiltonian, thus obtaining the self-consistent BCS gap equation,

$$\Delta^{s/t}_{\mathbf{k}} = \sum_{\mathbf{k}'}\Gamma^{s/t}_{\mathbf{k},\mathbf{k}'}\frac{\Delta^{s/t}_{\mathbf{k}'}}{2E_{\mathbf{k}'}}\tanh\frac{E_{\mathbf{k}'}}{2k_BT}, \tag{1.48}$$

where for simplicity we have now omitted the spin indices in the gap.

The linearized gap equation is obtained close to the critical temperature. In this case, the mean-field order parameter is very small, and therefore we can approximate

$$E_{\mathbf{k}} = \sqrt{\xi_k^2 + \Delta^2_{\mathbf{k}}} \approx |\xi_k|. \tag{1.49}$$

Hence, in this limit the BCS gap equation can be written as [86]

$$\Delta_{\mathbf{k}}^{s/t} = \left[-\frac{1}{(2\pi)^2} \int_{\mathrm{FS}} \frac{d\mathbf{k}'}{|v_{\mathbf{k}'}|} \Gamma_{\mathbf{k},\mathbf{k}'}^{s/t} \Delta_{\mathbf{k}'}^{s/t} \right] \int_{-\xi_c}^{\xi_c} d\xi \frac{1}{2|\xi|} \tanh \frac{|\xi|}{2k_B T_c}, \tag{1.50}$$

with the Fermi velocity corresponding to $v_{\mathbf{k}} = \frac{d\xi_{\mathbf{k}}}{d\mathbf{k}}$, FS denoting the integral over the Fermi surface and ξ_c being the energy cutoff. The energy integral can be done in the limit $\xi_c < k_B T$, obtaining $\ln \frac{1.13\xi_c}{k_B T}$. Thus, the linearized gap equation corresponds to an eigenvalue problem,

$$-\frac{1}{(2\pi)^2} \int_{\mathrm{FS}} \frac{d\mathbf{k}'}{|v_{\mathbf{k}'}|} \Gamma_{\mathbf{k},\mathbf{k}'}^{s/t} \Delta_{\mathbf{k}'}^{s/t} = \lambda \Delta_{\mathbf{k}}^{s/t}, \tag{1.51}$$

where we diagonalize the matrix

$$M_{\mathbf{k},\mathbf{k}'}^{s/t} = -\frac{1}{(2\pi)^2} \frac{l_{\mathbf{k}'}}{|v_{\mathbf{k}'}|} \Gamma_{\mathbf{k},\mathbf{k}'}^{s/t}, \tag{1.52}$$

with $l_{\mathbf{k}'}$ denoting the length associated to the Fermi point $\mathbf{k}'$. In particular, to obtain the results we have parametrized the Fermi surface with 160 $\mathbf{k}$-points. The largest eigenvalue of this matrix corresponds to the leading superconducting instability, as it has the highest critical temperature, and the associated eigenvector encodes the information about the symmetry of the superconducting gap.

1.4 Gap symmetries and self-consistent solution

The aim of this section is to classify the symmetries of the superconducting gap to study the phase transitions and coexistence between phases with different symmetries. With this purpose, we have also solved self-consistently the full BCS gap equation, decomposing it into basis functions that transform as irreducible representations (irreps) under the point group D_{4h}, which is the relevant point group for the square lattice. To begin with, we focus on the point group operations and irreps of D_{4h} to rewrite the pairing interaction, allowing us to identify basis functions that transform according to these irreps. Finally, we use this result to classify the symmetries of the order parameter from the gap equation.

Let us first introduce the notation used to denote the point group symmetry operations. Firstly, E denotes the identity. Secondly, C_n corresponds to a rotation of $2\pi/n$ around the z axis, while $2C_n'$ denotes the two rotations of $2\pi/n$ around the x and y axes. Analogously, $2C_n''$ corresponds to the two rotations around the $x = y$ and $-x = y$ axes. Thirdly, σ_h, $2\sigma_v$, $2\sigma_d$ denote the mirror operations in the horizontal plane ($z = 0$), two vertical planes ($x = 0$ and $y = 0$) and two diagonal planes ($x = y$ and $x = -y$), respectively. Finally, $\mathcal{I}$ denotes the inversion (or parity) operation, and S_n is an improper rotation, which is composed of a rotation of $4\pi/n$ around the z axis followed by the inversion operation.

In Fig. 1.5 we illustrate some of the symmetry operations that leave the square lattice invariant, which act as follows on the space coordinates,

$$\begin{aligned} &E(x,y,z) = (x,y,z), \quad && C_2(x,y,z) = (-x,-y,z), \quad && C_4(x,y,z) = (y,-x,z), \\ &\sigma_v(x,y,z) = (x,-y,z), \quad && \sigma_d(x,y,z) = (y,x,z), \quad && \mathcal{I}(x,y,z) = (-x,-y,-z). \end{aligned} \tag{1.53}$$

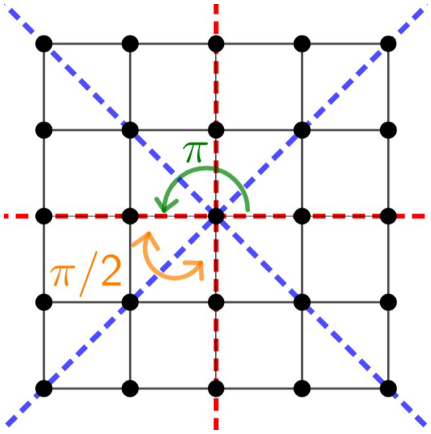

Figure 1.5: Illustration of some of the symmetry operations that leave the square lattice invariant, including a π rotation (C_2), two $\pi/2$ rotations ($2C_4$), two vertical mirrors ($2\sigma_v$) and two diagonal mirrors ($2\sigma_d$).

In addition, in Table 1.1 we show the character table for the point group D_{4h}, which includes how the irreducible representations transform under the point group operations. Since we consider a two-dimensional lattice model for the calculations, we focus only on the irreps with basis functions in the two-dimensional $x-y$ plane. The character of the identity operation specifies the dimension of the irrep. In particular, we see that A_{1g}, A_{2g}, B_{1g} and B_{2g} are one-dimensional, in contrast to E_u, which is two-dimensional. The right column of the table indicates the usual notation to denote the lowest harmonic for the superconducting symmetry belonging to the different irreps, showing that the basis function for the E_u irrep is of odd parity, as opposed to the one-dimensional irreps. Hence, since the superconducting order parameter must be antisymmetric under the exchange of two electrons, even-parity basis functions (A_{1g}, A_{2g}, B_{1g} and B_{2g} irreps) must correspond to spin singlet, whereas odd-parity basis functions (E_u irrep) correspond to spin triplet.

To illustrate how we classify the symmetries of the superconducting gap, let us consider the case of nearest-neighbors interactions only and focus on the pairing interaction, which is given

Table 1.1: Character table for the point group D_{4h}, including only the irreducible representations (irreps) with two-dimensional basis functions, with some operations illustrated in Fig. 1.5. The right column of the table lists the notation for the lowest harmonic usually associated with each superconducting symmetry.

Irrep	E	C_2	$2C_4$	$2C_2'$	$2C_2''$	$\mathcal{I}$	σ_h	$2S_4$	$2\sigma_v$	$2\sigma_d$	Lowest harmonic
A_{1g}	1	1	1	1	1	1	1	1	1	1	s
A_{2g}	1	1	1	−1	−1	1	1	1	−1	−1	g
B_{1g}	1	1	−1	1	−1	1	1	−1	1	−1	$d_{x^2-y^2}$
B_{2g}	1	1	−1	−1	1	1	1	−1	−1	1	d_{xy}
E_u	2	−2	0	0	0	−2	2	0	0	0	p

by

$$\begin{aligned}[V(\mathbf{k},\mathbf{k}')]^{\sigma_1\sigma_2}_{\sigma_3\sigma_4} &= \sum_{\boldsymbol{\delta}=\{\pm\hat{\boldsymbol{x}},\pm\hat{\boldsymbol{y}}\}} [V(\boldsymbol{\delta})]^{\sigma_1\sigma_2}_{\sigma_3\sigma_4} e^{-i\boldsymbol{\delta}\cdot(\mathbf{k}-\mathbf{k}')} \\ &= [V^{\text{tot}}_{\text{NN}}]^{\sigma_1\sigma_2}_{\sigma_3\sigma_4}\left(\cos\big(k_x-k'_x\big)+\cos\big(k_y-k'_y\big)\right),\end{aligned} \tag{1.54}$$

where $[V^{\text{tot}}_{\text{NN}}]^{\sigma_1\sigma_2}_{\sigma_3\sigma_4}$ is the full interaction for nearest neighbors in real space obtained after Fourier transforming $[V_0(\mathbf{k},\mathbf{k}')+V_{\text{eff}}(\mathbf{k},\mathbf{k}')]^{\sigma_1\sigma_2}_{\sigma_3\sigma_4}$ in Eqs. (1.29) and (1.40), respectively. More details on how we perform the Fourier transform can be found in Appendix A. By expanding the cosine of the differences, the pairing interaction can also be written as

$$\begin{aligned}[V(\mathbf{k},\mathbf{k}')]^{\sigma_1\sigma_2}_{\sigma_3\sigma_4} = [V^{\text{tot}}_{\text{NN}}]^{\sigma_1\sigma_2}_{\sigma_3\sigma_4}\Big([\cos k_x+\cos k_y][\cos k'_x+\cos k'_y]+[\cos k_x-\cos k_y][\cos k'_x-\cos k'_y] \\ +2\sin k_x\sin k'_x+2\sin k_y\sin k'_y\Big).\end{aligned} \tag{1.55}$$

Thus, in the case of nearest neighbors we can identify four different basis functions transforming as irreps of the point group D_{4h} (see Table 1.1). Specifically, we find the functions

$$\begin{aligned} g^{A_{1g}}_{\mathbf{k}} &= \cos k_x+\cos k_y, & g^{E^x_u}_{\mathbf{k}} &= \sqrt{2}\sin k_x, \\ g^{B_{1g}}_{\mathbf{k}} &= \cos k_x-\cos k_y, & g^{E^y_u}_{\mathbf{k}} &= \sqrt{2}\sin k_y. \end{aligned} \tag{1.56}$$

Importantly, the $\mathbf{k}$ and $\mathbf{k}'$ dependence in the interaction in Eq. (1.55) is now separated, which will be useful when solving for the gap. In the same way, we can follow this procedure for next-nearest neighbors, third neighbors, etc., to identify the basis functions, as summarized in Tables 1.2-1.3. We consider up to fifth neighbors in addition to the on-site term to capture the largest interactions in real space, which usually occur on the closest sites, as we demonstrate in the following Section. Note that the basis function for the A_{2g} irrep can also be written as $2\sqrt{2}(\cos k_x-\cos k_y)\sin k_x\sin k_y$, explicitly showing that the lowest order harmonic for this irrep has g-wave symmetry (see Table 1.1).

As described in Eq. (1.45), within the mean-field approximation the superconducting order parameter can be written as

$$[\Delta_{\mathbf{k}}]^{\sigma_1}_{\sigma_3} = \sum_{\mathbf{k}',\sigma_2,\sigma_4} [V(\mathbf{k},\mathbf{k}')]^{\sigma_1\sigma_2}_{\sigma_3\sigma_4}\langle c_{-\mathbf{k}'\sigma_2}c_{\mathbf{k}'\sigma_4}\rangle, \tag{1.57}$$

with $[V(\mathbf{k},\mathbf{k}')]^{\sigma_1\sigma_2}_{\sigma_3\sigma_4} = [V_0(\mathbf{k},\mathbf{k}')+V_{\text{eff}}(\mathbf{k},\mathbf{k}')]^{\sigma_1\sigma_2}_{\sigma_3\sigma_4}$ denoting the full pairing interaction in momentum space (see Eqs. (1.29) and (1.40)). Recalling Eqs. (1.55)-(1.56), this equation can be more conveniently written as

$$[\Delta_{\mathbf{k}}]^{\sigma_1}_{\sigma_3} = \sum_{\Gamma\in\text{irrep}} g^{\Gamma}_{\mathbf{k}}[\Delta_{\Gamma}]^{\sigma_1}_{\sigma_3}, \tag{1.58}$$

where $g^{\Gamma}_{\mathbf{k}}$ denotes the $\mathbf{k}$-dependent basis function for the irrep Γ and

$$[\Delta_{\Gamma}]^{\sigma_1}_{\sigma_3} = \sum_{\mathbf{k}',\sigma_2,\sigma_4} [V(\Delta\mathbf{r})]^{\sigma_1\sigma_2}_{\sigma_3\sigma_4}\, g^{\Gamma}_{\mathbf{k}'}\,\langle c_{-\mathbf{k}'\sigma_2}c_{\mathbf{k}'\sigma_4}\rangle, \tag{1.59}$$

where $[V(\Delta\mathbf{r})]^{\sigma_1\sigma_2}_{\sigma_3\sigma_4}$ is the real-space pairing interaction (see Appendix A). Hence, we can identify the symmetries of the superconducting gap equation by calculating all $[\Delta_{\Gamma}]^{\sigma_1}_{\sigma_3}$ self-consistently,

Table 1.2: Basis functions for first, second and third nearest neighbors in the two-dimensional square lattice, indicating the corresponding irreducible representation (irrep).

Irrep	1st neighbors	2nd neighbors	3rd neighbors
A_{1g}	$\cos k_x + \cos k_y$	$2\cos k_x \cos k_y$	$\cos 2k_x + \cos 2k_y$
A_{2g}	-	-	-
B_{1g}	$\cos k_x - \cos k_y$	-	$\cos 2k_x - \cos 2k_y$
B_{2g}	-	$2\sin k_x \sin k_y$	-
E_u^x	$i\sqrt{2}\sin k_x$	$2i \sin k_x \cos k_y$	$i\sqrt{2}\sin 2k_x$
E_u^y	$i\sqrt{2}\sin k_y$	$2i \sin k_y \cos k_x$	$i\sqrt{2}\sin 2k_y$

Table 1.3: Basis functions for fourth and fifth nearest neighbors in the two-dimensional square lattice, indicating the corresponding irreducible representation (irrep).

Irrep	4th neighbors	5th neighbors
A_{1g}	$\sqrt{2}\cos 2k_x \cos k_y + \sqrt{2}\cos k_x \cos 2k_y$	$2\cos 2k_x \cos 2k_y$
A_{2g}	$\sqrt{2}\sin 2k_x \sin k_y - \sqrt{2}\sin k_x \sin 2k_y$	-
B_{1g}	$\sqrt{2}\cos 2k_x \cos k_y - \sqrt{2}\cos k_x \cos 2k_y$	-
B_{2g}	$\sqrt{2}\sin 2k_x \sin k_y + \sqrt{2}\sin k_x \sin 2k_y$	$2\sin 2k_x \sin 2k_y$
E_u^x	$2i \sin k_x \cos 2k_y,\ 2i \sin 2k_x \cos k_y$	$2i \sin 2k_x \cos 2k_y$
E_u^y	$2i \sin k_y \cos 2k_x,\ 2i \sin 2k_y \cos k_x$	$2i \sin 2k_y \cos 2k_x$

as described in Appendix B. In addition to classifying the symmetries, this way of rewriting the gap equation is extremely convenient as the $\mathbf{k}'$ sum can be done independently of the $\mathbf{k}$ sum, improving the efficiency of the numerical calculation. Thus, to solve for the gap we will consider lattice sizes of 120×120. We will use the self-consistent solution in Sec. 1.8 to analyze the gap symmetries and coexistence between different phases at low temperatures. Furthermore, the gap classification into the different irreps will be used throughout this Chapter, also for the linearized gap equation solution, see Secs. 1.6-1.9.

1.5 Effect of the Coulomb repulsion on the pairing interaction

In the previous section, we have identified the symmetries of the superconducting gap based on the irreps of the point group D_{4h}, as presented in Table 1.1. Moreover, we have classified the symmetries of the gap for the different neighbors, as seen in Tables 1.2-1.3. We can now use these results to inspect the full pairing interaction, $[V(\mathbf{k},\mathbf{k}')]^{\sigma_1\sigma_2}_{\sigma_3\sigma_4} = [V_0(\mathbf{k},\mathbf{k}') + V_{\text{eff}}(\mathbf{k},\mathbf{k}')]^{\sigma_1\sigma_2}_{\sigma_3\sigma_4}$ (see Eqs. (1.29) and (1.40), respectively), by Fourier transforming it to real space, as detailed in Appendix A. This is useful to visualize which neighbors provide an attractive interaction within the spin-fluctuation approach, and subsequently provides information on the possible

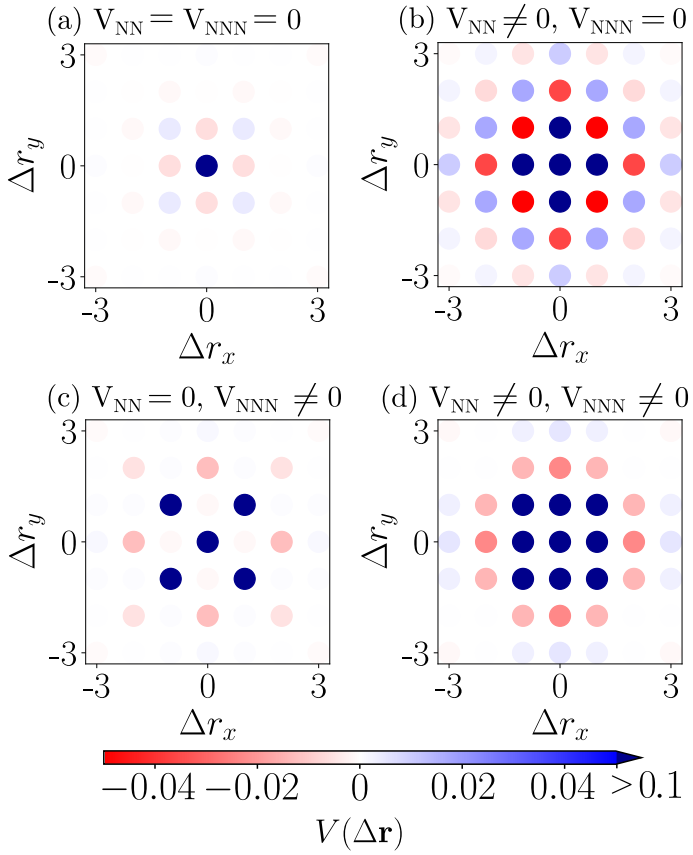

Figure 1.6: Real-space interaction strength $V(\Delta \mathbf{r})$ within the RPA approach, obtained from Fourier transforming Eqs. (1.29), (1.40) and projecting to the singlet channel (see Eq. (1.47)), for a filling $\langle n \rangle = 0.8$ and $t' = 0$. (a) Considering only on-site repulsion $U = 0.5$, (b) adding also $V_{\mathrm{NN}} = 0.25$, and (c) including $V_{\mathrm{NNN}} = 0.125$, but setting $V_{\mathrm{NN}} = 0$. (d) Full interaction for $U = 0.5$, $V_{\mathrm{NN}} = 0.25$, and $V_{\mathrm{NNN}} = 0.125$.

symmetries of the order parameter by comparing to Tables 1.2-1.3.

In Fig. 1.6 we display the real space pairing interaction $V(\Delta \mathbf{r})$ projected to the singlet channel (see Eq. (1.47)) as a function of the intersite spacing $\Delta \mathbf{r} = (\Delta r_x, \Delta r_y)$. When including only on-site Coulomb repulsion U, as seen from Fig. 1.6(a) there is a nearest-neighbor attraction generated through the spin-fluctuation mechanism. This gives rise to $d_{x^2-y^2}$ symmetry for the order parameter close to half filling [31, 36, 50, 57]. Figure 1.6(b) includes NN repulsion, leading to attraction at $\Delta \mathbf{r} = (\pm 1, \pm 1)$, $\Delta \mathbf{r} = (\pm 2, 0)$ and $\Delta \mathbf{r} = (0, \pm 2)$. Including only NNN repulsion in addition to U gives rise to attraction at $\Delta \mathbf{r} = (\pm 2, \pm 2)$, $\Delta \mathbf{r} = (\pm 2, 0)$ and $\Delta \mathbf{r} = (0, \pm 2)$, as seen in Fig. 1.6(c).

Finally, the general case including on-site, NN and NNN repulsion in shown in Fig. 1.6(d). As observed, the longer-range interactions give rise to attraction in further neighbors. Consequently, there should be pairing in higher-angular momentum channels, leading to more nodes in the gap structure (see the basis functions in Table 1.3). The generated attraction in the fourth neighbors at $\Delta \mathbf{r} = (\pm 2, \pm 1)$ and $\Delta \mathbf{r} = (\pm 1, \pm 2)$ usually stabilizes an A_{2g} gap symmetry, whereas the attraction at $\Delta \mathbf{r} = (\pm 2, 0)$ and $\Delta \mathbf{r} = (0, \pm 2)$ leads to higher-order basis functions for A_{1g}, B_{1g} and E_u symmetries, as seen from Table 1.3.

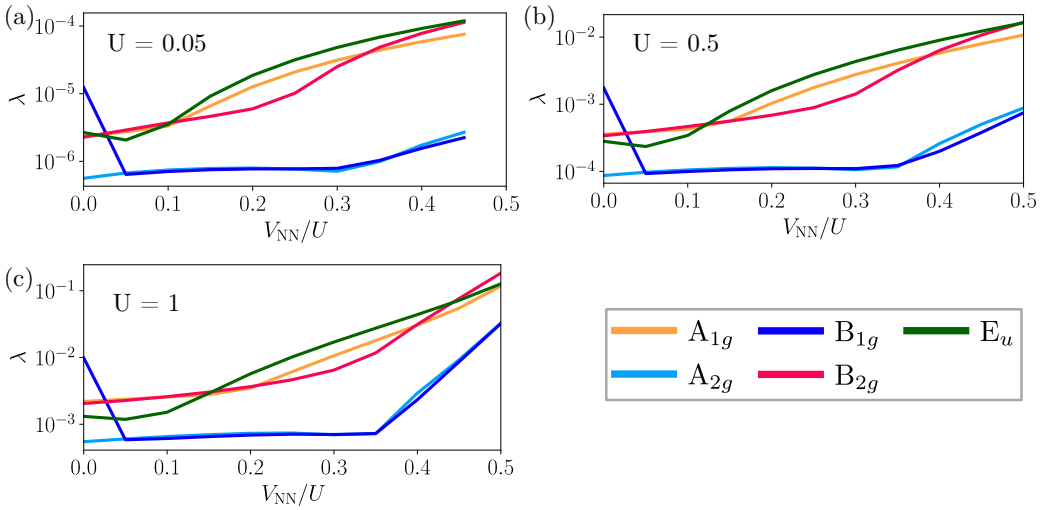

Figure 1.7: Evolution of the eigenvalues obtained from the linearized gap equation in Eq. (1.51) for different symmetry channels as a function of the NN repulsion V_{NN}/U in the case (a) $U = 0.05$, (b) $U = 0.5$ and (c) $U = 1$, for $\langle n \rangle = 0.7$, $V_{NNN} = 0$ and $t' = 0$.

1.6 Phase diagrams

In this section, we use the linearized gap equation method introduced in Eq. (1.51) to solve for the superconducting instabilities and construct phase diagrams for the leading gap symmetry as a function of filling and longer-range repulsion. This is shown in Fig. 1.8 for a fixed U and varying V_{NN} and V_{NNN}, considering $t' = 0$ (Figs. 1.8(a)-(d)) and $t' = -0.35$ (Figs. 1.8(e)-(h)), which is relevant for the cuprate Fermi surface. In particular, Fig. 1.8(a) and Fig. 1.8(e) correspond to the absence of NNN Coulomb repulsion, while in Figs. 1.8(b),(f), Figs. 1.8(c),(g) and Figs. 1.8(d),(h) we set $V_{NNN} = 0.1V_{NN}$, $0.3V_{NN}$ and $0.5V_{NN}$, respectively.

In all phase diagrams, we set the on-site Coulomb repulsion to $U = 0.5$. Since the critical U_c depends on the band structure and longer-range repulsion, it varies a lot through the phase diagrams. Specifically, the choice of U is based on the agreement between RPA and other methods in the low-U regime, as discussed in Ref. [57]. We have verified that moderate changes of the Coulomb repulsion U shift the overall eigenvalues while still showing almost the same phase transitions, as shown in Fig. 1.7 for $U = 0.05$, $U = 0.5$ and $U = 1$. The value $U = 0.5$ is generically below the critical U_c in which either the spin or the charge susceptibility diverge, thus leading to a non-superconducting instability. The exception is close to half filling in the case $t' = 0$, as indicated by the gray color in Fig. 1.8(a)-(d). This can be circumvented by increasing the temperature or lowering the on-site Coulomb repulsion, but we keep these parameters fixed in the phase diagrams for comparison.

In the case $t' = 0$ shown in Fig. 1.8(a)-(d), the band is particle-hole symmetric, and therefore the phase diagrams are symmetric for hole and electron dopings. Considering only on-site interactions (lower row on Fig. 1.8(a)-(d) for $V_{NN} = V_{NNN} = 0$), the leading superconducting instability has B_{1g} symmetry close to half filling or B_{2g} for smaller fillings, in agreement with previous works [52, 61, 66, 71].

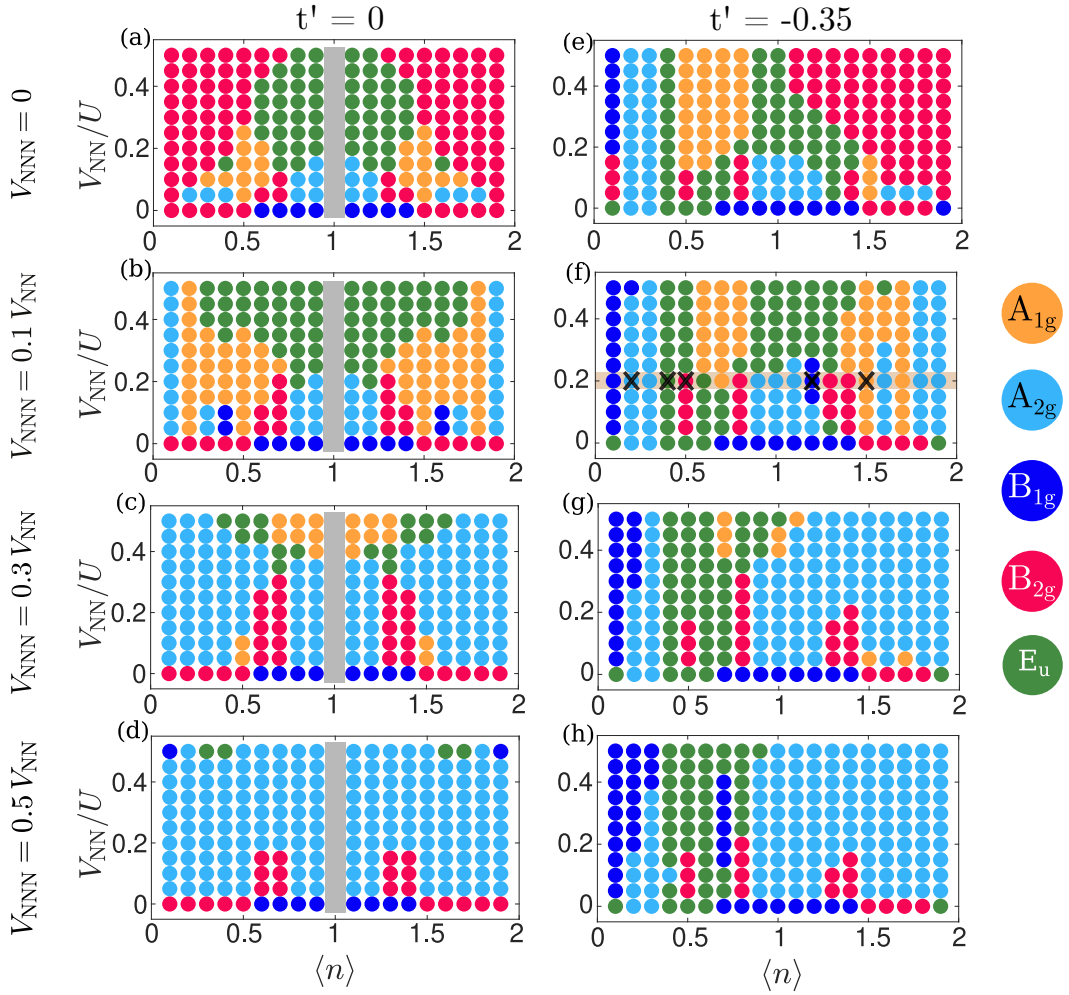

Figure 1.8: Phase diagrams of the leading superconducting gap symmetry obtained by solving the linearized gap equation (see Eq. (1.51)) for the nearest-neighbor Coulomb repulsion V_{NN} as a function of the filling $\langle n \rangle$, keeping the on-site repulsion fixed to $U = 0.5$. The colors of the dots indicate the irrep of the leading solution. In (a)-(d) we choose $t' = 0$, whereas (e)-(h) correspond to $t' = 0.35$. In (a) and (e) we set $V_{\mathrm{NNN}} = 0$, while in (b),(f), (c),(g) and (d),(h) we increase it to $V_{\mathrm{NNN}} = 0.1V_{\mathrm{NN}}$, $0.3V_{\mathrm{NN}}$ and $0.5V_{\mathrm{NN}}$, respectively. In the case $t' = 0$, for our choice of U there is a small region close to half filling ($\langle n \rangle = 1$) in which either the spin or the charge susceptibility diverge, giving rise to a non-superconducting instability, colored in gray. The black crosses in (f) denote the parameters used to show the momentum dependence of the gap in Fig. 1.9.

When NN and NNN Coulomb repulsion are included, they give rise to different leading superconducting symmetries. In particular, close to half filling the B_{1g} symmetry is rapidly suppressed due to V_{NN}, as expected from the repulsive pairing interaction on NN displayed in Fig. 1.6. As a consequence, the leading symmetry becomes A_{2g}, which dominates the phase diagram in the case of large V_{NNN}, as seen in Fig. 1.8(c)-(d) for $t' = 0$. In contrast, for smaller V_{NNN} there is another transition from A_{2g} to spin-triplet E_u superconductivity (see Fig. 1.8(a)-(b)). In the case $t' = -0.35$, displayed in Fig. 1.8(e)-(h), the E_u order is also favored against A_{2g} in the hole-doped regime.

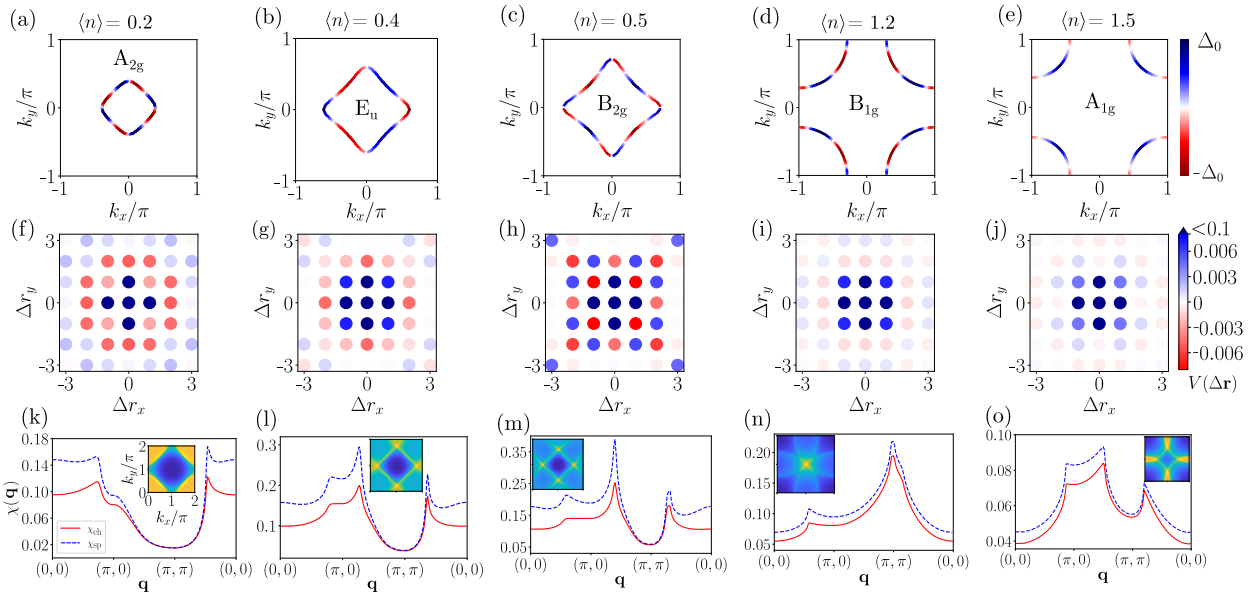

Figure 1.9: (a)-(e) Leading symmetry for the superconducting order parameter plotted at the Fermi surface obtained by solving the linearized gap equation (see Eq. (1.51)), for fillings $\langle n\rangle = 0.2$, 0.4, 0.5, 1.2, and 1.5, as indicated in Fig. 1.8(f) with black crosses. We take $U = 0.5$, $V_{\rm NN} = 0.2U$, $V_{\rm NNN} = 0.1V_{\rm NN}$, and $t' = -0.35$. (f)-(j) Real-space pairing interaction from the RPA approach in Eqs. (1.29)-(1.40) for the gap structures in (a)-(e). (k)-(o) Charge (red solid line) and spin (blue dashed line) RPA susceptibilities using Eq. (1.43) for the same parameters as panels (a)-(e) and (f)-(j). The insets show the full momentum dependence of the spin susceptibility, displaying C_4 symmetry.

1.7 Gap structure in momentum space

In the previous section, we have presented the phase diagrams for the leading superconducting instability, displayed in Fig. 1.8. Here, we analyze the momentum-dependent gap structure together with the attraction from the real-space projected pairing interaction. In some cases, this reveals the importance of higher-order basis functions within each irrep (see Tables 1.2-1.3) and therefore explains the nodal structure of the gap.

In Fig. 1.9(a)-(e) we show the gap structure on the Fermi surface for the parameters marked with black crosses in Fig. 1.8(f). Hence, they correspond to $U = 0.5$, $V_{\rm NN} = 0.2U$, $V_{\rm NNN} = 0.1V_{\rm NN}$, $t' = -0.35$ and fillings $\langle n\rangle = 0.2$, 0.4, 0.5, 1.2, and 1.5, for panels (a)-(e), respectively. Considering the same parameters, Fig. 1.9(f)-(j) show the related real-space pairing strength, and Fig. 1.9(k)-(o) are the corresponding charge and spin susceptibilities.

Focusing first on the smallest filling, $\langle n\rangle = 0.2$, there is a dominant induced attraction at sites $\Delta\mathbf{r} = (\pm 2, \pm 1)$ and $(\pm 1, \pm 2)$ that favors the A_{2g} irrep with g-wave symmetry. At $\langle n\rangle = 0.4$, the dominant irrep corresponds to E_u with the higher-order basis function $(\sin 2k_x, \sin 2k_y)$, as expected from the attraction to third neighbors $\Delta\mathbf{r} = (\pm 2, 0)$, $(0, \pm 2)$, see Table 1.2. The susceptibility shows a leading nesting peak at $(\pi, 0.2\pi)$ connecting regions of the Fermi surface with the same sign, as there is an opposite sign in the pairing interaction for the triplet channel, see Eq. (1.47). To analyze the gap structure at low temperatures for the E_u phase, we have

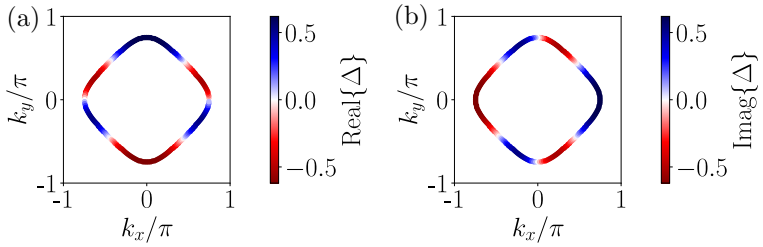

Figure 1.10: Real and imaginary part of the gap for the E_u irrep obtained by solving the full self-consistent equation in Eq. (1.58), corresponding to a $p_x + ip_y$ phase. We consider $\langle n \rangle = 0.8$, $U = 0.5$, $V_{\mathrm{NN}} = 0.3U$, $V_{\mathrm{NNN}} = 0$, $t' = 0$ and a temperature $k_B T = 0.015$.

also solved the full gap equation in Eq. (1.58). As shown in Fig. 1.10, this reveals that at low temperatures the E_u phase always condenses into a $p_x + ip_y$ solution, therefore breaking time-reversal symmetry as this gives rise to a fully gapped phase.

For a larger electron filling, $\langle n \rangle = 0.5$, the largest attraction corresponds to the diagonal sites at $\Delta\mathbf{r} = (\pm 2, \pm 2)$, $\Delta\mathbf{r} = (\pm 1, \pm 1)$, which give rise to a leading B_{2g} solution with a higher-order nodal structure. At $\langle n \rangle = 1.2$, the nesting peak at (π, π) gives rise to B_{1g} symmetry. Nevertheless, since the attraction is in further neighbors, there are many nodes in the gap structure indicating the presence of higher harmonics. Finally, in the case $\langle n \rangle = 1.5$, the real-space pairing interaction in Fig. 1.9(j) displays a small attraction to $\Delta\mathbf{r} = (0, \pm 2)$, $(\pm 2, 0)$, $(0, \pm 3)$ and $(\pm 3, 0)$, which generates a leading gap structure with A_{1g} symmetry and a higher-order nodal structure.

1.8 Coexistence phases and time-reversal symmetry breaking

The phase diagrams in Fig. 1.8 obtained by solving the linearized gap equation show that there are many transitions between different irreps, thus allowing for a possible coexistence of symmetries. To study if there exists such a coexistence region between different symmetries at low temperatures, we have solved the full self-consistent gap equation along certain cuts in the phase diagrams using Eq. (1.58).

To begin with, in Fig. 1.11(a) we show a transition between B_{1g} and B_{2g} irreps as a function of the filling $\langle n \rangle$ in the case $V_{\mathrm{NN}} = V_{\mathrm{NNN}} = 0$, $U = 0.5$ and $t' = 0$ (see the phase diagram in Fig. 1.11(b)). There is a small coexistence region where the gap prefers a complex time-reversal symmetry breaking (TRSB) phase, $B_{1g} + iB_{2g}$, as seen from the real and imaginary parts of the gap included in the inset in Fig. 1.11(a).

In addition, we have verified that TRSB is stabilized by analyzing the effect of non-magnetic inhomogeneities. In particular, non-magnetic point-like impurities directly display the symmetry of the complex superconducting gap in the currents formed around the disorder [94–97]. With this purpose, we have solved for the current densities from the Bogoliubov-de Gennes equations

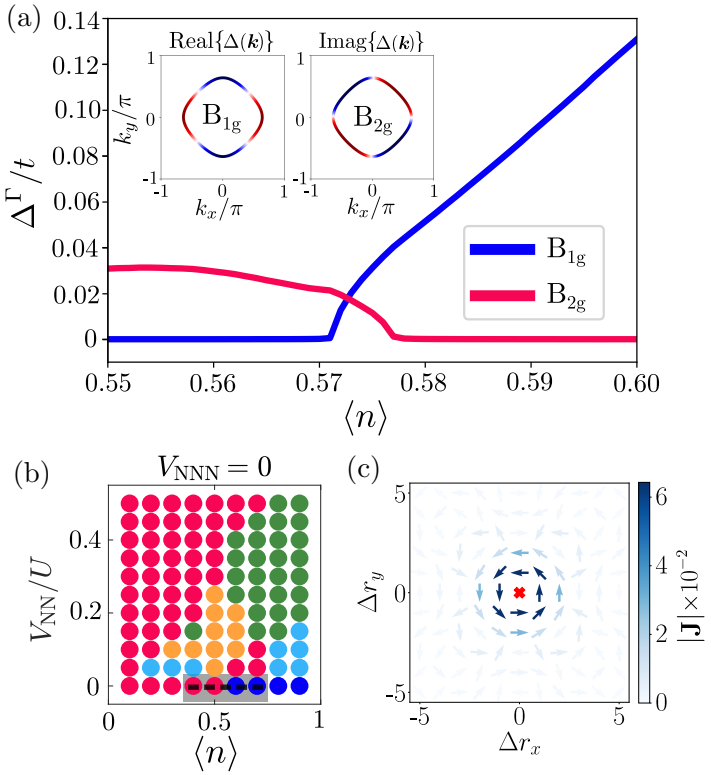

Figure 1.11: (a) Superconducting order parameters for B_{1g} and B_{2g} irreps as a function of the filling $\langle n\rangle$, obtained by solving the full self-consistent equation, see Eq. (1.58), for $V_{\mathrm{NN}} = V_{\mathrm{NNN}} = 0$, $U = 0.5$ and $t' = 0$. The inset shows the real and imaginary parts of the gap at $\langle n\rangle = 0.573$. (b) Corresponding crossing in the phase diagram from Fig. 1.8(a), denoted by the black dashed line. (c) Current patterns in the TRSB region in panel (a), induced due to the presence of a non-magnetic impurity indicated by the red cross. The currents are in units of $et/\hbar a^2$, where a corresponds to the lattice spacing.

between each lattice site $\mathbf{i}$ and the NN and NNN bonds (see Appendix C for the details),

$$J^{\mathrm{NN}}_{\mathbf{i},\boldsymbol{\delta}} = it\sum_{\sigma}\Big[\Big\langle c^{\dagger}_{\mathbf{i}+\boldsymbol{\delta}\sigma}c_{\mathbf{i}\sigma}\Big\rangle - \mathrm{h.c.}\Big],$$
$$J^{\mathrm{NNN}}_{\mathbf{i},\boldsymbol{\delta}} = it'\sum_{\sigma}\Big[\Big\langle c^{\dagger}_{\mathbf{i}+\boldsymbol{\delta}\sigma}c_{\mathbf{i}\sigma}\Big\rangle - \mathrm{h.c.}\Big], \tag{1.60}$$

where in the case of NN we have $\boldsymbol{\delta} = \{\pm\hat{\mathbf{x}}, \pm\hat{\mathbf{y}}\}$, while NNN correspond to $\boldsymbol{\delta} = \{\hat{\mathbf{x}} \pm \hat{\mathbf{y}}, -(\hat{\mathbf{x}} \pm \hat{\mathbf{y}})\}$. We project the current density for the next-nearest neighbors to the nearest-neighbors directions $\{\pm\hat{\mathbf{x}}, \pm\hat{\mathbf{y}}\}$,

$$J_{\mathbf{i},\boldsymbol{\delta}} = J^{\mathrm{NN}}_{\mathbf{i},\boldsymbol{\delta}} + \frac{\delta_{\boldsymbol{\delta},\pm\hat{\mathbf{x}}}}{\sqrt{2}}\big(J^{\mathrm{NNN}}_{\mathbf{i},\boldsymbol{\delta}+\hat{\mathbf{y}}} + J^{\mathrm{NNN}}_{\mathbf{i},\boldsymbol{\delta}-\hat{\mathbf{y}}}\big) + \frac{\delta_{\boldsymbol{\delta},\pm\hat{\mathbf{y}}}}{\sqrt{2}}\big(J^{\mathrm{NNN}}_{\mathbf{i},\boldsymbol{\delta}+\hat{\mathbf{x}}} + J^{\mathrm{NNN}}_{\mathbf{i},\boldsymbol{\delta}-\hat{\mathbf{x}}}\big). \tag{1.61}$$

Therefore, we can obtain the $\hat{\mathbf{x}}$ and the $\hat{\mathbf{y}}$ components of the total current vector at each lattice site, which are calculated by taking the average of the nearest neighbors in the $\pm\hat{\mathbf{x}}$ and $\pm\hat{\mathbf{y}}$ direction, respectively, obtaining

$$\mathbf{J}_{\mathbf{i}} = \frac{1}{2}\sum_{\boldsymbol{\delta}}\boldsymbol{\delta}J_{\mathbf{i},\boldsymbol{\delta}} = \frac{1}{2}\Big[\hat{\mathbf{x}}\big(J_{\mathbf{i},\hat{\mathbf{x}}} - J_{\mathbf{i},-\hat{\mathbf{x}}}\big) + \hat{\mathbf{y}}\big(J_{\mathbf{i},\hat{\mathbf{y}}} - J_{\mathbf{i},-\hat{\mathbf{y}}}\big)\Big]. \tag{1.62}$$

Table 1.4: Symmetries of the B_{1g} and the B_{2g} irreps and the product of both of them $B_{1g} \otimes B_{2g}$ under some operations of the point group D_{4h} (see the character table in Tab. 1.1 and Fig. 1.5). The current pattern in the coexistence phase between these two irreps shown in Fig. 1.11(c) satisfies the symmetries of $B_{1g} \otimes B_{2g}$.

	B_{1g}	B_{2g}	$B_{1g} \otimes B_{2g}$
C_2	1	1	1
$2C_4$	−1	−1	1
$2\sigma_v$	1	−1	−1
$2\sigma_d$	−1	1	−1

We use this expression to determine the current patterns due to the non-magnetic impurities at the coexistence phases in Figs. 1.11-1.12. Non-magnetic impurities are implemented as repulsive local potentials,

$$H_{\text{imp}} = V_{\text{imp}} \sum_{\mathbf{i},\sigma} c^{\dagger}_{\mathbf{i}\sigma} c_{\mathbf{i}\sigma} \delta_{\mathbf{i},\mathbf{r}_{\text{imp}}}, \tag{1.63}$$

with V_{imp} corresponding to the potential of the non-magnetic impurities placed at $\mathbf{r}_{\text{imp}}$.

Figure 1.11(c) displays the current pattern at the coexistence region in Fig. 1.11(a) in the presence of a non-magnetic impurity, denoted by the red cross. The disorder induces supercurrent loops, as also found in earlier works [94–97]. Importantly, the current pattern directly reveals the symmetry of the superconducting gap. For instance, the pattern in Fig. 1.11(c) has the symmetries of $B_{1g} \otimes B_{2g} = A_{2g}$, as seen from Table 1.4, considering the operations of D_{4h} illustrated in Fig. 1.5.

Additionally, we have also considered a crossing between B_{1g} and A_{2g} irreps, shown in Fig. 1.12(a), but in this case as a function of V_{NN}/U for a constant filling (see the phase diagram in Fig. 1.12(b)). Similarly to the previous case, there is a region where the gap condenses in a TRSB phase $B_{1g} + iA_{2g}$, as seen from the inset of Fig. 1.12, which displays the real and imaginary parts of the order parameter. The current pattern shown in Fig. 1.12(c) now exhibits the symmetries of the $B_{1g} \otimes A_{2g} = B_{2g}$ irrep, as seen from Table 1.5 for the square lattice operations depicted in Fig. 1.5. Consequently, imaging of the current patterns should directly provide information about the symmetries of the superconducting phase [98].

Previous results have shown that TRSB can also arise from the local magnetic moments

Table 1.5: Symmetries of the B_{1g} and the A_{2g} irreps and the product of both of them $B_{1g} \otimes A_{2g}$ under some operations of the point group D_{4h} (see the character table in Tab. 1.1 and Fig. 1.5). The current pattern in the coexistence phase between these two irreps shown in Fig. 1.12(c) satisfies the symmetries of $B_{1g} \otimes A_{2g}$.

	B_{1g}	A_{2g}	$B_{1g} \otimes A_{2g}$
C_2	1	1	1
$2C_4$	−1	1	−1
$2\sigma_v$	1	−1	−1
$2\sigma_d$	−1	−1	1

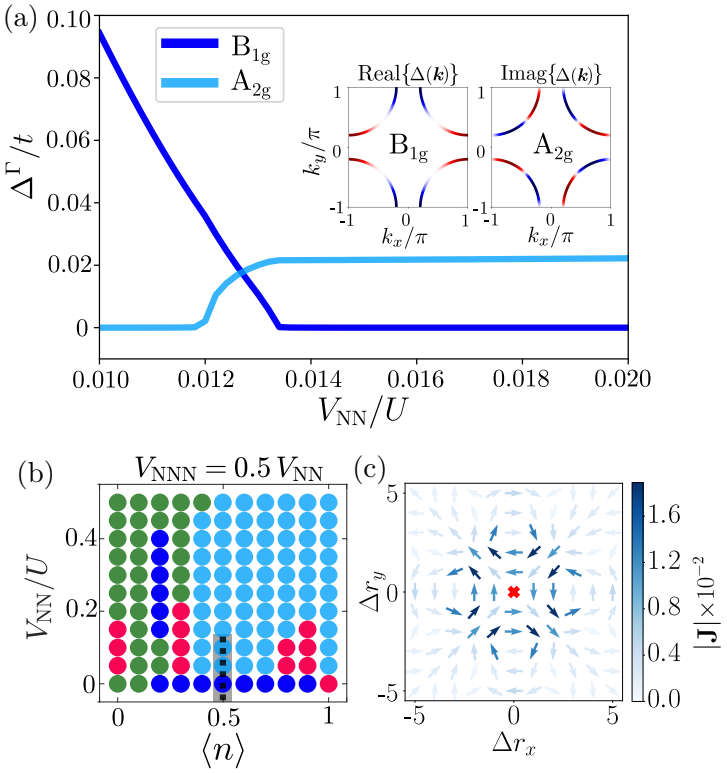

Figure 1.12: (a) Superconducting order parameters for B_{1g} and A_{2g} irreps as a function of the NN repulsion V_{NN}/U, obtained by solving the full self-consistent equation, see Eq. (1.58), for $V_{\mathrm{NNN}} = 0.5V_{\mathrm{NN}}$, $U = 0.5$ and $t' = -0.35$. The inset shows the real and imaginary parts of the gap at $V_{\mathrm{NN}}/U = 0.0126$. (b) Corresponding crossing in the phase diagram from Fig. 1.8(h), denoted by the black dashed line. (c) Current patterns in the TRSB region in panel (a), induced due to the presence of a non-magnetic impurity indicated by the red cross. The currents are in units of $et/\hbar a^2$, where a corresponds to the lattice spacing.

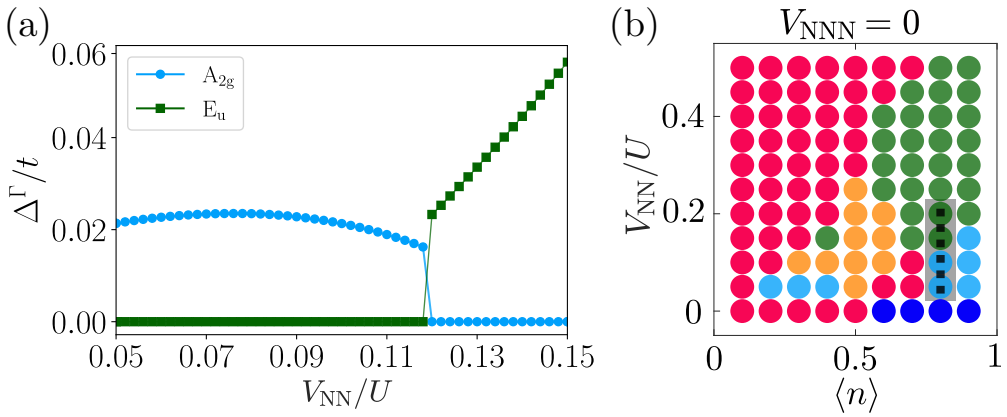

Figure 1.13: (a) Superconducting order parameters for A_{2g} and E_u irreps as a function of the NN repulsion V_{NN}/U, obtained by solving the full self-consistent equation, see Eq. (1.58), for $V_{\mathrm{NNN}} = 0$, $U = 0.5$ and $t' = 0$. (b) Corresponding crossing in the phase diagram from Fig. 1.8(a), denoted by the black dashed line.

induced by non-magnetic impurities [99–109], which is different from the TRSB emerging in our case. As given in Eq. (1.45), the mean-field Hamiltonian relevant for the study of the superconducting effects is obtained by including correlations only in the Cooper channel (particle-particle channel). To analyze the effects of magnetism, we have also included the mean-field decoupling in the particle-hole channel. We have observed numerically that the induced local magnetic moments compete with the impurity-induced local supercurrents.

Finally, we have also studied transitions between spin-singlet and spin-triplet regions from the full self-consistent gap equation. In Fig. 1.13(a) we show an example of a crossing between A_{2g} and E_u irreps as a function of $V_{\rm NN}/U$ for a constant filling in the case $V_{\rm NNN} = 0$, as seen from the phase diagram in Fig. 1.13(b). As opposed to the previous transitions studied in this section, we now include the points in Fig. 1.13(a) where we performed the self-consistent calculation of the gap, to show that, in this case, there is no coexistence region between the two symmetries, and we observe a first-order phase transition. We also find the same behavior in other regions of the phase diagrams for the crossings between triplet and singlet order parameters, which may indicate that the two phases do not coexist in our model. To understand the origin of this and the transitions between singlet and triplet irreps one could construct the Ginzburg-Landau theory including the two orders and analyze the stability and the phase diagram, which we leave for future work as this is beyond the scope of this Chapter.

1.9 Additional nearest-neighbor interaction

As discussed in Sec. 1.1, recent ARPES experiments have revealed a nearest-neighbor attractive interaction in a doped cuprate compound [79, 80]. Thus, this motivates studying the role of NN attraction in the preferred superconducting symmetry. With this purpose, we have calculated the effective pairing interaction from spin fluctuations within RPA, including first only the on-site Coulomb repulsion U (see Eq. (1.22)), and then also adding the nearest-neighbor bare attractive interaction ($V_{\rm NN} < 0$) as in Eq. (1.29). This contrasts with previous studies where both on-site and nearest-neighbor pairing were considered attractive [72, 110, 111].

Figure 1.14 displays the evolution of the leading eigenvalues for different irreps, obtained by solving the linearized gap equation (see Eq. (1.51)) as a function of filling $\langle n \rangle$, increasing the bare NN attraction. First, in Fig. 1.14(a) we show the case with no additional bare interaction, which corresponds to the bottom cut in Fig. 1.8(e) for $V_{\rm NN} = V_{\rm NNN} = 0$ and $t' = -0.35$. Within the RPA approach, the on-site Coulomb interaction U generates a nearest-neighbor attraction, which is of the order of -0.01 (for instance, see the real-space pairing interaction in Fig. 1.6(a) for the case $t' = 0$).

Including NN attraction at the bare level leads to a preferred B_{1g} (E_u) symmetry at the small (large) electron density region, as seen from Fig. 1.14(b). Increasing the NN attraction (see Fig. 1.14(c)) further boosts the B_{1g} and E_u channels, which split from the other irreps. This can be understood from the basis functions obtained by NN interactions only, shown in Eqs. (1.55)-(1.56). As seen, an attractive $V_{\rm NN}$ would directly boost the B_{1g} and E_u solutions, therefore displaying a nodal structure dominated by these lowest harmonics.

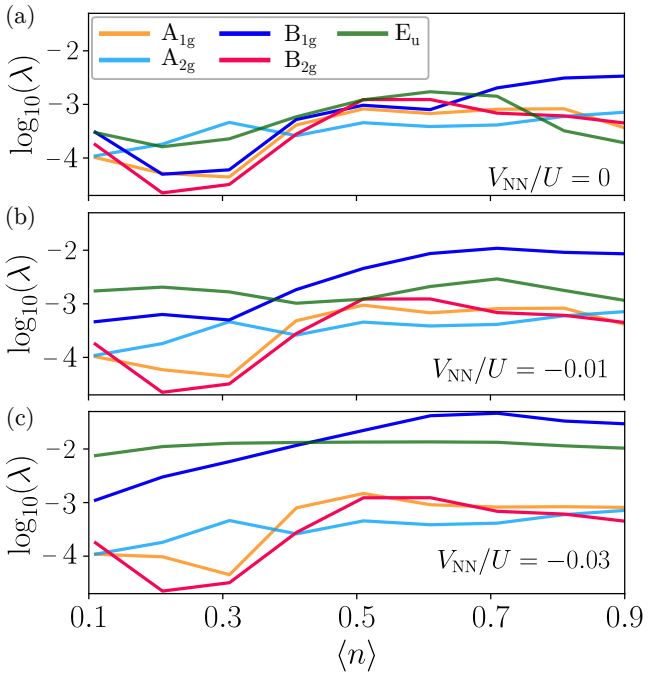

Figure 1.14: Eigenvalues for the different irreps as a function of filling $\langle n \rangle$ obtained from the linearized gap equation in Eq. (1.51), for (a) $V_{NN}/U = 0$, (b) $V_{NN}/U = -0.01$, and (c) $V_{NN}/U = -0.03$, with $U = 0.5$ and $t' = -0.35$. The additional NN attractive interaction is added at the bare level (see Eq. (1.29)).

Although these results may not be directly related to the cuprate material in Refs. [79, 80], Fig. 1.14 shows that adding a small NN attraction to the pairing interaction obtained from the repulsive on-site interaction U can significantly enhance the transition temperature of the B_{1g} irrep. Therefore, our results suggest that the strong NN attractive interaction identified in Ref. [112] could have an important role in generating high-temperature superconductivity in the cuprate compounds.

1.10 Discussion and conclusions

In this Chapter, we have analyzed the leading superconducting symmetries of the extended one-band two-dimensional Hubbard model from spin-fluctuation pairing obtained within the RPA approximation by summing up all bubble and ladder diagrams. With this purpose, we have first derived the effective interaction considering only the on-site Coulomb repulsion. Then, we have generalized the previous result by obtaining an expression for the pairing in the presence of longer-range Coulomb interactions.

We have introduced two methods to solve for the superconducting gap: the linearized gap equation and the full self-consistent solution. Even though the former is derived considering that the system is close to the critical temperature, while the full self-consistent equation allows us to analyze the gap at low temperatures, the two methods show a remarkable agreement, as seen by comparing the crossings in Fig. 1.11(a)-(b), Fig 1.12(a)-(b), and Fig. 1.13(a)-(b), where in all cases (a) corresponds to the full self-consistent solution and (b) is obtained by solving the

linearized gap equation.

We have classified the gap symmetries by rewriting the interaction for different neighbors in terms of basis functions, and identifying how these functions transform under the operations of the point group D_{4h}, as summarized in Tables 1.2-1.3. By analyzing the full interaction in real space, the classification of the gap into basis functions gives insight into the leading superconducting symmetry, as it shows the sites where the interaction becomes attractive.

In addition, we have constructed phase diagrams for the leading superconducting symmetry as a function of the filling and the nearest-neighbor repulsion, considering also different values for the next-nearest-neighbor repulsion. The results show that the phase diagram is rich, with different symmetry regions close by, and there is also a clear dominance of the A_{2g} symmetry as the NN and NNN repulsion is increased. We have also determined the momentum dependence of the gap structure and identified the origin of the nodal structure by comparing with the real-space pairing interaction, showing that the NN and NNN repulsion generally push the attraction to further away sites.

Focusing on the phase transitions, we have solved the full BCS gap equation at low temperatures, revealing a coexistence region between different symmetries that breaks time-reversal symmetry. We have explicitly demonstrated this by adding a non-magnetic impurity and calculating the currents, which reflect the symmetries of the condensate and provide evidence for TRSB. The situation is different for the transition between the spin-triplet E_u and a one-dimensional irrep. In this case, we identified a first-order phase transition and no region of coexistence between the two symmetries. As future work, to fully understand the transition between singlet and triplet phases, the Ginzburg-Landau theory could be constructed, including the interplay of the two superconducting orders. However, this would require including two order parameters, one two-dimensional describing the E_u irrep and the other one-dimensional corresponding to the spin-singlet irrep ordering.

Motivated by ARPES results in a cuprate compound where a strong NN attraction was identified [79,80], we have also added a negative V_{NN} at the bare level to the usual spin-fluctuation mediated pairing including only local repulsion U. This has shown that a small NN attraction is sufficient to enhance notably the critical temperature of the B_{1g} and the E_u symmetry channels, with a nodal structure dominated by the lowest harmonics.

Finally, our work shows that the inclusion of longer-range repulsion within the spin-fluctuation mediated pairing gives rise to a rich phase diagram, leading to many transitions between different symmetries when increasing the repulsion strength. These results could be useful to identify the nature of the superconducting gap in new unconventional superconductors where longer-range Coulomb repulsion may play a role. In particular, the importance of longer-range Coulomb interactions and the coexistence of different symmetries have been pointed out in $SrRuO_2$ or the Kagome metals [19,113]. The large number of phase transitions between different symmetry channels also opens the possibility of exotic condensates with an accidental degeneracy between two different irreducible representations breaking time-reversal symmetry.

Chapter 2

Pairing in multiorbital systems with repulsive interactions

Info: *Part of the content and figures of this Chapter have been published together with A.T. Rømer, A. Kreisel, P.J. Hirschfeld and B.M. Andersen in Ref. [2], available at Phys. Rev. B* **106**, L100501 (2022).

2.1 Introduction

In systems where all local interactions are repulsive superconductivity cannot be mediated by phonons. As discussed in Chapter 1, pairing in one-band models can arise from including the screened Coulomb interaction [114], allowing electrons to take advantage of the effective interaction in higher angular momentum channels and form Cooper pairs [29,115–118]. However, in reality many unconventional systems involve multiple bands close to the Fermi level with a strong local Coulomb repulsion [87]. A common approach to describe the interactions in these multiorbital systems is to use the Hubbard-Kanamori Hamiltonian,

$$\begin{aligned} H_{\text{int}} = U \sum_{\mathbf{i},\mu} n_{\mathbf{i}\mu\uparrow} n_{\mathbf{i}\mu\downarrow} + U' \sum_{\mathbf{i},\mu<\nu,\sigma} n_{\mathbf{i}\mu\sigma} n_{\mathbf{i}\nu\bar{\sigma}} + (U' - J) \sum_{\mathbf{i},\mu<\nu,\sigma} n_{\mathbf{i}\mu\sigma} n_{\mathbf{i}\nu\sigma} \\ + J \sum_{\mathbf{i},\mu<\nu,\sigma} c^\dagger_{\mathbf{i}\mu\sigma} c^\dagger_{\mathbf{i}\nu\bar{\sigma}} c_{\mathbf{i}\mu\bar{\sigma}} c_{\mathbf{i}\nu\sigma} + J' \sum_{\mathbf{i},\mu<\nu,\sigma} c^\dagger_{\mathbf{i}\mu\sigma} c^\dagger_{\mathbf{i}\mu\bar{\sigma}} c_{\mathbf{i}\nu\bar{\sigma}} c_{\mathbf{i}\nu\sigma}. \end{aligned} \tag{2.1}$$

Differently from the one-band case, where only the intra-orbital Hubbard U is included, now other parameters also enter at the bare level. Specifically, we also have to incorporate the inter-orbital Coulomb interaction U', the Hund's exchange J, and the pair hopping term J'.

In multiorbital systems, pairing can also arise from the screening of the Coulomb interactions, which can be investigated from the RPA approach following a similar procedure as in Chapter 1, but accounting for all bare interactions. This scenario has been considered for iron-based superconductors, where magnetic fluctuations are believed to play an important role in the superconducting pairing [119–121].

As opposed to single-band systems, a different mechanism for obtaining superconducting pairing is possible in multiorbital models. As seen from Eq. (2.1), on-site interactions can become attractive for a sufficiently large Hund's exchange J, which we refer to as Hund's pairing or Hund's mechanism. Consequently, a direct attraction at the bare level can occur for certain symmetry channels of the superconducting order parameter. This has been investigated by a different number of works [20, 21, 122–133]. Equation (2.1) shows that this mechanism gives an attraction in an inter-orbital spin-triplet channel, and therefore can induce exotic superconducting pairing states, as proposed for iron-based systems [129–131], Sr_2RuO_4 [20, 21, 125–127] and uranium-based superconductors [123–125].

In the regime where Hund's pairing can be stabilized, this mechanism should compete with spin-fluctuation pairing arising from the screening of the bare interactions. Thus, comparing the two mechanisms on equal footing is crucial to determine which one is more favorable and leads to a higher critical temperature. Since the competition of both pairing mechanisms may also depend on the band structure, this question should also be addressed by considering different systems.

In this Chapter, we compare the Hund's mechanism with the spin-fluctuation mediated pairing by analyzing the superconducting states and the corresponding critical temperature. In particular, we perform the comparison for two multiorbital systems. On the one hand, we consider a two-orbital system relevant for iron-based superconductors with two Fermi pockets centered around the Γ-point [130]. On the other hand, we take a three-orbital model relevant for Sr_2RuO_4 [18, 134]. In both systems, we use the linearized gap equation (LGE) and the self-consistent solution introduced in Secs. 1.3-1.4 to determine the gap structure, generalizing the two approaches to multiorbital systems.

We show that for multiorbital systems where the susceptibility has almost no momentum structure, both mechanisms give the same superconducting state. By contrast, when the susceptibility has sufficient momentum structure, the spin-fluctuation pairing dominates over Hund's pairing. At the bare level, the Hund's mechanism gives rise to an attraction only for $J > U'$ [20, 130]. However, when higher-order interactions are included, the Hund's pairing regime can be extended [125, 135]. We verify this result and generalize the expression for a multiorbital system with different susceptibilities.

This Chapter is organized as follows: in Sec. 2.2 we generalize the effective pairing interaction within the RPA derived in Sec. 1.2 to describe multiorbital systems. In Sec. 2.3, we classify the symmetries of the superconducting order parameter for both the two-orbital and the three-orbital models. This requires identifying how the orbital and spin matrices transform under the point group operations. We use these results in Secs. 2.4-2.5 to identify the leading symmetry channel obtained by solving the full self-consistent equation in orbital and spin space. First, Sec. 2.4 discusses the two-orbital model from Ref. [130], while in Sec. 2.5 we turn to the three-orbital model relevant for Sr_2RuO_4, and examine the leading superconducting symmetry channels from Hund's pairing and spin-fluctuation pairing in both systems. Next, in Sec. 2.6 we investigate whether the higher-order interactions included within the RPA renormalize the extent of the Hund's regime. Finally, Sec. 2.7 presents the discussion and conclusions.

2.2 Multiorbital interaction

In this section, we derive the multiorbital interaction for both Hund's pairing and spin-fluctuation mediated pairing. In the multiorbital case, the effective interaction in Eq. (1.11) can be written as

$$H_{\text{int}} = \sum_{\mathbf{k},\mathbf{k}',\tilde{\mu}} [V(\mathbf{k},\mathbf{k}')]^{\tilde{\mu}_i,\tilde{\mu}_l}_{\tilde{\mu}_j,\tilde{\mu}_k} c^\dagger_{\mathbf{k}\tilde{\mu}_i} c^\dagger_{-\mathbf{k}\tilde{\mu}_j} c_{-\mathbf{k}'\tilde{\mu}_l} c_{\mathbf{k}'\tilde{\mu}_k}, \tag{2.2}$$

where now the indices in the effective interaction are separated by a comma since $\tilde{\mu}_i = \mu_i \sigma_i$ denotes both orbital and spin indices. Considering first Hund's pairing, the effective interaction simply corresponds to

$$[V(\mathbf{k},\mathbf{k}')]^{\tilde{\mu}_i,\tilde{\mu}_l}_{\tilde{\mu}_j,\tilde{\mu}_k} = [U]^{\tilde{\mu}_i,\tilde{\mu}_l}_{\tilde{\mu}_j,\tilde{\mu}_k}, \tag{2.3}$$

where we include the bare interactions from the multiorbital Hubbard-Kanamori Hamiltonian in Eq. (2.1),

$$\begin{aligned}
&[U]^{\mu\sigma,\mu\bar{\sigma}}_{\mu\bar{\sigma},\mu\sigma} = U, \quad [U]^{\nu\sigma,\mu\bar{\sigma}}_{\mu\bar{\sigma},\nu\sigma} = U', \quad [U]^{\mu\sigma,\nu\bar{\sigma}}_{\mu\bar{\sigma},\nu\sigma} = J', \quad [U]^{\mu\sigma,\mu\bar{\sigma}}_{\nu\bar{\sigma},\nu\sigma} = J, \quad [U]^{\mu\sigma,\nu\sigma}_{\nu\sigma,\mu\sigma} = U' - J, \\
&[U]^{\mu\sigma,\mu\sigma}_{\mu\bar{\sigma},\mu\bar{\sigma}} = -U, \quad [U]^{\nu\sigma,\nu\sigma}_{\mu\bar{\sigma},\mu\bar{\sigma}} = -U', \quad [U]^{\mu\sigma,\nu\sigma}_{\mu\bar{\sigma},\nu\bar{\sigma}} = -J', \quad [U]^{\mu\sigma,\nu\sigma}_{\nu\bar{\sigma},\mu\bar{\sigma}} = -J, \quad [U]^{\mu\sigma,\mu\sigma}_{\nu\sigma,\nu\sigma} = -U' + J,
\end{aligned} \tag{2.4}$$

with μ and ν denoting different orbitals. We assume spin-rotational invariance, so that $U' = U - 2J$ and $J' = J$ [136]. Therefore, in the Hund's mechanism, the on-site interactions give rise to attraction in certain channels, which can generate superconductivity. Specifically, for a repulsive inter-orbital interaction $U' > 0$, an attractive pairing arises for $J > U'$. Equivalently, using the spin-rotational invariance relations above, when $J/U < 1/2$ there is an attraction induced for $J/U > 1/3$. This can generate exotic orbital-singlet spin-triplet superconducting states [20, 125, 127, 130], as we will show in Sec. 2.4.

Turning now to the effective interaction from spin fluctuations, for multiorbital systems we can follow an analogous procedure as in Sec. 1.2, where we derived in detail the effective pairing for a one-band model within the RPA approach, by summing up bubble and ladder diagrams to infinite order. In particular, the results of Chapter 1 can be easily generalized to multiorbital systems, such that the effective pairing obtained in Eq. (1.22) can be written as

$$\begin{aligned}
[V(\mathbf{k},\mathbf{k}')]^{\tilde{\mu}_i,\tilde{\mu}_l}_{\tilde{\mu}_j,\tilde{\mu}_k} = \; & [U]^{\tilde{\mu}_i,\tilde{\mu}_l}_{\tilde{\mu}_j,\tilde{\mu}_k} - [U(\mathbb{1} - \chi_0(\mathbf{k}-\mathbf{k}')U)^{-1}\chi_0(\mathbf{k}-\mathbf{k}')U]^{\tilde{\mu}_i,\tilde{\mu}_k}_{\tilde{\mu}_j,\tilde{\mu}_l} \\
& + [U(\mathbb{1} - \chi_0(\mathbf{k}+\mathbf{k}')U)^{-1}\chi_0(\mathbf{k}+\mathbf{k}')U]^{\tilde{\mu}_i,\tilde{\mu}_l}_{\tilde{\mu}_j,\tilde{\mu}_k}.
\end{aligned} \tag{2.5}$$

Here, the dimensions of the susceptibility and the bare interaction matrices also include the orbital degree of freedom in addition to spin, and therefore correspond to $2^2 \cdot 2^{n_{\text{orb}}} \times 2^2 \cdot 2^{n_{\text{orb}}}$, where n_{orb} is the number of orbitals. The generalized susceptibility is given by [18, 30]

$$[\chi_0(\mathbf{q}, i\omega_n)]^{\mu_1\sigma_1,\mu_2\sigma_2}_{\mu_3\sigma_3,\mu_4\sigma_4} = \frac{1}{N}\int_0^\beta d\tau e^{i\omega_n\tau} \sum_{\mathbf{k},\mathbf{k}'} \langle T_\tau c^\dagger_{\mathbf{k}-\mathbf{q}\mu_1\sigma_1}(\tau) c_{\mathbf{k}\mu_2\sigma_2}(\tau) c^\dagger_{\mathbf{k}'+\mathbf{q}\mu_3\sigma_3}(0) c_{\mathbf{k}'\mu_4\sigma_4}(0)\rangle_0, \tag{2.6}$$

where, compared to Eq. (1.13), we have introduced the orbital indices in the fermionic operators. Performing the Matsubara sum, the susceptibility can now be written as

$$[\chi_0(\mathbf{q}, i\omega_n)]^{\mu_1\sigma_1,\mu_2\sigma_2}_{\mu_3\sigma_3,\mu_4\sigma_4} = -\frac{1}{N}\sum_{\mathbf{k}} \sum_{n_1,n_2,s_i} [M_{n_1,n_2}(\mathbf{k},\mathbf{q})]^{\mu_1 s_1,\mu_2 s_2}_{\mu_3 s_3,\mu_4 s_4} \frac{f(\xi_{\mathbf{k}-\mathbf{q},n_1,s_1}) - f(\xi_{\mathbf{k},n_2,s_2})}{i\omega_n + \xi_{\mathbf{k}-\mathbf{q},n_1,s_1} - \xi_{\mathbf{k},n_2,s_2}}. \tag{2.7}$$

In contrast to the expression found in Eq. (1.15), the transformation from the orbital and electronic spin basis (μ, σ) to the band and pseudospin basis (n, s) also enters,

$$[M_{n_1,n_2}(\mathbf{k},\mathbf{q})]^{\mu_1 s_1,\mu_2 s_2}_{\mu_3 s_3,\mu_4 s_4} = [u^{\mu_1\sigma_1}_{n_1 s_1}(\mathbf{k}-\mathbf{q})]^*[u^{\mu_3\sigma_3}_{n_2 s_3}(\mathbf{k})]^* u^{\mu_2\sigma_2}_{n_2 s_2}(\mathbf{k}) u^{\mu_4\sigma_4}_{n_1 s_4}(\mathbf{k}-\mathbf{q}), \tag{2.8}$$

with $u^{\mu\sigma}_{ns}(\mathbf{k})$ denoting the components of the eigenvector obtained from diagonalizing the non-interacting Hamiltonian.

Following the same approach as in Chapter 1, in order to obtain the superconducting gap we solve self-consistently the BCS gap equation and the linearized gap equation (LGE). In the case of multiorbital systems, classifying the symmetries of the gap from the self-consistent approach becomes more involved, as we will elaborate in the next section. For the LGE, following Sec. 1.3, the effective interaction in Eq. (2.5) is projected to band and pseudospin space [18, 19, 86],

$$-\frac{1}{(2\pi)^2}\int_{\mathrm{FS}}\frac{d\mathbf{k}'}{|v_{\mathbf{k}'}|}\Gamma^{l,l'}_{\mathbf{k},\mathbf{k}'}\Delta^{l'}_{\mathbf{k}'} = \lambda\Delta^{l}_{\mathbf{k}}, \tag{2.9}$$

where $\Gamma^{l,l'}_{\mathbf{k},\mathbf{k}'} = \sum_{n_i}[\Gamma^l]_{n_3 n_1}[V(\mathbf{k},\mathbf{k}')]^{n_1 n_2}_{n_3 n_4}[\Gamma^{l'}]_{n_4 n_2}$, with $[V(\mathbf{k},\mathbf{k}')]^{n_1 n_2}_{n_3 n_4}$ being the effective interaction in Eq. (2.5) projected to the band basis using the transformation in Eq. (2.8). In addition, the Γ^l matrices correspond to $\Gamma^l = \frac{i}{\sqrt{2}}\sigma_l\sigma_y$, which are constructed to project the solution onto pseudospin singlet ($l = 0$) and triplet ($l = 1, 2, 3$) [18]. This will become clearer in the following section where we classify the gap in spin space, in particular see Eqs. (2.22)-(2.23). By diagonalizing this matrix, we obtain the leading eigenvalues and the corresponding gap function on the Fermi surface. Specifically, to calculate the results we parametrize the Fermi surface with 160 $\mathbf{k}$-points. We will use this method to compare the superconducting gap and the eigenvalues obtained from Hund's pairing versus spin-fluctuation pairing for the two distinct models in Secs. 2.4-2.5.

2.3 Classification of gap symmetries

In multiorbital systems, classifying the symmetry of the gap is not as straightforward as it was in Sec. 1.4 for the one-band model, where we could directly identify the symmetry from the different basis functions. Therefore, in this section, we first follow the approach in Sec. 1.4 to rewrite the self-consistent gap equation in terms of different basis functions, and then we classify the gap in orbital and spin space. For this purpose, we need to identify how the spin and orbital matrices transform under the point group.

We classify the gap structure for the two-orbital system in Ref. [130] and the three-orbital model relevant for Sr_2RuO_2 [18, 134], i.e., considering a two-orbital model including $\{d_{xz}, d_{yz}\}$ orbitals and a three-orbital model with contributions from $\{d_{xz}, d_{yz}, d_{xy}\}$ orbitals. In this section, we focus only on the identification of the gap symmetries assuming the set of orbitals relevant for each system, but we will introduce and describe in detail the origin of the models in Sec. 2.4 and Sec. 2.5, respectively.

For multiple orbitals, the mean-field gap equation in Eq. (1.57) can be written as

$$[\Delta_{\mathbf{k}}]^{\tilde{\mu}_i}_{\tilde{\mu}_j} = \sum_{\mathbf{k}',\tilde{\mu}_k,\tilde{\mu}_l}[V(\mathbf{k},\mathbf{k}')]^{\tilde{\mu}_i,\tilde{\mu}_l}_{\tilde{\mu}_j,\tilde{\mu}_k}\langle c_{-\mathbf{k}'\tilde{\mu}_l}c_{\mathbf{k}'\tilde{\mu}_k}\rangle, \tag{2.10}$$

where it is now labelled by orbital and spin indices. The interacting Hamiltonian in Eq. (2.2) implies that the effective interaction must satisfy the following symmetries,

$$[V(\mathbf{k},\mathbf{k}')]^{\tilde{\mu}_i,\tilde{\mu}_l}_{\tilde{\mu}_j,\tilde{\mu}_k} = -[V(\mathbf{k},-\mathbf{k}')]^{\tilde{\mu}_i,\tilde{\mu}_k}_{\tilde{\mu}_j,\tilde{\mu}_l} = -[V(-\mathbf{k},\mathbf{k}')]^{\tilde{\mu}_j,\tilde{\mu}_l}_{\tilde{\mu}_i,\tilde{\mu}_k}, \tag{2.11}$$

obtained by anticommuting the fermionic operators. Therefore, the order parameter fulfills

$$[\Delta_{\mathbf{k}}]^{\tilde{\mu}_i}_{\tilde{\mu}_j} = -[\Delta_{-\mathbf{k}}]^{\tilde{\mu}_j}_{\tilde{\mu}_i}. \tag{2.12}$$

This symmetry will become useful in the following discussion.

Fourier transforming the effective interaction from momentum space to real space, Eq. (2.10) can be rewritten in terms of the real-space pairing and the basis functions that belong to the irreps of the point group for the different neighbors, similarly to Sec. 1.4 for the one-band model. In the two multiorbital systems considered in this Chapter, the relevant point group is also D_{4h}. For the Hund's mechanism, the effective interaction in Eq. (2.3) contains exclusively on-site terms. On the contrary, in the spin-fluctuation mediated pairing, we Fourier transform the interaction in Eq. (2.5) and include up to sixth neighbors, in addition to the on-site term. This allows us to capture the largest interactions in real space, which usually occur on the closest sites.

Following Sec. 1.4, we rewrite the self-consistent gap equation as a function of the irreducible representations (irreps) Γ of D_{4h} as

$$[\Delta_{\mathbf{k}}]^{\tilde{\mu}_i}_{\tilde{\mu}_j} = \sum_{\Gamma\epsilon\text{irrep}} g^{\Gamma}_{\mathbf{k}}[\Delta_\Gamma]^{\tilde{\mu}_i}_{\tilde{\mu}_j} = \sum_{\Gamma_g} g^{\Gamma_g}_{\mathbf{k}}[\Delta_{\Gamma_g}]^{\tilde{\mu}_i}_{\tilde{\mu}_j} + \sum_{\Gamma_u} g^{\Gamma_u}_{\mathbf{k}}[\Delta_{\Gamma_u}]^{\tilde{\mu}_i}_{\tilde{\mu}_j}, \tag{2.13}$$

where in the last equality we have separated the even (Γ_g) and odd (Γ_u) irreps, with the basis functions satisfying $g^{\Gamma_g}_{-\mathbf{k}} = g^{\Gamma_g}_{\mathbf{k}}$ and $g^{\Gamma_u}_{-\mathbf{k}} = -g^{\Gamma_u}_{\mathbf{k}}$, respectively. As previously discussed in Sec. 1.4, when compared to Eq. (2.10), we have separated the $\mathbf{k}$ and $\mathbf{k}'$ dependence. Thus, similarly to Eq. (1.59), the $\mathbf{k}$-independent gap function in orbital and spin space is given by

$$[\Delta_\Gamma]^{\tilde{\mu}_i}_{\tilde{\mu}_j} = \sum_{\mathbf{k}',\tilde{\mu}_k,\tilde{\mu}_l} [V(\Delta\mathbf{r})]^{\tilde{\mu}_i,\tilde{\mu}_l}_{\tilde{\mu}_j,\tilde{\mu}_k} g^{\Gamma}_{\mathbf{k}'} \left\langle c_{-\mathbf{k}'\tilde{\mu}_l} c_{\mathbf{k}'\tilde{\mu}_k} \right\rangle. \tag{2.14}$$

with $[V(\Delta\mathbf{r})]^{\tilde{\mu}_i,\tilde{\mu}_l}_{\tilde{\mu}_j,\tilde{\mu}_k}$ denoting the Fourier transform of the effective interaction for the neighbor $\Delta\mathbf{r}$ (see Appendix A). Equations (2.12)-(2.13) imply that the matrices coupling to even form factors satisfy $[\Delta_{\Gamma_g}]^{\tilde{\mu}_i}_{\tilde{\mu}_j} = -[\Delta_{\Gamma_g}]^{\tilde{\mu}_j}_{\tilde{\mu}_i}$, while those coupling to odd form factors obey $[\Delta_{\Gamma_u}]^{\tilde{\mu}_i}_{\tilde{\mu}_j} = [\Delta_{\Gamma_u}]^{\tilde{\mu}_j}_{\tilde{\mu}_i}$. These properties will be relevant in the following subsections. To solve self-consistently for the superconducting gap in Secs. 2.4-2.5, as detailed in Appendix B, we consider a system size 81×81.

The first step to classify the symmetries of the gap is to find the matrix representation in spin and orbital space of the point group generators. The point group D_{4h} can be written as $D_{4h} = C_{4v} \otimes \mathcal{I}$, where $\mathcal{I}$ denotes the inversion operation and $C_{4v} = \{E, C_2, 2C_4, 2\sigma_v, 2\sigma_d\}$, which contains the identity, $\pi/2$ and π rotations, and two mirror operations, as illustrated in Fig. 1.5. Since the two models examined contain inversion, it is sufficient to consider the following operations as the generators of the group:

$$\{E, C_2, C_4, \sigma_v, \sigma_d, \mathcal{I}\}. \tag{2.15}$$

Table 2.1: Transformation of the spin degrees of freedom $(\sigma_0, \sigma_x, \sigma_y, \sigma_z)$ under the generators of the point group D_{4h} in Eq. (2.15), obtained using the matrix representations in Eq. (2.18). The right column indicates the corresponding irrep.

	E	C_2	$2C_4$	$2\sigma_v$	$2\sigma_d$	$\mathcal{I}$	Irrep
σ_0	1	1	1	1	1	1	A_{1g}
σ_z	1	1	1	-1	-1	1	A_{2g}
(σ_x, σ_y)	2	-2	0	0	0	2	E_g

We recall that these operations act as follows on the spatial coordinates,

$$\begin{aligned} &E(x,y,z) = (x,y,z), \quad C_2(x,y,z) = (-x,-y,z), \quad C_4(x,y,z) = (y,-x,z), \\ &\sigma_v(x,y,z) = (x,-y,z), \quad \sigma_d(x,y,z) = (y,x,z), \quad \mathcal{I}(x,y,z) = (-x,-y,-z). \end{aligned} \tag{2.16}$$

First, we focus on spin space, and in the following subsections we turn to orbital space and identify the symmetries of the order parameter for both the two-orbital and three-orbital models. We denote $\boldsymbol{\sigma} = (\sigma_0, \sigma_x, \sigma_y, \sigma_z)$ as the set of Pauli matrices representing spin space,

$$\sigma_x = \begin{pmatrix} 0 & 1 \\ 1 & 0 \end{pmatrix}, \quad \sigma_y = \begin{pmatrix} 0 & -i \\ i & 0 \end{pmatrix}, \quad \sigma_z = \begin{pmatrix} 1 & 0 \\ 0 & -1 \end{pmatrix}, \quad \sigma_0 = \begin{pmatrix} 1 & 0 \\ 0 & 1 \end{pmatrix}, \tag{2.17}$$

and we want to identify the symmetry properties of these matrices, i.e., to which irreducible representation of D_{4h} they belong to. Hence, we need to calculate $d_\sigma^\dagger(g)\sigma_i d_\sigma(g)$, with $d_\sigma(g)$ denoting the matrix representation in spin space of the point group operations g in Eq. (2.15).

On the one hand, the matrix representation of the rotation operation corresponds to $d_\sigma(C_n) = e^{-i\boldsymbol{\sigma}\cdot\hat{\varphi}}$, where $\hat{\varphi}$ is the angle of the rotation. For instance, in the case of a $\pi/2$ rotation, the matrix representation corresponds to $d_\sigma(C_2) = -i\sin\frac{\pi}{2}\sigma_z$. On the other hand, for the mirror and inversion operations, we recall that the spin operator transforms in the same way as the angular momentum operator, $\mathbf{L} = \mathbf{r}\times\mathbf{p}$, with $\mathbf{r}$ and $\mathbf{p}$ corresponding to the space and momentum coordinates, respectively. Let us illustrate this with an example, focusing on the mirror operation σ_v. In this case, the x-component of the angular momentum $L_x = xp_y - yp_x$ changes sign under σ_v, since both the coordinates and the momentum transform under the point group operations as in Eq. (2.16). Similarly, we see that $\sigma_v(L_x, L_y, L_z) = (-L_x, L_y, -L_z)$. Thus, by inspection we identify that the matrix representation transforming $d_\sigma^\dagger(\sigma_v)(\sigma_x,\sigma_y,\sigma_z)d_\sigma(\sigma_v)$ in the previous way must correspond to $d_\sigma(\sigma_v) = -i\sigma_y$. Therefore, following the same procedure for the other group generators in Eq. (2.15), we find the following matrix representations [137],

$$\begin{aligned} &d_\sigma(E) = \sigma_0, \quad d_\sigma(C_2) = -i\sigma_z, \quad d_\sigma(C_4) = \frac{\sigma_0 - i\sigma_z}{\sqrt{2}}, \\ &d_\sigma(\sigma_v) = -i\sigma_y, \quad d_\sigma(\sigma_d) = -i\frac{\sigma_y - \sigma_x}{\sqrt{2}}, \quad d_\sigma(\mathcal{I}) = \sigma_0. \end{aligned} \tag{2.18}$$

Hence, we identify the transformation properties of the Pauli matrices under the point group operations g in Eq. (2.18) by calculating $d_\sigma^\dagger(g)\sigma_i d_\sigma(g)$. The results are shown in Table 2.1.

Table 2.2: Transformation of the matrices in orbital space (see Eq. (2.19)) under the generators of the point group D_{4h} in Eq. (2.15), obtained using the matrix representations in Eq. (2.20). The right column indicates the corresponding irrep.

	E	C_2	$2C_4$	$2\sigma_v$	$2\sigma_d$	$\mathcal{I}$	Irrep
κ_0	1	1	1	1	1	1	A_{1g}
κ_y	1	1	1	-1	-1	1	A_{2g}
κ_z	1	1	-1	1	-1	1	B_{1g}
κ_x	1	1	-1	-1	1	1	B_{2g}

2.3.1 Two-orbital model

Let us consider a two-orbital model relevant for iron-based materials, described by two Γ-centered hole pockets with contribution from d_{xz} and d_{yz} orbitals [130]. We introduce the Pauli matrices $\boldsymbol{\kappa}$ to denote orbital space, with

$$\kappa_x = \begin{pmatrix} 0 & 1 \\ 1 & 0 \end{pmatrix}, \qquad \kappa_y = \begin{pmatrix} 0 & -i \\ i & 0 \end{pmatrix}, \qquad \kappa_z = \begin{pmatrix} 1 & 0 \\ 0 & -1 \end{pmatrix}, \qquad \kappa_0 = \begin{pmatrix} 1 & 0 \\ 0 & 1 \end{pmatrix}. \tag{2.19}$$

Equation (2.16) is useful to determine how the group generators in Eq. (2.15) act in the orbital basis $\{d_{xz}, d_{yz}\}$. For instance, the C_4 rotation act on the basis as $C_4(xz, yz) = (yz, -xz)$. Thus, the matrix representation performing this transformation corresponds to $d_\kappa(C_4) = -i\kappa_y$. In the same way, we can identify the matrix representation for the other operations, obtaining

$$\begin{aligned} d_\kappa(E) &= \kappa_0, & d_\kappa(C_2) &= -\kappa_0, & d_\kappa(C_4) &= -i\kappa_y, \\ d_\kappa(\sigma_v) &= \kappa_z, & d_\kappa(\sigma_d) &= \kappa_x, & d_\kappa(\mathcal{I}) &= \kappa_0. \end{aligned} \tag{2.20}$$

Therefore, we can classify how the matrices in orbital space transform under the point group operations of Eq. (2.20) by calculating $d_\kappa^\dagger(g)\kappa_i d_\kappa(g)$. The results are included in Table 2.2.

Having determined how the matrices in orbital and spin space transform for the two-orbital model, we can now classify the symmetries of the gap. Recalling Eq. (2.13), we focus first on matrices coupling to even form factors, which satisfy $[\Delta_{\Gamma_g}]^{\tilde{\mu}_i}_{\tilde{\mu}_j} = -[\Delta_{\Gamma_g}]^{\tilde{\mu}_j}_{\tilde{\mu}_i}$. Therefore, we start from the matrix form

$$\Delta_{\Gamma_g} = \begin{pmatrix} 0 & [\Delta_{\Gamma_g}]^{xz\uparrow}_{xz\downarrow} & [\Delta_{\Gamma_g}]^{xz\uparrow}_{yz\uparrow} & [\Delta_{\Gamma_g}]^{xz\uparrow}_{yz\downarrow} \\ -[\Delta_{\Gamma_g}]^{xz\uparrow}_{xz\downarrow} & 0 & [\Delta_{\Gamma_g}]^{xz\downarrow}_{yz\uparrow} & [\Delta_{\Gamma_g}]^{xz\downarrow}_{yz\downarrow} \\ -[\Delta_{\Gamma_g}]^{xz\uparrow}_{yz\uparrow} & -[\Delta_{\Gamma_g}]^{xz\downarrow}_{yz\uparrow} & 0 & [\Delta_{\Gamma_g}]^{yz\uparrow}_{yz\downarrow} \\ -[\Delta_{\Gamma_g}]^{xz\uparrow}_{yz\downarrow} & -[\Delta_{\Gamma_g}]^{xz\downarrow}_{yz\downarrow} & -[\Delta_{\Gamma_g}]^{yz\uparrow}_{yz\downarrow} & 0 \end{pmatrix}. \tag{2.21}$$

We can parametrize the gap matrix in spin space to distinguish between spin singlet and spin triplet terms [138, 139]. For the spin singlet, it is sufficient to use a scalar function,

$$\Delta_s = \begin{pmatrix} \Delta_{\uparrow\uparrow} & \Delta_{\uparrow\downarrow} \\ \Delta_{\downarrow\uparrow} & \Delta_{\downarrow\downarrow} \end{pmatrix} = \begin{pmatrix} 0 & \psi \\ \psi & 0 \end{pmatrix} = i\sigma_y\psi. \tag{2.22}$$

Table 2.3: Classification of the order parameter components in Eq. (2.24) that couple to an even form factor ($g^{\Gamma_g}_{-\mathbf{k}} = g^{\Gamma_g}_{\mathbf{k}}$) in orbital and spin space, considering a two-orbital model with d_{xz} and d_{yz} orbitals. We include whether each combination corresponds to singlet or triplet in orbital and spin space and indicate when it is an intra-orbital term. The transformation of the spin and orbital matrices is detailed in Tables 2.1 and 2.2, respectively, which is used to obtain the total irrep for each combination.

Δ_{Γ_g} component	Orbital	$\boldsymbol{\kappa}_i$	Spin	$\boldsymbol{\sigma}_i$	Irrep
$\frac{1}{2}([\Delta_{\Gamma_g}]^{xz\uparrow}_{xz\downarrow} + [\Delta_{\Gamma_g}]^{yz\uparrow}_{yz\downarrow})$	Triplet, Intra	κ_0	Singlet	σ_0	A_{1g}
$\frac{1}{2}([\Delta_{\Gamma_g}]^{xz\uparrow}_{yz\downarrow} - [\Delta_{\Gamma_g}]^{xz\downarrow}_{yz\uparrow})$	Triplet	κ_x	Singlet	σ_0	B_{2g}
$\frac{1}{2}([\Delta_{\Gamma_g}]^{xz\uparrow}_{xz\downarrow} - [\Delta_{\Gamma_g}]^{yz\uparrow}_{yz\downarrow})$	Triplet, Intra	κ_z	Singlet	σ_0	B_{1g}
$\frac{1}{2}([\Delta_{\Gamma_g}]^{xz\uparrow}_{yz\uparrow} + [\Delta_{\Gamma_g}]^{xz\downarrow}_{yz\downarrow})$	Singlet	κ_y	Triplet	σ_y	E^y_g
$\frac{1}{2}([\Delta_{\Gamma_g}]^{xz\uparrow}_{yz\uparrow} - [\Delta_{\Gamma_g}]^{xz\downarrow}_{yz\downarrow})$	Singlet	κ_y	Triplet	σ_x	E^x_g
$\frac{1}{2}([\Delta_{\Gamma_g}]^{xz\downarrow}_{yz\uparrow} + [\Delta_{\Gamma_g}]^{xz\uparrow}_{yz\downarrow})$	Singlet	κ_y	Triplet	σ_z	A_{1g}

In contrast, the spin triplet requires three components, denoted by the vector $\vec{d}$,

$$\Delta_t = \begin{pmatrix} \Delta_{\uparrow\uparrow} & \Delta_{\uparrow\downarrow} \\ \Delta_{\downarrow\uparrow} & \Delta_{\downarrow\downarrow} \end{pmatrix} = \begin{pmatrix} -d_x + id_y & d_z \\ d_z & d_x + id_y \end{pmatrix} = i(\boldsymbol{d}\cdot\boldsymbol{\sigma})\sigma_y. \tag{2.23}$$

As a consequence, taking into account both configurations the gap matrix in spin space can be written as $\Delta = i(\psi + \boldsymbol{d}\cdot\boldsymbol{\sigma})\sigma_y$.

Rewriting Eq. (2.21) in this form, including also orbital space, we identify the following spin singlet and spin triplet terms:

$$\begin{aligned}
\psi &= \frac{1}{2}([\Delta_{\Gamma_g}]^{xz\uparrow}_{xz\downarrow} + [\Delta_{\Gamma_g}]^{yz\uparrow}_{yz\downarrow})\kappa_0\sigma_0 + \frac{1}{2}([\Delta_{\Gamma_g}]^{xz\uparrow}_{xz\downarrow} - [\Delta_{\Gamma_g}]^{yz\uparrow}_{yz\downarrow})\kappa_z\sigma_0 + \frac{1}{2}([\Delta_{\Gamma_g}]^{xz\uparrow}_{yz\downarrow} - [\Delta_{\Gamma_g}]^{xz\downarrow}_{yz\uparrow})\kappa_x\sigma_0, \\
\boldsymbol{d}\cdot\boldsymbol{\sigma} &= \frac{1}{2}([\Delta_{\Gamma_g}]^{xz\uparrow}_{yz\uparrow} + [\Delta_{\Gamma_g}]^{xz\downarrow}_{yz\downarrow})\kappa_y\sigma_y - \frac{i}{2}([\Delta_{\Gamma_g}]^{xz\uparrow}_{yz\uparrow} - [\Delta_{\Gamma_g}]^{xz\downarrow}_{yz\downarrow})\kappa_y\sigma_x + \frac{i}{2}([\Delta_{\Gamma_g}]^{xz\downarrow}_{yz\uparrow} + [\Delta_{\Gamma_g}]^{xz\uparrow}_{yz\downarrow})\kappa_y\sigma_z.
\end{aligned} \tag{2.24}$$

These results are summarized in Table 2.3, specifying how all terms couple to orbital and spin space and whether they correspond to singlet or triplet. The right column denotes the total irrep, obtained as the direct product of the irrep for the orbital and spin matrices, included in Tables 2.1-2.2. The classification is in agreement with Ref. [130]. As we will see in Secs. 2.4-2.5, for the two-orbital and three-orbital models considered, the order parameter components coupling to an odd form factor always vanish from the self-consistent solution. Therefore, we do not consider these components here, for the classification in this case see Appendix D.

2.3.2 Three-orbital model

Let us now turn to a three-orbital model relevant for $SrRuO_4$ including d_{xz}, d_{yz} and d_{xy} orbitals [18, 134]. Thus, we now need a set of 3×3 matrices standing for the orbital degree of freedom. For this purpose, we take the Gell-Mann matrices, which form a basis in this space,

Table 2.4: Transformation of the matrices in orbital space (see Eq. (2.25)) under the generators of the point group D_{4h}, obtained using the matrix representations in Eq. (2.26). The right column indicates the corresponding irrep.

	E	C_2	$2C_4$	$2\sigma_v$	$2\sigma_d$	$\mathcal{I}$	Irrep
λ_0, λ_8	1	1	1	1	1	1	A_{1g}
λ_2	1	1	1	-1	-1	1	A_{2g}
λ_3	1	1	-1	1	-1	1	B_{1g}
λ_1	1	1	-1	-1	1	1	B_{2g}
(λ_6, λ_4), (λ_7, λ_5)	2	-2	0	0	0	2	E_g

and correspond to

$$\begin{aligned}
\lambda_1 &= \begin{pmatrix} 0 & 1 & 0 \\ 1 & 0 & 0 \\ 0 & 0 & 0 \end{pmatrix}, \quad \lambda_2 = \begin{pmatrix} 0 & -i & 0 \\ i & 0 & 0 \\ 0 & 0 & 0 \end{pmatrix}, \quad \lambda_3 = \begin{pmatrix} 1 & 0 & 0 \\ 0 & -1 & 0 \\ 0 & 0 & 0 \end{pmatrix}, \\
\lambda_4 &= \begin{pmatrix} 0 & 0 & 1 \\ 0 & 0 & 0 \\ 1 & 0 & 0 \end{pmatrix}, \quad \lambda_5 = \begin{pmatrix} 0 & 0 & -i \\ 0 & 0 & 0 \\ i & 0 & 0 \end{pmatrix}, \quad \lambda_6 = \begin{pmatrix} 0 & 0 & 0 \\ 0 & 0 & 1 \\ 0 & 1 & 0 \end{pmatrix}, \\
\lambda_7 &= \begin{pmatrix} 0 & 0 & 0 \\ 0 & 0 & -i \\ 0 & i & 0 \end{pmatrix}, \quad \lambda_8 = \frac{1}{\sqrt{3}} \begin{pmatrix} 1 & 0 & 0 \\ 0 & 1 & 0 \\ 0 & 0 & -2 \end{pmatrix}, \quad \lambda_0 = \begin{pmatrix} 1 & 0 & 0 \\ 0 & 1 & 0 \\ 0 & 0 & 1 \end{pmatrix}.
\end{aligned} \tag{2.25}$$

Similarly to the two-orbital model, we use Eq. (2.16) to calculate how the operations in Eq. (2.15) act in the orbital basis $\{d_{xz}, d_{yz}, d_{xy}\}$, finding the matrix representations

$$\begin{aligned}
&d_\lambda(E) = \lambda_0, \quad d_\lambda(C_2) = \begin{pmatrix} -1 & 0 & 0 \\ 0 & -1 & 0 \\ 0 & 0 & 1 \end{pmatrix}, \quad d_\lambda(C_4) = \begin{pmatrix} 0 & -1 & 0 \\ 1 & 0 & 0 \\ 0 & 0 & -1 \end{pmatrix}, \\
&d_\lambda(\sigma_{xz}) = \begin{pmatrix} 1 & 0 & 0 \\ 0 & -1 & 0 \\ 0 & 0 & -1 \end{pmatrix}, \quad d_\lambda(\sigma_{x=y}) = \begin{pmatrix} 0 & 1 & 0 \\ 1 & 0 & 0 \\ 0 & 0 & 1 \end{pmatrix}, \quad d_\lambda(\mathcal{I}) = \lambda_0.
\end{aligned} \tag{2.26}$$

Hence, by calculating $d_\lambda^\dagger(g)\lambda_i d_\lambda(g)$ for the point group operations g in Eq. (2.15) we can obtain how the Gell-Mann matrices transform in orbital space, as detailed in Table 2.4.

We focus again on matrices coupling to even form factors (see Eq. (2.13)). Since they satisfy $[\Delta_{\Gamma_g}]^{\tilde{\mu}_i}_{\tilde{\mu}_j} = -[\Delta_{\Gamma_g}]^{\tilde{\mu}_j}_{\tilde{\mu}_i}$, in analogy with the previous two-orbital model we consider the following

Table 2.5: Classification of the order parameter components that couple to an even form factor ($g^{\Gamma_g}_{-\mathbf{k}} = g^{\Gamma_g}_{\mathbf{k}}$) in orbital and spin space, considering a three-orbital model with d_{xz}, d_{yz} and d_{xy} orbitals. We include whether each combination corresponds to singlet or triplet in orbital and spin space and indicate when it is an intra-orbital term. The transformation of the spin and orbital matrices is detailed in Tables 2.1 and 2.4, respectively, which is used to obtain the total irrep for each combination.

Δ_{Γ_g} component	Orbital	$\boldsymbol{\lambda}_i$	Spin	$\boldsymbol{\sigma}_i$	Irrep
$\frac{1}{3}([\Delta_{\Gamma_g}]^{xz\uparrow}_{xz\downarrow} + [\Delta_{\Gamma_g}]^{yz\uparrow}_{yz\downarrow} + [\Delta_{\Gamma_g}]^{xy\uparrow}_{xy\downarrow})$	Triplet, Intra	λ_0	Singlet	σ_0	A_{1g}
$\frac{1}{2}([\Delta_{\Gamma_g}]^{xz\uparrow}_{yz\downarrow} - [\Delta_{\Gamma_g}]^{xz\downarrow}_{yz\uparrow})$	Triplet	λ_1	Singlet	σ_0	B_{2g}
$\frac{1}{2}([\Delta_{\Gamma_g}]^{xz\uparrow}_{xz\downarrow} - [\Delta_{\Gamma_g}]^{yz\uparrow}_{yz\downarrow})$	Triplet, Intra	λ_3	Singlet	σ_0	B_{1g}
$\frac{1}{2}([\Delta_{\Gamma_g}]^{xz\uparrow}_{xy\downarrow} - [\Delta_{\Gamma_g}]^{xz\downarrow}_{xy\uparrow})$	Triplet	λ_4	Singlet	σ_0	$E^y_g(i)$
$\frac{1}{2}([\Delta_{\Gamma_g}]^{yz\uparrow}_{xy\downarrow} - [\Delta_{\Gamma_g}]^{yz\downarrow}_{xy\uparrow})$	Triplet	λ_6	Singlet	σ_0	$E^x_g(i)$
$\frac{1}{2\sqrt{3}}([\Delta_{\Gamma_g}]^{xz\uparrow}_{xz\downarrow} + [\Delta_{\Gamma_g}]^{yz\uparrow}_{yz\downarrow} - 2[\Delta_{\Gamma_g}]^{xy\uparrow}_{xy\downarrow})$	Triplet, Intra	λ_8	Singlet	σ_0	A_{1g}
$\frac{1}{2}([\Delta_{\Gamma_g}]^{xz\uparrow}_{yz\uparrow} + [\Delta_{\Gamma_g}]^{xz\downarrow}_{yz\downarrow})$	Singlet	λ_2	Triplet	σ_y	$E^y_g(ii)$
$\frac{i}{2}([\Delta_{\Gamma_g}]^{xz\uparrow}_{yz\downarrow} + [\Delta_{\Gamma_g}]^{xz\downarrow}_{yz\uparrow})$	Singlet	λ_2	Triplet	σ_z	A_{1g}
$\frac{-i}{2}([\Delta_{\Gamma_g}]^{xz\uparrow}_{yz\uparrow} - [\Delta_{\Gamma_g}]^{xz\downarrow}_{yz\downarrow})$	Singlet	λ_2	Triplet	σ_x	$E^x_g(ii)$
$\frac{1}{2}([\Delta_{\Gamma_g}]^{xz\uparrow}_{xy\uparrow} + [\Delta_{\Gamma_g}]^{xz\downarrow}_{xy\downarrow})$	Singlet	λ_5	Triplet	σ_y	Reducible
$\frac{i}{2}([\Delta_{\Gamma_g}]^{xz\uparrow}_{xy\downarrow} + [\Delta_{\Gamma_g}]^{xz\downarrow}_{xy\uparrow}$	Singlet	λ_5	Triplet	σ_z	$E^y_g(iii)$
$\frac{-i}{2}([\Delta_{\Gamma_g}]^{xz\uparrow}_{xy\uparrow} - [\Delta_{\Gamma_g}]^{xz\downarrow}_{xy\downarrow})$	Singlet	λ_5	Triplet	σ_x	Reducible
$\frac{1}{2}([\Delta_{\Gamma_g}]^{yz\uparrow}_{xy\uparrow} + [\Delta_{\Gamma_g}]^{yz\downarrow}_{xy\downarrow})$	Singlet	λ_7	Triplet	σ_y	Reducible
$\frac{i}{2}([\Delta_{\Gamma_g}]^{yz\uparrow}_{xy\downarrow} + [\Delta_{\Gamma_g}]^{yz\downarrow}_{xy\uparrow})$	Singlet	λ_7	Triplet	σ_z	$E^x_g(iii)$
$\frac{-i}{2}([\Delta_{\Gamma_g}]^{yz\uparrow}_{xy\uparrow} - [\Delta_{\Gamma_g}]^{yz\downarrow}_{xy\downarrow})$	Singlet	λ_7	Triplet	σ_x	Reducible

Table 2.6: Classification of the order parameter components obtained by combining the reducible representations in Table 2.5, for the order parameter matrices coupling to an even form factor ($g^{\Gamma_g}_{-\mathbf{k}} = g^{\Gamma_g}_{\mathbf{k}}$) in orbital and spin space, considering a three-orbital model for d_{xz}, d_{yz} and d_{xy} orbitals. We classify the terms in combined orbital and spin space, and indicate the corresponding irrep in each case.

Δ_{Γ_g} component	Combined spin and orbital	Orbital	Spin	Irrep
$\frac{1}{4}\big([\Delta_{\Gamma_g}]^{xz\uparrow}_{xy\uparrow} + [\Delta_{\Gamma_g}]^{xz\downarrow}_{xy\downarrow} - i([\Delta_{\Gamma_g}]^{yz\uparrow}_{xy\uparrow} - [\Delta_{\Gamma_g}]^{yz\downarrow}_{xy\downarrow})\big)$	$\lambda_5\sigma_y + \lambda_7\sigma_x$	Singlet	Triplet	A_{2g}
$\frac{1}{4}\big([\Delta_{\Gamma_g}]^{xz\uparrow}_{xy\uparrow} + [\Delta_{\Gamma_g}]^{xz\downarrow}_{xy\downarrow} + i([\Delta_{\Gamma_g}]^{yz\uparrow}_{xy\uparrow} - [\Delta_{\Gamma_g}]^{yz\downarrow}_{xy\downarrow})\big)$	$\lambda_5\sigma_y - \lambda_7\sigma_x$	Singlet	Triplet	B_{2g}
$\frac{1}{4}\big(-i([\Delta_{\Gamma_g}]^{xz\uparrow}_{xy\uparrow} - [\Delta_{\Gamma_g}]^{xz\downarrow}_{xy\downarrow}) + [\Delta_{\Gamma_g}]^{yz\uparrow}_{xy\uparrow} + [\Delta_{\Gamma_g}]^{yz\downarrow}_{xy\downarrow}\big)$	$\lambda_5\sigma_x + \lambda_7\sigma_y$	Singlet	Triplet	B_{1g}
$\frac{1}{4}\big(-i([\Delta_{\Gamma_g}]^{xz\uparrow}_{xy\uparrow} - [\Delta_{\Gamma_g}]^{xz\downarrow}_{xy\downarrow}) - [\Delta_{\Gamma_g}]^{yz\uparrow}_{xy\uparrow} - [\Delta_{\Gamma_g}]^{yz\downarrow}_{xy\downarrow}\big)$	$\lambda_5\sigma_x - \lambda_7\sigma_y$	Singlet	Triplet	A_{1g}

matrix in orbital and spin space,

$$\Delta_{\Gamma_g} = \begin{pmatrix} 0 & [\Delta_{\Gamma_g}]^{xz\uparrow}_{xz\downarrow} & [\Delta_{\Gamma_g}]^{xz\uparrow}_{yz\uparrow} & [\Delta_{\Gamma_g}]^{xz\uparrow}_{yz\downarrow} & [\Delta_{\Gamma_g}]^{xz\uparrow}_{xy\uparrow} & [\Delta_{\Gamma_g}]^{xz\uparrow}_{xy\downarrow} \\ -[\Delta_{\Gamma_g}]^{xz\uparrow}_{xz\downarrow} & 0 & [\Delta_{\Gamma_g}]^{xz\downarrow}_{yz\uparrow} & [\Delta_{\Gamma_g}]^{xz\downarrow}_{yz\downarrow} & [\Delta_{\Gamma_g}]^{xz\downarrow}_{xy\uparrow} & [\Delta_{\Gamma_g}]^{xz\downarrow}_{xy\downarrow} \\ -[\Delta_{\Gamma_g}]^{xz\uparrow}_{yz\uparrow} & -[\Delta_{\Gamma_g}]^{xz\downarrow}_{yz\uparrow} & 0 & [\Delta_{\Gamma_g}]^{yz\uparrow}_{yz\downarrow} & [\Delta_{\Gamma_g}]^{yz\uparrow}_{xy\uparrow} & [\Delta_{\Gamma_g}]^{yz\uparrow}_{xy\downarrow} \\ -[\Delta_{\Gamma_g}]^{xz\uparrow}_{yz\downarrow} & -[\Delta_{\Gamma_g}]^{xz\downarrow}_{yz\downarrow} & -[\Delta_{\Gamma_g}]^{yz\uparrow}_{yz\downarrow} & 0 & [\Delta_{\Gamma_g}]^{yz\downarrow}_{xy\uparrow} & [\Delta_{\Gamma_g}]^{yz\downarrow}_{xy\downarrow} \\ -[\Delta_{\Gamma_g}]^{xz\uparrow}_{xy\uparrow} & -[\Delta_{\Gamma_g}]^{xz\downarrow}_{xy\uparrow} & -[\Delta_{\Gamma_g}]^{yz\uparrow}_{xy\uparrow} & -[\Delta_{\Gamma_g}]^{yz\downarrow}_{xy\uparrow} & 0 & [\Delta_{\Gamma_g}]^{xy\uparrow}_{xy\downarrow} \\ -[\Delta_{\Gamma_g}]^{xz\uparrow}_{xy\downarrow} & -[\Delta_{\Gamma_g}]^{xz\downarrow}_{xy\downarrow} & -[\Delta_{\Gamma_g}]^{yz\uparrow}_{xy\downarrow} & -[\Delta_{\Gamma_g}]^{yz\downarrow}_{xy\downarrow} & -[\Delta_{\Gamma_g}]^{xy\uparrow}_{xy\downarrow} & 0 \end{pmatrix}. \tag{2.27}$$

Using the notation $\Delta = i(\psi + \boldsymbol{d}\cdot\boldsymbol{\sigma})\sigma_y$ and following the same procedure as before, we obtain the classification summarized in Table 2.5, where the last column corresponds to the total irrep in orbital and spin space. Note that, in this case, there are some combinations that do not transform as an irrep of the point group D_{4h}. However, combining the reducible representations we can obtain terms transforming like an irrep, as specified in Table 2.6. The classification is in agreement with Refs. [140, 141]. Similarly, since for this model the matrices coupling to odd-parity basis functions are not stabilized in the self-consistent solution, we include them in Appendix D.

2.4 Two-orbital model with no nesting

In this section, we consider again the two-orbital model from Ref. [130] relevant for iron-based superconductors to compare the superconducting gap from Hund's pairing and spin-fluctuation pairing. First, we detail how to construct the non-interacting Hamiltonian for a two-orbital model including d_{xz} and d_{yz} orbitals from symmetry arguments, and then we proceed to study the Fermi surface and the susceptibility from this model. Next, we turn to the comparison of the two mechanisms, and we investigate the role of spin-orbit coupling (SOC) in inducing superconducting pairing using analytical calculations.

The non-interacting Hamiltonian is constructed by finding all terms that transform like invariants under all point group operations, i.e., the A_{1g} irrep of D_{4h} in our case (see Table 1.1). The same analysis will also be used in Chapter 4 to construct minimal models based on symmetry considerations. The first step is to identify how the orbital and spin matrices transform, which in our two-orbital case include the Pauli matrices $\boldsymbol{\kappa} = \{\kappa_0, \kappa_1, \kappa_2, \kappa_3\}$ and $\boldsymbol{\sigma} = \{\sigma_0, \sigma_1, \sigma_2, \sigma_3\}$ denoting orbital and spin space, respectively. As described in the previous section, the corresponding irrep for each matrix can be identified and is listed in Tables 2.1-2.2. Then, we can find the combinations of these matrices together with the $\mathbf{k}$-dependent functions that belong to the A_{1g} irrep.

For instance, since κ_x transforms like the B_{2g} irrep and $B_{2g}\otimes B_{2g} = A_{1g}$, we need to find the basis function transforming also like B_{2g}. In particular, the lowest-order harmonic coupling to this matrix is $k_x k_y$ (see Table 1.1). Analogously, as Table 2.2 shows that κ_z transforms like the B_{1g} irrep, the lowest-order harmonic coupling to this matrix is $k_x^2 - k_y^2$. In addition, the SOC terms are given by combinations of the imaginary matrix κ_y and the spin matrices $\sigma_x, \sigma_y, \sigma_z$. However, from Tables 2.1-2.2 we see that there is only one on-site spin-orbit coupling term, which is obtained when combining σ_z and κ_y, since both matrices transform like A_{2g}.

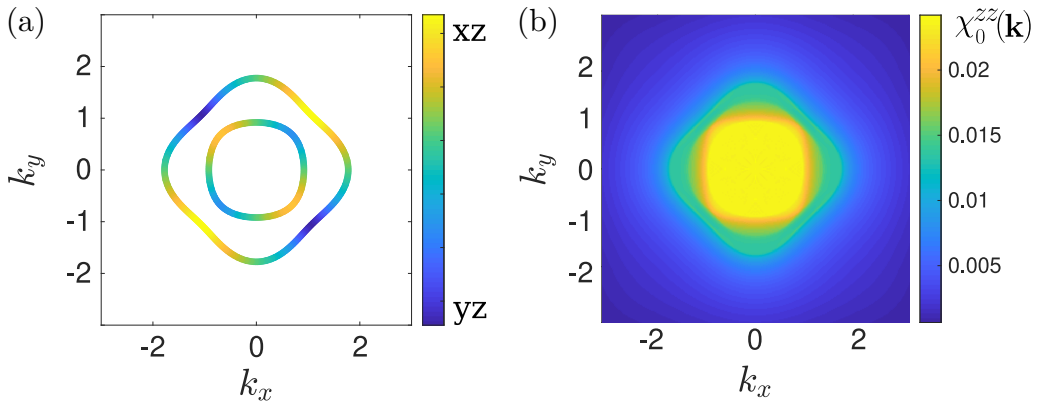

Figure 2.1: (a) Fermi surface for the two-orbital model in Eq. (2.29), with $a = 1$, $b = c = \lambda_{\rm soc} = 0.5$, and $\mu = 1.5$. The color bar denotes the orbital character. (b) Momentum structure of the bare static susceptibility $\chi_0^{zz}(\mathbf{k})$, considering the same parameters as in panel (a).

Thus, in agreement with Ref. [132], the non-interacting Hamiltonian including SOC is given by

$$H_0^{4\times4}(\mathbf{k}) = \sigma_0\left[(\mu - a\mathbf{k}^2)\kappa_0 + bk_xk_y\kappa_x + c(k_x^2 - k_y^2)\kappa_z\right] + \lambda_{\rm soc}\sigma_z\kappa_y, \tag{2.28}$$

where we have chosen the basis $\{c_{\mathbf{k}xz\uparrow}, c_{\mathbf{k}yz\uparrow}, c_{\mathbf{k}xz\downarrow}, c_{\mathbf{k}yz\downarrow}\}$. Here, $a = 1/2m$ is the energy unit, the coefficients μ, m, b, c depend on the material, and finally $\lambda_{\rm soc}$ is the SOC strength. Using the doublet $\{c_{\mathbf{k}xz\alpha}, c_{\mathbf{k}yz\alpha}\}$, we can consider only a 2×2 block of the previous Hamiltonian,

$$H_0(\mathbf{k}) = \begin{pmatrix} \mu - a\mathbf{k}^2 + bk_xk_y & c(k_x^2 - k_y^2) - i\alpha\lambda_{\rm soc} \\ c(k_x^2 - k_y^2) + i\alpha\lambda_{\rm soc} & \mu - a\mathbf{k}^2 - bk_xk_y \end{pmatrix}, \tag{2.29}$$

where $\alpha = +$ or $-$ for spin up and spin down, respectively, and we have redefined k_x and k_y by rotating the basis $\pi/4$ to find the same form of the Hamiltonian as in Ref. [130]. This redefinition does not affect our results since, as we will see in this section, the stabilized superconducting order parameters have A_{1g} symmetry.

In Fig. 2.1(a) we show the Fermi surface indicating the orbital content by the color code. As seen, there are regions with predominant d_{xz} and regions with dominant d_{yz} orbital contribution. The corresponding spin susceptibility at zero energy (static limit) is shown in Fig. 2.1(b). In particular, we show the $\chi_0^{zz}(\mathbf{q})$ component of physical spin susceptibility, defined in Eq. (1.43) and in Ref. [18], since in the presence of SOC all components are no longer equivalent. Importantly, the susceptibility displays a weak momentum dependence, and therefore this indicates that there is no nesting vector connecting regions of the Fermi surface.

Focusing on the Hund's mechanism, the classification of the gap structure from Sec. 2.3 is now relevant for understanding the channels that can give rise to superconductivity. Specifically, we consider only the first (A_{1g}, spin singlet) and the last channels (A_{1g}, spin triplet) in Table 2.3. The spin-triplet channel $\frac{1}{2}([\Delta]_{yz\uparrow}^{xz\downarrow} + [\Delta]_{yz\downarrow}^{xz\uparrow})$ can be written as

$$\Delta_2 = (U' - J)\sum_{\mathbf{k}'}\left(\left\langle c_{-\mathbf{k}'yz\downarrow}c_{\mathbf{k}'xz\uparrow}\right\rangle + \left\langle c_{-\mathbf{k}'yz\uparrow}c_{\mathbf{k}'xz\downarrow}\right\rangle\right), \tag{2.30}$$

explicitly showing the orbital-singlet, spin-triplet structure, in agreement with Refs. [130, 132]. The spin-singlet channel $\frac{1}{2}([\Delta]^{xz\uparrow}_{xz\downarrow} + [\Delta]^{yz\uparrow}_{yz\downarrow})$ corresponds to

$$\Delta_0 = (U + J) \sum_{\mathbf{k}'} \left(\langle c_{-\mathbf{k}'xz\downarrow} c_{\mathbf{k}'xz\uparrow} \rangle + \left\langle c_{-\mathbf{k}'yz\downarrow} c_{\mathbf{k}'yz\uparrow} \right\rangle \right), \tag{2.31}$$

which, as opposed to the previous case, has a spin-singlet intra-orbital structure. As seen from Eq. (2.30), a direct attraction is expected in the spin-triplet channel in the Hund's regime ($J > U'$). As detailed in Ref. [130] and as we will demonstrate in Sec. 2.4.2, SOC plays a crucial role in inducing this attraction.

Having introduced the Hamiltonian and the relevant channels in the superconducting state, in the following subsections we first investigate the solution of the linearized gap equation and the gap in the band basis, followed by an analysis of the gap structure using analytical calculations. Then, we explore the role of SOC in the Hund's mechanism in driving superconducting pairing, and finally we turn to the self-consistent solution to examine the spin-singlet and spin-triplet characters of the superconducting state.

2.4.1 Linearized gap equation results and superconducting gap in the band basis

As shown in Fig. 2.2(a), solving the linearized gap equation reveals that Hund's pairing is in close agreement with spin-fluctuation pairing, since both mechanisms result in almost identical eigenvalues. This occurs because, in the Hund's regime ($J/U > 1/3$), there is an attractive interaction at the bare level that dominates over the weak momentum dependence of the RPA pairing in Eq. (2.5) (see Fig. 2.1(b)). In Fig. 2.2(b) we show the gap structure of the superconducting order parameter in the band basis. As seen, it has an A_{1g} symmetry with a sign change between the two bands, commonly referred to as an s^{+-} gap structure.

To explore the origin of the gap structure, let us find an analytic expression for the gap in the band basis, similarly to the analysis performed in Ref. [130]. With this purpose, we construct the Bogoliubov-de Gennes (BdG) Hamiltonian,

$$\mathcal{H} = \sum_{\mathbf{k}} \Psi^\dagger_{\mathbf{k}} H_{\mathrm{BdG}}(\mathbf{k}) \Psi_{\mathbf{k}}, \tag{2.32}$$

where the Nambu spinor corresponds to $\Psi_{\mathbf{k}} = \left(c_{\mathbf{k}xz\uparrow}, c_{\mathbf{k}yz\uparrow}, c^\dagger_{-\mathbf{k}xz\downarrow}, c^\dagger_{-\mathbf{k}yz\downarrow} \right)$ and

$$H_{\mathrm{BdG}}(\mathbf{k}) = \begin{pmatrix} H_0(\mathbf{k}) & \kappa_0\Delta_0 + \kappa_2\Delta_2 \\ \kappa_0\Delta_0 + \kappa_2\Delta_2 & -H_0(\mathbf{k}) \end{pmatrix}, \tag{2.33}$$

with κ_i corresponding to the Pauli matrices in orbital space. For simplicity, we only include the channels given by Eqs. (2.30)-(2.31), and we assume that Δ_0 and Δ_2 are real. The matrix form for both order parameters is obtained from Table 2.3, since Δ_0 and Δ_2 couple to κ_0 and κ_2, respectively. To obtain the equation above, we have also used that $H_0(\mathbf{k}) = H_0^\top(-\mathbf{k})$. Diagonalizing this Hamiltonian, we find the Bogoliubov quasiparticle dispersion

$$E^{\pm}_{\mathbf{k}} = \sqrt{A^2_{\mathbf{k}} + \vec{B}^2_{\mathbf{k}} + \Delta_0^2 + \Delta_2^2 \pm 2\sqrt{A^2_{\mathbf{k}}\vec{B}^2_{\mathbf{k}} + \Delta_0^2\Delta_2^2 + 2\Delta_0\Delta_2 A_{\mathbf{k}}\lambda_{\mathrm{soc}} + \Delta_2^2(\vec{B}^2_{\mathbf{k}} - \lambda^2_{\mathrm{soc}})}}, \tag{2.34}$$

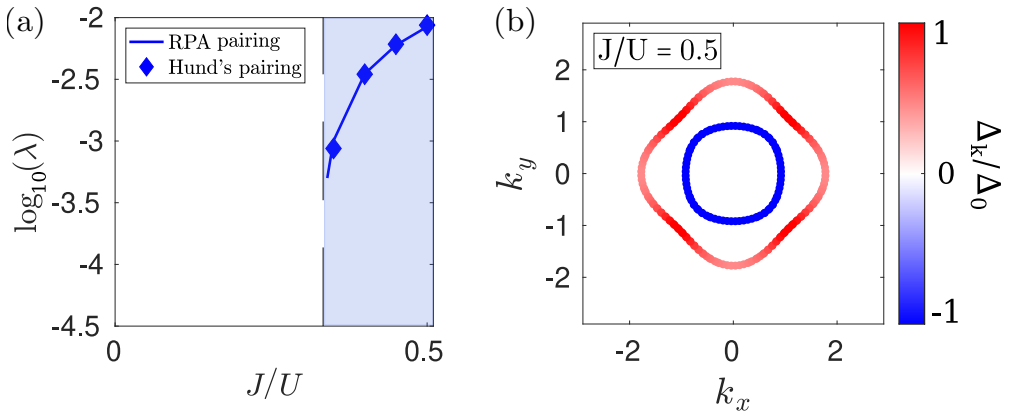

Figure 2.2: (a) Leading eigenvalue of the LGE as a function of J/U, considering $U/a = 1$, $a = 1$, $b = c = \lambda_{\rm soc} = 0.5$, and $\mu = 1.5$. The eigenvalues from Hund's pairing are indicated by diamonds, while the solid line corresponds to the results from spin-fluctuation pairing. The blue region indicates the Hund's regime ($J/U > 1/3$), where on-site Hund's pairing J induces a direct attraction at the bare level. (b) Gap structure for the superconducting order parameter in the band basis, for $J/U = 0.5$ and the same parameters as in panel (a).

where $A_{\mathbf{k}}$ and $\vec{B}_{\mathbf{k}}$ are related to the non-interacting Hamiltonian in Eq. (2.29),

$$H_0(\mathbf{k}) = A_{\mathbf{k}}\mathbb{1} + \vec{B}_{\mathbf{k}} \cdot \vec{\boldsymbol{\kappa}}, \tag{2.35}$$

so that denoting $\vec{B} = \left(B^{(1)}_{\mathbf{k}}, B^{(2)}_{\mathbf{k}}, B^{(3)}_{\mathbf{k}}\right)$,

$$A_{\mathbf{k}} = \mu - \frac{\mathbf{k}^2}{2m}, \quad B^{(1)}_{\mathbf{k}} = c(k_x^2 - k_y^2), \quad B^{(2)}_{\mathbf{k}} = \lambda_{\rm soc}, \quad B^{(3)}_{\mathbf{k}} = bk_xk_y. \tag{2.36}$$

Hence, the normal-state band dispersion corresponds to

$$\xi^{\pm}_{\mathbf{k}} = A_{\mathbf{k}} \pm \left|\vec{B}_{\mathbf{k}}\right|. \tag{2.37}$$

To transform the superconducting order parameter from orbital to band space, we first have to find the unitary operation $\mathcal{U}$ that diagonalizes the non-interacting Hamiltonian in Eq. (2.35). Using this transformation, the BdG Hamiltonian can be written as

$$\mathcal{U}H_{\rm BdG}(\mathbf{k})\mathcal{U}^{\dagger} = \begin{pmatrix} \xi_+ & 0 & \Delta_0 + \frac{\lambda_{\rm soc}}{|\vec{B}_{\mathbf{k}}|}\Delta_2 & \Delta_2 u \\ 0 & \xi_- & \Delta_2 u^* & \Delta_0 - \frac{\lambda_{\rm soc}}{|\vec{B}_{\mathbf{k}}|}\Delta_2 \\ \Delta_0 + \frac{\lambda_{\rm soc}}{|\vec{B}_{\mathbf{k}}|}\Delta_2 & \Delta_2 u & -\xi_+ & 0 \\ \Delta_2 u^* & \Delta_0 - \frac{\lambda_{\rm soc}}{|\vec{B}_{\mathbf{k}}|}\Delta_2 & 0 & -\xi_- \end{pmatrix}, \tag{2.38}$$

where we have defined $u = \frac{\Delta_2}{\sqrt{\left(B^{(1)}_{\mathbf{k}}\right)^2 + \left(B^{(2)}_{\mathbf{k}}\right)^2}}\left(-iB^{(1)}_{\mathbf{k}} + \frac{B^{(2)}_{\mathbf{k}}B^{(3)}_{\mathbf{k}}}{|\vec{B}_{\mathbf{k}}|}\right)$. Following Ref. [130], at low energies the Bogoliubov quasiparticle dispersion can be approximated by ignoring the off-diagonal terms in the pairing blocks, obtaining

$$E^{\pm}_{\mathbf{k}} \approx \sqrt{(\xi^{\pm}_{\mathbf{k}})^2 + \left(\Delta_0 \pm \frac{\lambda_{\rm soc}}{|\vec{B}_{\mathbf{k}}|}\Delta_2\right)^2}. \tag{2.39}$$

Thus, in the band basis the gaps on the two pockets correspond to

$$\Delta_{\pm} = \Delta_0 \pm \frac{\lambda_{\text{soc}}}{|\vec{B}_{\mathbf{k}}|}\Delta_2, \tag{2.40}$$

with Δ_+ (Δ_-) the gap on the larger (smaller) pocket.

Since in the Δ_0 channel the interaction is repulsive (see Eq. (2.31)), Δ_2 will be larger than Δ_0. Consequently, analyzing Eq. (2.40), we see that the gap in the band basis will have opposite signs on the two pockets, displaying the s^{+-} symmetry, with C_4 symmetry as both channels belong to the A_{1g} irrep. In addition, the gap $|\Delta_+|$ is smaller compared to $|\Delta_-|$, since the factor $|\vec{B}_{\mathbf{k}}|$ is larger on the outer pocket. These conclusions are in agreement with the gap structure shown in Fig. 2.2(b).

2.4.2 Role of spin-orbit coupling

As pointed out in Ref. [130], SOC is key to inducing pairing from the Hund's mechanism. In this section, we follow a similar analysis as in Ref. [130] to investigate the role of SOC. As seen from Eq. (2.30) and Table 2.3, in the absence of SOC the order parameter for the A_{1g} spin-triplet channel is purely inter-orbital. In general, the inter-orbital particle-particle susceptibility in the static limit and at zero energy for a dispersion $\xi_{\mathbf{k}}$ and orbitals μ, ν is given by

$$\chi^{\text{inter}} \sim -\int \frac{d^2\mathbf{k}}{(2\pi)^2}\frac{f(\xi^{\mu}_{\mathbf{k}}) - f(-\xi^{\nu}_{\mathbf{k}})}{\xi^{\mu}_{\mathbf{k}} + \xi^{\nu}_{\mathbf{k}}}, \tag{2.41}$$

where $f(\xi^{\mu}_{\mathbf{k}})$ is the Fermi function. Importantly, this quantity does not diverge logarithmically at low temperatures T. Thus, even though the Δ_2 channel has an attractive interaction (see Eq. (2.30)), it cannot give rise to pairing by itself. In contrast, the A_{1g} spin-singlet channel corresponds to an intra-orbital pairing, and at zero energy the susceptibility is generally written as

$$\chi^{\text{intra}} \sim \int \frac{d^2\mathbf{k}}{(2\pi)^2}\frac{\tanh\frac{\xi^{\mu}_{\mathbf{k}}}{2k_BT}}{2\xi^{\mu}_{\mathbf{k}}}, \tag{2.42}$$

which contains a Cooper logarithm at low temperatures T. However, in the Hund's mechanism this channel has a repulsive interaction (see Eq. (2.31)), and hence we also do not obtain pairing. To circumvent the pairing problem, we need to include SOC in the model. Given that the two channels have the same symmetry (A_{1g}), both must be present below the critical temperature in the presence of SOC. This gives rise to a superconducting state where spin-triplet and spin-singlet characters are mixed. Therefore, the Δ_2 channel gets an intra-orbital contribution sufficient to generate the logarithmic divergence at low temperatures and, consequently, superconducting pairing.

To verify this, we have calculated the self-consistent equations for the two gaps. Using the unitary transformation that diagonalizes the BdG Hamiltonian in Eq. (2.33), Eqs. (2.30)-(2.31)

can be written as

$$-\frac{\Delta_0}{U+J} = \sum_{p=\pm}\sum_{\mathbf{k}} \frac{\tanh\frac{E^p_{\mathbf{k}}}{2T}}{2E^p_{\mathbf{k}}}\left(\Delta_0 + 4\Delta_2 \frac{A_{\mathbf{k}}\lambda_{\rm soc}+\Delta_0\Delta_2}{(E^p_{\mathbf{k}})^2-(E^{-p}_{\mathbf{k}})^2}\right), \tag{2.43}$$

$$-\frac{\Delta_2}{U'-J} = \sum_{p=\pm}\sum_{\mathbf{k}} \frac{\tanh\frac{E^p_{\mathbf{k}}}{2T}}{2E^p_{\mathbf{k}}}\left(\Delta_2 + 4\Delta_2 \frac{\vec{B}^2_{\mathbf{k}}-\lambda_{\rm soc}}{(E^p_{\mathbf{k}})^2-(E^{-p}_{\mathbf{k}})^2} + 4\Delta_0 \frac{A_{\mathbf{k}}\lambda_{\rm soc}+\Delta_0\Delta_2}{(E^p_{\mathbf{k}})^2-(E^{-p}_{\mathbf{k}})^2}\right). \tag{2.44}$$

Close to the critical temperature T_c, we can assume that Δ_0 and Δ_2 are very small, and hence the dispersion corresponds to the normal state case,

$$E^{\pm}_{\mathbf{k}} \simeq \xi^{\pm}_{\mathbf{k}} = A_{\mathbf{k}} \pm \left|\vec{B}_{\mathbf{k}}\right| \Rightarrow (E^{\pm}_{\mathbf{k}})^2 - (E^{\mp}_{\mathbf{k}})^2 = \pm 4 A_{\mathbf{k}}\left|\vec{B}_{\mathbf{k}}\right|. \tag{2.45}$$

Therefore, considering only the linear terms in the order parameter, from Eqs. (2.43)-(2.44) we can obtain the linearized mean-field self-consistent equations,

$$-\frac{\Delta_0}{U+J} = \sum_{p=\pm}\int \frac{d^2\mathbf{k}}{(2\pi)^2}\frac{\tanh\frac{\xi^p_{\mathbf{k}}}{2T_c}}{2\xi^p_{\mathbf{k}}}\left(\Delta_0 + p\Delta_2\frac{\lambda_{\rm soc}}{\left|\vec{B}_{\mathbf{k}}\right|}\right), \tag{2.46}$$

$$-\frac{\Delta_2}{U'-J} = \sum_{p=\pm}\int \frac{d^2\mathbf{k}}{(2\pi)^2}\frac{\tanh\frac{\xi^p_{\mathbf{k}}}{2T_c}}{2\xi^p_{\mathbf{k}}}\left(\Delta_2\left[\frac{\lambda^2_{\rm soc}}{\left|\vec{B}_{\mathbf{k}}\right|} + \frac{\xi^p_{\mathbf{k}}}{A_{\mathbf{k}}}\left(1-\frac{\lambda^2_{\rm soc}}{\left|\vec{B}_{\mathbf{k}}\right|}\right)\right] + p\Delta_0\frac{\lambda_{\rm soc}}{\left|\vec{B}_{\mathbf{k}}\right|}\right). \tag{2.47}$$

These equations have the form

$$\begin{pmatrix} -\frac{1}{U+J}-\chi_{00}(T_c) & -\chi_{02}(T_c) \\ -\chi_{02}(T_c) & -\frac{1}{U'-J}-\chi_{22}(T_c)\end{pmatrix}\begin{pmatrix}\Delta_0(T_c)\\ \Delta_2(T_c)\end{pmatrix} = 0, \tag{2.48}$$

confirming that in the presence of SOC the following susceptibilities contain the logarithmic divergence at low temperatures,

$$\chi_{00}(T_c) = \sum_{p=\pm}\int \frac{d^2\mathbf{k}}{(2\pi)^2}\frac{\tanh\frac{\xi^p_{\mathbf{k}}}{2T_c}}{2\xi^p_{\mathbf{k}}}, \tag{2.49}$$

$$\chi_{22}(T_c) = \sum_{p=\pm}\int \frac{d^2\mathbf{k}}{(2\pi)^2}\frac{\tanh\frac{\xi^p_{\mathbf{k}}}{2T_c}}{2\xi^p_{\mathbf{k}}}\left[\frac{\lambda^2_{\rm soc}}{\left|\vec{B}_{\mathbf{k}}\right|} + \frac{\xi^p_{\mathbf{k}}}{A_{\mathbf{k}}}\left(1-\frac{\lambda^2_{\rm soc}}{\left|\vec{B}_{\mathbf{k}}\right|}\right)\right], \tag{2.50}$$

while the mixed susceptibility,

$$\chi_{02}(T_c) = \sum_{p=\pm}\int \frac{d^2\mathbf{k}}{(2\pi)^2}\frac{\tanh\frac{\xi^p_{\mathbf{k}}}{2T_c}}{2\xi^p_{\mathbf{k}}} p\frac{\lambda_{\rm soc}}{\left|\vec{B}_{\mathbf{k}}\right|}, \tag{2.51}$$

is finite as the logarithms cancel, as discussed in Ref. [130].

We will not elaborate further here, but Ref. [130] also notes that pairing exists for a finite SOC with any attractive interaction $U'-J$, independent of the repulsive pairing $U+J$. In Fig. 2.3(a) we show the leading eigenvalue obtained by solving the linearized gap equation as a function of the SOC strength, considering the Hund's mechanism. As seen for two different values of J/U, SOC is crucial to obtain a finite eigenvalue, confirming the previous analytical results.

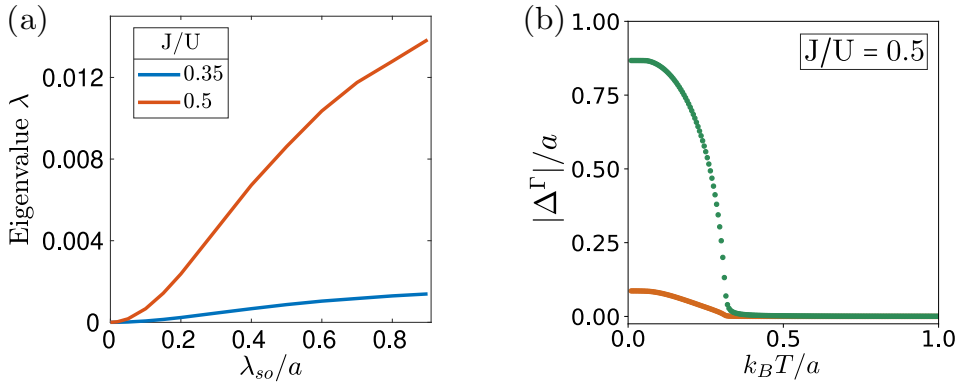

Figure 2.3: (a) Eigenvalue obtained by solving the LGE (see Eq. (2.9)) as a function of $\lambda_{\rm soc}$ for two values of J/U in the Hund's pairing regime, with U/a = 1, a = 1, b = c = $\lambda_{\rm soc}$ = 0.5, and μ = 1.5. (b) Self-consistent solution in orbital and spin space as a function of temperature from the Hund's pairing mechanism, for the same parameters as in (a) but with U/a = 6 and J/U = 0.5. The symmetry of the superconducting channels is detailed in Table 2.7.

Table 2.7: Symmetry channels from Table 2.3 that give a non-vanishing order parameter from the self-consistent calculation, as seen in Fig. 2.3(b). We indicate the orbital and spin character and the corresponding irrep.

	Channel	Orbital	Spin	Irrep
●	$\frac{1}{2}([\Delta]^{xz\downarrow}_{yz\uparrow} + [\Delta]^{xz\uparrow}_{yz\downarrow})$	Singlet	Triplet	A_{1g}
●	$\frac{1}{2}([\Delta]^{xz\uparrow}_{xz\downarrow} + [\Delta]^{yz\uparrow}_{yz\downarrow})$	Triplet	Singlet	A_{1g}

2.4.3 Self-consistent solution

In the previous subsections, we have discussed the results from the linearized gap equation and the role of SOC in the Hund's mechanism. However, since the linearized gap equation is solved in the band basis, it is not straightforward to project the superconducting order parameter into singlet and triplet character. With this purpose, we have also solved the full self-consistent equation in orbital and spin space, classifying the gap as described in Sec. 2.3. In Fig. 2.3(b) we show the non-zero superconducting channels obtained from Hund's pairing, detailed in Table 2.7, as a function of temperature. The dominant A_{1g} channel (green curve) has a spin-triplet structure, as expected from the direct attractive interaction induced in this channel (see Eq. (2.30)). However, due to the presence of SOC a subleading channel with spin-singlet structure is also present, which is smaller since the interaction for this combination is repulsive (see Eq. (2.31)).

Recalling the analytic expression for the gap in the orbital basis that we found in Eq. (2.40), we have demonstrated in Fig. 2.3(b) that the spin-triplet channel (Δ_2) is larger when compared to the spin-singlet combination (Δ_0). Thus, this confirms that there should be a sign change in the superconducting gap between the inner and the outer pocket in the band basis, in agreement with the result shown in Fig. 2.2(b).

2.5 Three-orbital model with nesting

In the previous section, we demonstrated numerically that in a multiorbital model where the susceptibility exhibits a weak momentum dependence, the pairing strength and gap structure resulting from Hund's and spin-fluctuation pairings yield compatible results. Here, let us consider a different multiorbital system in which the bands feature some nesting, as is usually the case in many unconventional superconductors. Specifically, we focus on a model relevant for Sr_2RuO_4 due to previous proposals suggesting that Hund's pairing generates its superconducting state [20, 21]. The Fermi surface of this material has been experimentally determined, revealing three distinct bands with predominant contributions from d_{xz}, d_{yz} and d_{xy} orbitals [142–144], characterized by a strong two-dimensional behavior and thus weak k_z dispersion [145].

Following the same procedure as in Sec. 2.4 for the two-orbital model, we can construct the non-interacting Hamiltonian by combining terms that transform in total like the A_{1g} irrep of D_{4h}. To this end, the first step is to recall how the spin and orbital matrices transform under the point group operations, as identified in Tables 2.1 and 2.4, respectively. We consider a two-dimensional lattice model including only intra-orbital hoppings, and therefore we only include hopping terms that couple to the Gell-Mann matrices λ_0 and λ_3, since these are the only diagonal matrices in the set from Eq. (2.25) (and λ_8 transforms like λ_0, as seen from Table 2.4). First, λ_0 transforms like A_{1g}, which couples to the usual orbital-independent dispersion. Secondly, since λ_3 transforms like the B_{1g} irrep, it must enter in the Hamiltonian together with a hopping term transforming in the same way, i.e., $\cos k_x - \cos k_y$. Thus, combining these two terms, the non-interacting part of the Hamiltonian without SOC corresponds to

$$\sum_{\mathbf{k},\nu,\sigma} \xi^{\nu}_{\mathbf{k}} c^{\dagger}_{\mathbf{k}\nu\sigma} c_{\mathbf{k}\nu\sigma}, \tag{2.52}$$

where the dispersions that reproduce the ARPES experiments [134, 146] are given by

$$\begin{aligned} \xi^{xz/yz}_{\mathbf{k}} &= -2t_{1/2}\cos k_x - 2t_{2/1}\cos k_y - \mu, \\ \xi^{xy}_{\mathbf{k}} &= -2t_3(\cos k_x + \cos k_y) - 4t_4 \cos k_x \cos k_y - 2t_5(\cos 2k_x + \cos 2k_y) - \mu, \end{aligned} \tag{2.53}$$

with t_1, t_2 (t_3) the nearest-neighbor hoppings for d_{xz}/d_{yz} (d_{xy}) orbitals, and t_4 and t_5 the second- and third-neighbor hoppings for d_{xy} orbitals, respectively. Finally, considering only on-site SOC, there are three allowed terms corresponding to the three imaginary matrices λ_2, λ_7, λ_5. These matrices must couple to the spin degree of freedom transforming in the same way to obtain invariants (see Table 2.1). Thus, the SOC Hamiltonian corresponds to

$$H_{\mathrm{SOC}} = \lambda_{\mathrm{soc}}(\lambda_2\sigma_z + \lambda_7\sigma_y - \lambda_5\sigma_x), \tag{2.54}$$

where we have chosen the basis $\{c_{\mathbf{k}xz\uparrow}, c_{\mathbf{k}yz\uparrow}, c_{\mathbf{k}xz\downarrow}, c_{\mathbf{k}yz\downarrow}, c_{\mathbf{k}xy\downarrow}, c_{\mathbf{k}xy\downarrow}\}$. The minus sign between the last two terms is needed to preserve the mirror symmetries.

The normal state Hamiltonian decomposes into two blocks, and therefore it is sufficient to consider the basis $\{c_{\mathbf{k}xz\alpha}, c_{\mathbf{k}yz\alpha}, c_{\mathbf{k}xy\bar{\alpha}}\}$ [18, 134]. Hence, in this basis, the non-interacting

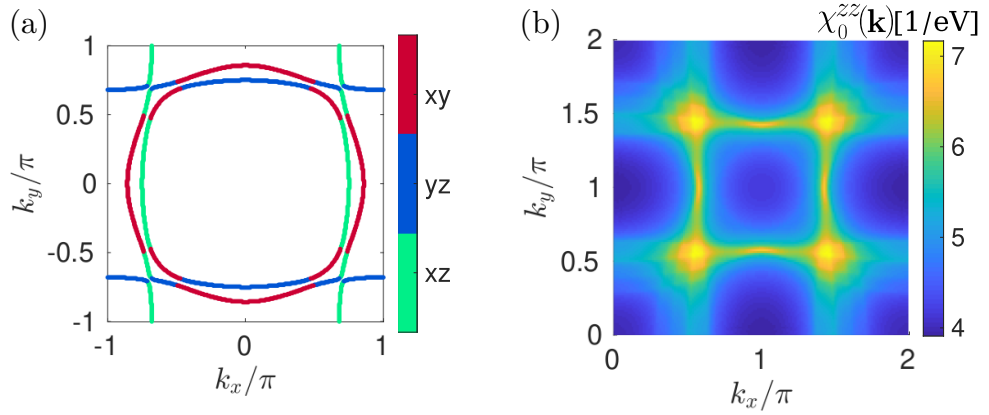

Figure 2.4: (a) Fermi surface for the three-orbital model in Eq. (2.55), for $(t_1, t_2, t_3, t_4, t_5, \mu) = (88, 9, 80, 40, 5, 109)$ meV and SOC $\lambda_{\rm soc} = 20$ meV to reproduce the ARPES experiments [134, 146]. The color code indicates the orbital content of each band. (b) Momentum structure of the bare static susceptibility $\chi_0^{zz}(\mathbf{k})$, considering the same parameters as in panel (a).

Hamiltonian including SOC can be written as

$$H_0(\mathbf{k}) = \begin{pmatrix} \xi_{\mathbf{k}}^{xz} & -i\alpha\lambda_{\rm soc}/2 & i\lambda_{\rm soc}/2 \\ i\alpha\lambda_{\rm soc}/2 & \xi_{\mathbf{k}}^{yz} & -\alpha\lambda_{\rm soc}/2 \\ -i\lambda_{\rm soc}/2 & -\alpha\lambda_{\rm soc}/2 & \xi_{\mathbf{k}}^{xy} \end{pmatrix}. \tag{2.55}$$

In Fig. 2.4(a) we show the Fermi surface indicating the orbital content by the color code. As seen, there are three different bands, one with a dominant d_{xy} orbital content, and two bands with a majority of d_{xz} and d_{yz} character. Figure 2.4(b) displays the corresponding spin susceptibility at zero energy. In contrast to the susceptibility obtained from the two-orbital model shown in Fig. 2.1(b), the nesting peaks are now well-defined and exhibit a stronger momentum dependence.

In the following subsections, similarly to Sec. 2.4, we use the model in Eq. (2.55) to solve the linearized gap equation for the superconducting order parameter, and then we classify the symmetry channels using the self-consistent solution.

2.5.1 Linearized gap equation

Let us first solve the linearized gap equation to compare Hund's and spin-fluctuation pairing for the three-orbital model in Eq. (2.55). In this case, the analytical analysis becomes more involved, as the Hamiltonian corresponds to a larger matrix. Consequently, we focus on the numerical results, although the mechanism generating Hund's pairing in the presence of SOC is similar to Sec. 2.4. However, in the two-orbital model considered in Sec. 2.4, Hund's pairing could only generate a superconducting gap with A_{1g} symmetry, as it was the only irrep that included both a spin-singlet and a spin-triplet channel (see Table 2.3). Therefore, as discussed in Sec. 2.4.2, only in the presence of SOC does the triplet channel contain the Cooper logarithm necessary for pairing. In contrast, by inspecting Tables 2.5-2.6, we observe that in the three-orbital model the Hund's mechanism can generate superconducting gaps with different symmetries, which

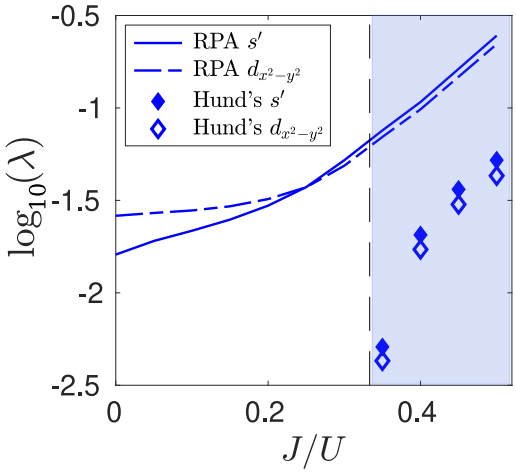

Figure 2.5: Leading eigenvalue of the LGE as a function of J/U, considering $U = 100$ meV and the same parameters as in Fig. 2.4. The eigenvalues from Hund's pairing are indicated by diamonds, while the solid line corresponds to the results from spin-fluctuation pairing. The blue region indicates the Hund's regime ($J/U > 1/3$), where on-site Hund's pairing J induces a direct attraction at the bare level.

include a spin-triplet and a spin-singlet channel that induce the logarithmic divergence at low temperatures in the presence of SOC. However, to stabilize the E_g solution a three-dimensional model is needed [21].

Figure 2.5 shows the leading eigenvalues from the linearized gap equation as a function of J/U. Importantly, now the spin-fluctuation mechanism generates a gap structure with A_{1g} (s') or B_{1g} ($d_{x^2-y^2}$) symmetry, as shown by the solid and dashed blue line, respectively. In the regime where a bare interaction is induced ($J/U > 1/3$), the Hund's mechanism can also generate pairing and give rise to an A_{1g} and B_{1g} gap structure, denoted by the diamond symbols. In contrast to the two-orbital model shown in Fig. 2.2(a), Hund's pairing in this case generates smaller eigenvalues and, consequently, lower critical temperatures ($T_c \propto e^{1/\lambda}$, with λ denoting the eigenvalue). These results reveal that spin-fluctuation mediated pairing dominates in Fig. 2.5 due to the significant momentum dependence of the RPA pairing in Eq. (2.5), as displayed in Fig. 2.4(b).

2.5.2 Self-consistent solution

Having compared both mechanisms from the linearized gap equation results, we proceed to analyze the gap structure from the full self-consistent solution in orbital and spin space (see Sec. 2.3). The full classification of the different channels is detailed in Tables 2.5-2.6, while the non-zero channels obtained from the self-consistent solution for the Hund's and spin-fluctuation pairings are listed in Table 2.8.

Focusing first on the spin-fluctuation pairing, in Figs. 2.6(a)-(c) we show the leading superconducting channels (see Table 2.8) as a function of temperature, considering $J/U = 0.3$, $J/U = 0.35$ and $J/U = 0.4$, respectively. The corresponding gap structures at low temperatures are shown in the panels below, see Figs. 2.6(d)-(g). First, Fig. 2.6(a) shows that the dominant

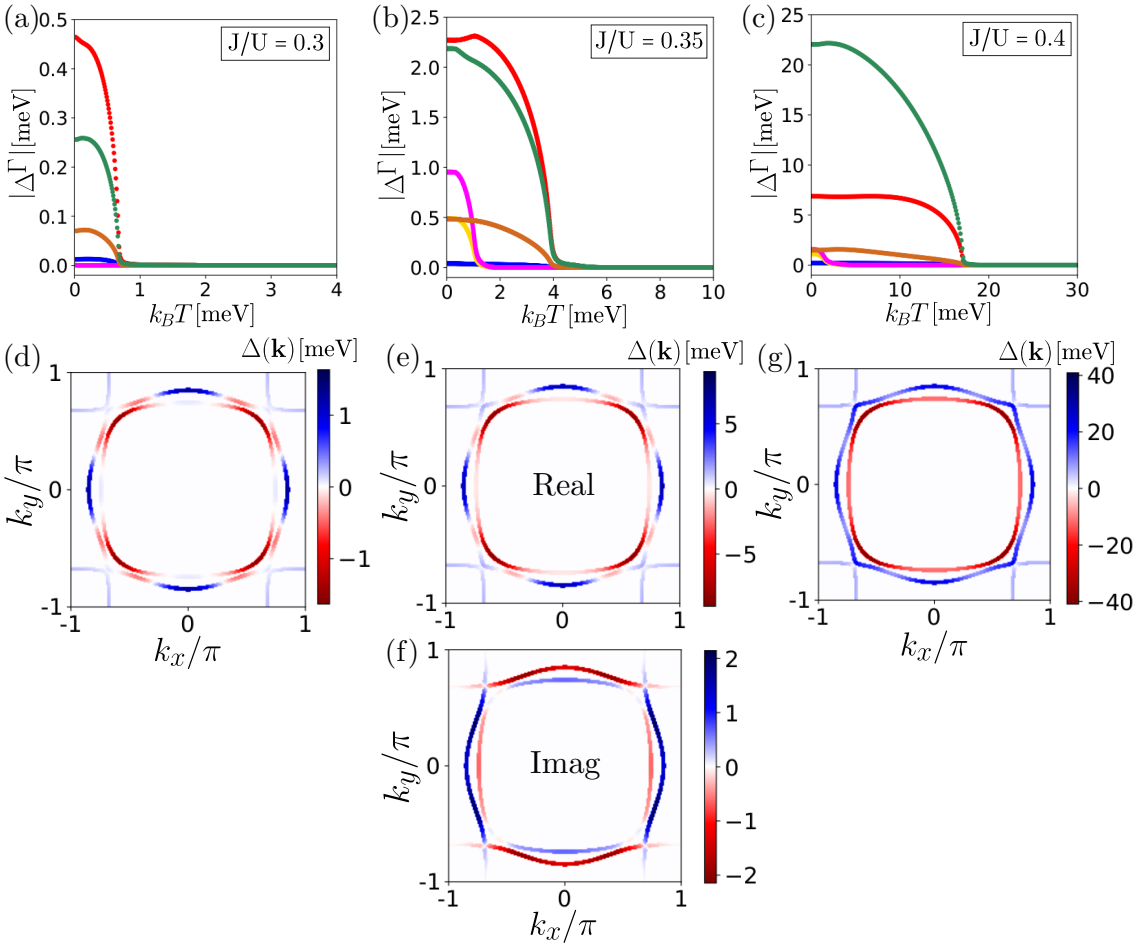

Figure 2.6: Self-consistent solution in orbital and spin space as a function of temperature from the spin-fluctuation mechanism, for the same parameters as in Fig. 2.4, in addition to $U = 110$ meV and (a) $J/U = 0.3$, (b) $J/U = 0.35$ and (c) $J/U = 0.4$. The symmetry of the superconducting channels and their color code are detailed in Table 2.8. Panels (d)-(g) show the corresponding gap structure on the Fermi surface in the band basis at $k_BT = 0.01$ meV. From panel (b) we see that at low temperatures two symmetries coexist (A_{1g} and B_{1g}), and thus panels (e) and (f) display the real and imaginary parts of the gap, showing a time-reversal symmetry broken combination of both symmetries.

gap structure (red curve) has A_{1g} symmetry with orbital-triplet and spin-singlet character. As shown in Table 2.8, this channel couples to the basis function $\cos 2k_x + \cos 2k_y$, as seen also from the nodal gap structure in Fig. 2.6(d), and therefore corresponds to a next-nearest-neighbor pairing state. Secondly, in the Hund's regime, in particular in the case $J/U = 0.35$ displayed in Fig. 2.6(b), the previous A_{1g} channel still dominates. Nevertheless, there is a subleading solution with orbital-singlet spin-triplet gap structure (green curve). This case also reveals that there are non-zero channels with B_{1g} symmetry with mixed spin-singlet and spin-triplet character that set in at a lower critical temperature (see Table 2.8). Therefore, as seen from Figs. 2.6(e)-(f), the real and imaginary parts of the gap demonstrate that it stabilizes the combination $A_{1g} + iB_{1g}$ at low temperatures, which breaks time-reversal symmetry. Finally, for a larger J/U, the spin-triplet gap structure is favored, as seen in Fig. 2.6(c), and the gap structure displays an s^{+-} structure

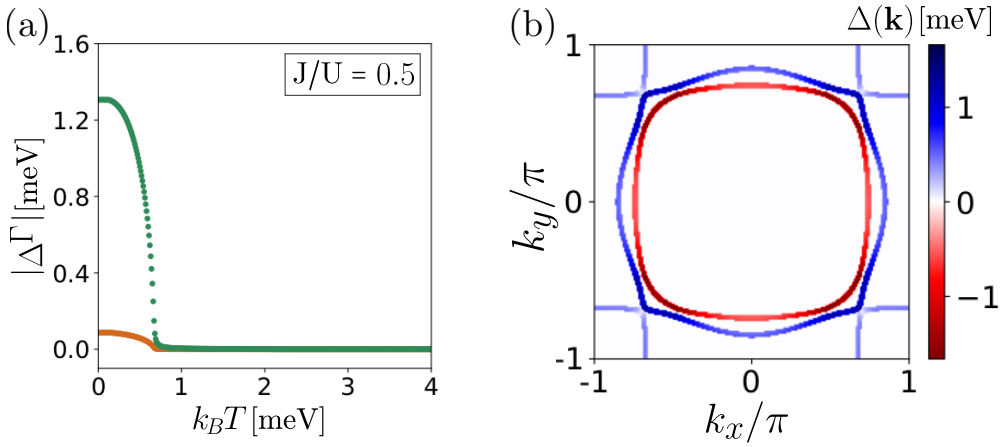

Figure 2.7: (a) Self-consistent solution in orbital and spin space as a function of temperature from Hund's mechanism, for the same parameters as in Fig. 2.4, $U = 110$ meV and $J/U = 0.5$. The symmetry of the superconducting channels is detailed in Table 2.8. (b) Gap structure on the Fermi surface in the band basis at $k_BT = 0.01$ meV.

and changes sign between the inner and the two outer bands, similarly to the two-orbital model result presented in Fig. 2.2(b).

If we now turn to the results from Hund's pairing, shown in Fig. 2.7, the solution is simpler since there are only two non-zero channels. As seen from Table 2.8, the dominant one corresponds to the inter-orbital spin-triplet state (green curve), while the subleading solution has spin singlet (brown curve). The gap structure shown in Fig. 2.7(b) is representative throughout the Hund's regime ($J/U > 1/3$), and it is similar to Fig. 2.6(g). However, a comparison of Fig. 2.6(c) and Fig. 2.7(a) reveals that the critical temperature and the gap magnitude are remarkably smaller from Hund's mechanism compared to spin-fluctuation pairing, in agreement with Fig. 2.5. Note that in Fig. 2.7(a) we choose $J/U = 0.5$ to resolve the small gap, while in Fig. 2.6(g), $J/U = 0.4$.

Table 2.8: Symmetry channels from Tables 2.5-2.6 that give a non-vanishing order parameter from the self-consistent calculation, as shown in Figs. 2.6-2.7. We indicate the orbital and spin character and the corresponding irrep, in addition to the basis function obtained after projecting the gap, as detailed in Eq. (2.13).

	Channel	Basis function	Orbital	Spin	Irrep
●	$\frac{1}{2\sqrt{3}}([\Delta]^{xz\uparrow}_{xz\downarrow} + [\Delta]^{yz\uparrow}_{yz\downarrow} - 2[\Delta]^{xy\uparrow}_{xy\downarrow})$	$\cos 2k_x + \cos 2k_y$	Triplet	Singlet	A_{1g}
●	$\frac{1}{4}\big(i[\Delta]^{xz\downarrow}_{xy\downarrow} - i[\Delta]^{xz\uparrow}_{xy\uparrow} - [\Delta]^{yz\uparrow}_{xy\uparrow} - [\Delta]^{yz\downarrow}_{xy\downarrow}\big)$	$\cos 2k_x + \cos 2k_y$	Singlet	Triplet	A_{1g}
●	$\frac{1}{3}([\Delta]^{xz\uparrow}_{xz\downarrow} + [\Delta]^{yz\uparrow}_{yz\downarrow} + [\Delta]^{xy\uparrow}_{xy\downarrow})$	$\cos 2k_x - \cos 2k_y$	Triplet	Singlet	B_{1g}
●	$\frac{1}{4}\big(i[\Delta]^{xz\downarrow}_{xy\downarrow} - i[\Delta]^{xz\uparrow}_{xy\uparrow} + [\Delta]^{yz\uparrow}_{xy\uparrow} + [\Delta]^{yz\downarrow}_{xy\downarrow}\big)$	1	Singlet	Triplet	B_{1g}
●	$\frac{1}{4}\big(i[\Delta]^{xz\downarrow}_{xy\downarrow} - i[\Delta]^{xz\uparrow}_{xy\uparrow} - [\Delta]^{yz\uparrow}_{xy\uparrow} - [\Delta]^{yz\downarrow}_{xy\downarrow}\big)$	1	Singlet	Triplet	A_{1g}
●	$\frac{1}{3}([\Delta]^{xz\uparrow}_{xz\downarrow} + [\Delta]^{yz\uparrow}_{yz\downarrow} + [\Delta]^{xy\uparrow}_{xy\downarrow})$	1	Triplet	Singlet	A_{1g}

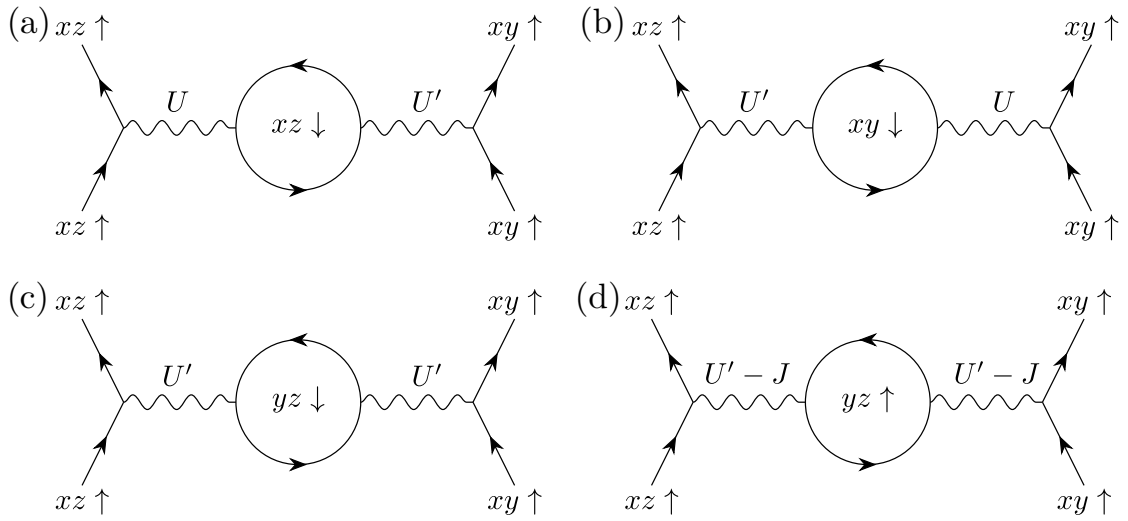

Figure 2.8: Second-order bubble diagrams restricting to intra-orbital susceptibilities for interactions between same-spin electrons on d_{xz} and d_{xy} orbitals. These diagrams give rise to an effective attractive pairing, even though the bare interaction is repulsive.

Therefore, for the same parameters the critical temperature obtained from Hund's pairing would be even lower.

Thus, the self-consistent solution confirms the results from the linearized gap equation shown in Fig. 2.5, indicating that the critical temperature from Hund's mechanism is significantly lower than for spin-fluctuation pairing.

2.6 Renormalization of the on-site interaction

In this section, we investigate whether the extent of the Hund's regime ($J/U > 1/3$) can become larger when renormalized by higher-order interactions. This has been previously discussed in Ref. [125] for the case of degenerate orbitals, but we generalize this result including the orbital dependence of the susceptibility. To illustrate this point, for simplicity we include only the intra-orbital susceptibility components, and thus we restrict to $\chi_0^{\mu\sigma}(\mathbf{q}) \equiv [\chi_0(\mathbf{q})]^{\mu\sigma\mu\sigma}_{\mu\sigma\mu\sigma}$.

As a particular example, we focus on the interactions between same-spin electrons on orbitals xz and xy. The four relevant diagrams contributing in this case are displayed in Fig. 2.8, obtaining the following correction to the bare interaction to second order,

$$\begin{aligned}[V^{(2)}(\mathbf{k},\mathbf{k}')]^{xz\uparrow xz\uparrow}_{xy\uparrow xy\uparrow} \simeq (U'-J) - UU'[\chi_0^{xz\downarrow}(\mathbf{k}-\mathbf{k}') + \chi_0^{xy\downarrow}(\mathbf{k}-\mathbf{k}')] \\ - (U')^2\chi_0^{yz\downarrow}(\mathbf{k}-\mathbf{k}') - (U'-J)^2\chi_0^{yz\uparrow}(\mathbf{k}-\mathbf{k}').\end{aligned} \tag{2.56}$$

Since we are interested in the on-site pairing interaction driving the green superconducting channels in Figs. 2.6(a)-(c) and Fig. 2.7(a), we Fourier transform the previous equation to real

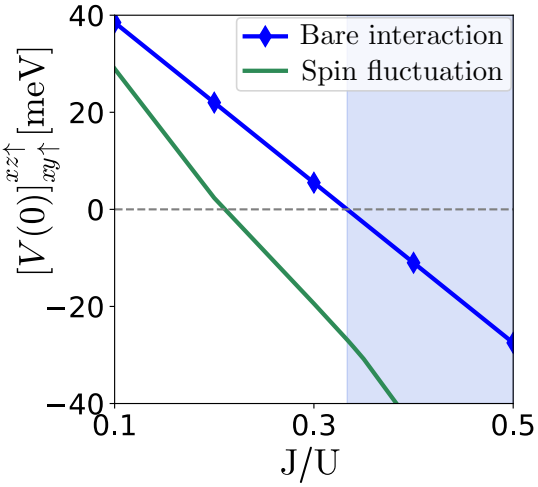

Figure 2.9: On-site spin-triplet pairing interaction in real space between xz and xy orbitals, $[V(0)]^{xz\uparrow}_{xy\uparrow}$ (see Eq. (2.58) and Appendix A), as a function of J/U, for Hund's pairing (blue line) and spin-fluctuation pairing (green line). These interactions determine the behavior of the green curve in Figs. 2.6(a)-(c) and Fig. 2.7(a).

space and consider only the on-site term,

$$[V^{(2)}(\mathbf{r}=0)]^{xz\uparrow xz\uparrow}_{xy\uparrow xy\uparrow} \simeq (U'-J) - UU' \sum_{\mathbf{q}} [\chi_0^{xz\downarrow}(\mathbf{q}) + \chi_0^{xy\downarrow}(\mathbf{q})] - (U')^2 \sum_{\mathbf{q}} \chi_0^{yz\downarrow}(\mathbf{q}) - (U'-J)^2 \sum_{\mathbf{q}} \chi_0^{yz\uparrow}(\mathbf{q}), \tag{2.57}$$

where we have used that the Fourier transform of the susceptibility is given by $\chi_0^{\mu\sigma}(\mathbf{r}) = \sum_{\mathbf{q}} \chi_0^{\mu\sigma}(\mathbf{q}) e^{i\mathbf{q}\cdot\mathbf{r}}$, and thus for the on-site term $\chi_0^{\mu\sigma}(\mathbf{r}=0) = \sum_{\mathbf{q}} \chi_0^{\mu\sigma}(\mathbf{q})$. This expression explicitly demonstrates that the contribution from second-order bubble diagrams can induce an attractive on-site interaction even when the bare interactions are repulsive ($J < U'$).

To verify the regime where on-site interactions become attractive, in Fig. 2.9 we show the on-site triplet pairing interaction between electrons on orbitals xz and xy as a function of J/U. To comply with the symmetries of the Hamiltonian (see Eq. (2.11)), the on-site interaction shown in Fig. 2.9 is symmetrized as

$$[V(\mathbf{r}=0)]^{xz\uparrow}_{xy\uparrow} = [U]^{xz\uparrow,xy\uparrow}_{xy\uparrow,xz\uparrow} + [V(\mathbf{r}=0)]^{xz\uparrow,xy\uparrow}_{xy\uparrow,xz\uparrow} - [V(\mathbf{r}=0)]^{xz\uparrow,xz\uparrow}_{xy\uparrow,xy\uparrow}. \tag{2.58}$$

As seen from the Hund's mechanism (blue line), an attractive on-site interaction is induced only in the regime $J/U > 1/3$, driving the spin-triplet channel denoted by the green color in Fig. 2.7(a). Let us now focus instead on the on-site part of the spin-fluctuation pairing (green line), obtained by Fourier transforming the full effective pairing vertex in Eq. (2.5). Figure 2.9 reveals that the spin-fluctuation mechanism enhances the on-site attraction compared to Hund's pairing, since the former can induce an on-site attraction for $J/U < 1/3$, even when the bare interaction is still repulsive. This on-site interaction drives the spin-triplet superconducting channel denoted by the green color in Figs. 2.6(a)-(c).

Hence, we have derived the correction to the bare Hund's interaction between same-spin electrons on orbitals xz and yz in Eq. (2.57). We have shown that, in agreement with Ref. [125],

when the second-order diagrams dominate the bare interaction an attractive on-site interaction can be induced. This is indeed what we obtain by Fourier transforming the full effective pairing interaction from spin fluctuations, since the on-site term becomes attractive even when $U' - J > 0$ (see Fig. 2.9).

2.7 Discussion and conclusions

In this Chapter, we have compared two different mechanisms inducing superconductivity: 1) Hund's pairing, which induces an attraction at the bare level in the regime where Hund's coupling is sufficiently large, $J/U > 1/3$; and 2) spin-fluctuation pairing, which includes higher-order processes renormalizing the bare interaction by summing the contributions from bubble and ladder diagrams to all orders. We have classified the gap symmetries and confirmed that Hund's mechanism generates an inter-orbital spin-triplet superconducting gap. This state has been proposed as a candidate to describe the superconducting gap in many materials, including iron-based superconductors and Sr_2RuO_4 [20, 122–133, 147].

By considering a two-orbital model relevant for iron-based systems [130], we have demonstrated that, in band structures where there is no nesting, Hund's pairing gives comparable results to spin-fluctuation mediated pairing in the regime where the bare interaction becomes attractive. We have performed analytical calculations to understand the form of the gap in the band basis and to demonstrate why a finite spin-orbit coupling strength is crucial to obtain superconducting pairing. The full self-consistent solution in orbital and spin space confirmed that the leading solution corresponds to an inter-orbital spin-triplet state, although a small intra-orbital spin-singlet channel with the same symmetry (A_{1g}) is also generated due to the presence of SOC .

We have also analyzed a three-orbital model with nesting, considering a model relevant for Sr_2RuO_4, where the susceptibility exhibits a strong momentum dependence. We have observed that the spin-fluctuation mechanism gives rise to significantly higher critical temperatures for the different channels when compared to the Hund's mechanism. For the Hund's pairing case, the gap in the band basis also changes sign between the inner and the outer pockets, similarly to the two-orbital model results. By contrast, the self-consistent solution demonstrates that the spin-fluctuation pairing leads to a gap with a different nodal structure, and also stabilizes other gap symmetries with different critical temperatures. Specifically, we have obtained that the A_{1g} and B_{1g} symmetries coexist at lower temperatures, leading to time-reversal symmetry breaking.

We have also verified that the extent of the Hund's regime is enhanced when higher-order interactions are included, since the spin-fluctuation pairing induces an on-site attraction for $J/U < 1/3$. This can generate the inter-orbital spin-triplet channel even when the bare interaction is still repulsive.

In the particular case of Sr_2RuO_4, previous works have estimated $J/U \simeq 0.1 - 0.2$ [148, 149], and thus it might not be realistic that this material has such a large Hund's coupling, $J > 1/3$, which is necessary to generate superconducting pairing from the Hund's mechanism. To investigate the role of SOC, we have also performed self-consistent calculations for a larger

value of the SOC, comparing the order parameter in orbital and spin space from Hund's and spin-fluctuation pairing. We have obtained that the two mechanisms give rise to a similar gap structure for a smaller value of J/U, although Hund's pairing still generates significantly lower critical temperatures.

Finally, our calculations point out that in nested band structures the Hund's pairing approach gives a different superconducting state when compared to the spin-fluctuation mechanism, which is probably relevant for most unconventional superconductors of current interest. Given that Hund's coupling is generally small in these materials, our results suggest that the inter-orbital spin-triplet states might not be realized.

Part II

Superconducting diode effect

Chapter 3

Superconducting diodes from magnetization gradients

Info: *Part of the content and figures of this Chapter have been published together with P. Kotetes and B.M. Andersen in Ref.* [3]*, available at Phys. Rev. B* **109**, 144503 (2024).

3.1 Introduction

The superconducting diode effect has recently attracted a lot of interest after being observed for the first time [22]. To motivate the importance of this effect, it is instructive to discuss first the usual semiconductor diodes, which are formed by two semiconductors that are doped differently. These devices have been known for a long time and are characterized by an asymmetric relation between the current and the resistance. The origin of this behavior is the built-in electric field, which breaks spatial inversion and therefore gives rise to a nonreciprocal transport between opposite directions, i.e., there is a larger resistance in one direction and a smaller resistance along the opposite direction.

Semiconductor diodes are nowadays the basis of many electronic compounds, such as rectifiers, which can convert alternating current (AC) to direct current (DC), as they allow current to flow only in a single direction. However, semiconductor diodes are dissipative, since there is an energy loss due to the finite resistance. Remarkably, this contrasts with the superconducting analogue of the diode effect, which should have zero resistance along one direction, therefore being non-dissipative. As a consequence, this motivates studying the mechanisms giving rise to the superconducting diode effect, particularly after the first recent experimental observation [22].

In the superconducting diode effect, it is the critical currents that become different along opposite directions. Notably, there are two requirements to obtain an asymmetric critical current. On the one hand, spatial inversion must be broken. This can be achieved, for instance, by considering spin-orbit coupling, which breaks the spin up and spin down degeneracy. On the other hand, breaking of time-reversal symmetry must also occur. The simplest phenomenon breaking this symmetry is magnetism, and therefore in Ref. [22] an in-plane magnetic field was

applied to the system. Shortly after this work, Ref. [150] also observed the superconducting diode effect in a material breaking inversion symmetry, but without any applied field. This has also been reported in magic angle twisted bilayer graphene and trilayer graphene [151,152], leading to different proposals for the origin of time-reversal symmetry breaking in these materials, including the possibility that it could be an intrinsic property of these systems.

Recently, many experimental works have confirmed the observation of the superconducting diode effect in different setups [150–165], even though the efficiency of the rectification obtained from a superconducting diode significantly depends on the design [166]. As explored in these works, the superconducting diode effect can have different origins. It can arise due to the tunnel junction [150, 151, 154, 156, 162], vortex physics [158, 163, 165] or due to a finite Cooper pair momentum in the superconducting state [152, 153, 155, 157, 159–161, 164].

In this work, we focus on the latter mechanism. As we will demonstrate in Secs. 3.2 and 3.4, in superconductors with a strong spin-orbit coupling (SOC) and broken inversion symmetry the Fermi surfaces are split. By additionally applying an in-plane magnetic field, the Fermi surfaces are shifted and the superconductor generates a ground state in which the Cooper pairs carry a finite center-of-mass momentum $\mathbf{q}$, which is determined by the field orientation. This is known as the helical superconducting phase, in which the superconducting gap becomes $\Delta(\mathbf{r}) = \Delta_0 e^{i\mathbf{q}\cdot\mathbf{r}}$, with a constant magnitude and a spatially varying phase [24, 25]. The presence of finite-momentum superconductivity gives rise to a preferred direction along the Cooper pair momentum $\mathbf{q}$, which allows for a nonreciprocal critical current [167–179].

However, the helical phase is not uniquely obtained by the application of an in-plane field. In Ref. [23] it was shown that magnetization gradients also break time-reversal symmetry, and therefore they could also provide a platform to realize the superconducting diode effect. Figures 3.1(a) and (b) illustrate the Josephson junction setups considered in this thesis for an applied in-plane magnetic field B_y and a uniform spatially varying out-of-plane magnetization $M_z(y)$ with gradient $\partial_y M_z$, respectively. Spatially varying magnetizations can be externally imposed, similarly to the in-plane field case, or they can also be considered as an intrinsic property of the system, such as a generated spin-density wave phase or due to the presence of magnetic impurities. Therefore, to distinguish both mechanisms, throughout this Chapter we refer to the in-plane applied field as B_y, while we denote the out-of-plane field as the magnetization $M_z(y)$.

The main focus of this Chapter is the uniform out-of-plane magnetization gradient illustrated in Fig. 3.1(b). Nevertheless, since the device design will determine the efficiency of the diode effect, we also analyze different setups. Note that for the out-of-plane magnetization gradients we will always consider a profile with no net magnetization, since we want to identify the underlying mechanism for the diode effect, while a finite net magnetization could lead to additional effects.

In this Chapter, we demonstrate that out-of-plane magnetization gradients induce the helical phase in a two-dimensional Rashba superconductor, and we compare this setup to the in-plane field case. In addition, we analyze the Josephson diode effect by introducing a junction setting, as illustrated in Fig. 3.1 by the orange region, and we show that out-of-plane magnetization gradients also exhibit nonreciprocal transport. To determine the real-space current pattern and the current-phase relations, we solve numerically the mean-field self-consistent gap equation in

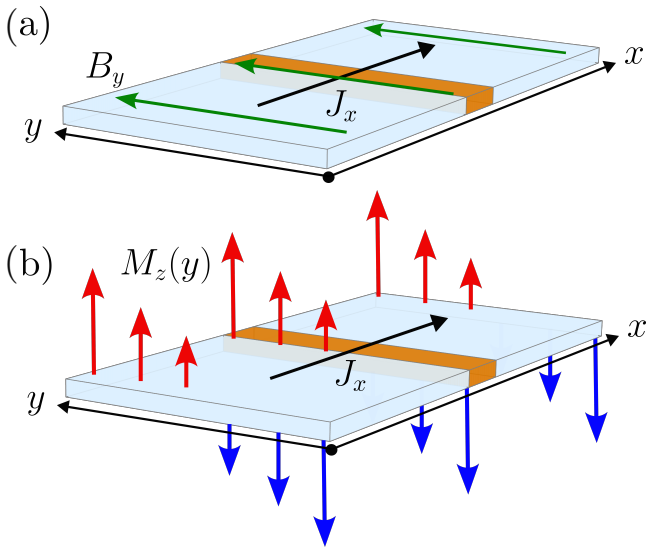

Figure 3.1: Illustration of the Josephson junction setups for (a) an in-plane field B_y applied in the y direction, and (b) an out-of-plane magnetization gradient $M_z(y)$. The supercurrent generated in the x direction is denoted by J_x, and the orange region corresponds to the weak link in the junction area, which we model as a softening of the nearest-neighbor hopping t, see Sec. 3.5.

real space considering a two-dimensional Rashba superconductor. We find that magnetization gradients show similar diode efficiencies when compared to the usual in-plane field case for a different range of parameters. Moreover, we also examine alternative magnetization gradients profiles, specifically focusing on a ferromagnetic domain wall function and arrays of magnetic impurities, and show that these setups also feature the diode effect.

This Chapter is organized as follows: in Sec. 3.2 we include a phenomenological analysis based on the results of Ref. [23], and we introduce a method to compare the helical phase for an in-plane field and an out-of-plane magnetization by calculating the superconducting phase gradient. Section 3.3 introduces the lattice model and the method used to obtain the numerical results in the remainder of the Chapter. The numerical evidence for helical superconductivity for the in-plane field and out-of-plane magnetization is presented in Sec. 3.4, including a free energy analysis for the in-plane field to demonstrate that a state with a finite Cooper pair momentum has a lower energy. In addition, by comparing the superconducting phase gradient from both field configurations, we numerically verify the phenomenological expression obtained in Sec. 3.2. Next, in Sec. 3.5 we study the current-phase relations for the Josephson diode effect by introducing a junction in the model, and examine the efficiency of the effect for a different range of parameters. In Sec. 3.6 we propose and study alternative designs based on out-of-plane magnetization gradients. Finally, we present the discussion and conclusions in Sec. 3.7.

3.2 Helical superconductivity in a Rashba system

In this section, we briefly introduce the foundations of the phenomenological analysis based on Ref. [23]. This analysis is key to motivating the existence of the helical phase also in the case of

out-of-plane magnetization gradients, and to finding an expression to compare the helical phase with the in-plane field case.

Following Ref. [23], we can obtain an expression for the energy density of the Rashba superconductor from a symmetry analysis. Similarly to Chapters 1 and 2, the symmetry classification is based on identifying how the different fields transform under the operations of the point group. The relevant point group is now C_{4v}, as it does not contain inversion but includes the operations illustrated in Fig. 1.5. Let us introduce $\mathbf{A}(\mathbf{r})$ as the real-space vector potential and $\mathbf{M}(\mathbf{r})$ as the real-space magnetization vector. In order to find the combinations of these fields entering in the free energy, we have to find the terms transforming as invariants, i.e., like the A_1 irreducible representation (irrep) of C_{4v}. Focusing on the in-plane components, the vector potential transforms like a vector, $(A_x, A_y) \sim (k_x, k_y)$, whereas the magnetization transforms like a pseudovector, $(M_x, M_y) \sim (\sigma_x, \sigma_y)$, since it transforms like the magnetic field $\mathbf{B} = \nabla \times \mathbf{A}$. From inspecting the character table of C_{4v}, we identify that both quantities belong to the E irrep.

As noticed in Ref. [23], the form for the invariant is obtained by considering (A_x, A_y) as the basis of the two-dimensional irrep E. Thus, we can identify how the in-plane components of the magnetization transform relative to the vector potential, which can be determined from $\mathbf{B} = \nabla \times \mathbf{A} = (\partial_y A_z - \partial_z A_y, -\partial_x A_z + \partial_z A_x, \partial_x A_y - \partial_y A_x)$. Hence, focusing on the in-plane components, this shows that (M_x, M_y) transforms like $(-A_y, A_x)$, and consequently the combination transforming like an invariant corresponds to $A_x(\mathbf{r})M_y(\mathbf{r}) - A_y(\mathbf{r})M_x(\mathbf{r})$. Note that this invariant can also be rewritten as

$$\mathbf{A}(\mathbf{r}) \cdot (M_y(\mathbf{r}), -M_x(\mathbf{r})) = -\mathbf{A}(\mathbf{r}) \cdot \hat{\boldsymbol{z}} \times \mathbf{M}(\mathbf{r}). \tag{3.1}$$

Following analogous arguments, Ref. [23] identified that the combination $A_x(\mathbf{r})\partial_y M_z(\mathbf{r}) - A_y(\mathbf{r})\partial_x M_z(\mathbf{r})$ is also an invariant, allowing similar phenomena for in-plane fields and out-of-plane magnetization gradients, as we will show in this Chapter. Similarly, it can be rewritten as follows,

$$\mathbf{A}(\mathbf{r}) \cdot (\partial_y M_z(\mathbf{r}), -\partial_x M_z(\mathbf{r})) = -\mathbf{A}(\mathbf{r}) \cdot \nabla \times \hat{\boldsymbol{z}} M_z(\mathbf{r}). \tag{3.2}$$

Let us now introduce the gauge-invariant vector potential $\mathcal{A}(\mathbf{r}) = \mathbf{A}(\mathbf{r}) + \hbar\nabla\varphi(\mathbf{r})/2e$, since it is this quantity that must enter in the energy density, which transforms in the same way as $\mathbf{A}(\mathbf{r})$. Here, $\varphi(\mathbf{r})$ denotes the superconducting phase, $\hbar$ corresponds to the reduced Planck constant and $e > 0$ is the electron charge unit. Finally, including the invariants in Eqs. (3.1)-(3.2), we find the following expression for the energy density [23],

$$E(\mathbf{r}) = \mathcal{A}(\mathbf{r}) \cdot \Big[D\mathcal{A}(\mathbf{r})/2 - \big(\underbrace{\Lambda \hat{\boldsymbol{z}} \times \mathbf{M}(\mathbf{r}) + \mathcal{X} \nabla \times \hat{\boldsymbol{z}} M_z(\mathbf{r})}_{\mathbf{J}_{\mathrm{mag}}(\mathbf{r})} \big) \Big], \tag{3.3}$$

where D is the superfluid stiffness and we have identified the current as the term coupling to the vector potential [180]. As a consequence, the coefficients Λ and $\mathcal{X}$ determine the strength of the currents due to the in-plane magnetization and the out-of-plane magnetization gradient, respectively. The energy density in Eq. (3.3) directly shows that the contribution to the current from in-plane magnetic fields and out-of-plane magnetization gradients has a similar form.

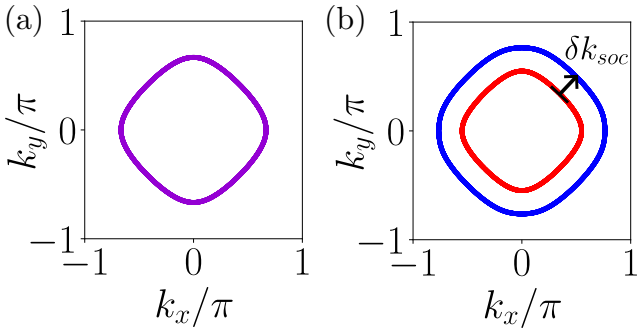

Figure 3.2: Fermi surface (a) in the absence of spin-orbit coupling (spin degenerate) and (b) spin split bands due to the Rashba SOC effect, considering a dispersion with nearest-neighbor hopping, chemical potential $\mu = -1$ and $\lambda_{\text{soc}} = 0.5$ (see Eq. (3.10)). In (b) we indicate the parameter δk_{soc} denoting the splitting of the two Fermi surfaces.

Therefore, we expect that in both cases the superconducting state will enter the helical phase, as we will demonstrate numerically in Sec. 3.4.

The expression for the coefficients Λ and $\mathcal{X}$ can be calculated from the second-order free-energy expansion using microscopic models [23, 181]. Note that we will precisely follow this approach in Chapter 5 to obtain the coefficients for the Landau theory of altermagnetism. On the one hand, Λ corresponds to the Edelstein effect [182, 183]. In the limit where the spin-orbit coupling energy at the Fermi level (E_{soc}) is much larger than the pairing gap (Δ), the expression for this coefficient is given by [23]

$$\Lambda = \frac{2m_e \upsilon}{\hbar} \frac{e}{4\pi\hbar}, \tag{3.4}$$

where m_e is the electron mass and υ is the strength of the Rashba spin-orbit coupling (SOC). On the other hand, $\mathcal{X}$ corresponds to the interconversion coefficient and, in the limit $E_{\text{soc}} >> \Delta$, it can be written as [23]

$$\mathcal{X} = \frac{e}{4\pi\hbar}. \tag{3.5}$$

Thus, in this limit we can identify the following relation between the two coefficients,

$$\Lambda/\mathcal{X} = \delta k_{\text{soc}}, \tag{3.6}$$

where $\delta k_{\text{soc}} = \frac{2m_e\upsilon}{\hbar}$ denotes the Rashba SOC wave number and gives rise to the splitting of the two Fermi surfaces due to SOC, as illustrated in Fig. 3.2.

To compare the in-plane magnetic field and the out-of-plane magnetization mechanisms, we first need to find an expression for the current of the system, which corresponds to

$$\mathbf{J}(\mathbf{r}) = -\left.\frac{\delta E(\mathbf{r})}{\delta \mathbf{A}(\mathbf{r})}\right|_{\mathbf{A}=\mathbf{0}} = -D\frac{\hbar}{2e}\nabla\varphi(\mathbf{r}) + \mathbf{J}_{\text{mag}}(\mathbf{r}). \tag{3.7}$$

In the helical phase, there is no net electric current. Consequently, for a spatially uniform $\mathbf{J}_{\text{mag}}(\mathbf{r}) = \mathbf{J}_{\text{mag}}$, the system cancels out the magnetization-induced current [25], and the superconducting phase gradient is given by

$$\nabla\varphi = \frac{1}{D}\frac{2e}{\hbar}\mathbf{J}_{\text{mag}}. \tag{3.8}$$

Hence, using Eq. (3.3) and the form for the coefficients given in Eqs. (3.4)-(3.6), the in-plane field and the out-of-plane magnetization gradient lead to the same superconducting phase gradient $\nabla\varphi$ if the following relation is satisfied,

$$\delta k_{\mathrm{soc}}|B_y| = |\partial_y M_z| \sim \frac{2M_z^{\max}}{\xi_{\mathrm{grad}}}. \tag{3.9}$$

We recall that B_y corresponds to the in-plane magnetic field, as seen in Fig. 3.1(a), and $\partial_y M_z$ denotes the out-of-plane magnetization gradient, illustrated in Fig. 3.1(b). In this case, $\partial_y M_z$ can be approximated as the maximum value of the out-of-plane magnetization, $2M_z^{\max}$, where the factor of 2 arises since we are considering a profile with no net magnetization, divided by the length scale ξ_{grad}, denoting the steps over which the out-of-plane magnetization gradient increases in the y direction.

Equation (3.9) shows that the strength of the two effects is determined by the SOC splitting of the two Fermi surfaces δk_{soc} and the length scale ξ_{grad}. In Sec. 3.4 we will demonstrate numerically that both mechanisms stabilize the helical phase and indeed give rise to a similar phase gradient when the condition in Eq. (3.9) is fulfilled.

3.3 Lattice model and method for the numerical approach

Throughout this Chapter, we use numerical results to demonstrate the existence of the diode effect for the out-of-plane magnetization gradients, and also to compare the diode effect with the in-plane field case. In this section, we introduce the lattice model and describe the method used to calculate the superconducting order parameter and the supercurrents.

First of all, let us neglect for now the magnetization effects and introduce the Hamiltonian for a Rashba superconductor,

$$H = H_{\mathrm{kin}} + H_{\mathrm{soc}} + H_{\mathrm{SC}}, \tag{3.10}$$

with

$$H_{\mathrm{kin}} = -t \sum_{\langle \mathbf{i},\mathbf{j}\rangle,\sigma} c^\dagger_{\mathbf{i}\sigma} c_{\mathbf{j}\sigma} - \mu \sum_{\mathbf{i},\sigma} c^\dagger_{\mathbf{i}\sigma} c_{\mathbf{i}\sigma}, \tag{3.11}$$

$$H_{\mathrm{soc}} = -\frac{\lambda_{\mathrm{soc}}}{2} \sum_{\mathbf{i}} \Big[(c^\dagger_{\mathbf{i}-\hat{\mathbf{x}}\downarrow} c_{\mathbf{i}\uparrow} - c^\dagger_{\mathbf{i}+\hat{\mathbf{x}}\downarrow} c_{\mathbf{i}\uparrow}) + i(c^\dagger_{\mathbf{i}-\hat{\mathbf{y}}\downarrow} c_{\mathbf{i}\uparrow} - c^\dagger_{\mathbf{i}+\hat{\mathbf{y}}\downarrow} c_{\mathbf{i}\uparrow}) + \mathrm{h.c.} \Big], \tag{3.12}$$

$$H_{\mathrm{SC}} = \sum_{\mathbf{i}} \Delta_{\mathbf{i}} (c^\dagger_{\mathbf{i}\uparrow} c^\dagger_{\mathbf{i}\downarrow} + \mathrm{h.c.}). \tag{3.13}$$

The first term corresponds to the kinetic part, with nearest-neighbor hopping $t = 1$ and chemical potential μ, whereas H_{soc} denotes the Rashba SOC term with strength λ_{soc}. Finally, H_{SC} is the superconducting term, where $\Delta_{\mathbf{i}}$ is the site-dependent superconducting order parameter,

$$\Delta_{\mathbf{i}} = V_{\mathrm{SC}} \left(\langle c_{\mathbf{i}\uparrow} c_{\mathbf{i}\downarrow} \rangle - \langle c_{\mathbf{i}\downarrow} c_{\mathbf{i}\uparrow} \rangle \right), \tag{3.14}$$

with $V_{\mathrm{SC}} < 0$ corresponding to the on-site pairing interaction. We construct the $4N^2 \times 4N^2$ Bogoliubov-de Gennes (BdG) Hamiltonian using the spinor $\Psi^\dagger_{\mathbf{i}} = (c^\dagger_{\mathbf{i}\uparrow}, c^\dagger_{\mathbf{i}\downarrow}, c_{\mathbf{i}\uparrow}, c_{\mathbf{i}\downarrow})$, and solve self-consistently Eq. (3.14) for the superconducting order parameter at each lattice site (for more

details see Appendix B). Throughout this Chapter, we consider $V_{\mathrm{SC}} = -1$, which results in a superconducting gap $\Delta = 0.2$ in the homogeneous system, i.e., in the absence of imposed magnetizations, assuming the values $\mu = -1$ and $\lambda_{\mathrm{soc}} = 0.2$.

As illustrated in Fig. 3.1, the junction area of reduced transparency corresponds to the orange region, which we model by reducing the nearest-neighbor hopping t to t' on two columns of lattice sites in the center region of the device, as we will detail in Sec. 3.5 when we discuss the Josephson diode effect. However, in Sec. 3.5 we first set $t' = t$ to demonstrate the emergence of the helical phase in the homogeneous system.

In Chapter 1, we derived an expression for the current density in the case of a one-band model with nearest-neighbor hopping. However, in the presence of Rashba SOC, the current density has an additional contribution,

$$J_{\mathbf{i},\boldsymbol{\delta}} = J^{t}_{\mathbf{i},\boldsymbol{\delta}} + J^{\mathrm{soc}}_{\mathbf{i},\boldsymbol{\delta}}, \tag{3.15}$$

where $\boldsymbol{\delta} = \{\hat{\mathbf{x}}, -\hat{\mathbf{x}}, \hat{\mathbf{y}}, -\hat{\mathbf{y}}\}$ denotes the four nearest neighbors to the lattice site $\mathbf{i}$. As given in Sec. 1.8 and derived in Appendix C, the first term is obtained from the Hamiltonian in Eq. (3.11), and is given by

$$J^{t}_{\mathbf{i},\boldsymbol{\delta}} = it \sum_{\sigma} \langle c^{\dagger}_{\mathbf{i}+\boldsymbol{\delta}\sigma} c_{\mathbf{i}\sigma} - \mathrm{h.c.} \rangle. \tag{3.16}$$

The second contribution arises due to the Rashba SOC term in Eq. (3.12), and can be derived following an analogous procedure as in Appendix C, obtaining

$$J^{\mathrm{soc}}_{\mathbf{i},\pm\hat{\mathbf{x}}} = i\frac{\lambda_{\mathrm{soc}}}{2} \sum_{\mathbf{i},\sigma} \langle \pm\sigma c^{\dagger}_{\mathbf{i}\pm\hat{\mathbf{x}}\sigma} c_{\mathbf{i}\bar{\sigma}} - \mathrm{h.c.} \rangle, \tag{3.17}$$

$$J^{\mathrm{soc}}_{\mathbf{i},\pm\hat{\mathbf{y}}} = \pm\frac{\lambda_{\mathrm{soc}}}{2} \sum_{\mathbf{i},\sigma} \langle c^{\dagger}_{\mathbf{i}\pm\hat{\mathbf{y}}\sigma} c_{\mathbf{i}\bar{\sigma}} - \mathrm{h.c.} \rangle, \tag{3.18}$$

with $\bar{\sigma} = -\sigma$. Note that in Eqs. (3.16)-(3.18) there is an additional prefactor corresponding to $e/(\hbar a^2)$, which also enters in the current units in the figures shown in the following sections. Finally, to obtain the total current at each lattice site, we take the average over the two nearest-neighbor bonds in the $\hat{\mathbf{x}}$ and the $\hat{\mathbf{y}}$ direction,

$$\mathbf{J}_{\mathbf{i}} = \frac{1}{2} \sum_{\boldsymbol{\delta}} \boldsymbol{\delta} J_{\mathbf{i},\boldsymbol{\delta}}. \tag{3.19}$$

This expression gives the current at each lattice site, which we use to illustrate the current patterns and obtain the current-phase relations in Secs. 3.4-3.6. Current conservation is guaranteed at all lattice sites once the self-consistency condition is achieved, since the incoming and the outgoing currents are equal in magnitude at each site [184, 185].

Having introduced the Hamiltonian for a Rashba superconductor and the resulting current density, let us now focus on the Hamiltonian for the magnetization effects. On the one hand, the in-plane field term can be written as

$$H_B = -B_y \sum_{\mathbf{i},\sigma,\sigma'} (\sigma_y)_{\sigma\sigma'} c^{\dagger}_{\mathbf{i}\sigma} c_{\mathbf{i}\sigma'}, \tag{3.20}$$

and, on the other hand, the out-of-plane magnetization gradient contribution corresponds to

$$H_{M_z} = -\sum_{\mathbf{i},\sigma,\sigma'} M_{z,\mathbf{i}}(\sigma_z)_{\sigma\sigma'} c^{\dagger}_{\mathbf{i}\sigma} c_{\mathbf{i}\sigma'}, \tag{3.21}$$

with $M_{z,\mathbf{i}}$ denoting the site-dependent magnetization in the z direction.

In the following sections, we consider the Hamiltonian for the Rashba superconductor in Eq. (3.10), and add the Hamiltonian for the in-plane field in Eq. (3.20) or the out-of-plane magnetization gradient in Eq. (3.21) to solve self-consistently for the order parameter, using Eq. (3.14). In addition, we impose open boundary conditions in the system, except otherwise explicitly indicated. Moreover, in Secs. 3.4-3.6 we use Eq. (3.19) to obtain the current at each lattice site and illustrate the current patterns. Finally, to calculate the current-phase relations we impose a phase difference between both ends of the device, as we will detail in Sec. 3.5. By insisting on the phase difference at each iteration of the self-consistency, the superconducting gap eventually induces a current in the x direction, as depicted in Fig. 3.1.

3.4 Helical superconductivity from the numerical results

In this section, we verify that the helical phase is the preferred ground state for a Rashba superconductor in the presence of an in-plane magnetic field, as discussed in previous works [24, 25, 170]. We calculate the free energy and show that, for a finite in-plane field and SOC, the state with a finite Cooper pair momentum has a lower energy. Next, we turn to the case of an out-of-plane magnetization gradient and demonstrate numerically that it also induces the helical phase. In both cases, we see that the superconducting gap acquires the form $\Delta(\mathbf{r}) = \Delta_0 e^{i\mathbf{q}\cdot\mathbf{r}}$, with a constant homogeneous magnitude and a spatially varying phase, which characterizes the helical phase.

3.4.1 In-plane magnetic field

Let us focus first on the superconducting Rashba system with an in-plane magnetic field and no junction in the central region, as illustrated in Fig. 3.3(a). In Fig. 3.3(b) we show the two Fermi surfaces in the presence of SOC and an in-plane field. As seen, in contrast to the case with no field displayed in Fig. 3.2(b), the center of the two Fermi surfaces is shifted, in agreement with Ref. [24].

Using periodic boundary conditions and calculating self-consistently the superconducting order parameter, we have verified that the ground state has no net current, since the two contributions in Eq. (3.15) exactly cancel each other [25]. If we turn now to the case of open boundary conditions, shown in Fig. 3.3(c), we observe the presence of dominant currents only at the edges due to finite size effects, while at the system center they are almost negligible. Note that the currents develop a certain pattern ensuring conservation at all lattice sites. In addition, as seen from Fig. 3.3(d), the superconducting state develops a phase gradient in the system, confirming the helical phase.

To further demonstrate the emergence of a superconducting state with a finite Cooper pair momentum in the presence of Rashba SOC and an in-plane magnetic field, we can calculate the

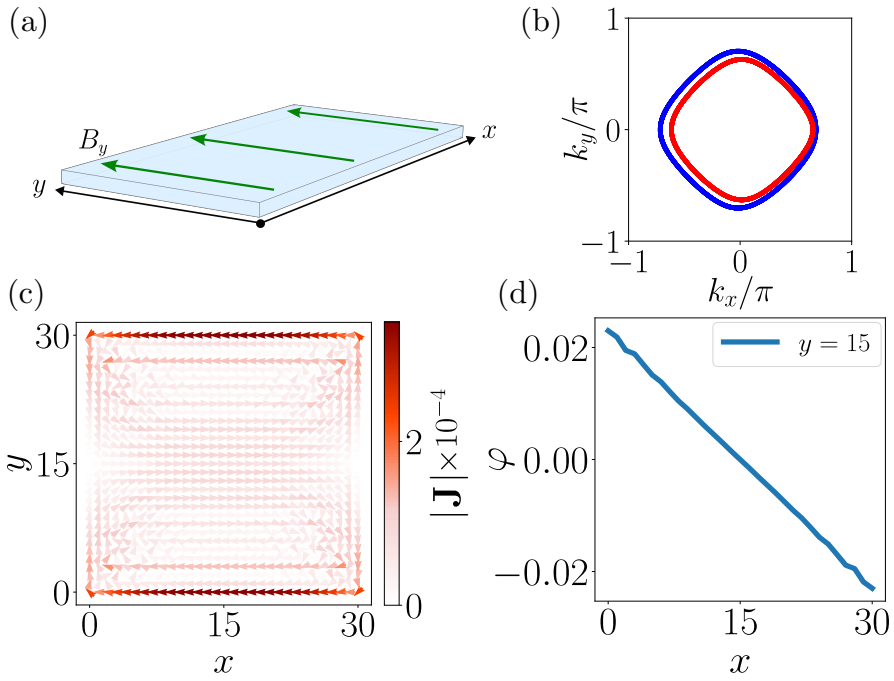

Figure 3.3: Helical superconductivity generated in a Rashba superconductor with an in-plane magnetic field. (a) Device illustration for a field in the y direction and no junction in the central region. (b) Fermi surfaces in the presence of SOC and the in-plane field, with $\lambda_{\text{soc}} = 0.2$, $B_y = 0.1$ and $\mu = -1$. (c) Self-consistent solution with open boundary conditions for the supercurrent patterns obtained at each lattice site, for a 31×31 system size. (d) Superconducting phase for a cut in (c) at $y = 15$ as a function of the position on the x axis. The finite constant gradient with a homogeneous gap magnitude $\Delta \sim 0.2$ and the negligible current at the system center (away from the edges) are characteristic of the helical ground state.

free energy. Specifically, we perform the calculation in momentum space for the homogeneous case with periodic boundary conditions, since this allows us to work with larger system sizes. Therefore, we first have to Fourier transform the real space Hamiltonian in Eq. (3.10) with the in-plane field in Eq. (3.20).

For this purpose, the challenge is to implement in momentum space the spatial variation of the gap in the helical phase, with the form $\Delta(\mathbf{r}) = \Delta_0 e^{i\mathbf{q}\cdot\mathbf{r}}$. To circumvent this problem, we use the gauge transformation $c_{\mathbf{i}} \to e^{i\mathbf{q}\cdot\mathbf{i}/2} c_{\mathbf{i}}$ for the creation and annihilation operators in Eqs. (3.10), (3.20), so that the superconducting term simplifies to

$$H_{\text{SC}} = \Delta_0 \sum_{\mathbf{i}} (c^\dagger_{\mathbf{i}\uparrow} c^\dagger_{\mathbf{i}\downarrow} + \text{h.c.}). \tag{3.22}$$

However, with this transformation the kinetic term in Eq. (3.10) becomes

$$H_{\text{kin}} = -t \sum_{\mathbf{i},\sigma} (e^{iq_x/2} c^\dagger_{\mathbf{i}\sigma} c_{\mathbf{i}+\hat{\mathbf{x}}\sigma} + e^{-iq_x/2} c^\dagger_{\mathbf{i}\sigma} c_{\mathbf{i}-\hat{\mathbf{x}}\sigma} + c^\dagger_{\mathbf{i}\sigma} c_{\mathbf{i}+\hat{\mathbf{y}}\sigma} + c^\dagger_{\mathbf{i}\sigma} c_{\mathbf{i}-\hat{\mathbf{y}}\sigma}) - \mu \sum_{\mathbf{i},\sigma} c^\dagger_{\mathbf{i}\sigma} c_{\mathbf{i}\sigma}, \tag{3.23}$$

where we have used that $\mathbf{q} = (q_x, 0)$, as seen from the shift of the two Fermi surfaces in Fig. 3.3(b). Using this transformation also for the other terms in Eq. (3.10), the Hamiltonian in momentum

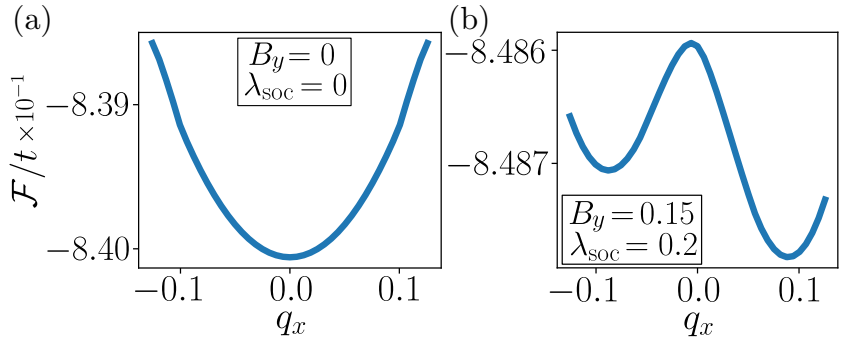

Figure 3.4: Free energy density as a function of the Cooper pair momentum q_x (a) in the absence of in-plane field and SOC and (b) for $B_y = 0.15$ and $\lambda_{\rm soc} = 0.2$, considering in both cases a homogeneous gap $\Delta = 0.2$, $\mu = -1$, and a system size 2000×2000.

space is given by

$$\mathcal{H} = \mathcal{H}_{\rm kin} + \mathcal{H}_{\rm soc} + \mathcal{H}_{\rm SC} + \mathcal{H}_B, \tag{3.24}$$

where the different contributions correspond to

$$\begin{aligned}
\mathcal{H}_{\rm kin} &= -2t \sum_{\mathbf{k},\sigma} \left[\cos\left(k_x + \frac{q_x}{2}\right) + \cos k_y \right] - \mu \sum_{\mathbf{k},\sigma} c^\dagger_{\mathbf{k}\sigma} c_{\mathbf{k}\sigma}, \\
\mathcal{H}_{\rm soc} &= \frac{\lambda_{\rm soc}}{2} \sum_{\mathbf{k}} \left[\left(i \sin\left(k_x + \frac{q_x}{2}\right) + \sin k_y \right) c^\dagger_{\mathbf{k}\uparrow} c_{\mathbf{k}\downarrow} + \text{h.c.} \right], \\
\mathcal{H}_{\rm SC} &= \Delta_0 \sum_{\mathbf{k}} (c_{-\mathbf{k}\downarrow} c_{\mathbf{k}\uparrow} + \text{h.c.}), \\
\mathcal{H}_B &= -B_y \sum_{\mathbf{k}} (-i c^\dagger_{\mathbf{k}\uparrow} c_{\mathbf{k}\downarrow} + i c^\dagger_{\mathbf{k}\downarrow} c_{\mathbf{k}\uparrow}).
\end{aligned} \tag{3.25}$$

Here, the homogeneous superconducting order parameter in momentum space given by

$$\Delta_0 = \frac{V_{\rm SC}}{N^2} \sum_{\mathbf{k}} \left(\langle c_{\mathbf{k}\uparrow} c_{-\mathbf{k}\downarrow} \rangle - \langle c_{\mathbf{k}\downarrow} c_{-\mathbf{k}\uparrow} \rangle \right), \tag{3.26}$$

Thus, the zero-temperature free-energy density is obtained by evaluating $\mathcal{F} = \frac{1}{N^2}\langle \mathcal{H} \rangle - \frac{|\Delta_0|^2}{V_{\rm SC}}$ using the unitary transformation that diagonalizes the Hamiltonian (see Appendix B), where the constant term $\frac{|\Delta_0|^2}{V_{\rm SC}}$ comes from the mean-field expansion of the interacting Hamiltonian. The free energy density is shown in Fig. 3.4 as a function of the Cooper pair momentum. In the absence of SOC and in-plane field, the free energy minimum is at $q_x = 0$. Therefore, the Cooper pairs have zero center-of-mass momentum and the gap is homogeneous with a constant magnitude and no phase. This contrasts with the case in Fig. 3.4(b) with finite SOC and an applied field, since now the free energy displays a clear minimum at a finite $q_x \neq 0$. The free energy is not symmetric for $q_x \to -q_x$, which shows that there is a preferred direction along $+q_x$, generating the nonreciprocal current in the superconducting diode effect. These results confirm the self-consistent calculations in Fig. 3.3, in which the superconducting gap shows a spatially varying phase with $q_x = \frac{\partial \varphi}{\partial x}$ and a constant magnitude.

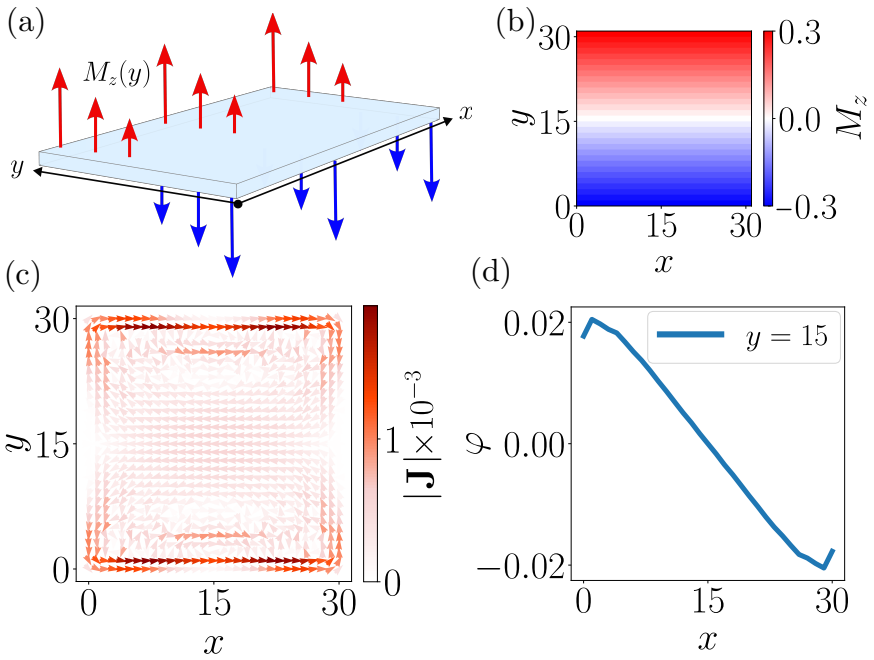

Figure 3.5: Helical superconductivity generated in a Rashba superconductor with an out-of-plane magnetization gradient. (a) Device illustration for a gradient in the z direction and no junction in the central region. (b) Out-of-plane magnetization gradient profile. (c) Self-consistent solution with open boundary conditions for the supercurrent patterns obtained at each lattice site, for a 31×31 system size. (d) Superconducting phase for a cut in (c) at $y = 15$ as a function of the position on the x axis. The gap magnitude is homogeneous in the system center, with $\Delta \sim 0.2$, while it is suppressed close to the edges due to the large out-of-plane magnetization.

3.4.2 Out-of-plane magnetization gradient

Having established that the helical phase is the ground state for a Rashba superconductor with an in-plane applied field, we now demonstrate numerically that out-of-plane magnetization gradients also induce the same finite Cooper pair momentum phase. With this purpose, we consider a uniform out-of-plane magnetization gradient, as illustrated in Fig. 3.5(a). Specifically, the profile is shown in Fig. 3.5(b), emphasizing the uniform increase in the y direction with vanishing total magnetization. Figure 3.5(c) shows the current pattern obtained from the self-consistent solution and, similarly to Fig. 3.3(c), the bulk currents in the system center are almost vanishing, while larger contributions are observed due to edge effects. In addition, the finite phase gradient seen in Fig. 3.5(d) confirms that the system also enters the helical phase in this case, since the gap magnitude is also homogeneous in the system.

As derived in Eq. (3.9) from the phenomenological model, when the in-plane field $\delta k_{\mathrm{soc}} B_y$ and the out-of-plane magnetization gradient $\frac{2M_z^{\max}}{\xi_{\mathrm{grad}}}$ have comparable magnitudes, they should generate similar superconducting phase gradients in the helical phase. To verify this, we have solved self-consistently for the superconducting order parameter imposing open boundary conditions, extracting numerically the phase gradient $\partial\varphi/\partial x$ in the x direction as the average of different cuts in the y direction from the center region, excluding the cuts close to the edge, since

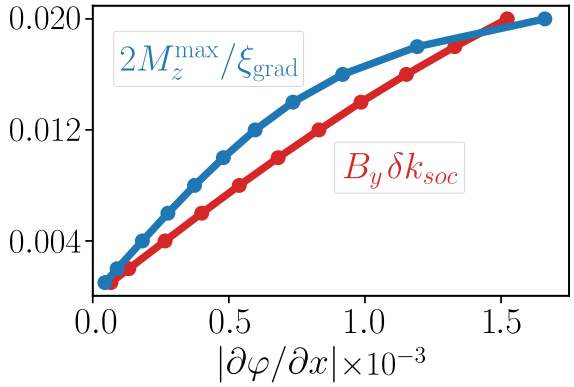

Figure 3.6: Comparison of the superconducting phase gradient calculated self-consistently in the helical phase for the case of an in-plane magnetic field and an out-of-plane magnetization configuration. As derived in Eq. (3.9), we compare $B_y\delta k_{\text{soc}}$ (red curve), where B_y is the in-plane field in the y direction and δk_{soc} is the splitting of the two Fermi surfaces due to SOC shown in Fig. 3.2(b), with $2M_z^{\max}/\xi_{\text{grad}}$ (blue curve), where $M_z^{\max}$ denotes the maximum value for the magnetization gradient at the y edge and ξ_{grad} is the length scale for which the magnetization is modified (see Fig. 3.5(b)). We consider the parameters $\lambda_{\text{soc}} = 0.2$, $\mu = -1$ and a 31×31 system size.

they lead to significant finite size effects (see the large currents in Fig. 3.3(c) and Fig. 3.5(c)).

In Fig. 3.6 we compare the superconducting phase gradient obtained from both mechanisms. Remarkably, the superconducting phase gradients show notable consistency, in particular in the limit where $|\partial\varphi/\partial x|$ is small. For a larger out-of-plane magnetization, the gap becomes more inhomogeneous, as it is suppressed close to the edges where M_z is larger (see Fig. 3.5(a)-(b)). This may be the origin of the crossing between the two curves in the non-linear regime.

Hence, we have demonstrated that the in-plane field and the out-of-plane magnetization gradient configurations illustrated in Fig. 3.1 yield to the helical state, and the superconducting phase gradients become similar when Eq. (3.9) is satisfied. The numerical confirmation of the helical phase therefore suggests that both field configurations should exhibit the diode effect, which we will explore in the following section.

3.5 Superconducting Josephson diode effect

3.5.1 Current-phase relation

In the previous section, we have shown that the ground state for the Rashba superconductor with an out-of-plane magnetization gradient is the helical phase, similarly to the in-plane field case. We have compared the superconducting phase gradients from both configurations, obtaining compatible results in the linear regime, as expected from the phenomenological theory discussed in Sec. 3.2. Therefore, out-of-plane magnetization gradients should also give rise to a nonreciprocal current. In this section, we verify this from the numerical results and we also determine quantitatively the efficiency of the diode effect to compare both field configurations.

We consider the Josephson junction devices illustrated in Fig. 3.1. The lattice model for the

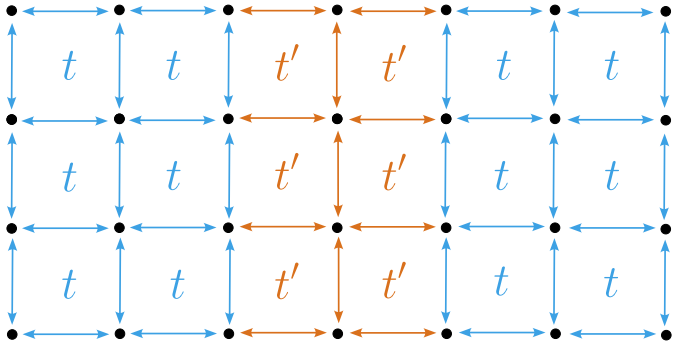

Figure 3.7: Illustration of the modified hoppings in the lattice corresponding to the orange junction region depicted in Fig. 3.1. Only two column bonds in the central region are changed to t', in contrast to the hopping t used for all other bonds.

junction and the modified hoppings are shown in Fig. 3.7, so that only the hoppings between the central bonds are modified to t'. The currents in the system are generated by imposing a phase difference φ between the two edges in the x direction (across the junction). Concretely, we impose that for the sites at $x = 0$ the gap is Δ, while at the opposite edge there is phase difference $\Delta e^{i\varphi}$, as illustrated in the insets of Fig 3.8. Therefore, numerically the current is obtained by insisting on the phase difference at each iteration of the self-consistency procedure [184]. Eventually, once the convergence condition is achieved, there is an induced current in the x direction, fulfilling current conservation.

Following this procedure, we obtain the current-phase relations shown in Fig. 3.8. Here, I denotes the normalized current calculated by summing all currents in the y direction for the same x value and dividing by the length along the y direction. Due to current conservation, all x-cuts give the same I. In the absence of applied field or magnetizations, the current-phase relation is symmetric around $\varphi = 0$. On the contrary, both in the case of an in-plane field, see Fig. 3.8(a), and an out-of-plane magnetization, see Fig. 3.8(b), the curve is slightly shifted and the current-phase relation is asymmetric. These results numerically showcase that both configurations exhibit the Josephson diode effect, even though the shift of the current-phase relations is small.

In the case of no applied magnetization, the current-phase relation for $t' = t$ shows a saw-tooth shaped curve, which approaches the sinusoidal curve as the junction transparency t' is reduced. We specifically focus on the Josephson diode effect ($t' < t$), since the effect is stronger than in the case with no junction ($t' = t$).

To understand how the current is generated in the system, it is also instructive to examine the current patterns in real space. In particular, we focus on the out-of-plane magnetization, shown in Fig. 3.8(b), and determine the real space currents for different phases, as seen in Fig. 3.9. In the case of open boundary conditions with no imposed phase (see Fig. 3.9(a)), there are currents of similar magnitude at all sites due to finite size effects, forming loops to satisfy momentum conservation. However, there is no current flow along any direction after taking the sum of any cut in the system. As the system size increases, the bulk currents vanish similarly

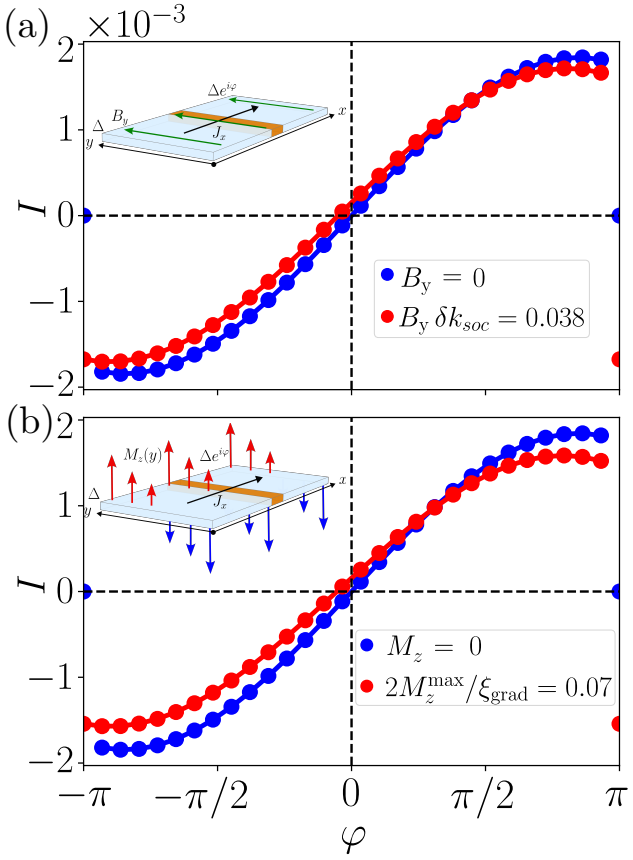

Figure 3.8: Current-phase relations for (a) an in-plane field, and (b) an out-of-plane magnetization, with $\lambda_{\rm soc} = 0.2$, $\mu = -1$, $t' = 0.1$ and a 21×11 system size. The red and blue curves correspond to the case with and without magnetic field/magnetization gradients, respectively. The insets illustrate the device considered in each case, with Δ and $\Delta e^{i\varphi}$ the phase difference imposed at both ends of the lattice, generating a current J_x in the x direction.

to Fig. 3.5(c), and there are only significant contributions close to the edges.

If we turn now to the cases with an imposed phase gradient, see Figs. 3.9(b)-(d), they give rise to a non-vanishing net current along the x direction. For a smaller imposed phase, the current pattern in real space still resembles the case with open boundary conditions. However, as the phase increases, the current direction at all lattice sites becomes aligned along x. In Fig. 3.9(e) we show the superconducting phase corresponding to Fig. 3.9(d). Notably, there is a larger jump across the junction (orange region in the inset), since the system compensates for the reduced hopping to preserve current conservation.

Having explored how the current is generated in the system by observing the real space patterns and how the current-phase relations are obtained, let us now proceed to quantify the diode effect by introducing the superconducting diode effect efficiency to compare the in-plane field with the out-of-plane magnetization gradient, investigating the role of the different parameters.

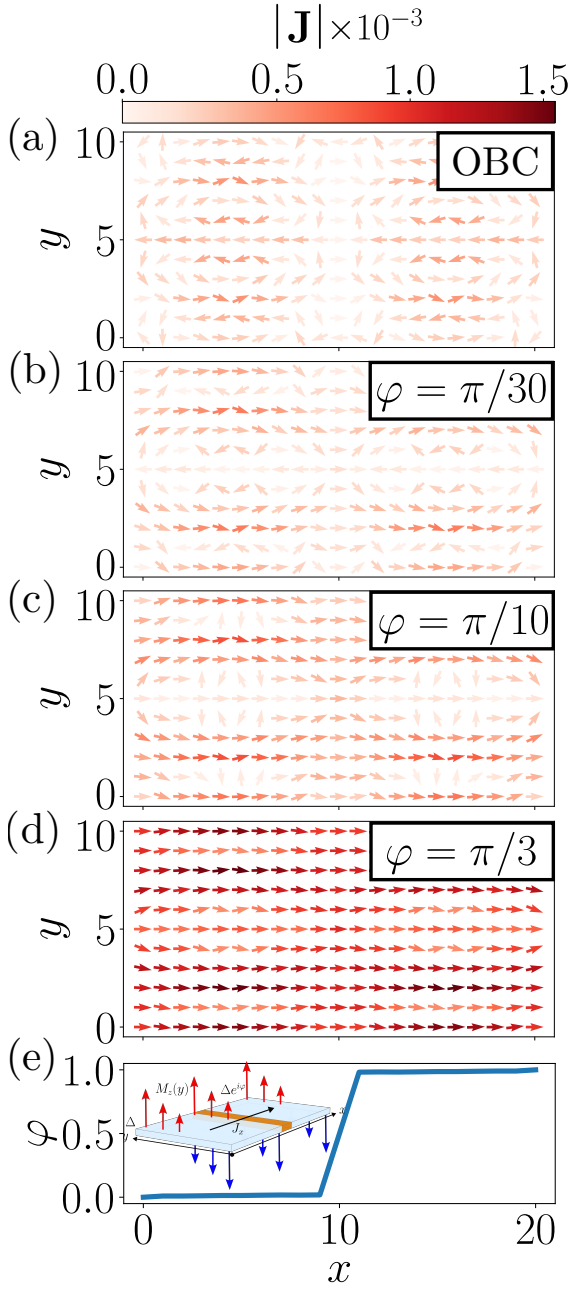

Figure 3.9: Current patterns evolution in real space for (a) open boundary conditions, and (b)-(d) an increasing imposed phase of $\varphi = \pi/30$, $\pi/10$, and $\pi/3$. We consider an out-of-plane magnetization gradient with $2M_z^{\max}/\xi_{\text{grad}} = 0.04$, $\lambda_{\text{soc}} = 0.4$, $\mu = -1$, $t' = 0.1$ and a 21×11 system size. (e) Superconducting phase for the case in panel (d) considering the cut $y = 5$, which shows that the phase principally increases at the junction (central orange region illustrated in the inset).

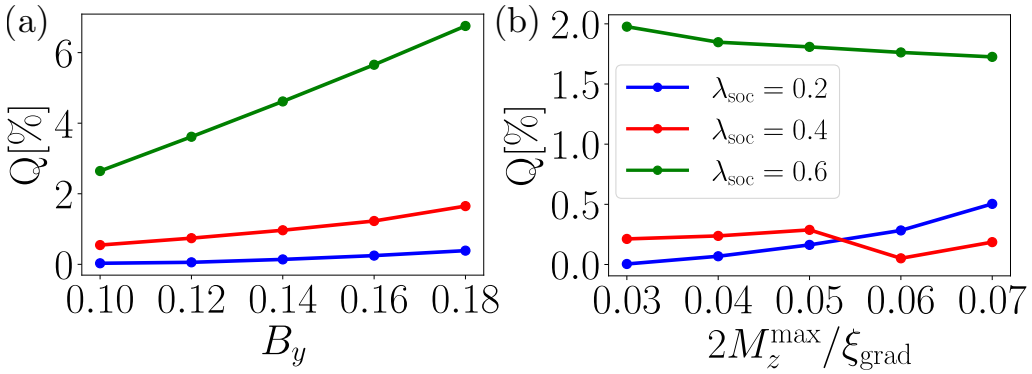

Figure 3.10: Diode efficiency Q as a function of (a) the in-plane field B_y, and (b) the out-of-plane magnetization gradient $2M_z^{\max}/\xi_{\text{grad}}$, for $\mu = -1$, $t' = 0.1$ and a 21×11 system size. We consider different values for the Rashba SOC strength: $\lambda_{\text{soc}} = 0.2$ (blue), 0.4 (red) and 0.6 (green).

3.5.2 Superconducting diode effect efficiencies

In order to compare and quantify the superconducting diode effect for both field configurations, let us introduce the diode efficiency Q [167, 169–171, 174],

$$Q = \frac{|I_{\max}| - |I_{\min}|}{|I_{\max}| + |I_{\min}|}, \tag{3.27}$$

where $I_{\max}$ and $I_{\min}$ correspond to the maximum and minimum normalized currents obtained from the current-phase relations. Since the efficiency depends on the parameters, we explore different strengths for the Rashba SOC and magnetization as well as different values for the chemical potential μ, which changes the Fermi surface.

As shown in Fig. 3.10, we first examine the diode efficiency as a function of the in-plane field and the out-of-plane magnetization strength, for different values of the Rashba SOC. Focusing first on the in-plane field, see Fig. 3.10(a), the efficiency is higher as the magnetic field becomes larger. In addition, increasing the SOC parameter also enhances the effect. In contrast, the out-of-plane magnetization displays a slightly different behavior, as seen from Fig. 3.10(b). In particular, as the magnetization increases, the efficiency is not higher for all λ_{soc}. However, similarly to the in-plane field case, the effect is generally enhanced for an increasing SOC. In both configurations, there is an upper limit to the efficiency since superconductivity is destroyed when the field is too large.

In Fig. 3.11 we show the effect of the chemical potential on the Fermi surface and the efficiency. The Fermi surface for the case of a constant in-plane field is shown in Figs. 3.11(a)-(d) for $\mu = -1$, -0.5, -0.2, and -0.1, respectively, displaying two split Fermi surfaces with a shifted center from zero momentum, which give rise to the helical phase (see Sec. 3.4). As seen from Fig. 3.11(e), the maximum efficiency for the case of an in-plane field occurs for $\mu = -0.1$, when one of the split Fermi surfaces is close to the van Hove singularity. If we turn to the out-of-plane magnetization gradient configuration, shown in Fig. 3.11(f), the high efficiency regions may also originate from enhanced density of states contributions.

Figures 3.11(e)-(f) also show that the efficiency at $\mu = 0$ vanishes for the lattice model

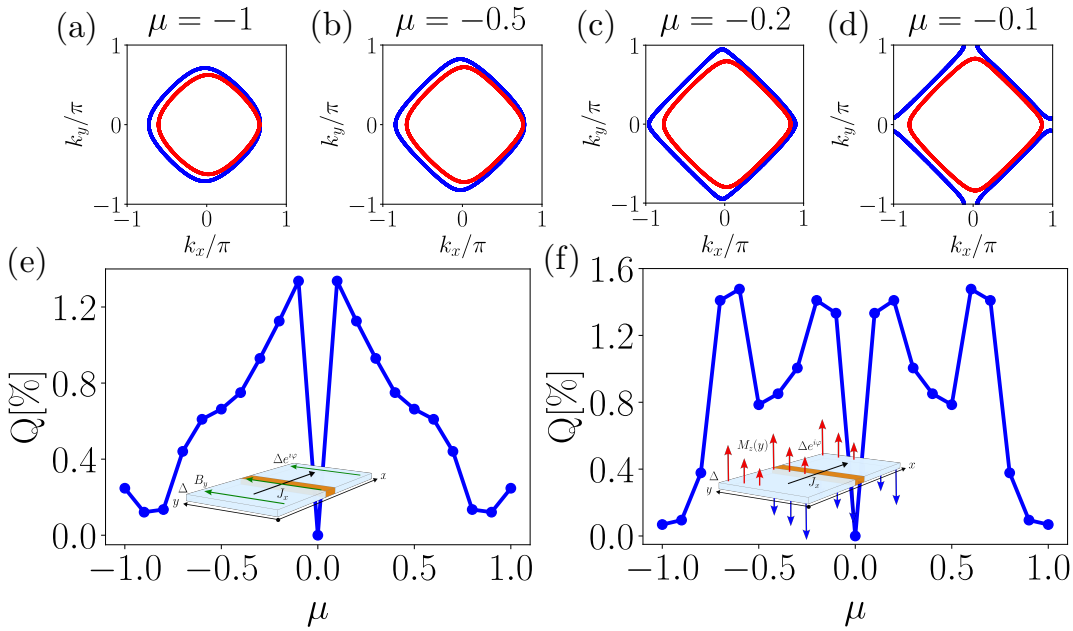

Figure 3.11: (a)-(d) Fermi surface evolution for a varying chemical potential $\mu = \{-1, -0.5, -0.2, -0.1\}$ in the presence of an in-plane magnetic field, with $\lambda_{\text{soc}} = 0.2$ and $B_y = 0.16$. Diode efficiency Q as a function of the chemical potential μ for (e) an in-plane field $B_y = 0.16$, and (f) an out-of-plane magnetization gradient $2M_z^{\max}/\xi_{\text{grad}} = 0.04$ (f), with $\lambda_{\text{soc}} = 0.2$, $t' = 0.1$ and a 21×11 system size.

considered here, which contrasts with the results in Ref. [171] found for an analogue continuum model. The origin of this discrepancy is that for the lattice model there is a symmetry at $\mu = 0$, which leads to no currents in the system. As seen from the BdG Hamiltonian in momentum space, see Eq. (3.24), the symmetry is obtained by shifting the wave vector $\mathbf{k} \to \mathbf{k} + (\pi, \pi)$, together with the exchange of time-reversed electron and hole pairs.

Therefore, the numerical results in Figs. 3.11-3.10 evidence that the two diode mechanisms have comparable efficiencies. Conversely, the in-plane field setup has the disadvantage that a larger amplitude eventually destroys superconductivity, whereas for the case of an out-of-plane magnetization gradient, superconductivity can survive in some regions of the system where the magnetization is smaller and still show the diode effect. This motivates exploring different spatial profiles for the out-of-plane magnetization gradient to seek a higher diode efficiency Q, as we will explore in the next section.

3.6 Other diode designs

In this section, we investigate alternative setups with different profiles for the out-of-plane magnetization gradient. Specifically, in Sec. 3.6.1 we introduce a ferromagnetic domain wall junction to the Rashba superconductor. By contrast, in Sec. 3.6.2 we explore different configurations for arrays of magnetic impurities. We have verified that in both cases the helical phase is the preferred ground state, since a superconducting phase gradient is developed with no net currents away from the edges, similarly to the results presented in Sec. 3.4 for the in-plane field and

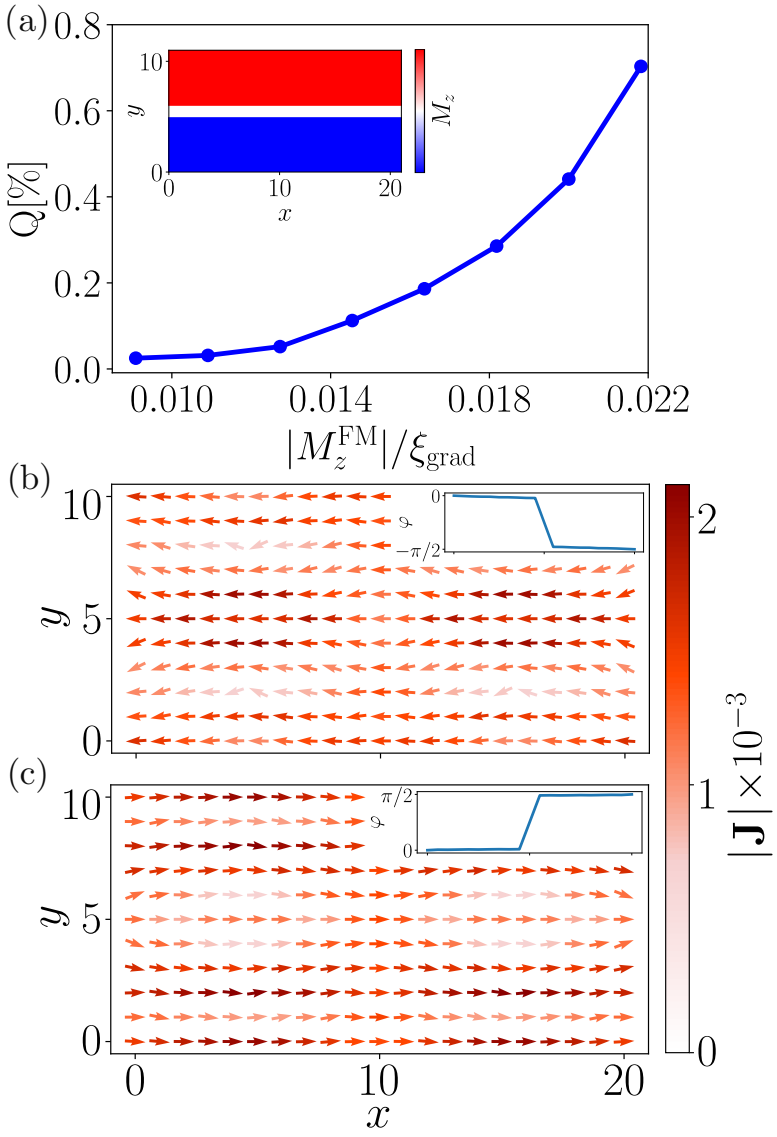

Figure 3.12: Josephson diode efficiency as a function of the out-of-plane magnetization amplitude $|M_z^{\mathrm{FM}}|/\xi_{\mathrm{grad}}$ for the ferromagnetic domain wall magnetization profile, shown in the inset. We consider $\lambda_{\mathrm{soc}} = 0.2$, $\mu = -1$, $\xi_{\mathrm{grad}} = 11$, $t' = 0.1$ and a 21×11 system size. (b)-(c) Current patterns in real space for opposite phase differences ($\varphi = \pm\pi/2$) across the Rashba superconductor, as depicted in each inset. This demonstrates that the current is not restricted to the domain wall region.

out-of-plane magnetization gradient. Therefore, these setups also exhibit the Josephson diode effect and, as we show in the following subsections, we can calculate and compare the efficiencies.

3.6.1 Ferromagnetic domain wall junction

The ferromagnetic domain wall magnetization profile that we consider is displayed in the inset of Fig. 3.12(a). We have numerically obtained the current-phase relations, as introduced in Fig. 3.8, and determined the efficiency for each set of parameters using Eq. (3.27). In Fig. 3.12(a) we show the efficiency as a function of the domain wall magnetization amplitude. As seen, the efficiency

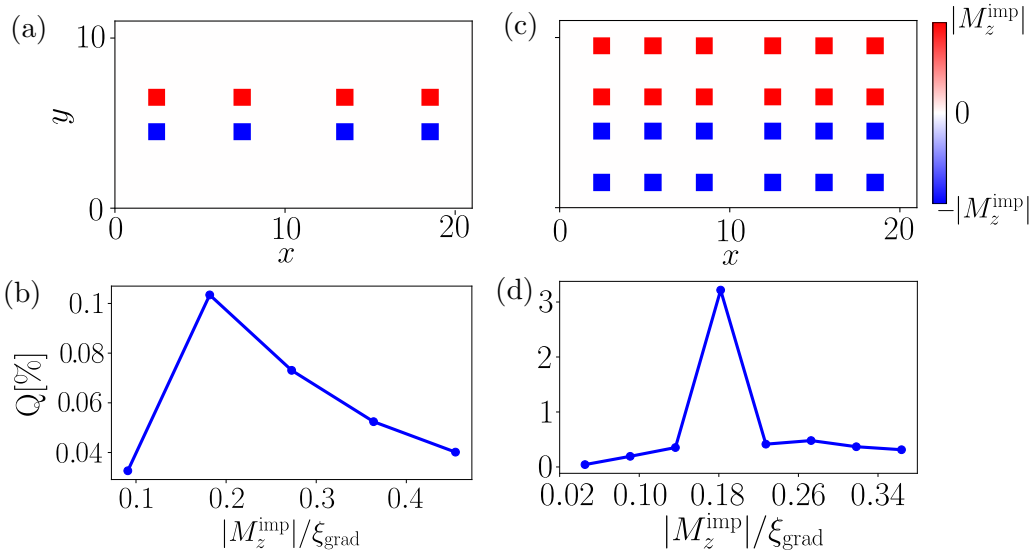

Figure 3.13: Out-of-plane magnetization configuration with (a) 8 and (c) 24 magnetic impurities. Josephson diode efficiency as a function of the out-of-plane impurities magnetization amplitude $|M_z^{\mathrm{imp}}|/\xi_{\mathrm{grad}}$ for the (b) 8 impurities case shown in (a) and (d) 24 impurities configuration shown in (c), with $\lambda_{\mathrm{soc}} = 0.2$, $\mu = -1$, $\xi_{\mathrm{grad}} = 11$, $t' = 0.1$ and a 21×11 system size.

becomes higher as the magnetization increases, similarly to the blue curve in Fig. 3.10.

The current patterns in real space are shown in Figs. 3.12(b)-(c) for opposite imposed phases, as depicted in the insets. The patterns reveal that current flows over the entire device, and is not only restricted close to the domain wall region, where the magnetization gradient is located (see the inset in Fig. 3.12(a)). For a negative phase bias, see Fig. 3.12(b), the current flow is higher close to the domain wall. This contrasts with the positive phase bias result, see Fig. 3.12(c), where the current flow in the vicinity of the domain wall region is lower than at the edges.

The diode efficiency for the ferromagnetic domain wall magnetization can also be optimized by tuning the Rashba SOC strength λ_{soc} and the chemical potential μ. For instance, considering $\lambda_{\mathrm{soc}} = 0.6$ and $\mu = -0.2$ we can achieve efficiencies of $Q \simeq 3\%$, which is comparable to the results presented in Figs. 3.10-3.11 for the in-plane field and the out-of-plane magnetization gradient.

3.6.2 Arrays of impurities

Having investigated the diode efficiency in the domain wall junction, we further examine other configurations. Specifically, we consider two different configurations of arrays of single impurities, which generate a magnetization gradient sufficient to induce the helical phase and the superconducting diode effect, and we calculate the diode efficiency by varying the magnetization strength of the impurities.

In Figs. 3.13(a) and (c) we display two different configurations with 8 and 24 magnetic impurities, respectively, and the corresponding diode efficiency as a function of the impurities magnetization is shown in Figs. 3.13(b) and (d). Note that all impurities have the same magnetization magnitude, and there is an equal number of positive and negative magnetization

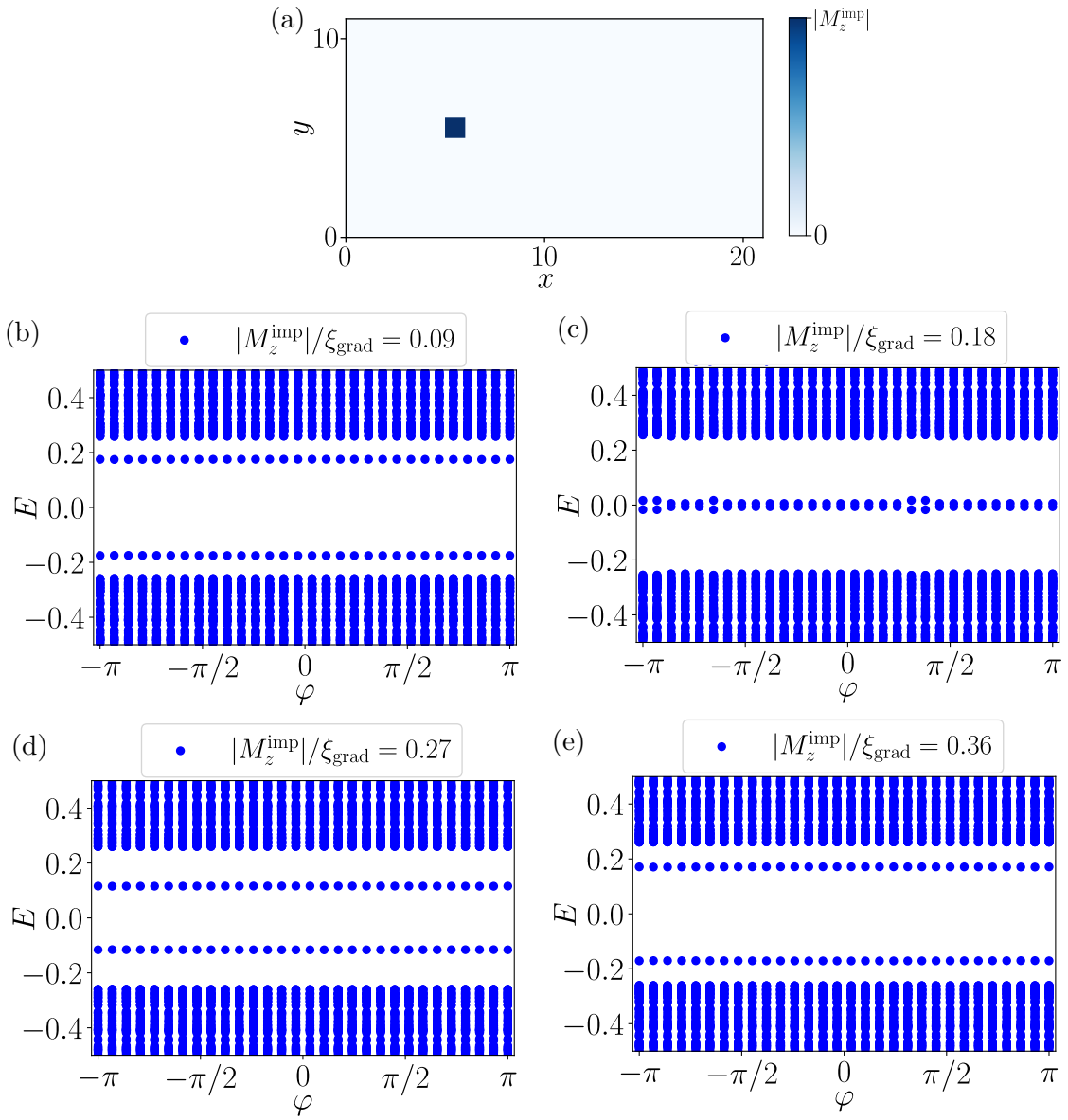

Figure 3.14: (a) Out-of-plane magnetization for the single-impurity configuration. (b)-(e) Energy dispersion E as a function of the imposed superconducting phase φ for increasing values of the impurity magnetization, with $\lambda_{\mathrm{soc}} = 0.2$, $\mu = -1$, $\xi_{\mathrm{grad}} = 11$, $t' = 0.1$ and a 21×11 system size.

impurities. Figures 3.13(b) and (d) show that, in both cases, the diode efficiency is significantly enhanced for a similar magnetization, corresponding to $\left|M_z^{\mathrm{imp}}\right|/\xi_{\mathrm{grad}} \simeq 0.18$.

Thus, it is important to analyze why the efficiency is higher for this particular magnetization. With this purpose, let us consider the case of a single magnetic impurity and calculate the spectrum as a function of the superconducting phase difference imposed on the device. The impurity configuration is shown in Fig. 3.14(a), whereas the energy dispersions for different magnetizations are displayed in Figs. 3.14(b)-(e). Focusing first on Fig. 3.14(b), for a small impurity magnetization there are bound states inside of the superconducting gap close to the continuum. As the magnetization is increased, the bound states move closer to zero energy.

However, when the magnetization is further increased, the bound states split from zero energy and move closer to the continuum again, as seen from Figs. 3.14(d)-(e).

Notably, precisely when the bound states are close to zero energy (see Fig. 3.14(c)), the magnetization of the impurity is $\left|M_z^{\text{imp}}\right|/\xi_{\text{grad}} = 0.18$, which corresponds to the peak in the efficiency observed in Figs. 3.13(b) and (d) for the multiple impurities configurations. As a cross-check, we have verified that for the configurations with 8 and 24 impurities the bound states are also close to zero energy for $\left|M_z^{\text{imp}}\right|/\xi_{\text{grad}} = 0.18$.

Hence, we have demonstrated that the out-of-plane magnetization gradient in both the ferromagnetic domain wall and the arrays of impurities can induce the Josephson diode effect. However, the mechanism in the latter setup seems to be distinct, as our results point to the importance of bound states close to zero energy to enhance the efficiency. The purpose of this work was to verify whether the diode effect could be induced by out-of-plane magnetization gradients and propose alternative profiles that enhance the efficiency. Thus, investigating the role of bound states close to zero energy is beyond the scope of this Chapter and we leave it for future work.

3.7 Discussion and conclusions

In this Chapter, we have investigated and compared different setups that stabilize the helical phase and show the Josephson diode effect. We have explored a phenomenological model based on the results from Ref. [23]. This model motivated comparing the helical phase induced by in-plane fields and out-of-plane magnetization gradients in a Rashba superconductor with spin-split Fermi surfaces. With this purpose, we have introduced a lattice model and solved self-consistently for the superconducting order parameter. We have first demonstrated numerically that for both field/magnetization configurations the helical phase is the preferred ground state and the Cooper pairs acquire a finite center-of-mass momentum. As discussed in Ref. [170], this implies that the diode effect can be used as a new probe to identify finite-momentum superconductivity, since experimental evidence for this exotic phase is scarce. In addition, as expected from the phenomenological model and demonstrated through the numerical calculations, in the linear regime the superconducting phase gradient in the helical phase is similar for both mechanisms when $B_y \delta k_{\text{soc}} \sim \frac{2M_z^{\max}}{\xi_{\text{grad}}}$.

After confirming that the helical state is the ground state for both magnetization configurations, which leads to a preferred direction for the current flow along the Cooper pair momentum, we have introduced the junction in the lattice model to study the Josephson diode effect. We have demonstrated that the current-phase relations are shifted and become asymmetric around zero phase when a magnetization is introduced to the Rashba superconductor. Consequently, similarly to the in-plane field setup, an out-of-plane magnetization can also generate nonreciprocal currents.

We have performed an extensive study of the role of the different parameters, including the field/magnetization magnitude, the SOC and the Fermi surface shape (by tuning the chemical potential). We have observed that, in general, a larger SOC strength leads to a higher efficiency.

Moreover, the field magnitude also enhances the effect, but there is an upper limit to the efficiency due to the suppression of superconductivity. Interestingly, in the in-plane magnetic field setup, the efficiency is significantly enhanced when one of the split Fermi surfaces is close to the van Hove singularity. Similarly, regions with an enhanced density of states contribution may also give rise to the high-efficiency peaks in the out-of-plane magnetization gradient case. These results demonstrate that, in both cases, comparable magnitudes for the diode efficiencies can be obtained, and out-of-plane magnetization gradients are therefore a realistic alternative to generate the Josephson diode effect.

In this direction, we emphasize that it would be interesting to repeat the experiments that reported the superconducting diode effect in the presence of an applied in-plane field, for instance, in Refs. [22, 155], but using out-of-plane magnetization gradients. Experimentally, this may be realized by proximity effects of a ferromagnetic insulator to the Rashba superconductor, or by exposing the Rashba system to the fields of an array of nearby nanomagnets, as discussed in Ref. [23]. From the numerical results obtained in this Chapter, we predict that the superconducting diode effect should also be experimentally detectable.

We have also introduced different profiles for the out-of-plane magnetization gradient, and we have demonstrated that they also generate the Josephson diode effect. On the one hand, we have examined a ferromagnetic domain wall magnetization, and we have observed that the currents are also large away from the domain wall. This configuration also shows that imposing phases in opposite directions leads to distinct current patterns in the superconductor, since depending on the phase the current flows more in the center or closer to the edges. Thus, a possible application of the magnetization gradients could be to guide the nonreciprocal current in circuits along certain paths. On the other hand, we have analyzed arrays of magnetic impurities, which revealed that bound states close to zero energy may give rise to an enhanced efficiency. Moreover, we have also observed that they generate anomalous current-phase relations, in agreement with Ref. [186]. Thus, as a first step, we are currently working on studying in detail the role of bound states in the Josephson diode effect, considering a minimal model with two magnetic impurities.

Importantly, in this Chapter we restricted the magnetization gradients to have no net magnetization in total. Firstly, this is beneficial as superconductivity is less destroyed and, secondly, our purpose was to identify the underlying mechanism for the diode effect, whereas a finite magnetization could give rise to additional effects. Along these lines, we could consider alternative configurations with a non-vanishing net magnetization, since we also expect that these will generate the superconducting diode effect. We have indeed verified the simplest case, by adding a constant out-of-plane field to the gradient configuration in Fig. 3.5(b). This allows more control of the current flow, as superconductivity will be further suppressed in the largest magnetization regions.

Finally, we emphasize that magnetization gradients could also be relevant for real systems, such as the superconducting diode effect reported for twisted bilayer graphene at zero applied field [151, 152]. Previous theoretical works showed that, in this system, superconductivity may coexist with a spontaneous time-reversal symmetry broken phase, for instance, some inhomogeneous magnetic phase [187, 188]. Hence, a magnetization gradient with a profile relevant for

this material could indeed give rise to the diode effect. From the opposite perspective, this consequently implies that the superconducting diode effect could be used as a probe of spontaneously generated magnetic order in certain materials. Motivated by the case of twisted bilayer graphene, we have demonstrated that clusters of magnetic impurities also lead to nonreciprocal transport, and give rise to an enhanced efficiency. Hence, magnetization gradients open up many new possibilities to generate the superconducting diode effect, and by optimizing the profile it is also likely that the diode efficiency can be significantly enhanced.

Part III

Altermagnetism

Chapter 4

Minimal models for altermagnetism

Info: *Part of the content and figures of this Chapter have been submitted for publication together with A. Kreisel, Y. Yu, B.M. Andersen and D.F. Agterberg, and are available in Ref.* [4] *as a preprint* [arXiv:2402.15616].

4.1 Introduction

Traditionally, the basic magnetic states have been classified either as ferromagnets or antiferromagnets. The former are characterized by a strong macroscopic magnetization, as opposed to antiferromagnets, which exhibit a vanishing net magnetization. This traditional view was recently challenged when a new class of unique materials, dubbed altermagnets, was recognized, which differs from both conventional ferromagnets and antiferromagnets [26, 27, 189–195]. In particular, altermagnets feature a vanishing net magnetization, similar to antiferromagnets, but show time-reversal symmetry breaking and spin-split band structures, akin to ferromagnets.

The symmetries of the magnetic states define the properties of each phase. First, as shown in Fig. 4.1(a), in ferromagnets all spins are aligned in the same direction, which gives rise to a net magnetization and time-reversal symmetry breaking. Therefore, this results in a uniform Zeeman splitting of the bands. On the contrary, antiferromagnets feature a vanishing net magnetization, as illustrated in Fig. 4.1(b). Since time reversal followed by a translation or inversion is a symmetry of these systems, there is no splitting of the bands due to Kramers degeneracy. Finally, altermagnets also feature vanishing net magnetization, but there is a different local environment for the two spin sublattices due to the non-magnetic atoms, as illustrated in Fig. 4.1(c). Thus, in contrast to antiferromagnets, only time reversal followed by a rotation is now a symmetry of these systems, which gives rise to a momentum-dependent spin-split band structure that, as opposed to ferromagnets, has symmetry-imposed nodes. Note that the altermagnetic spin-splitting of the bands does not require relativistic spin-orbit coupling (SOC). Even though the term altermagnetism is new, the idea of a magnetic state with these symmetries was already introduced in the context of cuprates more that 20 years ago, but in that case it was referred to as a "nematic spin nematic" state [196, 197].

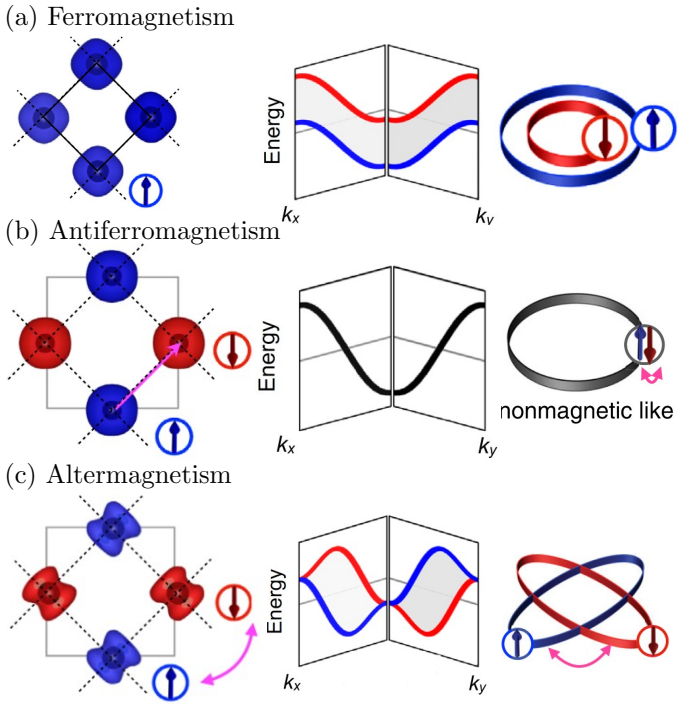

Figure 4.1: Illustration of the crystal structure in real space and the nonrelativistic electronic structure in momentum space for (a) ferromagnetism, (b) antiferromagnetism and (c) altermagnetism. The red and blue colors represent the opposite spin sublattices. Adapted from Šmejkal *et al.*, Refs. [26, 27].

Many compounds were initially proposed as altermagnetic candidates [26, 27], but recently a large ab-initio study identified up to 62 material candidates [198]. Among others, the list includes RuO_2 [190, 191, 199], MnF_2 [192, 194], κ-Cl [200, 201], $FeSb_2$ [193], CrSb [202] and MnTe [203]. In these compounds, the different local environments for the two sublattices characterizing altermagnets (see Fig 4.1(c)) originate from the non-magnetic atoms, e.g., the oxygen atoms in RuO_2 or the tellurium atoms in MnTe [198, 203, 204].

The exceptional properties of altermagnets make them ideal candidates for spintronic applications due to the spin-split electronic structure in momentum space [192, 204–206]. Differently from antiferromagnets, the spin splitting does not require relativistic spin-orbit coupling. In addition, since altermagnets feature no net magnetization, these materials are not sensitive to external magnetic field perturbations, a key advantage over ferromagnets. Altermagnets have also been predicted to show a finite anomalous Hall effect, previously associated mainly with ferromagnets and fundamentally different from relativistic antiferromagnets [191, 207].

Recent experimental works are consistent with the predictions for an altermagnetic phase in RuO_2 and MnTe, including the anomalous Hall effect [208, 209], the broken Kramer's degeneracy [203, 210–213], and the spin currents and spin torque phenomena [214–216]. However, in the case of RuO_2, whether the ground state is magnetic or non-magnetic is still controversial [217, 218].

The band structure in Fig. 4.1(c) shows that altermagnets do not exhibit a uniform spin splitting. Instead, there are symmetry-imposed nodes that reflect the rotation connecting the

two sublattices. In analogy with even-parity unconventional superconductivity, altermagnetic states can be classified according to the symmetry of the order parameter, which can be d-wave, g-wave, or i-wave, and determines the number of nodes. For instance, when the symmetry relating the two sublattices is a $\pi/2$ rotation, the spin splitting exhibits d-wave symmetry, with nodes along two orthogonal directions. Note that unconventional magnets with odd-parity, such as p-wave or f-wave symmetry, are distinct from altermagnets, as they require a noncollinear magnetic structure and inversion symmetry breaking of the band structure. However, odd-parity unconventional magnets must preserve time-reversal symmetry, since this operation followed by a translation protects the zero net magnetization [219].

To understand the origin of altermagnetism and the properties of this phase, an important step is to obtain realistic minimal tight-binding models. These models allow us to study the altermagnetic phase in space groups with different symmetries, and should be able to describe d-wave, g-wave and i-wave altermagnetism. Hence, the minimal models can provide insight into which mechanism stabilizes this phase over conventional magnetic phases, such as ferromagnetism. Moreover, minimal models provide a platform to calculate analytically the Berry curvature and analyze the anomalous Hall response.

The remainder of this Chapter is organized as follows. In Sec. 4.2, we first present the general minimal model describing altermagnetism, and introduce the different terms appearing in the model. We apply the model to the altermagnetic candidates RuO_2 and MnF_2 in Sec. 4.3, and compare the band structure to density functional theory (DFT) results. In order to identify which mechanism stabilizes altermagnetism over ferromagnetism, we derive analytic expressions for the bare susceptibilities in Sec. 4.4. In Sec. 4.5, we use the previous susceptibilities to investigate why most altermagnets belong to non-symmorphic groups (we will introduce this concept in Sec. 4.2). Then, in Sec. 4.6, we show that the minimal models stabilize a leading altermagnetic instability within RPA and Hartree-Fock self-consistent approaches, introducing intra-orbital on-site Coulomb interactions. We use the minimal model to derive an analytic expression for the Berry curvature in Sec. 4.7, revealing that it is linear in the spin-orbit coupling strength. Finally, we extend the discussion to other altermagnetic candidates in Sec. 4.8, where we introduce the specific form of the minimal model for different space groups, demonstrating that it can describe d-wave, g-wave and i-wave altermagnetism. Finally, in Sec. 4.9 we present the conclusions of this Chapter.

4.2 Minimal models for altermagnetism

4.2.1 General considerations

Since it will be important in this Chapter, we first introduce the distinction between symmorphic and non-symmorphic space groups. In a symmorphic space group, all point group operations (including rotations, reflections and inversion) leave one common point fixed, as opposed to non-symmorphic space groups, where the point group operations are combined with translations to recover the original crystal structure. Without considering spin-orbit coupling, non-symmorphic symmetries ensure band degeneracies on the Brillouin zone boundary, in ad-

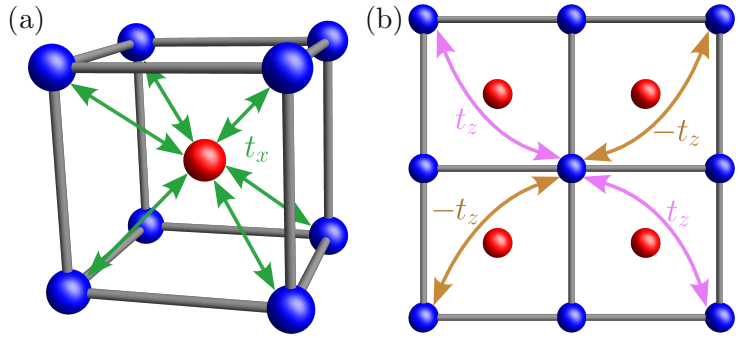

Figure 4.2: Illustration of the (a) inter- and (b) intra-sublattice hoppings introduced in the minimal model of Eq. (4.1), for the particular case of a tetragonal system (see Eq. (4.4)). The two colors denote the two sublattices.

dition to spin degeneracy [147]. As we will demonstrate in Sec. 4.5, they play a crucial role in stabilizing altermagnetism.

The large ab-initio study performed in Ref. [198] revealed that most of the 62 material candidates belong to non-symmorphic space groups. Motivated by this insight, we focus on minimal models for these space groups. However, to investigate why altermagnetic materials with symmorphic space groups are less frequent, we will also discuss a symmorphic example in Sec. 4.5. To construct minimal tight-binding models, we consider two sublattices defined by two magnetic atoms which belong to a given Wyckoff position, which defines the location of the atoms in the system. In addition, we mainly focus on materials that contain inversion symmetry, as this applies to 53 of the 62 material candidates in Ref. [198]. We will extend the discussion to a case without inversion symmetry in Sec. 4.8.

A minimal model is obtained by combining the lowest-order functions that give rise to invariants, i.e. terms transforming like the trivial irreducible representation (see Chapter 1). We start by introducing the generic minimal model and describing the role of the parameters involved, and then we provide the explicit form of the model for specific cases. In general, it can be written as

$$H(\mathbf{k}) = \varepsilon_{0,\mathbf{k}} + t_{x,\mathbf{k}}\tau_x + t_{z,\mathbf{k}}\tau_z + \tau_y\vec{\lambda}_{\mathbf{k}}\cdot\vec{\sigma} + \tau_z\vec{J}\cdot\vec{\sigma}, \tag{4.1}$$

where τ_i corresponds to sublattice space and σ_i labels the spin degree of freedom. This form of the model assumes a single orbital per site, although we will extend the discussion to a two orbital model for the case of RuO_2 in Sec. 4.3.

As seen from Eq. (4.1), the minimal model for altermagnetism contains only five parameters. First, $\varepsilon_{0,\mathbf{k}}$ is a sublattice-independent dispersion, while $t_{x,\mathbf{k}}$ and $t_{z,\mathbf{k}}$ are the inter- and intra-sublattice hoppings, illustrated in Fig. 4.2 for the case of a tetragonal system. In addition, $\vec{\lambda}_{\mathbf{k}}$ is the general form for the spin-orbit coupling and, finally, $\vec{J}$ is the altermagnetic order parameter. The specific form of these parameters depends on the space group, the point group and the Wyckoff position. In the case of space groups containing inversion symmetry, all parameters in Eq. (4.1) are even under $\mathbf{k} \to -\mathbf{k}$.

In order to classify the symmetries of the sublattice operators $\tau_i = \{\tau_0, \tau_x, \tau_y, \tau_z\}$, we first

have to determine how they transform under the point group operations g, similarly to the procedure followed in Chapter 2. However, in sublattice space, there are only two possibilities for the point group operations. On the one hand, if g preserves the two sublattices, the matrix representation in sublattice space simply corresponds to $d_\tau(g) = \mathbb{1}_2$. On the other hand, if the point group operation acts non trivially and exchanges the two sublattices, the representation corresponds to $d_\tau(g) = \tau_x$. To classify how the sublattice operators transform, we calculate

$$d_\tau^\dagger(g)\tau_i d_\tau(g). \tag{4.2}$$

Since $d_\tau(g)$ can only be either $\mathbb{1}_2$ or τ_x, this shows that the operators τ_0 and τ_x are invariant under all point group operations, and therefore have the full symmetry of the point group. By contrast, τ_z and τ_y must be odd under the operations that exchange the two sublattices. Hence, the operations that flip the two sublattices in each point group define the symmetry of τ_z and τ_y in Eq. (4.1).

As discussed above Eq. (4.1), the terms entering in the Hamiltonian correspond to invariants, and therefore transform trivially under all point group operations. As a consequence, the $\mathbf{k}$-dependence of the hopping term $t_{z,\mathbf{k}}$ shares the same symmetry as the τ_z operator. On the contrary, since $t_{x,\mathbf{k}}$ transforms like τ_x, it has the full symmetry of the point group. The spin operators $\vec{\sigma}$ and τ_y are odd under time-reversal symmetry $T = i\tau_0\sigma_y K$, where K denotes complex conjugation. Therefore, τ_y can only be part of the spin-orbit coupling terms, since the product will preserve T. We focus on materials that have inversion symmetry, $\vec{\lambda}_{\mathbf{k}} = \vec{\lambda}_{-\mathbf{k}}$, and thus the term $\tau_y\vec{\lambda}_{\mathbf{k}}\cdot\vec{\sigma}$ in Eq. (4.1) is also invariant under time-reversal symmetry. Finally, the altermagnetic order parameter $\vec{J}$ is $\mathbf{k}$-independent and has opposite signs on the two sublattices, as it couples to τ_z in the minimal model.

In the case of more than one magnetic atom in the unit cell, there are two possible conventions for the Fourier transform. One the one hand, the first convention corresponds to $\chi_{\mathbf{k},\alpha} = \sum_{\mathbf{R}} e^{i\mathbf{k}\cdot(\mathbf{R}+\mathbf{r}_\alpha)}\phi_{\mathbf{R},\alpha}$, where $\chi_{\mathbf{k},\alpha}$ and $\phi_{\mathbf{R},\alpha}$ are the basis functions in momentum and real space, respectively, with $\mathbf{R}$ being the position of the unit cell and $\mathbf{r}_\alpha$ the position of the atom within the unit cell. On the other hand, in the second convention the Fourier transform is written as $\chi_{\mathbf{k},\alpha} = \sum_{\mathbf{R}} e^{i\mathbf{k}\cdot\mathbf{R}}\phi_{\mathbf{R},\alpha}$, and thus the phase factor is not included in the basis functions. Here, we choose the first convention since, even though the Hamiltonian $H_{\mathbf{k},\alpha\beta} = \sum_{\mathbf{R}} e^{i\mathbf{k}\cdot(\mathbf{R}-\mathbf{r}_\alpha+\mathbf{r}_\beta)}H_{\mathbf{R},\alpha\beta}$ is not periodic in the Brillouin zone, the symmetries without translations are $\mathbf{k}$-independent. Consequently, since τ_x and τ_y couple the two sublattices, we have $t_{x,\mathbf{k}+\mathbf{G}} = e^{i\mathbf{G}\cdot\mathbf{t}_{12}}t_{x,\mathbf{k}}$ and $\vec{\lambda}_{\mathbf{k}+\mathbf{G}} = e^{i\mathbf{G}\cdot\mathbf{t}_{12}}\vec{\lambda}_{\mathbf{k}}$, where $\mathbf{G}$ is a reciprocal lattice vector and $\mathbf{t}_{12}$ is the translation vector between the two magnetic atoms. For the sublattice independent parameters, we have $\varepsilon_{0,\mathbf{k}} = \varepsilon_{0,\mathbf{k}+\mathbf{G}}$ and $t_{z,\mathbf{k}} = t_{z,\mathbf{k}+\mathbf{G}}$. As we will show with the example of space group 136 in the next subsections, the choice of Fourier transform determines the form of the $t_{x,\mathbf{k}}$ and $\vec{\lambda}_{\mathbf{k}}$ parameters.

4.2.2 Dispersion relations and Weyl lines

The minimal model introduced in Eq. (4.1) has four bands, and the dispersion corresponds to

$$E_{\mathbf{k}}^{(\alpha=\pm,\beta=\pm)} = \varepsilon_{0,\mathbf{k}} + \alpha\Big(t_{x,\mathbf{k}}^2 + t_{z,\mathbf{k}}^2 + \vec{\lambda}_{\mathbf{k}}^2 + \vec{J}^2 + \beta 2\sqrt{t_{z,\mathbf{k}}^2\vec{J}^2 + (\vec{\lambda}_{\mathbf{k}}\times\vec{J})^2}\Big)^{1/2}. \tag{4.3}$$

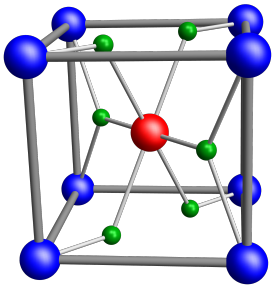

Figure 4.3: Illustration of the crystal structure for space group 136, relevant for RuO_2 and MnF_2. The red and blue colors denote the two sublattices (Ru and Mn atoms, respectively), while the green color corresponds to the non-magnetic atoms (O and F).

The bands can be degenerate in some cases, giving rise to what are known as Weyl planes and Weyl lines. As we will show for the case of RuO_2 in Sec. 4.7, identifying the degeneracies is important since they enhance the Berry curvature and allow us to predict regions with a large Hall conductivity response.

Focusing first on the limit $\vec{\lambda}_{\mathbf{k}} = 0$, in general the four bands are non-degenerate, except in two cases:

1) $t_{z,\mathbf{k}} = 0$: Defines symmetry-imposed Weyl planes in momentum space with two two-fold degenerate bands, which correspond to the nodes of the altermagnetic spin splitting.

2) $t_{x,\mathbf{k}} = 0$ and $t_{z,\mathbf{k}} = \pm\left|\vec{J}\right|$: Define Weyl lines with a two-fold degeneracy and two non-degenerate bands. These lines appear only when $\left|t_{z,\mathbf{k}}\right| > \left|\vec{J}\right|$, and are not symmetry-imposed.

In general, when $\vec{\lambda}_{\mathbf{k}} \neq 0$, the Weyl planes given by $t_{z,\mathbf{k}} = 0$ become gapped and typically result in Weyl points, although Weyl lines can occur when $\vec{\lambda}_{\mathbf{k}} \times \vec{J} = 0$. The Weyl lines discussed in the second case can survive with spin-orbit coupling if $\vec{\lambda}_{\mathbf{k}} \cdot \vec{J} \neq 0$ [220–223].

4.2.3 Example: space group 136

To illustrate the form of the minimal model for a particular example, let us consider the case of space group 136 ($P4_2/mnm$), which has point group D_{4h}. The crystal structure for this space group is illustrated in Fig. 4.3, including both magnetic (red/blue dots) and non-magnetic atoms (green dots). This applies to rutile RuO_2, MnF_2, NiF_2, and CoF_2, with Wyckoff position 2a for the magnetic atoms, which correspond to the positions $(0,0,0)$ and $(1/2,1/2,1/2)$. The first step to construct the minimal model is to find the symmetry of the τ_z and τ_y operators in Eq. (4.1), by identifying the point group operations that exchange the two sublattices.

The rutile lattice structure contains inversion symmetry, and consequently we can focus only on the rotation operations of D_{4h}. These include the four-fold rotation with respect to the z-axis (C_{4z}) and the two-fold rotations with respect to the z-axis (C_{2z}), the x-axis (C_{2x}), and the diagonal plane xy (C_{2xy}), as illustrated in Fig. 1.5. For space group 136, the origin

of coordinates is conventionally set at a magnetic site, and therefore the rotation axis crosses the origin. In this setting, as seen from Fig. 4.3, the operations $\{C_{2z}|000\}$ and $\{C_{2xy}|000\}$ leave the two sublattices invariant, whereas the non-symmorphic operations $\{C_{4z}|\frac{1}{2}\,\frac{1}{2}\,\frac{1}{2}\}$ and $\{C_{2x}|\frac{1}{2}\,\frac{1}{2}\,\frac{1}{2}\}$ exchange the two sublattices. The irreducible representation (irrep) in D_{4h} that has these symmetries is B_{2g}, which implies that τ_z and τ_y transform like this irrep.

Since the hopping $t_{z,\mathbf{k}}$ in Eq. (4.1) has the same symmetry as τ_z, it should also transform as the B_{2g} irrep. In momentum space, this irrep transforms like $k_x k_y$, and therefore the lowest-order hopping with this symmetry is $\sin k_x \sin k_y$. As depicted in Fig. 4.2(b), this involves a hopping between next-nearest neighbors and gives rise to symmetry-imposed sign changes. Instead, τ_x transforms like A_{1g}, and consequently the hopping $t_{x,\mathbf{k}}$ also transforms trivially under all point group operations. Given that τ_x (and thus $t_{x,\mathbf{k}}$) couple the two sublattices, with our choice of Fourier transform the translation between the two sublattices has to enter in the basis function transforming like the A_{1g} irrep, which for nearest neighbors corresponds to $\cos(k_x/2)\cos(k_y/2)\cos(k_z/2)$ (see Fig. 4.2(a)). Therefore, in this case, the hoppings for the minimal model are

$$\begin{aligned} t_{x,\mathbf{k}} &= t_{x0}\cos\frac{k_x}{2}\cos\frac{k_y}{2}\cos\frac{k_z}{2}, \\ t_{z,\mathbf{k}} &= t_{z0}\sin k_x \sin k_y, \end{aligned} \tag{4.4}$$

while for the spin-orbit coupling

$$\begin{aligned} \lambda_{x,\mathbf{k}} &= \lambda \sin\frac{k_x}{2}\cos\frac{k_y}{2}\sin\frac{k_z}{2}, \\ \lambda_{y,\mathbf{k}} &= -\lambda\cos\frac{k_x}{2}\sin\frac{k_y}{2}\sin\frac{k_z}{2}, \\ \lambda_{z,\mathbf{k}} &= \lambda_z\cos\frac{k_x}{2}\cos\frac{k_y}{2}\cos\frac{k_z}{2}(\cos k_x - \cos k_y). \end{aligned} \tag{4.5}$$

To obtain these terms, we have used that $\sigma_z \sim A_{2g}$ and $(\sigma_x, \sigma_y) \sim E_g$ in D_{4h}, as derived in Sec. 2.3 and summarized in Table 2.1. Note that in tetragonal systems the strength of the SOC is the same in the x and y directions (λ), while it is different for the z component. In addition, the minus sign for $\lambda_{y,\mathbf{k}}$ is needed to fulfill the mirror symmetries. As previously discussed, the factors of 1/2 in the $t_{x,\mathbf{k}}$ and $\vec{\lambda}_{\mathbf{k}}$ inter-sublattice hopping terms appear due to the translation $\mathbf{t}_{12} = (\frac{1}{2}, \frac{1}{2}, \frac{1}{2})$ between the two sublattices entering in the Fourier transformation from real to momentum space.

By expanding the tight-binding model around certain momentum points, we can verify that the form agrees with the kp theories in Ref. [147]. The relevant representation at each point can be checked at the Bilbao Crystallographic Server [224–226].[1] As seen from Ref. [147], different representations can have the same kp theory, and for space group 136 this shows that s and d_{xy}-orbitals have the same form for the tight-binding model.

[1] It can be found under: Topological Quantum Chemistry → Non-magnetic → BANDREP → Get the BRs with time-reversal symmetry from a Wyckoff position.

4.3 Application to RuO_2 and MnF_2

To demonstrate that the minimal model can describe the normal-state band structure and capture the altermagnetic spin splitting, we focus first on the case of RuO_2 and compare to DFT results [190]. Afterwards, we extend the discussion to another tetragonal system, MnF_2, and discuss the similarities and differences with DFT calculations [192]. Since we are constructing realistic minimal models for different material candidates, all energy units are given in eV.

4.3.1 Case 1: RuO_2

The DFT calculations shown in Fig. 4.4 reveal that there are three orbitals forming bands that cross the Fermi level: d_{xy}, d_{xz}, and d_{yz}. Therefore, we first construct a one-orbital tight-binding model for the d_{xy} orbitals with Wyckoff position 2a, which corresponds to the example discussed in Sec. 4.2. Then, we also show that the minimal model can be generalized to a two-orbital model to include the d_{xz}/d_{yz} orbitals. In this case, the altermagnetic order parameter in Eq. (4.1) has the same form as it is given by opposite signs on the two sublattices.

In order to reproduce the DFT results we consider the following form for the dispersion,

$$\begin{aligned}\varepsilon_{0,\mathbf{k}} = {} & t_1(\cos k_x + \cos k_y) - \mu + t_2 \cos k_z + t_3 \cos k_x \cos k_y \\ & + t_4(\cos k_x + \cos k_y)\cos k_z + t_5 \cos k_x \cos k_y \cos k_z,\end{aligned} \tag{4.6}$$

while for the hoppings we take

$$\begin{aligned}t_{z,\mathbf{k}} &= t_6 \sin k_x \sin k_y + t_7 \sin k_x \sin k_y \cos k_z, \\ t_{x,\mathbf{k}} &= t_8 \cos\frac{k_x}{2}\cos\frac{k_y}{2}\cos\frac{k_z}{2},\end{aligned} \tag{4.7}$$

with the SOC previously written in Eq. (4.5).

Figure 4.5(a) shows the bands obtained from the minimal model in Eq. (4.1) using the expressions above for the parameters, with the appropriate choice of hoppings detailed in Table 4.1. Importantly, when compared to the DFT calculations in Fig. 4.4, the minimal tight-binding model shows a remarkable resemblance, as it captures the behavior of the bands as well as the crossings at the Fermi level. In addition, it also reproduces the nodal lines along X-M and Z-R-A. The $t_{x,\mathbf{k}}$ term gives rise to a splitting along Γ-X and M-Γ-Z lines, while the $t_{z,\mathbf{k}}$ hopping is responsible for the splitting along the A-Z direction. In Fig. 4.5(b) we also include the altermagnetic order parameter J, reproducing the spin splitting along the M-Γ and A-Z lines reported in Ref. [190] (see also Fig. 4.4(c)). The minimal model reveals that, to obtain an altermagnetic spin splitting, we must have a finite $t_{z,\mathbf{k}}$ term, which defines the symmetry of the splitting.

As noted before, the d_{xz}/d_{yz} orbitals also cross the Fermi level (see Fig. 4.4). Thus, we have also constructed a two-orbital model without including correlations with the previous one-orbital model. In this case, the minimal model of Eq. (4.1) with the parameters in Eqs. (4.5)-(4.7) is duplicated to incorporate the orbital degree of freedom (and therefore couples to an identity in orbital space). In addition, we obtain the following terms transforming as invariants (A_{1g} irrep),

$$\gamma_z(t_{a,\mathbf{k}}+t_{b,\mathbf{k}}\tau_x+t_{c,\mathbf{k}}\tau_z) + \gamma_x(t_{d,\mathbf{k}}+t_{e,\mathbf{k}}\tau_x+t_{f,\mathbf{k}}\tau_z) + t_{g,\mathbf{k}}\gamma_y\tau_y + \lambda\gamma_y\tau_0\sigma_z, \tag{4.8}$$

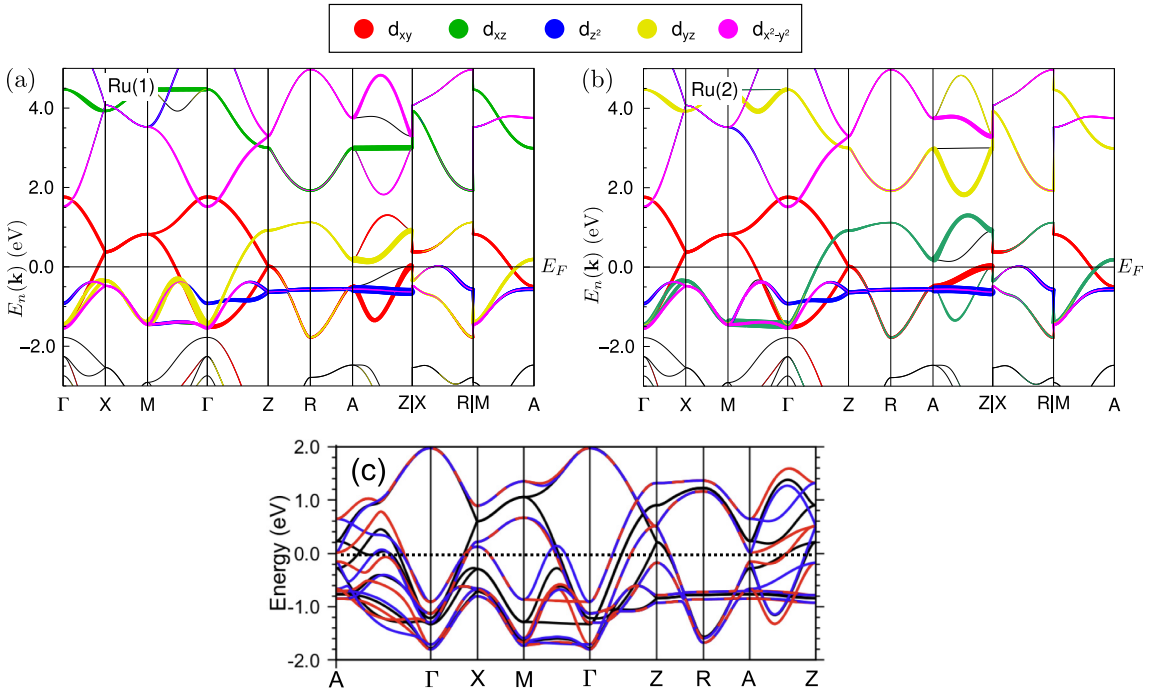

Figure 4.4: DFT band structure for RuO_2 projecting to the d-orbitals for (a) the Ru(1) and (b) the Ru(2) atoms. (c) Hartree-Fock calculation from Ref. [190] for the paramagnetic (black) and altermagnetic state (red,↑; blue,↓) from a Wannier projection of the DFT calculation.

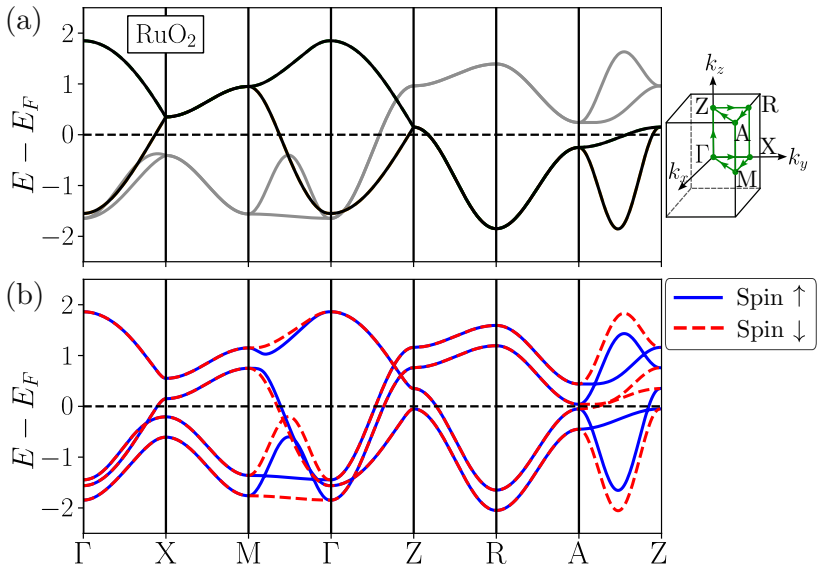

Figure 4.5: Band structure for RuO_2 in (a) the normal, and (b) the altermagnetic state, using the minimal model in Eq. (4.1) with the parameters given in Eqs. (4.6)-(4.7) and $J_z = 0.2$ in (b). The tetragonal Brillouin zone is sketched on the right. The gray bands are obtained from the two-orbital model in Eqs. (4.8)-(4.9). The specific hopping parameters used to reproduce the DFT results shown in Fig 4.4 are given in Tables 4.1-4.2.

Table 4.1: Hopping parameters used for RuO_2 and MnF_2 to obtain the bands in Fig. 4.5 and Fig. 4.7, respectively, which reproduce the DFT results [190, 192]. We use the minimal model in Eq. (4.1) with the parameters given in Eqs. (4.6)-(4.7).

Tetra.	t_1	t_2	t_3	t_4	t_5	t_6	t_7	t_8	μ
RuO_2	-0.05	0.7	0.5	-0.15	-0.4	-0.6	0.3	1.7	0.25
MnF_2	0	0.13	0	-0.02	0.015	0	0.03	0.33	-0.01

Table 4.2: Hopping parameters for the two-orbital model of RuO_2 given in Eqs. (4.8)-(4.9), which was used to obtain the gray bands in Fig. 4.5 reproducing the results shown in Fig. 4.4.

	t_1	t_2	t_3	t_4	t_5	t_6	t_7	t_8	μ
RuO_2	0.18	-1	-0.5	-0.1	-0.1	-0.6	0	-0.2	-3
	t_9	t_{10}	t_{11}	t_{12}	t_{13}	t_{14}	t_{15}	t_{16}	a_0
RuO_2	-0.1	0	-0.2	0	0	0	0.1	0	3

with

$$
\begin{aligned}
t_{a,\mathbf{k}} &= (t_9 + t_{10}\cos k_z)(\cos k_x - \cos k_y),\\
t_{b,\mathbf{k}} &= t_{11}\cos\frac{k_x}{2}\cos\frac{k_y}{2}\cos\frac{k_z}{2}(\cos k_x - \cos k_y),\\
t_{c,\mathbf{k}} &= t_{12}\sin k_x \sin k_y(\cos k_x - \cos k_y),\\
t_{d,\mathbf{k}} &= t_{13}\sin k_x \sin k_y,\\
t_{e,\mathbf{k}} &= t_{14}\sin\frac{k_x}{2}\sin\frac{k_y}{2}\cos\frac{k_z}{2},\\
t_{f,\mathbf{k}} &= a_0 + t_{15}(\cos k_x + \cos k_y),\\
t_{g,\mathbf{k}} &= t_{16}\cos\frac{k_x}{2}\cos\frac{k_y}{2}\cos\frac{k_z}{2}(\cos k_x - \cos k_y),
\end{aligned}
\tag{4.9}
$$

where γ_i are the Pauli matrices describing the $\{d_{xz}, d_{yz}\}$ orbital space, with $\gamma_x \sim B_{2g}$, $\gamma_y \sim A_{2g}$, and $\gamma_z \sim B_{1g}$, as discussed earlier in Sec. 2.3 and summarized in Table 2.2. In addition, a_0 is a $\mathbf{k}$-independent constant allowed since the coupling of γ_x and τ_z already transforms like the A_{1g} irrep. The last term in Eq. (4.8) corresponds to an on-site spin-orbit coupling, which was not allowed by symmetry in the one-orbital model in Eq. (4.1) and opens a splitting at the Γ point. In Fig. 4.5 we also include the bands from the two-orbital model using the choice of hopping parameters specified in Table 4.2, colored in gray in the normal state (see Fig. 4.5(a)). In this case, there is another set of bands with a two-fold spin-degeneracy with a higher energy (not shown). As seen, when compared to the DFT results in Fig. 4.4, the bands obtained from this model also correctly describe the crossings at the Fermi level and the degeneracies of the bands, as well as the characteristic altermagnetic spin splitting.

4.3.2 Case 2: MnF_2

We focus now on another tetragonal material candidate, MnF_2, where DFT calculations have also identified an altermagnetic state [192,194]. As shown in Fig. 4.6(a)-(b), DFT results indicate that, by introducing an on-site Coulomb interaction, U a single band close to the Fermi level can be obtained, in agreement with Ref. [192]. In Fig. 4.7(a) we show the normal state bands obtained from the minimal model in Eq. (4.1) with the hopping parameters given in Eqs. (4.6)-(4.7), with the specific values reproducing the DFT bands included in Table 4.1. Similarly to the RuO_2 case, the normal state bands obtained from the minimal model reproduce the crossings at the Fermi level and the general behavior and degeneracies of the bands.

In the magnetic state, DFT results in Fig 4.6(c)-(d) show that there is a spin splitting along M-Γ and A-Z lines, similarly to RuO_2, but there is a crossing of two bands close to the Fermi level along the Γ-Z direction due to the large correlation U [194, 227]. As shown in Fig. 4.7(b), the band structure in the altermagnetic state obtained from the minimal model cannot reproduce this crossing. Since we can impose a small moment J, differently from the DFT results in the magnetic state, there is still a single band close to the Fermi level displaying a splitting along the same directions. Focusing on the spin splitting in the A-Z directions, we can identify another subtle difference: the DFT results show that the opposite-spin bands approach each other, as opposed to the minimal model result. However, DFT calculations are performed at zero temperature, while the magnetic transition for MnF_2 occurs at $T = 67$ K [228]. The minimal model may indicate that in this material the small magnetic order can be obtained at a larger temperature.

4.4 Analysis of the susceptibilities

In the previous section, we identified relevant minimal models for altermagnetism and demonstrated that they can reproduce the nodal lines and the characteristic altermagnetic spin splitting. In order to understand the mechanisms stabilizing this phase over other conventional phases, such as ferromagnetism, in this section we obtain and analyze analytic expressions for the bare susceptibilities from the minimal model. To simplify the analysis, we neglect here the role of SOC, but in Sec. 4.7 we include it again to derive an analytic expression for the Berry curvature and investigate the anomalous Hall response. In the abscence of SOC, the minimal model in Eq. (4.1) is given by

$$H'(\mathbf{k}) = \varepsilon_{0,\mathbf{k}} + t_{x,\mathbf{k}}\tau_x + t_{z,\mathbf{k}}\tau_z. \tag{4.10}$$

The transformation from sublattice to band basis for this 2×2 model is straightforward and is given by

$$U(\mathbf{k}) = \begin{pmatrix} \cos\frac{\theta_\mathbf{k}}{2} & \sin\frac{\theta_\mathbf{k}}{2} \\ -\sin\frac{\theta_\mathbf{k}}{2} & \cos\frac{\theta_\mathbf{k}}{2} \end{pmatrix}, \tag{4.11}$$

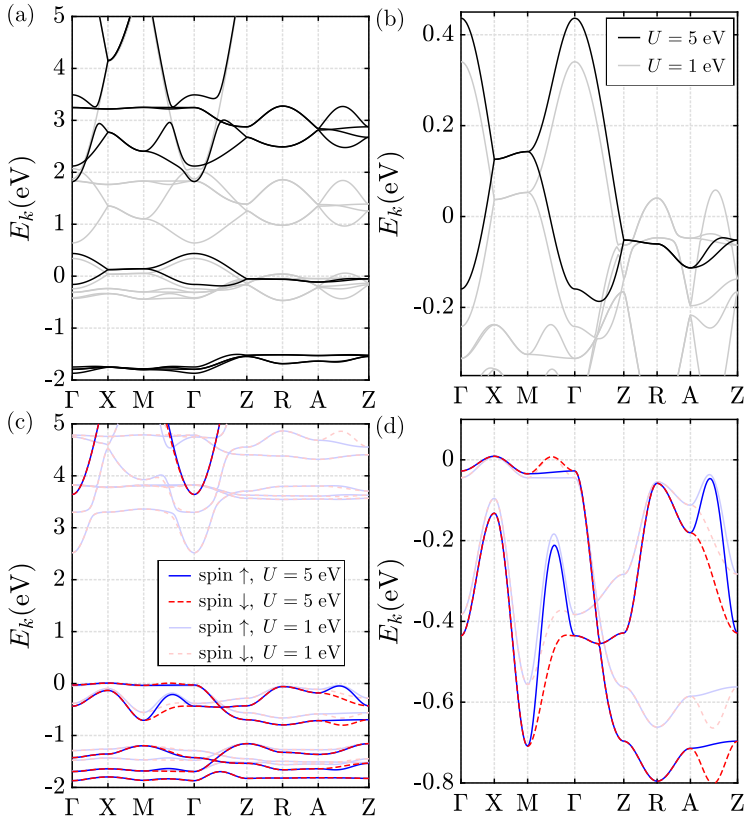

Figure 4.6: DFT band structure for MnF_2 in (a) the paramagnetic state and (c) performing a spin-polarized calculation, for two values of the parameter U, reproducing the results in Ref. [192]. (b), (d) Zoom of the bands close to zero energy for (a), (c), respectively.

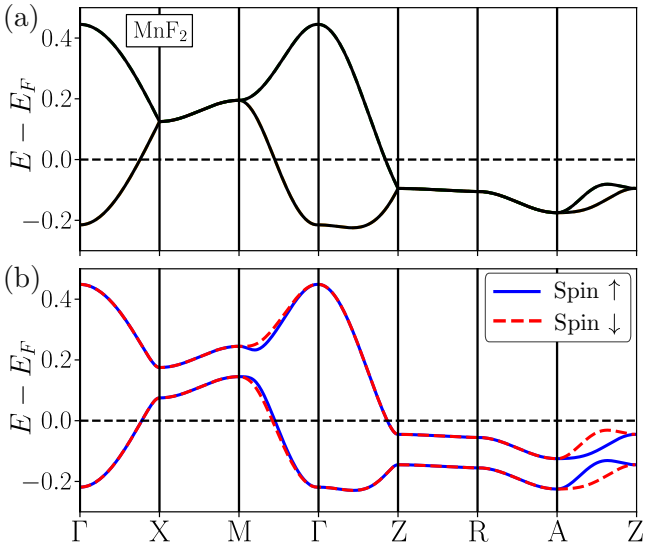

Figure 4.7: Band structure for MnF_2 in (a) the normal, and (b) the altermagnetic state, using the minimal model in Eq. (4.1) with the hopping parameters given in Eqs. (4.6)-(4.7) and $J_z = 0.05$ in (b). The specific hopping parameters to reproduce the DFT results shown in Fig 4.6 are detailed in Table 4.1.

where $\theta_{\mathbf{k}}$ depends on the hopping parameters in the minimal model as

$$\begin{aligned}\cos\theta_{\mathbf{k}} &= \frac{t_{z,\mathbf{k}}}{\sqrt{t_{z,\mathbf{k}}^2+t_{x,\mathbf{k}}^2}},\\ \sin\theta_{\mathbf{k}} &= \frac{t_{x,\mathbf{k}}}{\sqrt{t_{z,\mathbf{k}}^2+t_{x,\mathbf{k}}^2}}.\end{aligned} \tag{4.12}$$

Thus, this transformation diagonalizes the previous Hamiltonian $H'(\mathbf{k})$, $U(\mathbf{k})^\dagger H'(\mathbf{k})U(\mathbf{k}) = \mathrm{diag}\left(E_{\mathbf{k}}^{(+)}, E_{\mathbf{k}}^{(-)}\right)$, with $E_{\mathbf{k}}^{(\pm)} = \varepsilon_{0,\mathbf{k}} \pm \sqrt{t_{x,\mathbf{k}}^2+t_{z,\mathbf{k}}^2}$. As seen, this unitary transformation is in general $\mathbf{k}$-dependent, except at the M-point, which corresponds to $(\pi,\pi,0)$ (see the sketch in Fig. 4.5), where both hoppings have the same momentum dependence, $t_{x,\mathbf{k}}, t_{z,\mathbf{k}} \sim k_x k_y$.

As discussed in Eq. (1.43), the spin susceptibility is a relevant quantity as it can be directly related to the intensity measured in neutron scattering. Thus, let us introduce now the spin susceptibility in the usual spin channel for the case of multiple sublattices, which can be written as

$$\chi^{\mathrm{FM}}(\mathbf{q}, iq_n) = -\frac{1}{N}\int_0^\beta e^{iq_n\tau}\langle T_\tau S_{\mathbf{q}}(\tau) S_{-\mathbf{q}}(0)\rangle, \tag{4.13}$$

where iq_n denotes now the bosonic Matsubara frequency and the operator $S_{\mathbf{q}}(\tau)$ in sublattice space corresponds to

$$S_{\mathbf{q}}(\tau) = \sum_{\mathbf{k}} \Psi^\dagger_{\mathbf{k}+\mathbf{q}}(\tau)\tau_0\Psi_{\mathbf{k}}(\tau), \tag{4.14}$$

with the spinor $\Psi_{\mathbf{k}} = (\psi_{\mathbf{k},1}\ \psi_{\mathbf{k},2})^\intercal$ in the sublattice basis. We denote this susceptibility as the ferromagnetic channel since it diverges at $\mathbf{q}\to 0$ close to a ferromagnetic instability. Replacing the form for the previous operator in the susceptibility,

$$\chi^{\mathrm{FM}}(\mathbf{q}, iq_n) = -\frac{1}{N\beta}\sum_{\mathbf{k}, i\omega_n} \mathrm{Tr}\{G(\mathbf{k}, i\omega_n)G(\mathbf{k}+\mathbf{q}, i\omega_n+iq_n)\}, \tag{4.15}$$

where the Green's function projected to the band basis is given by

$$G(\mathbf{k}, i\omega_n) = \sum_{a=\pm} G^{(a)}(\mathbf{k}, i\omega_n)\left|u_{\mathbf{k}}^{(a)}\right\rangle\left\langle u_{\mathbf{k}}^{(a)}\right|, \tag{4.16}$$

with $G^{(\pm)}(\mathbf{k}, i\omega_n) = \frac{1}{i\omega_n - E_{\mathbf{k}}^{(\pm)}}$ denoting the Green's function in the band basis and $\left|u_{\mathbf{k}}^{(a)}\right\rangle\left\langle u_{\mathbf{k}}^{(a)}\right|$ the projection operator from sublattice basis onto band a and wavevector $\mathbf{k}$. Replacing this expression in the susceptibility, we obtain

$$\chi^{\mathrm{FM}}(\mathbf{q}, iq_n) = -\frac{1}{N\beta}\sum_{\mathbf{k}, i\omega_n} \mathrm{Tr}\left\{\sum_{a,b} G^{(a)}(\mathbf{k}, i\omega_n)G^{(b)}(\mathbf{k}+\mathbf{q}, i\omega_n+iq_n)\left|u_{\mathbf{k}}^{(a)}\right\rangle\left\langle u_{\mathbf{k}}^{(a)}\middle|u_{\mathbf{k}+\mathbf{q}}^{(b)}\right\rangle\left\langle u_{\mathbf{k}+\mathbf{q}}^{(b)}\right|\right\}. \tag{4.17}$$

Performing the Matsubara sum, the previous expression can be written as

$$\chi^{\mathrm{FM}}(\mathbf{q}, iq_n) = -\frac{1}{N}\sum_{\mathbf{k},a,b}\left|\left\langle u_{\mathbf{k}}^{(a)}\middle|u_{\mathbf{k}+\mathbf{q}}^{(b)}\right\rangle\right|^2 \frac{f\left(E_{\mathbf{k}}^{(a)}\right) - f\left(E_{\mathbf{k}+\mathbf{q}}^{(b)}\right)}{iq_n + E_{\mathbf{k}}^{(a)} - E_{\mathbf{k}+\mathbf{q}}^{(b)}}. \tag{4.18}$$

Focusing on the uniform static susceptibility ($\mathbf{q} \to 0, iq_n \to 0$), $\left\langle u_{\mathbf{k}}^{(a)} \middle| u_{\mathbf{k}}^{(b)} \right\rangle = \delta_{ab}$, we obtain that it only contains intra-band terms,

$$\chi^{\mathrm{FM}}(0) = -\frac{1}{N}\sum_{\mathbf{k}}\left\{ \left.\frac{df(\varepsilon)}{d\varepsilon}\right|_{\varepsilon=E_{\mathbf{k}}^{(+)}} + \left.\frac{df(\varepsilon)}{d\varepsilon}\right|_{\varepsilon=E_{\mathbf{k}}^{(-)}} \right\}. \tag{4.19}$$

Motivated by the form of the altermagnetic order parameter introduced in the general model in Eq. (4.1) and noticing that it couples to the τ_z matrix in sublattice space, let us introduce an analogous expression for the susceptibility in the altermagnetic channel,

$$\chi^{\mathrm{AM}}(\mathbf{q}, iq_n) = -\frac{1}{N}\int_0^\beta e^{iq_n\tau}\langle T_\tau \tilde{S}_{\mathbf{q}}(\tau)\tilde{S}_{-\mathbf{q}}(0)\rangle, \tag{4.20}$$

where now the operator $\tilde{S}_{\mathbf{q}}$ is given by

$$\tilde{S}_{\mathbf{q}} = \sum_{\mathbf{k}} \Psi^\dagger_{\mathbf{k}+\mathbf{q}}\tau_z\Psi_{\mathbf{k}}. \tag{4.21}$$

The susceptibility in the band basis now has the following form,

$$\chi^{\mathrm{AM}}(\mathbf{q}, iq_n) = -\frac{1}{N\beta}\sum_{\mathbf{k}, i\omega_n} \mathrm{Tr}\{G(\mathbf{k}, i\omega_n)\tau_z G(\mathbf{k}+\mathbf{q}, i\omega_n + iq_n)\tau_z\}. \tag{4.22}$$

Inserting the Green's functions projected onto the band basis,

$$\chi^{\mathrm{AM}}(\mathbf{q}, iq_n) = -\frac{1}{N\beta}\sum_{\mathbf{k}, i\omega_n} \mathrm{Tr}\left\{ \sum_{a,b} G^{(a)}(\mathbf{k}, i\omega_n)G^{(b)}(\mathbf{k}+\mathbf{q}, i\omega_n+iq_n) \left|u_{\mathbf{k}}^{(a)}\right\rangle \left\langle u_{\mathbf{k}}^{(a)}\right| \tau_z \left|u_{\mathbf{k}+\mathbf{q}}^{(b)}\right\rangle \left\langle u_{\mathbf{k}+\mathbf{q}}^{(b)}\right| \tau_z \right\}, \tag{4.23}$$

we obtain a similar result to the ferromagnetic channel in Eq. (4.18),

$$\chi^{\mathrm{AM}}(\mathbf{q}, iq_n) = -\frac{1}{N}\sum_{\mathbf{k},a,b} \left|\left\langle u_{\mathbf{k}}^{(a)}\right| \tau_z \left|u_{\mathbf{k}+\mathbf{q}}^{(b)}\right\rangle\right|^2 \frac{f\left(E_{\mathbf{k}}^{(a)}\right) - f\left(E_{\mathbf{k}+\mathbf{q}}^{(b)}\right)}{iq_n + E_{\mathbf{k}}^{(a)} - E_{\mathbf{k}+\mathbf{q}}^{(b)}}. \tag{4.24}$$

Using the transformation matrix given in Eq. (4.11), we can obtain the form of τ_z in the band basis,

$$U^\dagger(\mathbf{k})\tau_z U(\mathbf{k}) = \begin{pmatrix} \cos\theta_{\mathbf{k}} & \sin\theta_{\mathbf{k}} \\ \sin\theta_{\mathbf{k}} & -\cos\theta_{\mathbf{k}} \end{pmatrix}. \tag{4.25}$$

Thus, in the limit $\mathbf{q} \to 0, iq_n \to 0$, the altermagnetic susceptibility corresponds to

$$\chi^{\mathrm{AM}}(0) = -\frac{1}{N}\sum_{\mathbf{k}}\left\{ \cos^2\theta_{\mathbf{k}}\left[\left.\frac{df(\varepsilon)}{d\varepsilon}\right|_{\varepsilon=E_{\mathbf{k}}^{(+)}} + \left.\frac{df(\varepsilon)}{d\varepsilon}\right|_{\varepsilon=E_{\mathbf{k}}^{(-)}} \right] + \sin^2\theta_{\mathbf{k}}\frac{2\left[f\left(E_{\mathbf{k}}^{(-)}\right) - f\left(E_{\mathbf{k}}^{(+)}\right)\right]}{E_{\mathbf{k}}^{(-)} - E_{\mathbf{k}}^{(+)}} \right\}. \tag{4.26}$$

To directly compare both susceptibilities, this expression can be rewritten as

$$\chi^{\mathrm{AM}}(0) = \chi^{\mathrm{FM}}(0) - \frac{1}{N}\sum_{\mathbf{k}}\sin^2\theta_{\mathbf{k}}\left\{ \frac{2\left[f\left(E_{\mathbf{k}}^{(-)}\right) - f\left(E_{\mathbf{k}}^{(+)}\right)\right]}{E_{\mathbf{k}}^{(-)} - E_{\mathbf{k}}^{(+)}} - \left[\left.\frac{df(\varepsilon)}{d\varepsilon}\right|_{\varepsilon=E_{\mathbf{k}}^{(+)}} + \left.\frac{df(\varepsilon)}{d\varepsilon}\right|_{\varepsilon=E_{\mathbf{k}}^{(-)}} \right] \right\}. \tag{4.27}$$

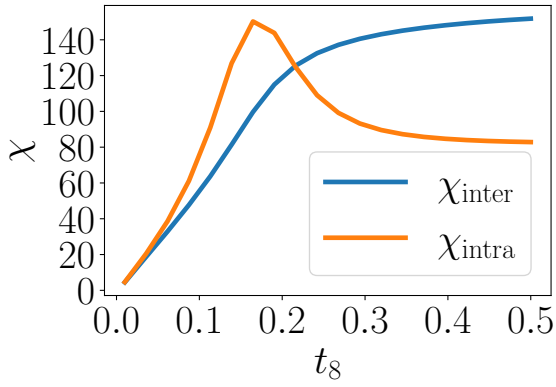

Figure 4.8: Intra-band (χ_{intra}) and inter-band (χ_{inter}) susceptibilities as a function of the hopping t_8, which enters in the minimal model in Eq. (4.1) through Eq. (4.7), considering the one-orbital RuO_2 normal state band structure in Fig. 4.5(a), for a temperature $k_BT = 0.02$ and a number of $\mathbf{k}$-points $N = 201^3$.

In contrast to the ferromagnetic channel, now the susceptibility has both intra-band and inter-band contributions,

$$\begin{aligned}\chi_{\text{inter}} &= -\frac{1}{N}\sum_{\mathbf{k}} \sin^2\theta_{\mathbf{k}} \frac{2\left[f\left(E^{(-)}_{\mathbf{k}}\right) - f\left(E^{(+)}_{\mathbf{k}}\right)\right]}{E^{(-)}_{\mathbf{k}} - E^{(+)}_{\mathbf{k}}}, \\ \chi_{\text{intra}} &= \frac{1}{N}\sum_{\mathbf{k}} \sin^2\theta_{\mathbf{k}} \left[\left.\frac{df(\varepsilon)}{d\varepsilon}\right|_{\varepsilon=E^{(+)}_{\mathbf{k}}} + \left.\frac{df(\varepsilon)}{d\varepsilon}\right|_{\varepsilon=E^{(-)}_{\mathbf{k}}}\right],\end{aligned} \tag{4.28}$$

where the inter-band term depends on the occupation between the two bands. Equation (4.27) reveals that the competition between intra-band and inter-band terms determines the leading instability. In particular, altermagnetism is stabilized if the inter-band contribution is larger, whereas a dominant intra-band part will give rise to ferromagnetism. For the two instabilities not to be degenerate, we need $\sin\theta_{\mathbf{k}} > 0$, which implies that we require a finite $t_{x,\mathbf{k}}$ hopping, as see from Eq. (4.12). This is typically the case since $t_{x,\mathbf{k}}$ corresponds to a nearest-neighbor hopping (see the illustration in Fig. 4.2).

In addition, Eq. (4.27) also shows that band degeneracies, corresponding to $E^{+}_{\mathbf{k}} - E^{-}_{\mathbf{k}} \to 0$, enhance the inter-band term and therefore are important in stabilizing altermagnetism. As seen from Fig. 4.5(a) and Fig. 4.7(a) for RuO_2 and MnF_2, respectively, there are such degeneracies in the band structure, in particular along the X-M and Z-R-A directions. This is in agreement with previous works that identified hot spots on the Brillouin zone boundary driving the altermagnetic phase in RuO_2 [190, 199].

In Fig. 4.8 we show the inter-band and intra-band susceptibilities as a function of the t_8 hopping for RuO_2, see Eq. (4.7), which are calculated from Eq. (4.28) using the minimal model in Eq. (4.1) taking Eqs. (4.6)-(4.7), with the band structure shown in Fig. 4.5(a). As seen, the inter-band term dominates when the inter-sublattice hopping $t_{x,\mathbf{k}}$ in the minimal model is sufficiently large.

4.5 Comparison of symmorphic versus non-symmorphic space groups

The analytic expressions of the susceptibility have revealed that band degeneracies play an important role in stabilizing altermagnetism, as they enhance the inter-band term in Eq. (4.28). In this section, motivated by the fact that most altermagnetic candidates identified in Ref. [198] belong to non-symmorphic space groups (see Sec. 4.2), which have symmetry-enforced band degeneracies on the Brillouin zone boundary [147], we would like to elucidate on the importance of these degeneracies by comparing the susceptibility for a symmorphic and a non-symmorphic space group.

For concreteness, let us focus on two-dimensional models for the space group (SG) 136 (non-symmorphic) and SG 123 (symmorphic). For the former, we consider Wyckoff position 2a, which has already been introduced in Sec. 4.3 since it is relevant for RuO_2 and MnF_2. In this case, the two-dimensional model can be written as

$$\begin{aligned} H_{\mathrm{2D}}^{\mathrm{SG136}} &= t_1(\cos k_x + \cos k_y) + t_2 \cos k_x \cos k_y - \mu \\ &\quad + t_3 \cos\frac{k_x}{2}\cos\frac{k_y}{2}\tau_x + t_4 \sin k_x \sin k_y \tau_z. \end{aligned} \tag{4.29}$$

The hoppings are illustrated in Fig. E.1 of Appendix E.

For the symmorphic case, we consider SG 123 with Wyckoff position 2e, which corresponds to $(0, 1/2)$ and $(1/2, 0)$, and has also point group D_{4h}. For this Wyckoff position, taking the origin at $(0, 0)$ we can identify that τ_y and τ_z belong to the B_{1g} irrep of D_{4h}, since the two sublattices are exchanged by the rotations C_{4z} and C_2'' (around the diagonal $x = y$ axis). Thus, the two-dimensional minimal model is now given by

$$\begin{aligned} H_{\mathrm{2D}}^{\mathrm{SG123}} &= t_1(\cos k_x + \cos k_y) + t_2 \cos k_x \cos k_y - \mu \\ &\quad + t_3 \cos\frac{k_x}{2}\cos\frac{k_y}{2}\tau_x + t_4(\cos k_x - \cos k_y)\tau_z. \end{aligned} \tag{4.30}$$

In Figs. 4.9(a) and (c) we show the normal-state band structure for the non-symmorphic SG 136 and the symmorphic SG 123, respectively. The bands are inspired by the RuO_2 case in Appendix E, where we construct a two-dimensional minimal model. The normal-state bands already demonstrate a crucial difference: the $t_4(\cos k_x - \cos k_y)$ term in Eq. (4.30) splits the band degeneracy at the Brillouin zone boundary and there is only a degeneracy at the M-point, in contrast to the model for SG 136 in Eq. (4.29), which shows a band degeneracy along the X-M direction. The bands in the altermagnetic state shown in Figs. 4.9(b) and (d) also display a completely different spin splitting due to the different symmetry of the $t_{z,\mathbf{k}}$ hopping.

In Fig. 4.9(e) we compare the bare altermagnetic susceptibility for both space groups. Notably, the altermagnetic susceptibility for SG 136 (non-symmorphic) is significantly larger when compared to SG 123 (symmorphic). This result seems to indicate that, in agreement with the prediction from the analytic expression for the altermagnetic susceptibility in Eq. (4.27), band degeneracies are important for stabilizing altermagnetism. In addition, this gives insight into why the majority of altermagnetic material candidates identified in Ref. [198] have non-symmorphic space groups.

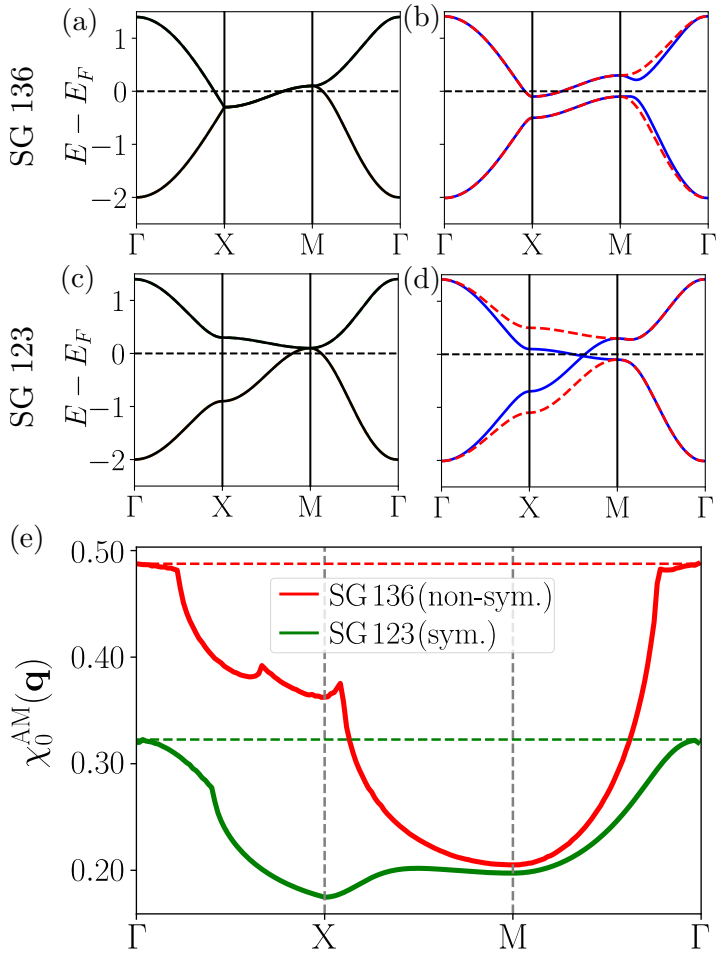

Figure 4.9: Band structure for a two-dimensional model for space group 136 (non-symmorphic, see Eq. (4.29)) and space group 123 (symmorphic, see Eq. (4.30)) in (a),(c) the normal, and (b),(d) the altermagnetic state, with $J_z = 0.2$. The hopping parameters in both cases are $\{t_1, t_2, t_3, t_4, \mu\} = \{-0.1, 0.1, 1.7, 0.3, 0.2\}$. (e) Comparison of the bare altermagnetic susceptibility for both space groups, with $k_B T = 10^{-4}$ and $N = 1200^2$.

4.6 Stabilization of altermagnetism

In the previous section, we analyzed the bare susceptibilities and the competition between ferromagnetic and altermagnetic instabilities. The purpose now is to verify that indeed the minimal models stabilize altermagnetism, focusing again on the one-orbital case and neglecting spin-orbit coupling. To do so, we use both the random phase approximation (RPA) and self-consistent Hartree-Fock calculations. We consider the Hamiltonian in Eq. (4.10) and introduce an intra-orbital Coulomb interaction,

$$H_{\mathrm{int}} = U \sum_{\mathbf{i},\mu} n_{\mathbf{i},\mu\uparrow} n_{\mathbf{i},\mu\downarrow}, \tag{4.31}$$

where μ corresponds to the sublattice index. The effect of the on-site Coulomb interaction has also been studied in Ref. [8], showing that it is sufficient to give rise to altermagnetism.

In the case of multiple sublattices, the RPA susceptibility can be generalized to [18, 30, 229, 230]

$$[\chi_{\mathrm{RPA}}(\mathbf{q}, iq_n)]^{\mu_1,\mu_2}_{\mu_3,\mu_4} = \Big[\chi_0(\mathbf{q}, iq_n)\big(\mathbb{1} - U\chi_0(\mathbf{q}, iq_n)\big)^{-1}\Big]^{\mu_1,\mu_2}_{\mu_3,\mu_4}, \tag{4.32}$$

with $[U]^{\mu_1,\mu_2}_{\mu_3,\mu_4}$ corresponding to a matrix in sublattice space including only interactions within the same sublattices,

$$[U]^{\mu_1,\mu_2}_{\mu_3,\mu_4} = U \quad \text{for} \quad \mu_1 = \mu_2 = \mu_3 = \mu_4, \tag{4.33}$$

and the bare susceptibility matrix

$$[\chi_0(\mathbf{q}, iq_n)]^{\mu_1,\mu_2}_{\mu_3,\mu_4} = -\frac{1}{N\beta}\sum_{\mathbf{k}, i\omega_n} G^{(0)}_{\mu_1\mu_3}(\mathbf{k}+\mathbf{q}, i\omega_n + iq_n) G^{(0)}_{\mu_2\mu_4}(\mathbf{k}, i\omega_n). \tag{4.34}$$

As detailed in Chapter 1, we construct the matrix elements combining the sublattice indices as $A_{\mu_1+\mu_2 D, \mu_3+\mu_4 D} = [A]^{\mu_1\mu_2}_{\mu_3\mu_4}$, with $A = \{\chi_0(\mathbf{q}, iq_n), U\}$, obtaining 4×4 matrices since $D = 2$ in the case of two sublattices. We use these matrices in sublattice space to compute the matrix product in Eq. (4.32), obtaining the RPA susceptibility. The bare Green's function is calculated as

$$G^{(0)}_{\mu\nu}(\mathbf{k}, i\omega_n) = \sum_m \frac{u^{\mu}_m(\mathbf{k}) u^{\nu *}_m(\mathbf{k})}{i\omega_n - E^{(m)}_{\mathbf{k}}}, \tag{4.35}$$

with $E^{(m)}_{\mathbf{k}}$ being the eigenvalue for band m of the Hamiltonian $H'(\mathbf{k})$ in Eq. (4.10), and $u^{\mu}_m(\mathbf{k})$ the eigenvector transforming from sublattice (μ) to band space (m).

The physical spin susceptibility can then be obtained as the sum over the two sublattices,

$$\chi^{\mathrm{FM}}_{\mathrm{RPA}}(\mathbf{q}, \omega) = \sum_{\mu,\nu}[\chi_{\mathrm{RPA}}(\mathbf{q}, iq_n \to \omega + i\eta)]^{\mu,\mu}_{\nu,\nu}. \tag{4.36}$$

Following the notation introduced in the previous section, we again denote this as the ferromagnetic channel since this susceptibility diverges at $\mathbf{q} \to 0$ close to a ferromagnetic instability. Similarly, we also introduce the susceptibility in the altermagnetic channel as

$$\chi^{\mathrm{AM}}_{\mathrm{RPA}}(\mathbf{q}, \omega) = \sum_{\mu,\nu}(-1)^{\mu}(-1)^{\nu}[\chi_{\mathrm{RPA}}(\mathbf{q}, iq_n \to \omega + i\eta)]^{\mu,\mu}_{\nu,\nu}, \tag{4.37}$$

where the minus signs arise due to the projection of the physical spin susceptibility in Eq. (4.34) to the τ_z channel, since the altermagnetic order parameter couples to τ_z in the minimal model in Eq. (4.1). The altermagnetic phase dominates if $\chi^{\mathrm{AM}}_{\mathrm{RPA}}$ diverges before the usual spin susceptibility $\chi^{\mathrm{FM}}_{\mathrm{RPA}}$ does, whereas the opposite result would indicate that ferromagnetism or a spin-density wave phase is favored.

In Figs. 4.10(a)-(d) and Figs. 4.10(f)-(i) we show the bare and RPA susceptibilities in the ferromagnetic and altermagnetic channels considering the one-orbital minimal model relevant for MnF_2 and RuO_2, with the band structures shown in Fig. 4.7(a) and Fig. 4.5(a), respectively. The RPA susceptibilities show a leading altermagnetic instability which diverges at $\mathbf{q} \to 0$ at the critical U for both minimal models. In addition, the bare and RPA susceptibilities display the same momentum dependence. As a consequence, this shows that the discussion in Sec. 4.4 on the competition between both phases and the mechanisms stabilizing altermagnetism over ferromagnetism also applies in this case.

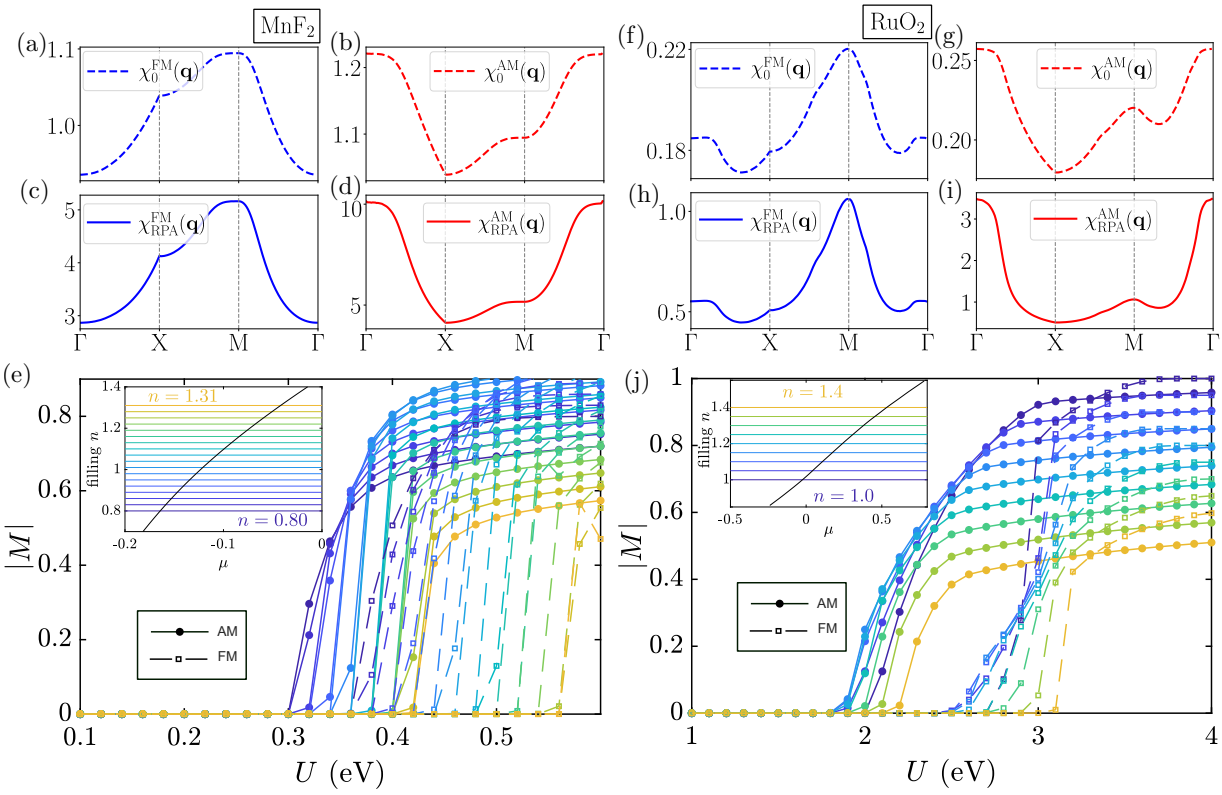

Figure 4.10: Bare and RPA susceptibilities in the ferromagnetic and altermagnetic channels (see Eqs. (4.36)-(4.37)) (a)-(d) for MnF_2, with the band structure shown in Fig. 4.7(a) and $U = 0.36$; and (f)-(i) for RuO_2, considering the one-orbital minimal model bands shown in Fig. 4.5(a) and $U = 1.8$. We take $k_BT = 0.02$ and $N = 60^3$ in both cases. (e),(j) Hartree-Fock calculation considering the Hamiltonian in Eq. (4.38) for an altermagnetic and ferromagnetic order parameters as a function of the Hubbard interaction at different fillings n, using the band structures for MnF_2 and RuO_2, respectively, with $k_BT = 0.02$ and $N = 40^3$.

To further verify that the altermagnetic phase is stabilized before the ferromagnetic phase, we have also solved the Hartree-Fock self-consistent equations for both order parameters. With this purpose, we perform a mean-field decoupling of the intra-sublattice Coulomb interactions,

$$H_{\mathrm{MF}}(\mathbf{k}) = \varepsilon_{0,\mathbf{k}} + t_{x,\mathbf{k}}\tau_x + t_{z,\mathbf{k}}\tau_z + U \sum_{\mathbf{i},\mu,\sigma} \langle n_{\mathbf{i},\mu,\sigma}\rangle n_{\mathbf{i},\mu,\bar{\sigma}}, \tag{4.38}$$

where we have used that $n_{\mathbf{i},\mu,\sigma} \to \langle n_{\mathbf{i},\mu,\sigma}\rangle + \delta n_{\mathbf{i},\mu,\sigma}$, keeping only terms that contain two fermionic operators. We calculate the expectation value $\langle n_{\mathbf{i},\mu,\sigma}\rangle$ self-consistently by using the eigenvalues and eigenvectors of $H_{\mathrm{MF}}(\mathbf{k})$, updating the mean-fields and chemical potential at each iteration and fixing the number of electrons. To determine if a phase is stabilized, we calculate the order parameter $|M| = \sum_\mu |\langle n_{\mu,\uparrow}\rangle - \langle n_{\mu,\downarrow}\rangle|$ initializing with a certain magnetic phase. Figures 4.10(e) and (j) show the order parameter for MnF_2 and RuO_2, respectively, as a function of the interaction strength U. As seen, both ferromagnetic and altermagnetic order parameters can be stabilized, but the altermagnetic phase has a lower critical U, indicating that this is the leading instability, in agreement with the RPA susceptibilities. This result is robust as a function of filling variations,

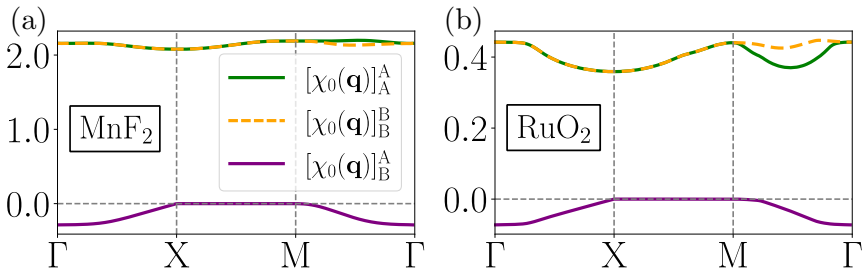

Figure 4.11: Intra- and inter-sublattice components of the bare susceptibility in Eq. (4.34) for the one-orbital minimal model bands relevant for (a) MnF_2 (see Fig 4.7(a)) and (b) RuO_2 (see Fig 4.5(a)), with $k_BT = 0.02$ and $N = 60^3$.

which correspond to the different colors specified in the insets.

Finally, we can compare the expressions for the susceptibility in the ferromagnetic channel and the altermagnetic channel in Eqs. (4.36)-(4.37), considering the two sublattices $\mu, \nu = \{A, B\}$,

$$\begin{aligned}\chi_0^{\mathrm{FM}}(\mathbf{q},\omega) &= [\chi_0(\mathbf{q},\omega)]^{A,A}_{A,A} + [\chi_0(\mathbf{q},\omega)]^{B,B}_{B,B} + [\chi_0(\mathbf{q},\omega)]^{A,A}_{B,B} + [\chi_0(\mathbf{q},\omega)]^{B,B}_{A,A},\\ \chi_0^{\mathrm{AM}}(\mathbf{q},\omega) &= [\chi_0(\mathbf{q},\omega)]^{A,A}_{A,A} + [\chi_0(\mathbf{q},\omega)]^{B,B}_{B,B} - [\chi_0(\mathbf{q},\omega)]^{A,A}_{B,B} - [\chi_0(\mathbf{q},\omega)]^{B,B}_{A,A}.\end{aligned} \tag{4.39}$$

This reveals that the altermagnetic instability dominates when the inter-sublattice components of the susceptibility become negative. Figure 4.11 shows the intra- and inter-sublattice components for the one-orbital minimal models for MnF_2 and RuO_2 (shown in Fig. 4.7(a) and Fig. 4.5(a), respectively), where the RPA and Hartree-Fock results in Fig. 4.10 predict a leading altermagnetic instability. Notably, the inter-sublattice components become negative along the Γ-X and M-Γ lines, with $[\chi_0(\mathbf{q})]^A_B = [\chi_0(\mathbf{q})]^B_A$. On the contrary, for band structures where ferromagnetism is the leading instability, the inter-sublattice components become positive in the same directions (not shown). In addition, Fig. 4.11 also shows a splitting of the intra-sublattice components $[\chi_0(\mathbf{q})]^A_A$ and $[\chi_0(\mathbf{q})]^B_B$ in the M-Γ direction, which is reversed in the orthogonal direction, M′-Γ, with $\mathrm{M} = (\pi, \pi, 0)$ and $\mathrm{M}' = (-\pi, \pi, 0)$. This is in agreement with the symmetry of the altermagnetic spin splitting.

4.7 Berry curvature and crystal Hall effect

In this section, we consider the general one-orbital minimal model in Eq. (4.1) and include SOC to derive an analytic expression for the Berry curvature in the four-band model. Previous works solved the four-band case numerically [191] or obtained and effective two-band Hamiltonian in the large J limit [27, 231]. In contrast, we derive an analytic expression using the results of Ref. [232], which describes an approach to calculate the Berry curvature based on obtaining a projector operator. Thus, it does not require calculating the eigenstates, and in general can be constructed for an N-band case.

Specifically, in Ref. [232] they provide an expression for the quantum geometric tensor

$$T^{(n)}_{ij} = \mathrm{Tr}\Big\{\Big(\partial_i P^{(n)}\Big)\Big(1 - P^{(n)}\Big)\Big(\partial_j P^{(n)}\Big)\Big\}, \tag{4.40}$$

where $P^{(n)} = \left|\psi^{(n)}\right\rangle\left\langle\psi^{(n)}\right|$ is the projection operator to band n. The Berry curvature is antisymmetric in the indices ij, and can be obtained as

$$\Omega_{ij}^{(\alpha)} = -\mathrm{Im}\Big[\,\mathrm{Tr}\Big\{\Big(\partial_i P^{(\alpha)}\Big)\Big(1-P^{(\alpha)}\Big)\Big(\partial_j P^{(\alpha)}\Big)\Big\} - \{i\leftrightarrow j\}\Big]. \tag{4.41}$$

In this approach, to solve analytically for the Berry curvature we must find the expression for the projector operator using our tight-binding Hamiltonian. In the four-band case, the expression for the projector operator is given by [232]

$$\begin{aligned} P_{\mathbf{k}}^{(n)} =& \frac{1}{4\big(E_{\mathbf{k}}^{(n)}\big)^2 - C_{\mathbf{k}}^{(2)}E_{\mathbf{k}}^{(n)} - \frac{C_{\mathbf{k}}^{(3)}}{3}}\Bigg[\left(\big(E_{\mathbf{k}}^{(n)}\big)^3 - \frac{C_{\mathbf{k}}^{(2)}}{2}E_{\mathbf{k}}^{(n)} - \frac{C_{\mathbf{k}}^{(3)}}{3}\right)\mathbb{1}_4 \\ &+\left(\big(E_{\mathbf{k}}^{(n)}\big)^2 - \frac{C_{\mathbf{k}}^{(2)}}{2}\right)H(\mathbf{k}) + E_{\mathbf{k}}^{(n)}H(\mathbf{k})^2 + H(\mathbf{k})^3\Bigg], \end{aligned} \tag{4.42}$$

where $E_{\mathbf{k}}^{(n)}$ is the eigenenergy for band n of the Hamiltonian $H(\mathbf{k})$, and $C_{\mathbf{k}}^{(l)} = \sum_n \big(E_{\mathbf{k}}^{(n)}\big)^l$ correspond to the Casimir invariants.

Before finding the explicit expression for the projector from our minimal model, we can get some insight on the Berry curvature by writing it in the common form

$$\Omega_{ij}^{(n)} = \mathrm{Im}\sum_{p\neq n}\left[\frac{\langle n|\,\partial_{k_i}H(\mathbf{k})\,|p\rangle\,\langle p|\,\partial_{k_j}H(\mathbf{k})\,|n\rangle}{\Big(E_{\mathbf{k}}^{(p)} - E_{\mathbf{k}}^{(n)}\Big)^2} - \{k_i\leftrightarrow k_j\}\right]. \tag{4.43}$$

This expression shows that the Berry curvature does not depend on the $\varepsilon_{0,\mathbf{k}}\mathbb{1}_{4\times4}$ term in the minimal model in Eq. (4.1). More importantly, it explicitly shows that the Berry curvature is large in the presence of band degeneracies, $\Big(E_{\mathbf{k}}^{(p)} - E_{\mathbf{k}}^{(n)}\Big) \to 0$, which precisely favor the altermagnetic instability, as discussed in Sec. 4.4.

We fix the altermagnetic moments in-plane, $\vec{J} = (J,0,0)$, consistent with previous observations in RuO_2 [208], and allow for all directions of the SOC $\lambda_{\mathbf{k}}$. Thus, the minimal model in Eq. (4.1) corresponds to

$$H(\mathbf{k}) = t_{x,\mathbf{k}}\tau_x + t_{z,\mathbf{k}}\tau_z + \tau_y\vec{\lambda}_{\mathbf{k}}\cdot\vec{\sigma} + J\tau_z\sigma_x, \tag{4.44}$$

with the eigenenergies given by

$$E_{\mathbf{k}}^{(\alpha=\pm,\beta=\pm)} = \alpha\Big(J^2 + t_{x,\mathbf{k}}^2 + t_{z,\mathbf{k}}^2 + \vec{\lambda}_{\mathbf{k}}^2 + \beta\,2J\sqrt{t_{z,\mathbf{k}}^2 + \lambda_{y,\mathbf{k}}^2 + \lambda_{z,\mathbf{k}}^2}\Big)^{1/2}. \tag{4.45}$$

Hence, for the minimal model we can label the bands by (α,β) indices. Using this form for the spectrum, we can see that

$$\begin{aligned} C_{\mathbf{k}}^{(2)} &= 4(J^2 + t_{x,\mathbf{k}}^2 + t_{z,\mathbf{k}}^2 + \lambda_{x,\mathbf{k}}^2 + \lambda_{y,\mathbf{k}}^2 + \lambda_{z,\mathbf{k}}^2), \\ C_{\mathbf{k}}^{(3)} &= 0, \end{aligned} \tag{4.46}$$

and therefore the projection operator in Eq. (4.42) in this case is

$$\begin{aligned} P_{\mathbf{k}}^{(\alpha,\beta)} =& \frac{1}{4\big(E_{\mathbf{k}}^{(\alpha,\beta)}\big)^2 - C_{\mathbf{k}}^{(2)}E_{\mathbf{k}}^{(\alpha,\beta)}}\Bigg[\left(\big(E_{\mathbf{k}}^{(\alpha,\beta)}\big)^2 - \frac{C_{\mathbf{k}}^{(2)}}{2}\right)E_{\mathbf{k}}^{(\alpha,\beta)}\mathbb{1}_4 \\ &+\left(\big(E_{\mathbf{k}}^{(\alpha,\beta)}\big)^2 - \frac{C_{\mathbf{k}}^{(2)}}{2}\right)H(\mathbf{k}) + E_{\mathbf{k}}^{(\alpha,\beta)}H(\mathbf{k})^2 + H(\mathbf{k})^3\Bigg]. \end{aligned} \tag{4.47}$$

Using that $H(\mathbf{k})^2$ can be written as

$$H(\mathbf{k})^2 = \frac{1}{4}C_{\mathbf{k}}^{(2)}\mathbb{1}_4 + 2J\widetilde{H}(\mathbf{k}), \tag{4.48}$$

with $\widetilde{H}(\mathbf{k}) = t_{z,\mathbf{k}}\sigma_x + \lambda_{y,\mathbf{k}}\tau_x\sigma_z - \lambda_{z,\mathbf{k}}\tau_x\sigma_y$, the projector can be simplified to

$$P_{\mathbf{k}}^{(\alpha,\beta)} = \frac{1}{4}\left[\mathbb{1}_4 + \frac{\widetilde{H}(\mathbf{k})}{\widetilde{E}_{\mathbf{k}}^{(\beta)}}\right]\left[\mathbb{1}_4 + \frac{H(\mathbf{k})}{E_{\mathbf{k}}^{(\alpha,\beta)}}\right], \tag{4.49}$$

with $\widetilde{E}_{\mathbf{k}}^{(\beta=\pm)} = \beta\sqrt{t_{z,\mathbf{k}}^2 + \lambda_{z,\mathbf{k}}^2 + \lambda_{y,\mathbf{k}}^2}$ being the eigenvalues of $\widetilde{H}(\mathbf{k})$.

Replacing the previous expression for the projector operator in Eq. (4.41), we can calculate the Berry curvature. When the SOC has the same spin direction as the altermagnetic order parameter, we find a term linear in the SOC,

$$\Omega_{ij}^{(\alpha,\beta)} = \frac{1}{\left(E_{\mathbf{k}}^{(\alpha,\beta)}\right)^3}\sum_{m,n=i,j}\varepsilon_{mn}\Big[(J+\beta t_{z,\mathbf{k}})\partial_m\lambda_{x,\mathbf{k}}\partial_n t_{x,\mathbf{k}} + \beta\, t_{x,\mathbf{k}}\partial_m t_{z,\mathbf{k}}\partial_n\lambda_{x,\mathbf{k}} + \beta\,\lambda_{x,\mathbf{k}}\partial_m t_{x,\mathbf{k}}\partial_n t_{z,\mathbf{k}}\Big], \tag{4.50}$$

where ε_{mn} is the antisymmetric tensor, so that it is antisymmetric in the indices i, j. Therefore, we find a Berry curvature that is linear in the SOC, as opposed to previous minimal models that found a quadratic behavior [191, 231]. Consequently, this result could naturally explain the large anomalous Hall effect observed in altermagnets [208, 209], since SOC is expected to be weak in these materials [26]. Note that so far we have not replaced explicit expressions for the hoppings and the SOC, and thus Eq. (4.50) is general and relevant for any system with the minimal model in Eq. (4.44).

4.7.1 Application to RuO_2

In the previous section, we provided a general analytic expression for the Berry curvature which is linear in the SOC. Let us now use the specific form for the hoppings and SOC in the tetragonal space group 136, which is relevant for RuO_2. In order to compare with previous works reporting anomalous Hall effect [191, 208], we calculate the Hall conductivity σ_{ij}, given by the integral over the Brillouin zone of the filled bands of the Berry curvature,

$$\sigma_{ij} = -\frac{e^2}{\hbar}\int_{\mathrm{BZ}}\frac{d\mathbf{k}}{(2\pi)^3}\sum_n f_n(\mathbf{k})\Omega_{ij}^{(n)}, \tag{4.51}$$

where $f_n(\mathbf{k})$ is the Fermi-Dirac distribution for band n. In this space group, the altermagnetic order parameter $\tau_z\sigma_x$ breaks the mirror symmetries M_x and M_z. As a consequence, there can be a non-vanishing Hall conductivity σ_{xz} [191, 206].

Recalling the form for the minimal model in Eqs. (4.5) and (4.7), we repeat here for convenience the relevant terms entering in Eq. (4.50),

$$\begin{cases} t_{x,\mathbf{k}} = t_8\cos\frac{k_x}{2}\cos\frac{k_y}{2}\cos\frac{k_z}{2}, \\ t_{z,\mathbf{k}} = t_6\sin k_x\sin k_y + t_7\sin k_x\sin k_y\cos k_z, \\ \lambda_{x,\mathbf{k}} = \lambda\sin\frac{k_x}{2}\cos\frac{k_y}{2}\sin\frac{k_z}{2}. \end{cases} \tag{4.52}$$

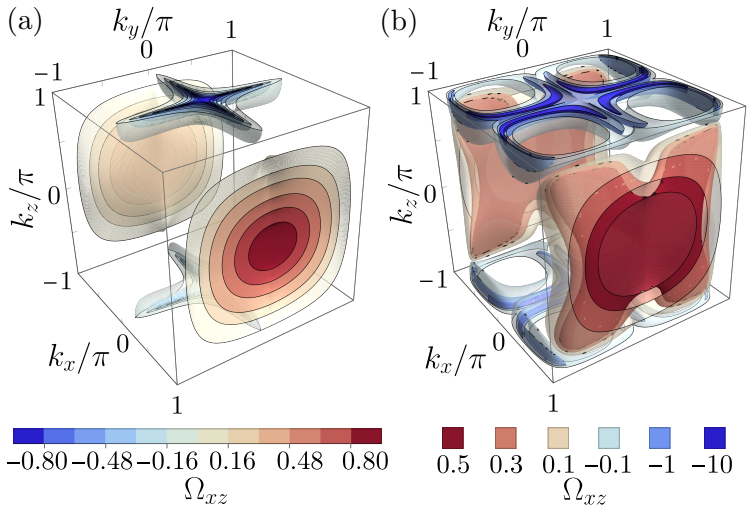

Figure 4.12: Three-dimensional Berry curvature obtained from Eq. (4.54) with (a) $\alpha = +$ and $\beta = +$ and (b) $\alpha = +$ and $\beta = -$, for the one-orbital minimal model band structure relevant for RuO_2 shown in Fig. 4.5(a), with hopping parameters detailed in Table 4.1. We take $J = 0.2$ and $\lambda = 0.1$ based on relativistic DFT calculations [4]. For $\alpha = -$ the same plots are obtained with the colors reversed due to inversion symmetry.

Therefore, the Berry curvature corresponds to

$$\begin{aligned}\Omega_{xz}^{(\alpha,\beta)} =& \frac{1}{16}\frac{1}{\left(E_{\mathbf{k}}^{(\alpha,\beta)}\right)^3}\lambda t_8 \cos^2\left(\frac{k_y}{2}\right)\Big[2J(\cos k_z - \cos k_x) \\ &+ \beta \sin k_x \sin k_y\big\{2\cos k_x(t_7 \cos k_z + t_6) + 2t_6 \cos k_z - t_7(\cos(2k_z) - 3)\big\}\Big].\end{aligned} \tag{4.53}$$

When performing the $\mathbf{k}$ integral to obtain the conductivity, the second line will vanish since it is proportional to $\sin k_x \sin k_y$. Therefore, we consider only the first term,

$$\Omega_{xz}^{(\alpha,\beta)} = \frac{1}{8\left(E_{\mathbf{k}}^{(\alpha,\beta)}\right)^3}\lambda t_8 J \cos^2\left(\frac{k_y}{2}\right)(\cos k_z - \cos k_x), \tag{4.54}$$

which in general gives rise to a finite Hall conductivity.

The Berry curvature in Eq. (4.54) is shown in Fig. 4.12 for (a) $\alpha = +$ and $\beta = +$, and (b) $\alpha = +$ and $\beta = -$ bands, considering the one-orbital minimal model normal-state bands relevant for RuO_2 shown in Fig. 4.5, with the specific hopping parameters detailed in Table 4.1. We have estimated a realistic strength for the altermagnetic order parameter and SOC from DFT calculations [4, 190]. As expected from Eq. (4.43), Fig. 4.12(a) shows that the Berry curvature is large at the nodal planes X-M and Z-R, as seen from the band degeneracies in Fig. 4.5(a). However, due to the $\mathbf{k}$ dependence in Eq. (4.54), the Berry curvature vanishes at the $k_y = \pm\pi$ plane and along the R-A direction due to the $\cos k_z - \cos k_x$ term in Eq. (4.54), although the bands also feature degeneracies.

Notably, Fig. 4.12(b) shows a much larger Berry curvature. To understand the origin of this result, we have to recall the form of the dispersion introduced in Eq. (4.45). Neglecting SOC, the dispersion reduces to $E_{\mathbf{k}}^{(\alpha=\pm,\beta=\pm)} = \alpha\sqrt{t_{x,\mathbf{k}}^2 + (J + \beta t_{z,\mathbf{k}})^2}$. When $t_{x,\mathbf{k}} = 0$, which occurs at

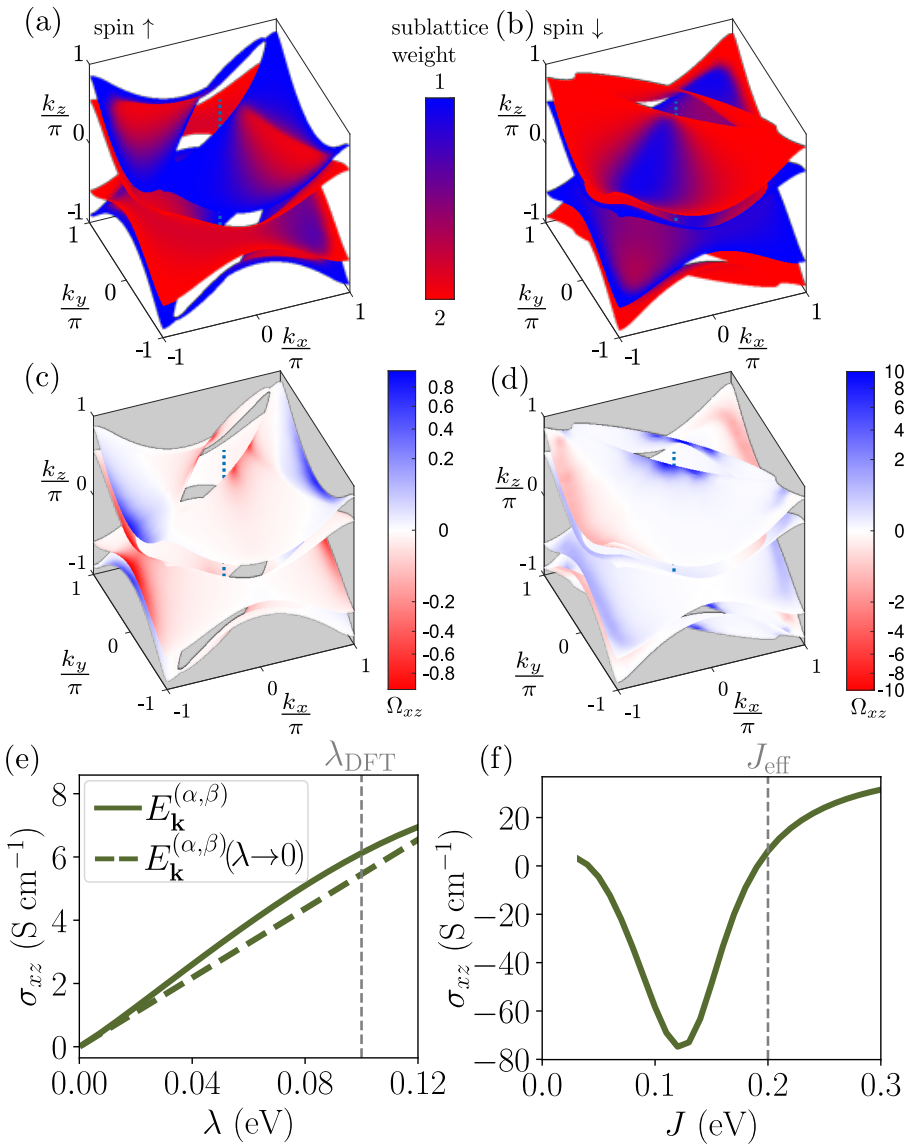

Figure 4.13: (a)-(b) Spin-up and spin-down Fermi surfaces using the one-orbital minimal model in Eq. (4.1) for the bands relevant to RuO_2 in the altermagnetic state shown in Fig. 4.5(b). The color bar denotes the sublattice weight. (c)-(d) Berry curvature shown in Fig. 4.12 projected onto the two Fermi surfaces. (e)-(f) Conductivity as a function of SOC and altermagnetic order parameter strength calculated using Eq. (4.51) for the minimal model relevant to RuO_2, with $k_BT = 0.01$. In (e) we take $J = 0.2$ and $N = 201^3$, whereas in (f) we choose $\lambda = 0.1$ and $N = 401^3$. λ_{DFT} and J_{eff} correspond to the effective parameters obtained by comparing to DFT results [4, 190]. In (e) the dashed line indicates the $\lambda \to 0$ limit, displaying a linear dependence as expected from Eq. (4.54). Non-linear contributions arise from the dependence of $E_{\mathbf{k}}^{(\alpha,\beta)}$ on the SOC (solid line).

the BZ boundaries, for $t_{z,\mathbf{k}} = \pm J$ one band is two-fold degenerate. Due to the form of the $t_{z,\mathbf{k}}$ hopping, this band degeneracy gives rise to Weyl loops on the $k_z = \pi$ face. However, the Weyl loops only appear when $|t_{z,\mathbf{k}}| > |J|$, which is the case in RuO_2, as seen from the specific hopping parameters in Table 4.1. The Weyl loops in this case survive when we add SOC, as seen from

Fig. 4.12(b), and further enhance the Berry curvature [207].

Figure 4.12 indicates the regions of the Brillouin zone that give rise to a large Berry curvature Ω_{xz} and Hall conductivity σ_{xz}, but the Fermi surface should intersect these regions to produce a large response. For this purpose, doping can be useful to move the Fermi surface to these large Berry curvature regions, as previously suggested for the altermagnetic material candidate $FeSb_2$ [193].

Using the one-orbital minimal model for RuO_2, we can plot the Fermi surface for spin up and down, as shown in Fig. 4.13(a) and (b), respectively, where the colorbar denotes the sublattice weight. Figure 4.13(c) and (d) correspond to the Berry curvature in Fig. 4.12 projected onto the two Fermi surfaces. Therefore, we can use Eq. (4.51) to calculate the Hall conductivity by integrating over the entire Brillouin zone, as seen in Fig. 4.13(e) as a function of the SOC strength. Importantly, from the minimal model we obtain a non-vanishing anomalous Hall effect, and the resulting conductivity is linear in the SOC. Non-linear contributions arise due to the dependence of $E_{\mathbf{k}}^{(\alpha,\beta)}$ on λ from Eq. (4.54). DFT results predict $\sigma_{xz} \sim 36$ S cm^{-1} for this material [191]. However, we expect contributions from other bands in RuO_2 (see Fig. 4.5). Consequently, the Berry curvature obtained from the minimal models could explain the large Hall conductivity. In addition, the conductivity exhibits a large dependence on the altermagnetic order parameter strength J, as shown in Fig. 4.13(f). Similar results have been reported for $FeSb_2$ [193], suggesting that band optimization of the order parameter J can give rise to an enhanced anomalous Hall effect.

4.8 Minimal models for other altermagnetic material candidates

In the previous sections, we have demonstrated that the minimal model introduced in Eq. (4.1) can be used to describe altermagnetic material candidates with tetragonal symmetry. Now, we want to show that it is sufficiently general and can be applied to other materials with different symmetries. First, we focus on orthorhombic systems, specifically $FeSb_2$ and the organic compound κ-Cl, and demonstrate that we also obtain a d-wave altermagnet in these cases. In addition, we use the minimal models to describe g-wave and i-wave altermagnetism in hexagonal and cubic materials, respectively.

4.8.1 $FeSb_2$

A recent DFT study has suggested that $FeSb_2$ is non-magnetic, but the doped compound could develop unconventional magnetism [193], even though it was first proposed to be ferromagnetically ordered [233]. $FeSb_2$ is an orthorhombic material with space group 58, point group D_{2h}, and Wyckoff position 2a for the Fe atoms, which corresponds to $(0,0,0)$ and $(1/2,1/2,1/2)$. Following the same discussion as for the space group 136 in Sec. 4.2, in this case the non-symmorphic operations $\{C_{2x}|\frac{1}{2}\,\frac{1}{2}\,\frac{1}{2}\}$ and $\{C_{2y}|\frac{1}{2}\,\frac{1}{2}\,\frac{1}{2}\}$ exchange the two sublattices, whereas $\{C_{2z}|0\,0\,0\}$ leaves them invariant. Hence, this implies that τ_z and τ_y belong to the B_{1g} irrep of D_{2h}.

We construct a minimal model for $d_{x^2-y^2}$-orbitals, based on Ref. [233]. Since τ_z and τ_y transform like $k_x k_y$ and we have the same Wyckoff position as in the case of space group 136

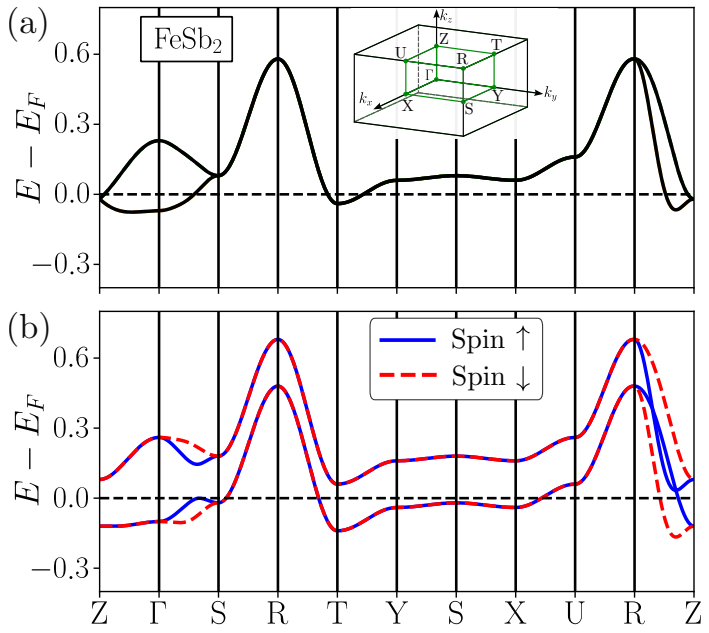

Figure 4.14: Band structure inspired by $FeSb_2$ in (a) the normal, and (b) the altermagnetic state, using the minimal model in Eq. (4.1) with Eqs. (4.7), (4.56) for the hopping parameters and $J_z = 0.1$ in (b). The tetragonal Brillouin zone is sketched in the inset. The specific values of the hopping parameters are detailed in Table 4.3.

Table 4.3: Hopping parameters for $FeSb_2$ and κ-Cl used to obtain the bands in Figs. 4.14 and 4.16, respectively, using the minimal model in Eq. (4.1) with Eqs. (4.7), (4.56) for $FeSb_2$ and Eqs. (4.57), (4.58) for κ-Cl.

Ortho.	t_{1x}	t_{1y}	t_2	t_3	t_{4x}	t_{4y}	t_5	t_6	t_7	t_8	μ
$FeSb_2$	-0.1	-0.05	-0.05	0.06	0.1	0.05	-0.05	0.05	-0.1	0.15	-0.12
κ-Cl	0.08	-0.01	-	-0.03	-	-	-	0.05	-	0.3	-0.1

(relevant for RuO_2 and MnF_2), the hoppings $t_{x,\mathbf{k}}$ and $t_{z,\mathbf{k}}$ in the minimal tight-binding model in Eq. (4.1) have the same form as in Eq. (4.7). Following a similar derivation as in Sec. 2.3, for the point group D_{2h} the spin degrees of freedom σ_x, σ_y, σ_z belong to the irreps B_{3g}, B_{2g}, B_{1g}, respectively. Thus, the form for the SOC is different and corresponds to

$$\begin{aligned}
\lambda_{x,\mathbf{k}} &= \lambda_x \sin\frac{k_x}{2}\cos\frac{k_y}{2}\sin\frac{k_z}{2},\\
\lambda_{y,\mathbf{k}} &= \lambda_y \cos\frac{k_x}{2}\sin\frac{k_y}{2}\sin\frac{k_z}{2},\\
\lambda_{z,\mathbf{k}} &= \lambda_z \cos\frac{k_x}{2}\cos\frac{k_y}{2}\cos\frac{k_z}{2}.
\end{aligned} \tag{4.55}$$

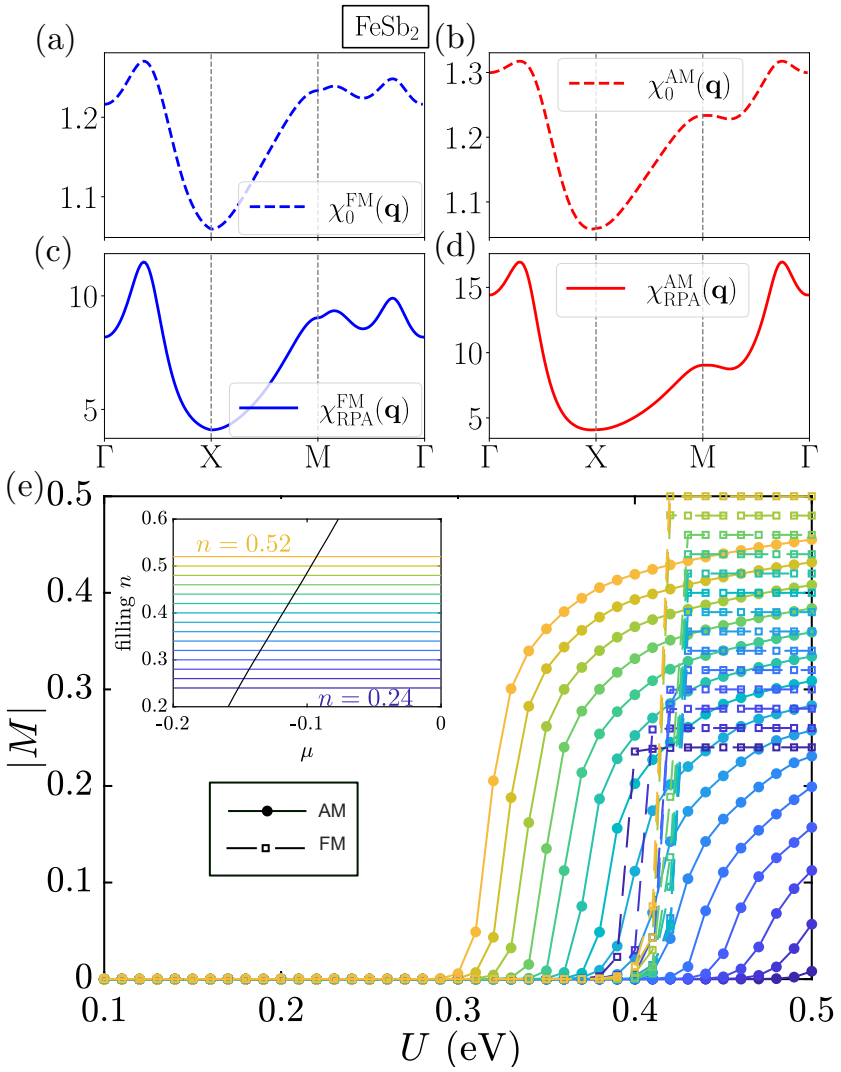

Figure 4.15: (a)-(d) Bare and RPA susceptibilities in the ferromagnetic and altermagnetic channels (see Eqs. (4.36)-(4.37)) for the bands inspired on $FeSb_2$, with the band structure shown in Fig. 4.14(a), for $U = 0.35$, $k_BT = 0.02$ and $N = 60^3$. (e) Hartree-Fock calculation using the Hamiltonian in Eq. (4.38) for an altermagnetic and ferromagnetic order parameters as a function of the Hubbard interaction at different fillings n, using the band structures for $FeSb_2$, with $k_BT = 0.002$ and $N = 40^3$.

The dispersion for this orthorhombic material also changes and is given by

$$\varepsilon_{0,\mathbf{k}} = t_{1x}\cos k_x + t_{1y}\cos k_y + t_2\cos k_z + t_3\cos k_x\cos k_y + t_{4x}\cos k_x\cos k_z + t_{4y}\cos k_y\cos k_z + t_5\cos k_x\cos k_y\cos k_z - \mu. \tag{4.56}$$

Using the previous parameters for the minimal model in Eq. (4.1), based on Refs. [193,233] we construct a single-band picture inspired on $FeSb_2$, shown in Fig. 4.14(a). The choice of hopping parameters is specified in Table 4.3, and the altermagnetic state is displayed in Fig. 4.14(b). Similarly to the previous cases, the $t_{z,\mathbf{k}}\tau_z$ term gives rise to the spin splitting along Γ-S and R-Z directions. Only for the low value of the chemical potential used in Fig. 4.14(a) we obtain a leading altermagnetic instability, as seen in Fig. 4.15(a)-(d), in agreement with Ref. [193].

Remarkably, in contrast to the previous results for RuO_2 and MnF_2 (see Fig. 4.10), Fig. 4.15(d) reveals that for $FeSb_2$ the altermagnetic susceptibility does not diverge at $\mathbf{q} \to 0$ close to the critical U. This indicates that the leading instability corresponds to an incommensurate altermagnetic state, which could be due to Fermi surface nesting. The Hartree-Fock calculation in Fig. 4.15(e) shows that altermagnetism is the leading instability for large fillings, but upon variations of the filling the ferromagnetic order has a smaller critical U.

The band structure for $FeSb_2$ shown in Fig. 4.14(a) has important differences that could lead to altermagnetism not being as stable as in the other materials considered before. On the one hand, the $t_{x,\mathbf{k}}$ hopping is smaller, giving rise to a smaller splitting along the Z-Γ-S direction. Recalling the susceptibility discussion in Sec. 4.4, the inter-band susceptibility only dominates for a sufficiently large inter-sublattice hopping $t_{x,\mathbf{k}}$. On the other hand, Fig. 4.14(a) also shows that along the R-Z line both bands disperse downwards, in contrast to the other cases where the bands disperse in opposite ways giving rise to a van Hove singularity, which could also be important in stabilizing altermagnetism [8].

However, a more complete model for $FeSb_2$ should include all d-orbitals [193], and therefore our predictions should be examined again in this case. Importantly, the minimal one-orbital model can capture the altermagnetic spin-splitting with the right symmetry, and the Berry curvature for this model is also given by the general expression in Eq. (4.50), which gives rise to a finite Hall conductivity.

4.8.2 κ-Cl

The organic compound κ-Cl is an orthorhombic material that provides a platform to study altermagnetism in a two-dimensional system. Characteristic properties of altermagnetism have been predicted for κ-Cl, such as the anomalous Hall effect or spin currents [200, 201]. Moreover, the interplay between an unconventional magnetic state and superconductivity has been studied for this material, suggesting that finite-momentum superconductivity can be induced [234].

κ-Cl has the 2D layer space group L25 and, as opposed to the other materials considered in this Chapter, it does not have inversion symmetry. As a consequence, the form for the SOC is different and lies beyond the scope of this thesis, therefore we do not include it in the following. Previous models considered a four sublattice unit cell, which split in two pairs due to bonding and antibonding [200, 201, 234]. We consider the large dimerization limit, and thus we focus only on the antibonding set of bands [235]. As we demonstrate below, considering this subset of the bands is sufficient to obtain a leading altermagnetic phase.

Similarly to $FeSb_2$, the minimal model in Eq. (4.1) is constructed taking into account Wyckoff positions $(0,0,0)$ and $(1/2,1/2,0)$, which gives

$$\begin{aligned} t_{z,\mathbf{k}} &= t_6 \sin k_x \sin k_y, \\ t_{x,\mathbf{k}} &= t_8 \cos\frac{k_x}{2} \cos\frac{k_y}{2}, \end{aligned} \tag{4.57}$$

and a dispersion

$$\varepsilon_{0,\mathbf{k}} = t_{1x} \cos k_x + t_{1y} \cos k_y + t_3 \cos k_x \cos k_y - \mu. \tag{4.58}$$

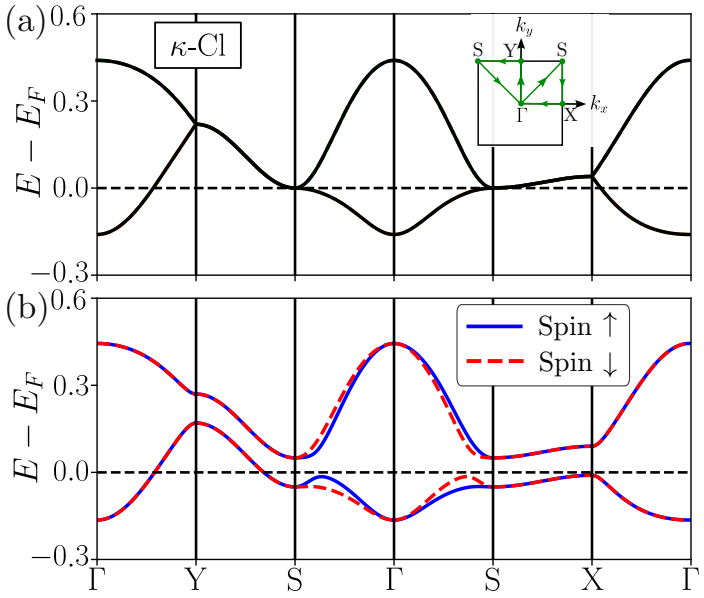

Figure 4.16: Band structure for κ-Cl in (a) the normal, and (b) the altermagnetic state, using the minimal model in Eq. (4.1) with Eqs. (4.57)-(4.58) for the hopping parameters and $J_z = 0.05$ in (b). The Brillouin zone path is illustrated in the inset. The specific values for the hopping parameters are detailed in Table 4.3.

The normal state band structure is shown in Fig. 4.16(a), in agreement with Refs. [200, 234], considering that the Fermi level is at the van Hove singularity at the S-point. The values for the hopping parameters are detailed in Table 4.3 and the Brillouin zone path is shown in the inset. In the altermagnetic state, the splitting is reversed along the Γ-S lines in the opposite directions $k_x = k_y$ and $k_x = -k_y$, as shown in Fig. 4.16(b), also in agreement with Refs. [200, 234].

Figures 4.17(a)-(d) show the altermagnetic and ferromagnetic susceptibilities for this material. As seen, both channels have a peak at $\mathbf{q} \to 0$ due to the van Hove singularity at the Fermi level (see Fig. 4.16(a)), but already at the level of the bare susceptibility the altermagnetic instability dominates. In Fig. 4.17(e) we display the Hartree-Fock results, confirming that the altermagnetic state can be stabilized at a smaller critical U than the ferromagnetic state. As the filling changes, the critical U becomes smaller (coinciding the minimum with the van Hove singularity) and then it increases again.

The altermagnetic state can be stabilized through a weak-coupling mechanism for κ-Cl, as demonstrated in Ref. [8]. In agreement with this work, examining the hoppings and the dispersions in Eqs. (4.57)-(4.58) show that the hopping t_8 has to be sufficiently large for the interband susceptibility to dominate, otherwise the ferromagnetic instability becomes the leading one. Motivated by κ-Cl and this mechanism, in Appendix E we introduce a minimal model for altermagnetism in a two-dimensional tetragonal system.

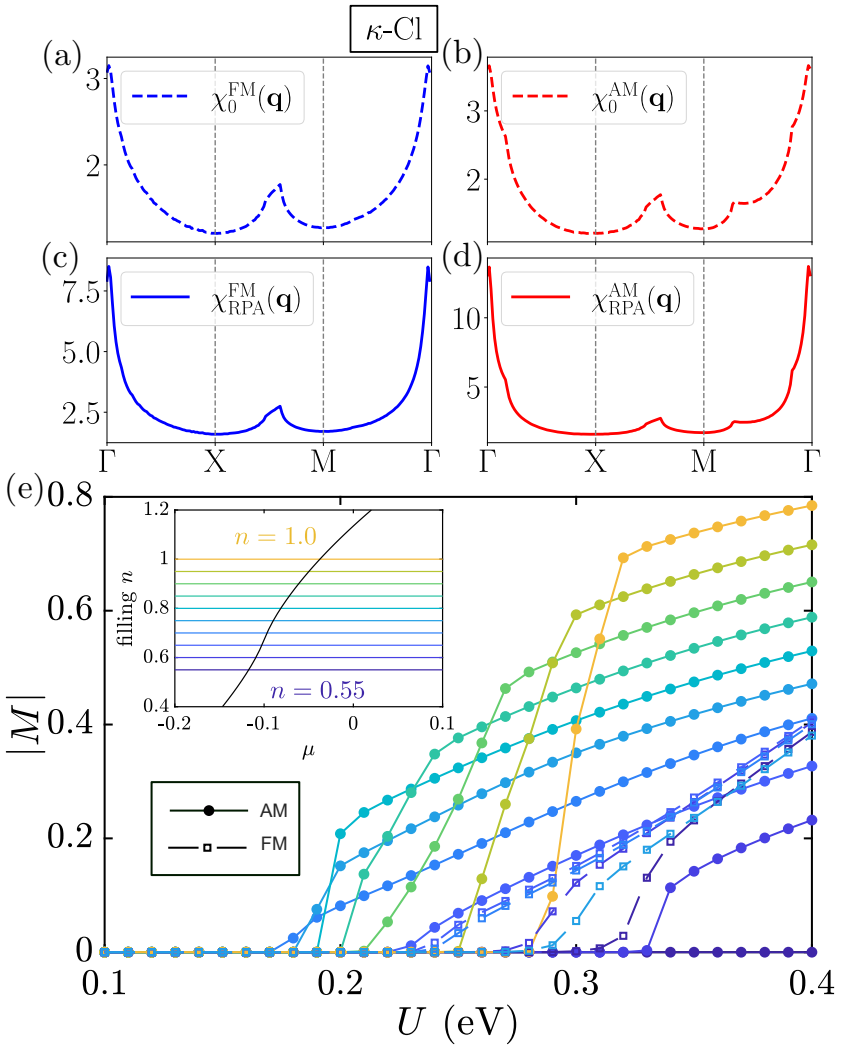

Figure 4.17: (a)-(d) Bare and RPA susceptibilities in the ferromagnetic and altermagnetic channels (see Eqs. (4.36)-(4.37)) for κ-Cl, with the band structure shown in Fig. 4.16(a), for $U = 0.1$, $k_BT = 10^{-4}$ and $N = 400^2$. (e) Hartree-Fock calculation considering the Hamiltonian in Eq. (4.38) for an altermagnetic and ferromagnetic order parameters as a function of the Hubbard interaction at different fillings n, using the band structures for κ-Cl, with $k_BT = 0.002$ and $N = 300^2$.

4.8.3 g-wave altermagnetism

In this section, we demonstrate that the minimal model in Eq. (4.1) can also describe g-wave altermagnetism. Different altermagnetic material candidates have been proposed to have this symmetry for the spin splitting, including CrSb and MnTe [26, 27, 198]. In particular, the case of CrSb is remarkable since a large spin splitting of 1.2 eV has been predicted [26, 27], and recently an experimental work has reported the altermagnetic spin splitting of the bands [202]. Also importantly, CrSb is a metallic system with magnetic order at room temperature [198, 236]. Similarly, the splitting of the bands in MnTe has also been recently observed [203].

Both CrSb and MnTe are hexagonal materials with space group 194, which has point group D_{6h} and the Mn/Cr atoms occupy Wyckoff position 2a, corresponding to $(0, 0, 0)$ and $(0, 0, 1/2)$.

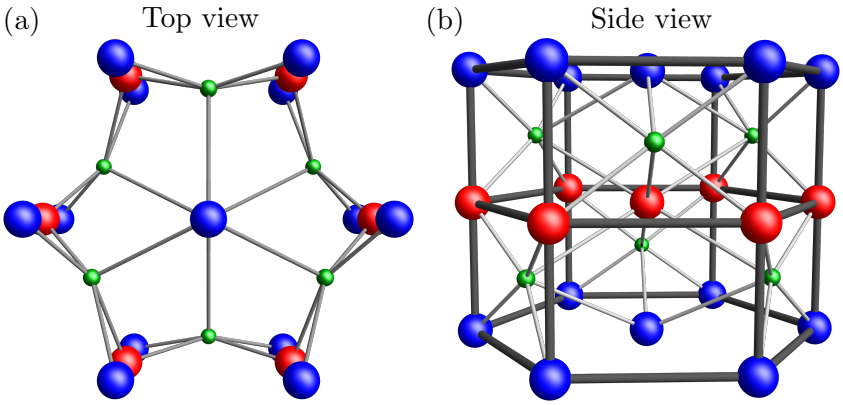

Figure 4.18: Illustration of the crystal structure for space group 194, relevant for CrSb and MnTe. The two colors red and blue denote the two sublattices (for Cr and Mn atoms), while the green color corresponds to the non-magnetic atoms (Sb and Te, respectively).

The crystal structure for this space group including magnetic (red/blue dots) and non-magnetic atoms (green dots) is illustrated in Fig. 4.18. As seen, the operations $\{C_3|0\,0\,0\}$ and $\{C_{2x}|0\,0\,0\}$ leave the two sublattices invariant, while the non-symmorphic operations $\{C_6|0\,0\,\frac{1}{2}\}$, $\{C_{2z}|0\,0\,\frac{1}{2}\}$ and $\{C_{2xy}|0\,0\,\frac{1}{2}\}$ exchange them. Thus, in this point group τ_z and τ_y transform as the B_{1g} irrep, and the minimal model in Eq. (4.1) is given by

$$\varepsilon_{0,\mathbf{k}} = t_1\left(\cos k_x + 2\cos\frac{k_x}{2}\cos\frac{\sqrt{3}k_y}{2}\right) + t_2\cos k_z - \mu, \tag{4.59}$$

and the hoppings correspond to

$$\begin{aligned} t_{x,\mathbf{k}} &= t_3\cos\frac{k_z}{2}, \\ t_{z,\mathbf{k}} &= t_4\sin k_z f_y(f_y^2 - 3f_x^2). \end{aligned} \tag{4.60}$$

For the SOC, we have

$$\begin{aligned} \lambda_{x,\mathbf{k}} &= \lambda\cos\frac{k_z}{2}(f_x^2 - f_y^2), \\ \lambda_{y,\mathbf{k}} &= 2\lambda\cos\frac{k_z}{2}f_x f_y, \\ \lambda_{z,\mathbf{k}} &= \lambda_z\sin\frac{k_z}{2}f_x(f_x^2 - 3f_y^2), \end{aligned} \tag{4.61}$$

where we have considered that $\sigma_z \sim A_{1g}$ and $(\sigma_x, \sigma_y) \sim E_{1g}$ in D_{6h}. In Eqs. (4.60)-(4.61) we have introduced $f_x \equiv \sin k_x + \sin\frac{k_x}{2}\cos\frac{\sqrt{3}k_y}{2}$ and $f_y \equiv \sqrt{3}\cos\frac{k_x}{2}\sin\frac{\sqrt{3}k_y}{2}$ due to the nearest-neighbor hopping form in hexagonal lattices, since $t_{z,\mathbf{k}}$ should describe the difference in the hopping along $(\frac{1}{2}, \frac{\sqrt{3}}{2})$ and $(-\frac{1}{2}, \frac{\sqrt{3}}{2})$. At the Γ-point, they reduce to $f_x \sim \frac{3}{2}k_x$ and $f_y \sim \frac{3}{2}k_y$, but at the zone boundaries they could be different.

Note that near the Γ-point, $t_{z,\mathbf{k}} \sim k_y k_z(k_y^2 - 3k_x^2)$. Hence, in this case, the symmetry of the hopping $t_{z,\mathbf{k}}$ and thus the symmetry of the altermagnetic spin splitting correspond to g-wave. Consequently, the minimal one-orbital model in Eq. (4.1) can capture the right symmetry also for hexagonal systems.

4.8.4 *i*-wave altermagnetism

Having shown that the minimal model in Eq. (4.1) can correctly describe *d*-wave and *g*-wave altermagnets, we now demonstrate that it can further describe the *i*-wave symmetry for the spin splitting. With this purpose, we consider space group 223 with point group O_h. We assume Wyckoff position 2a, corresponding to $(0,0,0)$ and $(1/2,1/2,1/2)$. In this case, the operations $\{C_3|0\,0\,0\}$ and $\{C_2|0\,0\,0\}$ leave the crystal structure invariant, while the non-symmorphic rotations $\{C_4|\frac{1}{2}\,\frac{1}{2}\,\frac{1}{2}\}$ and $\{C_{2'}|\frac{1}{2}\,\frac{1}{2}\,\frac{1}{2}\}$ interchange the two sublattices. Therefore, τ_z and τ_y belong to the A_{2g} irrep of O_h. In this case, the dispersion in the minimal model in Eq. (4.1) is given by

$$\varepsilon_{0,\mathbf{k}} = t_1(\cos k_x + \cos k_y + \cos k_z) - \mu, \tag{4.62}$$

while for the hoppings we have

$$\begin{aligned} t_{x,\mathbf{k}} &= t_2 \cos\frac{k_x}{2}\cos\frac{k_y}{2}\cos\frac{k_z}{2}, \\ t_{z,\mathbf{k}} &= t_3(\cos k_x - \cos k_y)(\cos k_x - \cos k_z)(\cos k_y - \cos k_z). \end{aligned} \tag{4.63}$$

Finally, the SOC has now the form

$$\begin{aligned} \lambda_{x,\mathbf{k}} &= \lambda \cos\frac{k_x}{2}\sin\frac{k_y}{2}\sin\frac{k_z}{2}, \\ \lambda_{y,\mathbf{k}} &= \lambda \sin\frac{k_x}{2}\cos\frac{k_y}{2}\sin\frac{k_z}{2}, \\ \lambda_{z,\mathbf{k}} &= \lambda \sin\frac{k_x}{2}\sin\frac{k_y}{2}\cos\frac{k_z}{2}, \end{aligned} \tag{4.64}$$

where we have used that the spin degree of freedom transforms as the T_{1g} irrep of O_h. Near the Γ-point, the altermagnetic spin splitting corresponds to $t_{z,\mathbf{k}} \sim x^4(y^2-z^2)+y^4(z^2-x^2)+z^4(x^2-y^2)$, and thus this model describes an *i*-wave altermagnet.

Hence, the minimal model is also able to capture the *g*-wave and the *i*-wave symmetry for the spin splitting. Note that the general Berry curvature expression in Eq. (4.50) linear in SOC is general and therefore is also relevant in these cases. By using the expressions for the hoppings and the SOC above, the large Berry curvature regions can be determined and the conductivity can be calculated, similarly to Figs. 4.12-4.13 for the case of RuO_2. This is particularly relevant for CrSb and MnTe, for which the anomalous Hall effect has already been measured [209], since so far no material candidates with an *i*-wave symmetry for the spin splitting have been experimentally identified.

4.9 Discussion and conclusions

In this Chapter, we have constructed minimal models for altermagnetism in non-symmorphic materials with two magnetic sublattices. We have demonstrated that the model is realistic for altermagnetic material candidates through the comparison to DFT calculations. We have applied the models to tetragonal, orthorhombic, hexagonal, and cubic materials, but they are sufficiently general and can also be applied to other altermagnetic candidates, for instance,

with monoclinic or rhombohedral non-symmorphic space groups [4]. We have shown that the intra-sublattice hopping $t_{z,\mathbf{k}}$ in the minimal model defines the symmetry of the spin splitting in reciprocal space, which corresponds to d-wave for the tetragonal and orthorhombic cases discussed, but also describes g-wave for the hexagonal compounds and i-wave for a cubic space group.

We have also derived an expression for the susceptibility in the usual spin channel and introduced an altermagnetic susceptibility, revealing the competition between intra- and inter-band contributions. The latter favors the altermagnetic phase over conventional ferromagnetic order. Importantly, the altermagnetic susceptibility shows that band degeneracies help stabilizing altermagnetism. The minimal tight-binding model also reveals that a large inter-sublattice hopping term $t_{x,\mathbf{k}}$ and the presence of van Hove singularities favor the inter-band susceptibility and thus the altermagnetic phase. We have verified that the minimal model gives rise to a leading altermagnetic instability using an RPA analysis and self-consistent Hartree-Fock calculations in the presence of on-site Hubbard interactions.

In addition, we have obtained an analytic expression for the Berry curvature, which is linear in the spin-orbit coupling strength and in general gives rise to a significant Hall conductivity. The Berry curvature is large at the nodal planes in the presence of an altermagnetic instability, and is further enhanced by Weyl lines. Motivated by this observation, an important next step would be to provide a general classification of nodal planes and lines in space groups relevant for material candidates, as well as to construct the corresponding minimal models in these cases. In particular, it could help to identify other experimental signatures that, similar to the anomalous Hall effect, are further enhanced in the presence of nodal planes and lines.

So far we have focused on Wyckoff positions with multiplicity 2, which is the minimum allowed in the non-symmorphic space groups discussed. Extending the minimal models to more atoms per unit cell is a necessary next step to describe other materials. Furthermore, a general minimal model for unconventional p-wave magnets could also be constructed, which would require at least four atoms per unit cell [219].

The minimal models can be useful to study the properties of altermagnetism and the interplay with other electronic instabilities, such as superconductivity. In particular, recent experimental evidence has suggested that superconductivity emerges under strain in RuO_2 [237–239]. To shed light on this discussion, we stress that strain can also be included in the minimal models as

$$H_{\epsilon_{xy}}(\mathbf{k}) = \epsilon_{xy} \cos k_x \cos k_y \tau_z, \tag{4.65}$$

which for RuO_2 splits the van Hove singularity at the A-point. Consequently, we expect that altermagnetism could be suppressed, favoring another nearby instability.

In addition, the minimal models can also be used to examine the properties of altermagnetism in the presence of spatial inhomogeneities, such as domain walls or impurities [240]. In this direction, it is crucial to identify the terms entering in the Landau theory of altermagnetism, as we will investigate in the following Chapter. The coefficients in Landau theory can be calculated using the microscopic model in Eq. (4.1), unveiling the role of spin-orbit coupling in determining the direction of the altermagnetic moments and the coupling of the altermagnetic

order parameter to the magnetization. With this insight, we could solve self-consistently for the order parameter in real space and reveal important differences with antiferromagnets, for instance by analyzing the effect of impurities or edge states.

Finally, in the same direction as in Chapter 1, we can study the spin-fluctuation mechanism for an altermagnet and find the leading superconducting instabilities, including both singlet and triplet channels [241]. In agreement with other works, this could point to exotic superconducting states such as finite-momentum pairing or triplet states [234, 242, 243].

Chapter 5

Landau theory of altermagnetism from microscopic models

Info: *This Chapter is in preparation for publication together with Andreas Kreisel, Yue Yu, Brian M. Andersen and Daniel F. Agterberg, and will be available soon in Ref. [5] as an arXiv preprint.*

5.1 Introduction

Altermagnets exhibit unique properties that distinguish them from conventional ferromagnets and antiferromagnets, as discussed in Chapter 4, since they feature a spin-split band structure that does not originate from relativistic effects while still exhibiting vanishing net magnetization [26, 27]. However, the presence of spin-orbit coupling (SOC) in altermagnetism also generates noteworthy effects. On the one hand, SOC modifies the crystal symmetries, leading to a preferred direction for the altermagnetic moments. On the other hand, depending on the orientation of the magnetic moments, in the presence of SOC altermagnetism can also induce what is known as weak ferromagnetism [220].

In particular, weak ferromagnetism has been recently studied both theoretically and experimentally for different altermagnetic material candidates [191,208,244–249], including RuO_2 [191, 208, 248], MnTe [244, 245] and CrSb [248, 249]. Nevertheless, the microscopic origin of this phenomenon remains unsettled. Therefore, it is crucial to study the role of SOC in altermagnets using realistic microscopic models to understand how altermagnetic properties are modified. In addition, as discussed in Sec. 4.7, SOC is essential to induce a large Berry curvature and an anomalous Hall effect, which by symmetry always appear together with a non-zero magnetization [250, 251]. Thus, another open question is the interplay between the anomalous Hall effect and the magnetization, which can also be addressed from the microscopic models.

Altermagnets have been proposed as excellent candidates for spintronic applications [26, 27]. However, a major experimental challenge is obtaining samples with a single altermagnetic domain, since the presence of multiple domains causes most effects of interest to cancel out, mak-

ing it difficult to experimentally identify altermagnets and to find practical applications [252]. Moreover, while the vanishing net magnetization in altermagnets provides an advantage over ferromagnets, which are sensitive to external magnetic field perturbations, it also presents a significant challenge, as manipulating altermagnetic domain walls with external fields is a difficult task. To this end, a fundamental first step is to understand how domain walls interact with magnetic order parameters and external fields.

Notably, both the role of SOC and domain walls can be analyzed by formulating a phenomenological Landau theory of altermagnetism. In this direction, Ref. [253] investigated the Landau theory capturing the properties of altermagnets, extending the discussion to the case of non-zero SOC. As pointed out in that work, the interplay between the altermagnetic order parameter and observables such as the magnetization or the anomalous Hall effect can be explored using general symmetry arguments. On the other hand, within the phenomenological Landau theory, Ref. [240] showed that, as opposed to antiferromagnets, the order parameter in altermagnets can couple to the magnetization gradient at domain walls, revealing that they may be manipulated by magnetic tips.

However, none of the previous works considered a microscopic model, which is necessary to provide explicit expressions for the Landau coefficients, in addition to investigate the microscopic origin of the weak ferromagnetism and the preferred altermagnetic moment orientation. In this Chapter, we derive the Landau theory of altermagnetism using the minimal tight-binding model constructed in Chapter 4. This allows us to study the role of the different parameters in the minimal model in the interplay between the altermagnetic order parameter and the magnetization. We first focus on domain walls in the zero SOC limit, and then include the role of SOC. We build upon the studies in Refs. [240, 253] by formulating a Landau theory for all space groups containing inversion symmetry with Wyckoff positions of multiplicity two, following the procedure introduced in Chapter 4.

This Chapter is organized as follows: in Sec. 5.2 we introduce the basic concepts of Landau theory and domain walls that are necessary for the remainder of the Chapter. The model and method used to derive the Landau theory of altermagnetism from the minimal models is detailed in Sec. 5.3. Focusing on the case of a d-wave altermagnet and neglecting first SOC, in Sec. 5.4 we formulate the phenomenological form of the free energy and derive expressions for the coefficients from the microscopic model, including the gradient terms. In Sec. 5.5 we go beyond the d-wave altermagnet and provide the phenomenological form of the coupling between the magnetization and the altermagnetic order parameter for other space groups. In the next sections, we include SOC and investigate how it modifies the altermagnetic properties. First, in Sec. 5.6 we formulate the general Landau theory, analyzing the role of SOC in the preferred altermagnetic moment orientation. Secondly, in Sec. 5.7 we analyze the bilinear coupling between the magnetization and the altermagnetic order parameter due to SOC, investigating the induced weak ferromagnetism and whether it is generated from the microscopic models. Finally, Sec. 5.8 contains the discussion and conclusions of this Chapter.

5.2 Landau theory and domain walls

In this section, we review the main concepts of Landau theory and domain walls, which will be used in the following sections. The Landau free energy has been extensively addressed in the literature and textbooks; see, for example, Ref. [254]. Let us first introduce the Landau free energy density f for a single-component magnetic order parameter ϕ, which due to time-reversal symmetry takes the form

$$f = \frac{a}{2}\phi^2 + \frac{b}{4}\phi^4, \tag{5.1}$$

where a and b are the temperature-dependent coefficients for the quadratic and quartic terms, respectively. The phase transition is set by the critical temperature T_c at which the coefficient a changes sign,

$$a(T) = a_0(T - T_c). \tag{5.2}$$

When this occurs, the magnetic phase is stabilized, since the free energy minimum is at $|\phi| > 0$.

In the case of an inhomogeneous order parameter, where the amplitude varies or the direction flips, as seen in a domain wall (see Fig. 5.1), there is an additional energy cost due to the gradients in the order parameter,

$$f = \frac{d}{2}(\nabla\phi)^2 + \frac{a}{2}\phi^2 + \frac{b}{4}\phi^4. \tag{5.3}$$

The gradient term introduces a new length scale, the correlation length

$$\xi(T) = \sqrt{\frac{d}{|a(T)|}} = \xi_0\left|1 - \frac{T}{T_c}\right|^{-1/2}, \tag{5.4}$$

which is the characteristic scale of the order parameter fluctuations, with the coherence length

$$\xi_0 = \xi(T = 0) = \sqrt{\frac{d}{a_0 T_c}}. \tag{5.5}$$

As illustrated in Fig. 5.1, in a domain wall the order parameter changes sign, passing through the local maximum of the free energy at $\phi = 0$. Thus, domain walls separate regions with $\phi = \pm\phi_0$, and the solution for the order parameter has the following form [254],

$$\phi(x) = \phi_0 \tanh\left(\frac{x}{\sqrt{2}\xi}\right). \tag{5.6}$$

As the starting point of our work, the two relevant order parameters are the magnetization, $m = M_1 + M_2$, and the altermagnetic order parameter (or Néel order), $J = M_1 - M_2$, where M_1 and M_2 are the magnetizations of the two sublattices, which are of opposite sign for an altermagnet, as depicted in Fig. 4.1. In this Chapter, we focus on obtaining expressions for the coefficients in Eq. (5.1) from the minimal model, as we will detail in Sec. 5.3.

The Landau theory for inhomogeneous order parameters in Eq. (5.3) can be extended to include both the altermagnetic order parameter and the magnetization to examine their coupling at domain walls [240]. In particular, we will use this formulation in Secs. 5.4-5.5 to show that gradient terms enter in the free energy when including the two magnetic order parameters. Moreover, in Secs. 5.6-5.7 we modify the Landau theory in Eq. (5.1) to include the role of SOC,

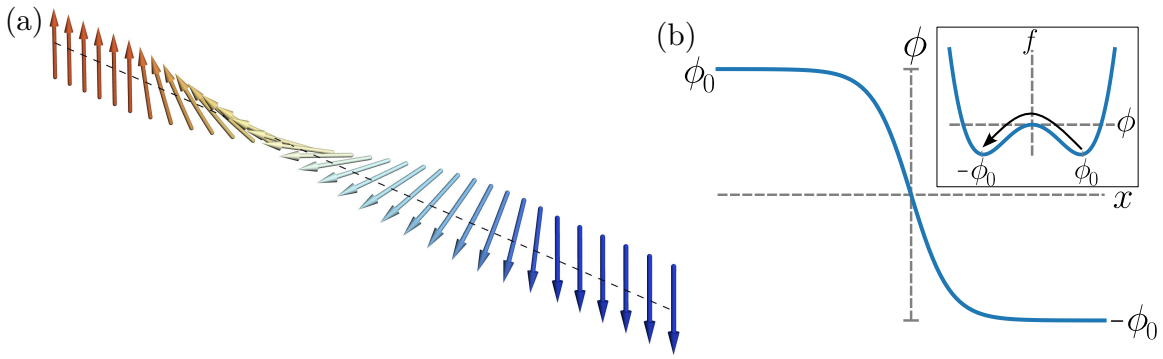

Figure 5.1: (a) Illustration of a domain wall where the order parameter varies in the out-of-plane direction. (b) Order parameter profile through the domain wall where the order parameter changes from ϕ_0 to $-\phi_0$. At the domain wall, the order parameter passes through the local maximum of the free energy at $\phi = 0$, as depicted in the inset.

and therefore we consider three-component order parameters for the magnetization and the Néel order. This allows us to analyze the preferred orientation of the moments, in addition to the bilinear coupling between both orders due to SOC.

5.3 Model and method

Since the minimal model constructed in Chapter 4 serves as the starting point for deriving the coefficients in the Landau free energy expansion, in this section we first restate the general form of the Hamiltonian and the interactions, emphasizing the key properties of the parameters involved. Next, we introduce the expression used to determine the quadratic and quartic contributions to the free energy from the magnetization and altermagnetic order parameters.

Let us focus first on the general non-interacting minimal model derived in Sec. 4.2, which is given by

$$H_0(\mathbf{k}) = \varepsilon_{0,\mathbf{k}} + t_{x,\mathbf{k}}\tau_x + t_{z,\mathbf{k}}\tau_z + \tau_y\vec{\lambda}_{\mathbf{k}}\cdot\vec{\sigma}, \tag{5.7}$$

where τ_i and σ_i denote the sublattice and spin degrees of freedom, respectively. The form of the parameters entering in the minimal model depend on the space group, the point group and the Wyckoff position. As introduced in Sec. 4.2, the inter-sublattice hopping $t_{x,\mathbf{k}}$ always has the full symmetry of the point group, since it transforms in the same way as τ_x, whereas the inter-sublattice hopping $t_{z,\mathbf{k}}$ must transform like τ_z, and thus it is odd under the operations that exchange the two sublattices. As a consequence, $t_{z,\mathbf{k}}$ belongs to a non-trivial irreducible representation (irrep) of the point group, which we denote by Γ_N, and defines the symmetry of the spin splitting.

If we now turn to the interaction term, the form of the altermagnetic order parameter is given in Eq. (4.1). However, since in this Chapter we are concerned with the interplay of both the altermagnetic order and magnetization, we consider the following interaction,

$$V = \tau_z\vec{J}\cdot\vec{\sigma} + \vec{m}\cdot\vec{\sigma}, \tag{5.8}$$

where we have introduced $\vec{J}$ as the Néel order, similarly to Sec. 4.2, while $\vec{m}$ denotes the magnetization.

To derive the free energy in terms of the order parameters $\vec{J}$ and $\vec{m}$, we calculate the corrections to the normal-state free energy as the magnetic orders set in by evaluating the loop expansion [254, 255]

$$F = -\operatorname{Tr}\ln[-{G_0}^{-1}] - \operatorname{Tr}\ln[\mathbb{1} + G_0 V]. \tag{5.9}$$

Note that here we have introduced the expansion for the free energy, $F = \int d\mathbf{r} f$, where f is the free energy density in Eq. (5.1). The first term in Eq. (5.9) is the free energy of the non-interacting system, whereas the second term introduces the change in the free energy due to the interaction. The latter can be rewritten as a loop expansion, and therefore the quadratic and quartic contributions that we will be interested in are given by

$$F^{(2)} = \frac{1}{2}\operatorname{Tr}[G_0 V G_0 V], \tag{5.10}$$

$$F^{(4)} = \frac{1}{4}\operatorname{Tr}\big[(G_0 V)^4\big]. \tag{5.11}$$

In Fig. 5.2 we illustrate the diagrammatic representation of these contributions, where α can denote both order parameters m and J.

In the previous expressions, V is the interaction given in Eq. (5.8) and G_0 is the bare Green's function projected to the band basis introduced in Sec. 4.4, which we repeat here for convenience,

$$G_0(\mathbf{k}, i\omega_n) = \sum_{a=\pm} G^{(a)}(\mathbf{k}, i\omega_n) \left|u_{\mathbf{k}}^{(a)}\right\rangle \left\langle u_{\mathbf{k}}^{(a)}\right|, \tag{5.12}$$

where $G^{(\pm)}(\mathbf{k}, i\omega_n) = \frac{1}{i\omega_n - E_{\mathbf{k}}^{(\pm)}}$ is the bare Green's function in the band basis and $\left|u_{\mathbf{k}}^{(a)}\right\rangle \left\langle u_{\mathbf{k}}^{(a)}\right|$ the projection operator from sublattice basis onto band a and wavevector $\mathbf{k}$. The dispersion of the non-interacting Hamiltonian in Eq. (5.7) corresponds to

$$E_{\mathbf{k}}^{(\pm)} = \varepsilon_{0,\mathbf{k}} \pm \sqrt{t_{x,\mathbf{k}}^2 + t_{z,\mathbf{k}}^2 + \vec{\lambda}_{\mathbf{k}}^2}, \tag{5.13}$$

which is two-fold degenerate. The form of the projection operator was introduced in Sec. 4.7, where we used it to obtain an analytic expression for the Berry curvature. However, since we are now considering the bare Green's function in the absence of magnetic order, the projector operator in Eq. (4.42) simplifies to

$$P_{\mathbf{k}}^{(\pm)} = \left|u_{\mathbf{k}}^{(\pm)}\right\rangle \left\langle u_{\mathbf{k}}^{(\pm)}\right| = \frac{1}{4}\left(\mathbb{1} + \frac{H_1(\mathbf{k})}{E_{1,\mathbf{k}}^{(\pm)}}\right), \tag{5.14}$$

with $H_1(\mathbf{k}) = t_{x,\mathbf{k}}\tau_x + t_{z,\mathbf{k}}\tau_z + \tau_y \vec{\lambda}_{\mathbf{k}} \cdot \vec{\sigma}$ and the corresponding dispersion

$$E_{1,\mathbf{k}}^{(\pm)} = \pm\sqrt{t_{x,\mathbf{k}}^2 + t_{z,\mathbf{k}}^2 + \vec{\lambda}_{\mathbf{k}}^2}, \tag{5.15}$$

which is also two-fold degenerate. In the absence of SOC, the projector in Eq. (5.14) can be reduced to a 2×2 matrix, which will simplify the free energy calculations in Sec. 5.4.

Finally, we note that the free energy expansion in Eq. (5.9) is obtained from the path integral formulation, including also the interactions. As demonstrated in Sec. 4.6, altermagnetism is

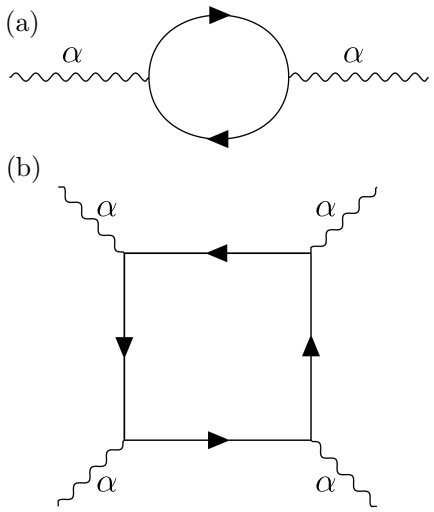

Figure 5.2: (a) Second-order and (b) fourth-order diagrammatic representation of the free-energy expansion in Eqs. (5.10)-(5.11), respectively. The parameter $\alpha = \{m, J\}$ can denote the two magnetic orders in Eq. (5.8).

stabilized by an intra-orbital Hubbard interaction U (see Eq. (4.31)). Therefore, when decoupling the Hubbard model, there is an additional term entering in the free energy, which is quadratic in the order parameters containing the interaction [254, 255], so that the coefficient a in Eq. (5.1) becomes

$$a \to \left(\frac{1}{U} - a\right), \tag{5.16}$$

which we omit in the following. Hence, the magnetic phase is only stabilized below a critical interaction U_c, where the quadratic coefficient becomes negative.

In the following sections, we use Eqs. (5.10)-(5.11) to evaluate the second- and fourth-order corrections to the free energy and find expressions for the coefficients. In Secs. 5.4-5.5, we first neglect SOC, and thus we consider one-component order parameters m and J. By contrast, when including the role of SOC in Secs. 5.6-5.7, we consider three-component order parameters $\vec{m}$ and $\vec{J}$, and thus the projector in Eq. (5.14) becomes a 4×4 matrix.

5.4 Free energy for a d-wave altermagnet

In this section, we introduce the form of the free energy and give expressions for the coefficients from the minimal model. Since the free energy will depend on the symmetry of the spin splitting, we focus first on the case of a d-wave altermagnet. We will generalize the discussion to other space groups that allow for Wyckoff positions of multiplicity two in Sec. 5.5.

Specifically, we consider a d-wave altermagnet with a symmetry of the spin splitting given by $k_x k_y$, which is relevant for RuO_2 and MnF_2 introduced in Sec. 4.3, in addition $FeSb_2$, discussed in Sec. 4.8. As we will show below by calculating the second- and fourth-order contributions using Eqs. (5.10)-(5.11), the phenomenological form of the free energy can be written as

$$f = \frac{d}{2}(\nabla J)^2 + \frac{a_{J^2}}{2} J^2 + \frac{b_{J^4}}{4} J^4 + \frac{a_{m^2}}{2} m^2 + c_{\text{grad}}\, m \partial_x \partial_y J - hm, \tag{5.17}$$

where h is an applied field that couples to the ferromagnetic moment, and a_{J^2}, b_{J^4}, a_{m^2} and c_{grad} are coefficients. Altermagnetism is stabilized if $a_{J^2} < 0$, while we assume $a_{m^2} > 0$ since the ferromagnetic order is only induced due to domain walls. Note that here we have neglected the role of SOC, which allows us to consider single-component order parameters, such that $V = \tau_z J + \tau_0 m$. Nevertheless, as we will investigate in Secs. 5.6-5.7, SOC has important consequences leading to direct couplings between the magnetization and the altermagnetic order parameter.

Notably, Eq. (5.17) shows that in the absence of SOC, the only symmetry-allowed coupling between the two orders m and J is through the gradients, in agreement with Ref. [240]. As discussed in Sec. 3.2, the terms entering in the free energy must transform as invariants. Since in this case the order parameter J transforms like $\tau_z \sim k_x k_y$ (see Eq. (5.8)), the gradients $\partial_x \partial_y$ compensate this to result in an invariant. As a consequence, the symmetry of the spin splitting dictates the form of the coupling between the altermagnetic order parameter and the magnetization gradients that enters in the free energy at domain walls.

Let us now obtain expressions for the coefficients a_{J^2}, b_{J^4}, a_{m^2} and c_{grad} using the minimal model in Eq. (5.7). First, from Eq. (5.10), the second-order contribution to the free energy which is quadratic in J corresponds to

$$F_J^{(2)} = \frac{J^2 \mathcal{V}}{\beta} \operatorname{Tr}\left\{ \sum_{a,b} G^{(a)}(\mathbf{k}, i\omega_n) G^{(b)}(\mathbf{k}, i\omega_n) \tau_z \left|u_{\mathbf{k}}^{(a)}\right\rangle \left\langle u_{\mathbf{k}}^{(a)}\right| \tau_z \left|u_{\mathbf{k}}^{(b)}\right\rangle \left\langle u_{\mathbf{k}}^{(b)}\right| \right\}, \tag{5.18}$$

where the volume $\mathcal{V}$ arises from $F = \int d\mathbf{r} f = \mathcal{V} f$. In this expression, the trace is over all degrees of freedom, including $\mathbf{k}$ and the Matsubara frequency $i\omega_n$, and is normalized by a prefactor $1/\beta$. By replacing the projector operator in Eq. (5.14), we obtain

$$F_J^{(2)} = \frac{J^2 \mathcal{V}}{\beta} \sum_{\mathbf{k}, i\omega_n} \frac{1}{t_{x,\mathbf{k}}^2 + t_{z,\mathbf{k}}^2} \Big(2t_{x,\mathbf{k}}^2 G^{(-)}(\mathbf{k}, i\omega_n) G^{(+)}(\mathbf{k}, i\omega_n) + t_{z,\mathbf{k}}^2 \Big[\Big(G^{(-)}(\mathbf{k}, i\omega_n) \Big)^2 + \Big(G^{(+)}(\mathbf{k}, i\omega_n) \Big)^2 \Big] \Big). \tag{5.19}$$

Thus, performing the Matsubara sum, we can directly identify the form for the a_{J^2} coefficient in Eq. (5.17),

$$a_{J^2} = -2 \sum_{\mathbf{k}} \frac{1}{t_{x,\mathbf{k}}^2 + t_{z,\mathbf{k}}^2} \left\{ t_{x,\mathbf{k}}^2 \frac{2\Big[f\Big(E_{\mathbf{k}}^{(-)}\Big) - f\Big(E_{\mathbf{k}}^{(+)}\Big) \Big]}{E_{\mathbf{k}}^{(-)} - E_{\mathbf{k}}^{(+)}} + t_{z,\mathbf{k}}^2 \left[\left. \frac{df(\varepsilon)}{d\varepsilon} \right|_{\varepsilon = E_{\mathbf{k}}^{(+)}} + \left. \frac{df(\varepsilon)}{d\varepsilon} \right|_{\varepsilon = E_{\mathbf{k}}^{(-)}} \right] \right\}. \tag{5.20}$$

This expression is in agreement with the susceptibility obtained in Sec. 4.4, revealing that the competition between intra- and inter-band terms determines whether altermagnetism or ferromagnetism is stabilized. In particular, we identified that band degeneracies play a crucial role, leading to a dominant inter-band susceptibility (see also Sec. 4.5).

Analogously, we can obtain an expression for the a_{m^2} coefficient in Eq. (5.17) by considering the coupling of m to quadratic order, yielding

$$F_m^{(2)} = \frac{m^2 \mathcal{V}}{\beta} \sum_{\mathbf{k}, i\omega_n} \Big[\Big(G^{(-)}(\mathbf{k}, i\omega_n) \Big)^2 + \Big(G^{(+)}(\mathbf{k}, i\omega_n) \Big)^2 \Big]. \tag{5.21}$$

Therefore, the coefficient corresponds to

$$a_{m^2} = -2 \sum_{\mathbf{k}} \left\{ \left. \frac{df(\varepsilon)}{d\varepsilon} \right|_{\varepsilon = E_{\mathbf{k}}^{(+)}} + \left. \frac{df(\varepsilon)}{d\varepsilon} \right|_{\varepsilon = E_{\mathbf{k}}^{(-)}} \right\}. \tag{5.22}$$

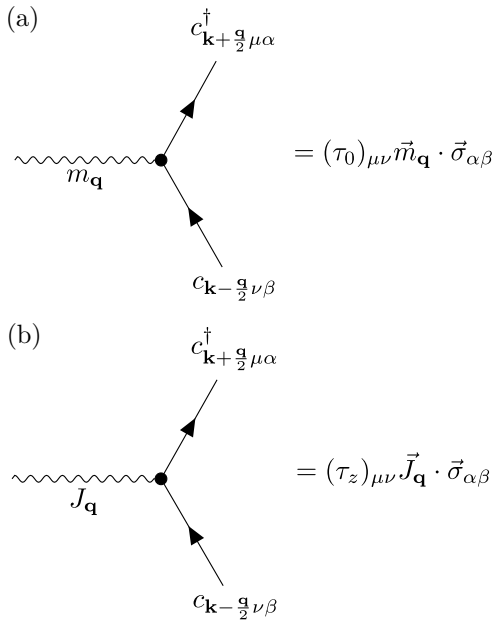

Figure 5.3: Interaction vertices for (a) the magnetization and (b) the altermagnetic order parameter. The **q**-dependence is included to derive the gradient terms.

As opposed to a_{J^2}, the ferromagnetic coefficient only contains intra-band terms, in agreement with the result found in Sec. 4.4.

As shown in Eq. (5.17), in the absence of SOC there is no bilinear direct coupling between J and m. To demonstrate this from the free energy expansion, we analyze the second-order crossed term in Eq. (5.10), obtaining

$$F^{(2)}_{J,m} = \frac{Jm\mathcal{V}}{2\beta} \sum_{\mathbf{k},i\omega_n,a} \left(G^{(a)}(\mathbf{k}, i\omega_n)\right)^2 \frac{t_{z,\mathbf{k}}}{E^{(a)}_{1,\mathbf{k}}} = 0. \tag{5.23}$$

Importantly, this terms vanishes because $t_{z,\mathbf{k}}$ belongs to a non-trivial irrep of the point group. In the particular case considered in this section, $t_{z,\mathbf{k}} = t_{z0} \sin k_x \sin k_y$. Consequently, since the Green's function and the dispersion have the full symmetry of the group, the **k**-sum vanishes.

Thus, to calculate the lowest-order coupling between the magnetization and the Néel order we have to derive an expression for the gradient terms. In the case of a superconducting order parameter, the gradient terms are derived by considering a finite Cooper pair momentum **q**; see, for instance, Ref. [256]. In analogy, here we generalize the order parameters to describe a spin-density wave phase. The reason for this is that, when expanding for small **q**, we can Fourier transform the order parameters to real space, which allows us to obtain the gradient terms. For instance, the gradient terms in Eq. (5.17) are given by

$$\int m_{-\mathbf{q}} q_x q_y J_{\mathbf{q}} d\mathbf{q} = -\int m(\mathbf{r}) \partial_x \partial_y J(\mathbf{r}) d\mathbf{r}. \tag{5.24}$$

Therefore, the amplitude of the order parameters J and m is now a function of the momentum **q**, $J \to J_{\mathbf{q}}$, $m \to m_{\mathbf{q}}$. The corresponding interaction vertices in this theory are depicted in Fig. 5.3.

Then, the contribution to the free energy is given by the diagram in Fig. 5.2(a), which yields

$$F^{(2)}_{\text{grad}} = \text{Tr}\Big[\tau_z J_{\mathbf{q}} G_0\Big(\mathbf{k}+\frac{\mathbf{q}}{2}, i\omega_n\Big) m_{-\mathbf{q}} G_0\Big(\mathbf{k}-\frac{\mathbf{q}}{2}, i\omega_n\Big)\Big], \tag{5.25}$$

where again the trace is implied over all degrees of freedom including $\mathbf{k}$, $\mathbf{q}$ and $i\omega_n$. In this case, notice that when projecting the bare Green's function matrix to the band basis using Eq. (5.12), the projection operator in Eq. (5.14) depends on both momenta $\mathbf{k}$ and $\mathbf{q}$. Replacing this operator and calculating the Matsubara frequency sum, we arrive at the following expression:

$$F^{(2)}_{\text{grad}} = \frac{1}{4}\sum_{\mathbf{k},\mathbf{q}}\sum_a J_{\mathbf{q}} m_{-\mathbf{q}} \left(\frac{t_{z,\mathbf{k}-\mathbf{q}/2}}{E^{(a)}_{1,\mathbf{k}-\mathbf{q}/2}} + \frac{t_{z,\mathbf{k}+\mathbf{q}/2}}{E^{(a)}_{1,\mathbf{k}+\mathbf{q}/2}}\right) \frac{f\Big(E^{(a)}_{\mathbf{k}+\mathbf{q}/2}\Big) - f\Big(E^{(a)}_{\mathbf{k}-\mathbf{q}/2}\Big)}{E^{(a)}_{\mathbf{k}+\mathbf{q}/2} - E^{(a)}_{\mathbf{k}-\mathbf{q}/2}}. \tag{5.26}$$

Assuming that the momentum $\mathbf{q}$ is small, we can expand Eq. (5.26) by using

$$\begin{aligned}
E^{(a)}_{\mathbf{k}\pm\mathbf{q}/2} &\simeq E^{(a)}_{\mathbf{k}} \pm \frac{\partial E^{(a)}_{\mathbf{k}}}{\partial \mathbf{k}}\cdot\frac{\mathbf{q}}{2} + \frac{1}{2}\sum_{i,j=1}^{3}\frac{\partial^2 E^{(a)}_{\mathbf{k}}}{\partial k_i \partial k_j}\frac{q_i}{2}\frac{q_j}{2},\\
f\Big(E^{(a)}_{\mathbf{k}\pm\mathbf{q}/2}\Big) &\simeq f\Big(E^{(a)}_{\mathbf{k}}\Big) \pm \frac{\partial f\Big(E^{(a)}_{\mathbf{k}}\Big)}{\partial \mathbf{k}}\cdot\frac{\mathbf{q}}{2} + \frac{1}{2}\sum_{i,j=1}^{3}\frac{\partial^2 f\Big(E^{(a)}_{\mathbf{k}}\Big)}{\partial k_i \partial k_j}\frac{q_i}{2}\frac{q_j}{2},\\
t_{z,\mathbf{k}\pm\mathbf{q}/2} &\simeq t_{z,\mathbf{k}} \pm \frac{\partial t_{z,\mathbf{k}}}{\partial \mathbf{k}}\cdot\frac{\mathbf{q}}{2} + \frac{1}{2}\sum_{i,j=1}^{3}\frac{\partial^2 t_{z,\mathbf{k}}}{\partial k_i \partial k_j}\frac{q_i}{2}\frac{q_j}{2}.
\end{aligned} \tag{5.27}$$

To simplify the expansion and identify the non-vanishing terms, we follow a similar argument as in Eq. (5.23). The key point is that for the d-wave altermagnet considered here the hopping $t_{z,\mathbf{k}}$ transforms like $k_x k_y$. Since the dispersions have the full symmetry of the point group, the only non-vanishing terms must contain ∂_{k_x} and ∂_{k_y}. This implies that it is sufficient to seek for terms $q_x q_y$ in the expansion, obtaining

$$\begin{aligned}
F^{(2)}_{\text{grad}} = \sum_{\mathbf{k},\mathbf{q}}\sum_a q_x q_y \frac{J_{\mathbf{q}} m_{-\mathbf{q}}}{24\Big(E^{(a)}_{1,\mathbf{k}}\Big)^3}\Bigg\{ & 6t_{z,\mathbf{k}} f'(\varepsilon)\Big|_{\varepsilon=E^{(a)}_{\mathbf{k}}}\Big(\partial_{k_y}E^{(a)}_{1,\mathbf{k}}\Big)\Big(\partial_{k_x}E^{(a)}_{1,\mathbf{k}}\Big)\\
& - 3E^{(a)}_{1,\mathbf{k}} f'(\varepsilon)\Big|_{\varepsilon=E^{(a)}_{\mathbf{k}}}\Big[(\partial_{k_y}t_{z,\mathbf{k}})\Big(\partial_{k_x}E^{(a)}_{1,\mathbf{k}}\Big) + (\partial_{k_x}t_{z,\mathbf{k}})\Big(\partial_{k_y}E^{(a)}_{1,\mathbf{k}}\Big) + t_{z,\mathbf{k}}\Big(\partial_{k_x}\partial_{k_y}E^{(a)}_{1,\mathbf{k}}\Big)\Big]\\
& + \Big(E^{(a)}_{1,\mathbf{k}}\Big)^2\Big[t_{z,\mathbf{k}} f^{(3)}(\varepsilon)\Big|_{\varepsilon=E^{(a)}_{\mathbf{k}}}\Big(\partial_{k_y}E^{(a)}_{\mathbf{k}}\Big)\Big(\partial_{k_x}E^{(a)}_{\mathbf{k}}\Big) + 3t_{z,\mathbf{k}} f^{(2)}(\varepsilon)\Big|_{\varepsilon=E^{(a)}_{\mathbf{k}}}\Big(\partial_{k_x}\partial_{k_y}E^{(a)}_{\mathbf{k}}\Big)\\
& + 3f'(\varepsilon)\Big|_{\varepsilon=E^{(a)}_{\mathbf{k}}}(\partial_{k_x}\partial_{k_y}t_{z,\mathbf{k}})\Big]\Bigg\}.
\end{aligned} \tag{5.28}$$

Using Eq. (5.24) we can identify the coefficient c_{grad} in Eq. (5.17), coupling to $m\partial_x\partial_y J$,

$$\begin{aligned}
c_{\text{grad}} = \sum_{\mathbf{k},a}\frac{-1}{24\Big(E^{(a)}_{1,\mathbf{k}}\Big)^3}\Bigg\{ & 6t_{z,\mathbf{k}} f'(\varepsilon)\Big|_{\varepsilon=E^{(a)}_{\mathbf{k}}}\Big(\partial_{k_y}E^{(a)}_{1,\mathbf{k}}\Big)\Big(\partial_{k_x}E^{(a)}_{1,\mathbf{k}}\Big) - 3E^{(a)}_{1,\mathbf{k}} f'(\varepsilon)\Big|_{\varepsilon=E^{(a)}_{\mathbf{k}}}\Big[(\partial_{k_y}t_{z,\mathbf{k}})\Big(\partial_{k_x}E^{(a)}_{1,\mathbf{k}}\Big)\\
& + (\partial_{k_x}t_{z,\mathbf{k}})\Big(\partial_{k_y}E^{(a)}_{1,\mathbf{k}}\Big) + t_{z,\mathbf{k}}\Big(\partial_{k_x}\partial_{k_y}E^{(a)}_{1,\mathbf{k}}\Big)\Big] + \Big(E^{(a)}_{1,\mathbf{k}}\Big)^2\Big[3f'(\varepsilon)\Big|_{\varepsilon=E^{(a)}_{\mathbf{k}}}(\partial_{k_x}\partial_{k_y}t_{z,\mathbf{k}})\\
& + 3t_{z,\mathbf{k}} f''(\varepsilon)\Big|_{\varepsilon=E^{(a)}_{\mathbf{k}}}\Big(\partial_{k_x}\partial_{k_y}E^{(a)}_{\mathbf{k}}\Big) + t_{z,\mathbf{k}} f'''(\varepsilon)\Big|_{\varepsilon=E^{(a)}_{\mathbf{k}}}\Big(\partial_{k_y}E^{(a)}_{\mathbf{k}}\Big)\Big(\partial_{k_x}E^{(a)}_{\mathbf{k}}\Big)\Big]\Bigg\}.
\end{aligned} \tag{5.29}$$

Notably, this expression shows that a finite hopping $t_{z,\mathbf{k}}$ is essential to obtain a non-zero coefficient for the gradient term entering in the free energy. However, this hopping is only present in the case of an altermagnet, as opposed to the conventional antiferromagnet, due to the different environment on the two magnetic sublattices (see Fig. 4.1). Hence, altermagnetic and antiferromagnetic domain walls are equivalent only at the nodal planes, where $t_{z,\mathbf{k}}$ vanishes. The maximum value for the c_{grad} coefficient is obtained along the diagonal directions $k_x = \pm k_y$, where the spin splitting is maximum.

This is in agreement with Ref. [240], where they pointed out that in an antiferromagnet there is a perfect cancellation of the Néel order, leading to no induced magnetization at domain walls. However, for an altermagnet there is an anisotropy permitting the gradient terms in Landau theory, giving rise to a finite gradient of the magnetization. From the perspective of the microscopic model in Eq. (5.7), this anisotropy is introduced by the hopping $t_{z,\mathbf{k}}$, which gives a finite coefficient c_{grad}.

Moreover, we can also derive an analytic expression for the quartic contribution to the free energy using Eq. (5.11), obtaining

$$\begin{aligned} b_{J^4} = 4\sum_{\mathbf{k}} \frac{1}{(t_{x,\mathbf{k}}^2+t_{z,\mathbf{k}}^2)^2} \Bigg\{ & \frac{t_{x,\mathbf{k}}^4}{\left(E_{\mathbf{k}}^{(-)}-E_{\mathbf{k}}^{(+)}\right)^2}\left(f'(\varepsilon)\Big|_{\varepsilon=E_{\mathbf{k}}^{(+)}} + f'(\varepsilon)\Big|_{\varepsilon=E_{\mathbf{k}}^{(-)}} - 2\frac{f\left(E_{\mathbf{k}}^{(-)}\right)-f\left(E_{\mathbf{k}}^{(+)}\right)}{E_{\mathbf{k}}^{(-)}-E_{\mathbf{k}}^{(+)}}\right) \\ & + \frac{t_{z,\mathbf{k}}^4}{12}\left(f'''(\varepsilon)\Big|_{\varepsilon=E_{\mathbf{k}}^{(+)}} + f'''(\varepsilon)\Big|_{\varepsilon=E_{\mathbf{k}}^{(-)}}\right) + \frac{t_{x,\mathbf{k}}^2 t_{z,\mathbf{k}}^2}{\left(E_{\mathbf{k}}^{(-)}-E_{\mathbf{k}}^{(+)}\right)^2}\left(f''(\varepsilon)\Big|_{\varepsilon=E_{\mathbf{k}}^{(+)}} + f''(\varepsilon)\Big|_{\varepsilon=E_{\mathbf{k}}^{(-)}}\right. \\ & \left. -4\left[f'(\varepsilon)\Big|_{\varepsilon=E_{\mathbf{k}}^{(+)}} + f'(\varepsilon)\Big|_{\varepsilon=E_{\mathbf{k}}^{(-)}}\right] + 8\frac{f\left(E_{\mathbf{k}}^{(-)}\right)-f\left(E_{\mathbf{k}}^{(+)}\right)}{E_{\mathbf{k}}^{(-)}-E_{\mathbf{k}}^{(+)}}\right)\Bigg\}. \end{aligned} \tag{5.30}$$

This expression is also relevant since the sign of the coefficient will determine whether there is a first-order ($b_{J^4} > 0$) or second-order ($b_{J^4} < 0$) phase transition.

Finally, to solve for the magnetization induced at domain walls, we can minimize the free energy in Eq. (5.17) with respect to m, leading to

$$m = -\frac{c_{\text{grad}}\partial_x\partial_y J - h}{a_{m^2}}. \tag{5.31}$$

Notably, this expression shows that the magnetization can be obtained from the altermagnetic order parameter by calculating the coefficients a_{m^2} and c_{grad}, which are given in Eq. (5.22) and Eq. (5.29), respectively. In addition, it also allows us to compare the size of m with the size of J and analyze the temperature dependence. With this purpose, we realize that the gradients introduce a length scale squared, $\partial_x\partial_y \sim 1/\xi^2$, with $\xi = \sqrt{d/|a_{J^2}|}$, which is associated with the domain wall structure and corresponds to the correlation length introduced in Eq. (5.4). Therefore, Eq. (5.31) can be written as

$$m \sim \frac{c_{\text{grad}}}{a_{m^2}\xi_0^2}\left(1-\frac{T}{T_c}\right)J - \frac{h}{a_{m^2}}, \tag{5.32}$$

with ξ_0 denoting the coherence length introduced in Eq. (5.5) and the temperature dependence for the a_{J^2} coefficient given in Eq. (5.2). As a consequence, this equation reveals that the

magnetization induced at domain walls vanishes linearly with temperature, and the size of m can be compared to the size of J by determining c_{grad}, a_{m^2} and ξ_0.

To summarize, we have obtained analytic expressions for the coefficients entering in the Landau theory in Eq. (5.17) from the microscopic model in Eq. (5.7), revealing the importance of a non-zero hopping $t_{z,\mathbf{k}}$ to obtain a finite c_{grad} coefficient and consequently an induced magnetization gradient at domain walls. In Sec. 5.6, we will investigate how these coefficients are modified in the presence of SOC.

5.5 Domain wall couplings

In the previous section, we analyzed the free energy in a d-wave altermagnet neglecting SOC, observing that the form of the gradient term coupling m and J directly depends on symmetry of the altermagnetic spin splitting, which is given by $t_{z,\mathbf{k}}$ and belongs to the irrep Γ_N. In this section, we generalize the previous result and provide the phenomenological form for the gradient term for other space groups. Specifically, we classify all space groups and point groups containing inversion symmetry that allow for Wyckoff positions of multiplicity two and, in each case, we identify the symmetry of the spin splitting and the corresponding irrep Γ_N.

The minimal models are developed following the procedure detailed in Chapter 4. The first step is to list all space groups that contain inversion symmetry and Wyckoff positions of multiplicity two. As discussed in Secs. 4.2 and 4.8, the next step is to identify the operations that exchange the two sublattices, which define the symmetry properties of the τ_z operator in Eq. (5.7) and, consequently, the form of the hopping $t_{z,\mathbf{k}}$ describing the spin splitting. Equivalently, we can check the Wyckoff site symmetry (S), which is the group formed by all symmetry operations that leave the specific Wyckoff position invariant within the space group, and which can be found in the Bilbao crystallographic server [224, 225]. Thus, we can determine the operations of the point group symmetry P of the space group that are not contained in the site symmetry S by comparing the character tables, directly displaying the operations that exchange the two sublattices. Following this procedure, in Tables 5.1-5.2 we list the space groups, the Wyckoff positions and the irrep Γ_N with the corresponding form for the spin splitting.

Once the spin splitting is identified for the different space groups, the form for gradient term entering in the free energy coupling the orders m and J follows. Importantly, the irrep Γ_N determines if the coupling is quadratic, such as the example discussed in Sec. 5.4, quartic or even of sixth order in the gradient terms. As seen from Tables 5.1-5.2, the latter coupling is only relevant for space groups 192 and 223, which have an i-wave symmetry for the spin splitting (see Sec. 4.8.4 for the minimal model of space group 223). In contrast, the coupling to quartic order is relevant for materials such as MnTe, CrSb, and the tetragonal altermagnetic candidates Nb_2FeB_2 and Ta_2FeB_2, which are compatible with a g-wave symmetry for the spin splitting [257].

Tables 5.1-5.2 directly show that the gradient direction is connected to the spin splitting for each space group. Notably, this provides information on both the direction where the induced magnetization gradient is maximum and where it vanishes due to nodal planes or lines. As

Table 5.1: Space groups (SG) and Wyckoff positions of multiplicity 2 that allow altermagnetism: monoclinic (C_{2h}) and orthorhombic (D_{2h}) groups, with P denoting the point group for each space group and S the Wyckoff site symmetry. The notation follows the Bilbao crystallographic server [224, 225]. Γ_N corresponds to the irrep of the spin splitting in each point group, and the last column specifies the form of the gradient term in the free energy coupling the two order parameters m and J.

SG (P)	Wyckoff (S)	Γ_N	Spin splitting	Free energy grad. term
11 (C_{2h})	2a-2d (C_i)	B_g	$\alpha k_x k_y + \beta k_y k_z$	$m(\alpha\partial_x\partial_x + \beta\partial_y\partial_z)J$
12 (C_{2h})	4e, 4f (C_i)	B_g	$\alpha k_x k_y + \beta k_y k_z$	$m(\alpha\partial_x\partial_y + \beta\partial_y\partial_z)J$
13 (C_{2h})	2a-2d (C_i)	B_g	$\alpha k_x k_y + \beta k_y k_z$	$m(\alpha\partial_x\partial_y + \beta\partial_y\partial_z)J$
14 (C_{2h})	2a-2d (C_i)	B_g	$\alpha k_x k_y + \beta k_y k_z$	$m(\alpha\partial_x\partial_y + \beta\partial_y\partial_z)J$
15 (C_{2h})	2a-2d (C_i)	B_g	$\alpha k_x k_y + \beta k_y k_z$	$m(\alpha\partial_x\partial_y + \beta\partial_y\partial_z)J$
49 (D_{2h})	2a-2d (C_{2h})	B_{1g}	$k_x k_y$	$m\partial_x\partial_y J$
51 (D_{2h})	2a-2d (C_{2h})	B_{2g}	$k_x k_z$	$m\partial_x\partial_z J$
53 (D_{2h})	2a-2d (C_{2h})	B_{3g}	$k_y k_z$	$m\partial_y\partial_z J$
55 (D_{2h})	2a-2d (C_{2h})	B_{1g}	$k_x k_y$	$m\partial_x\partial_y J$
58 (D_{2h})	2a-2d (C_{2h})	B_{1g}	$k_x k_y$	$m\partial_x\partial_y J$
63 (D_{2h})	4a,4b (C_{2h})	B_{3g}	$k_y k_z$	$m\partial_y\partial_z J$
64 (D_{2h})	4a,4b (C_{2h})	B_{3g}	$k_y k_z$	$m\partial_y\partial_z J$
65 (D_{2h})	4e,4f (C_{2h})	B_{1g}	$k_x k_z$	$m\partial_x\partial_z J$
66 (D_{2h})	4c-4f (C_{2h})	B_{1g}	$k_x k_y$	$m\partial_x\partial_y J$
67 (D_{2h})	4c-4f (C_{2h})	B_{3g}	$k_x k_y$	$m\partial_x\partial_y J$
72 (D_{2h})	4c,4d (C_{2h})	B_{1g}	$k_x k_y$	$m\partial_x\partial_y J$
74 (D_{2h})	4a,4b (C_{2h})	B_{3g}	$k_x k_y$	$m\partial_x\partial_y J$
74 (D_{2h})	4c,4d (C_{2h})	B_{2g}	$k_x k_y$	$m\partial_x\partial_y J$

discussed in the previous section, in regions where the spin splitting vanishes, the domain walls are equivalent to those in antiferromagnets, and no magnetization gradient is induced.

Similarly to Sec. 5.4, we can use the minimal model for MnTe and CrSb derived in Sec. 4.8.3 in order to obtain an expression for c_{grad} from the microscopic model. As seen form Table 5.2, the contribution to the free energy has the following form,

$$f_{\text{grad}}^{\text{SG194}} = c_{\text{grad}} m\partial_y\partial_z(3\partial_x^2 - \partial_y^2)J. \tag{5.33}$$

Using Eq. (5.26), we have also observed that the coefficient c_{grad} is finite when the hopping $t_{z,\mathbf{k}}$ is non-zero, in agreement with Eq. (5.29).

Thus, we have generalized the result in Sec. 5.4 by writing the phenomenological form of the lowest-order coupling between the magnetization and the altermagnetic order parameter for different space groups, following the minimal model construction of Chapter 4. This provides information about the direction of the induced magnetization gradient at domain walls, which, as suggested in Ref. [240], may be useful to manipulate them by magnetic tips.

Table 5.2: Space groups (SG) and Wyckoff positions that allow altermagnetism: tetragonal (C_{4h}, D_{4h}), rhombohedral (D_{3d}), hexagonal (C_{6h}, D_{6h}), and cubic (O_h) groups, where P is the point group for each space group and S the Wyckoff site symmetry. The notation follows the Bilbao crystallographic server [224, 225]. Γ_N denotes the irrep of the spin splitting in each point group, and the last column specifies the form of the gradient term in the free energy coupling the two order parameters m and J.

SG (P)	Wyckoff (S)	Γ_N	Spin splitting	Free energy grad. term
83 (C_{4h})	2e,2f (C_{2h})	B_g	$\alpha k_x k_y + \beta(k_x^2 - k_y^2)$	$m(\alpha\partial_x\partial_y + \beta(\partial_x^2 - \partial_y^2))J$
84 (C_{4h})	2a-2d (C_{2h})	B_g	$\alpha k_x k_y + \beta(k_x^2 - k_y^2)$	$m(\alpha\partial_x\partial_y + \beta(\partial_x^2 - \partial_y^2))J$
87 (C_{4h})	4c (C_{2h})	B_g	$\alpha k_x k_y + \beta(k_x^2 - k_y^2)$	$m(\alpha\partial_x\partial_y + \beta(\partial_x^2 - \partial_y^2))J$
123 (D_{4h})	2e,2f (D_{2h})	B_{1g}	$k_x^2 - k_y^2$	$m(\partial_x^2 - \partial_y^2)J$
124 (D_{4h})	2b,2d (C_{4h})	A_{2g}	$k_x k_y(k_x^2 - k_y^2)$	$m\partial_x\partial_y(\partial_x^2 - \partial_y^2)J$
127 (D_{4h})	2a,2b (C_{4h})	A_{2g}	$k_x k_y(k_x^2 - k_y^2)$	$m\partial_x\partial_y(\partial_x^2 - \partial_y^2)J$
127 (D_{4h})	2c,2d (D_{2h})	B_{2g}	$k_x k_y$	$m\partial_x\partial_y\mathbf{J}$
128 (D_{4h})	2a,2b (C_{4h})	A_{2g}	$k_x k_y(k_x^2 - k_y^2)$	$m\partial_x\partial_y(\partial_x^2 - \partial_y^2)J$
131 (D_{4h})	2a-2d (D_{2h})	B_{1g}	$k_x^2 - k_y^2$	$m(\partial_x^2 - \partial_y^2)J$
132 (D_{4h})	2a,2c (D_{2h})	B_{2g}	$k_x k_y$	$m\partial_x\partial_y J$
136 (D_{4h})	2a,2b (D_{2h})	B_{2g}	$k_x k_y$	$m\partial_x\partial_y J$
139 (D_{4h})	4c (D_{2h})	B_{1g}	$k_x^2 - k_y^2$	$m(\partial_x^2 - \partial_y^2)J$
140 (D_{4h})	4c (C_{4h})	A_{2g}	$k_x k_y(k_x^2 - k_y^2)$	$m\partial_x\partial_y(\partial_x^2 - \partial_y^2)J$
140 (D_{4h})	4d (D_{2h})	B_{2g}	$k_x k_y$	$m\partial_x\partial_y J$
163 (D_{3d})	2b (S_6)	A_{2g}	$k_y k_z(k_y^2 - 3k_x^2)$	$m\partial_y\partial_z(\partial_y^2 - 3\partial_x^2)J$
165 (D_{3d})	2b (S_6)	A_{2g}	$k_x k_z(k_x^2 - 3k_y^2)$	$m\partial_x\partial_z(\partial_x^2 - 3\partial_y^2)J$
167 (D_{3d})	6b (S_6)	A_{2g}	$k_x k_z(k_x^2 - 3k_y^2)$	$m\partial_x\partial_z(\partial_x^2 - 3\partial_y^2)J$
176 (C_{6h})	2b (S_6)	B_g	$\alpha k_y k_z(k_y^2 - 3k_x^2)$ $+\beta k_x k_z(k_x^2 - 3k_y^2)$	$m(\alpha\partial_y\partial_z(\partial_y^2 - 3\partial_x^2)$ $+\beta\partial_x\partial_z(\partial_x^2 - 3\partial_y^2))J$
192 (D_{6h})	2b (C_{6h})	A_{2g}	$k_x k_y(k_x^2 - 3k_y^2)(k_y^2 - 3k_x^2)$	$m\partial_x\partial_y(\partial_x^2 - 3\partial_y^2)(\partial_y^2 - 3\partial_x^2)J$
193 (D_{6h})	2b (D_{3d})	B_{2g}	$k_x k_z(k_x^2 - 3k_y^2)$	$m\partial_x\partial_z(\partial_x^2 - 3\partial_y^2)J$
194 (D_{6h})	2a (D_{3d})	B_{1g}	$k_y k_z(3k_x^2 - k_y^2)$	$m\partial_y\partial_z(3\partial_x^2 - \partial_y^2)J$
223 (O_h)	2a (D_{3d})	A_{2g}	$k_x^4(k_y^2 - k_z^2)$ $+k_y^4(k_z^2 - k_x^2)$ $+k_z^4(k_x^2 - k_y^2)$	$m(\partial_x^4(\partial_y^2 - \partial_z^2)$ $+\partial_y^4(\partial_z^2 - \partial_x^2)$ $+\partial_z^4(\partial_x^2 - \partial_y^2))J$

5.6 Role of spin-orbit coupling: orientation of the Néel order

In the previous sections, we derived the form of the free energy from microscopic models and provided the phenomenological expression for the coupling between the two order parameters m and J in different space groups. However, so far we have neglected the effect of SOC. In this section, we include this effect and discuss how it modifies the free energy, focusing here on the orientation of the altermagnetic moments driven by SOC. Notably, in the presence of SOC, a bilinear coupling between the magnetization and the altermagnetic order parameter is allowed by symmetry in the free energy, which we will discuss in detail in Sec. 5.7.

Following Sec. 5.4, we introduce first the phenomenological form of the free energy and then derive each term from the microscopic model in Eq. (5.7). In the presence of SOC, we have to consider three-component order parameters, so that the altermagnetic order parameter and the magnetization are now denoted by $\vec{J}$ and $\vec{m}$, respectively. In this case, the phenomenological form of the free energy given in Eq. (5.17) is modified to

$$f = \frac{a_{J_x^2}}{2}J_x^2 + \frac{a_{J_y^2}}{2}J_y^2 + \frac{a_{J_z^2}}{2}J_z^2 + \frac{b_{J^4}}{4}\vec{J}^4 + \frac{a_{m_x^2}}{2}m_x^2 + \frac{a_{m_y^2}}{2}m_y^2 + \frac{a_{m_z^2}}{2}m_z^2 + \vec{c}_{\text{soc}}\cdot\vec{m}\times\vec{J} - \vec{h}\cdot\vec{m}, \quad (5.34)$$

where we have omitted the gradient terms, as we are now focusing on homogeneous order parameters. In orthorhombic systems, the coefficients for the quadratic altermagnetic order parameter are all different, $a_{J_x^2} \neq a_{J_y^2} \neq a_{J_z^2}$, in contrast to tetragonal systems, where the splitting occurs only in the z direction, $a_{J_x^2} = a_{J_y^2} \neq a_{J_z^2}$. As mentioned above, the coefficient $\vec{c}_{\text{soc}}$ for the bilinear coupling between $\vec{J}$ and $\vec{m}$ will be addressed in Sec. 5.7, where we will obtain the form of the coupling from the microscopic model. Note that we have only included the effect of SOC to quadratic order, as it gives rise to the largest splitting, and the quartic terms are only considered to stabilize the magnetic phase.

The purpose of this section is to investigate the splitting of the altermagnetic order parameter $\vec{J}$ due to SOC. Therefore, we aim to obtain an expression for the coefficients $a_{J_x^2}$, $a_{J_y^2}$ and $a_{J_z^2}$ in Eq. (5.34). Hence, we consider the second-order free energy contribution in Eq. (5.10), and focus on the interaction term coupling the two order parameters $\vec{J}$,

$$F_J^{(2)} = \frac{\mathcal{V}}{2}\,\text{Tr}\left[\sum_{a,b} G^{(a)}(\mathbf{k}, i\omega_n)G^{(b)}(\mathbf{k}, i\omega_n)\tau_z\vec{J}\cdot\vec{\sigma}P_{\mathbf{k}}^{(a)}\tau_z\vec{J}\cdot\vec{\sigma}P_{\mathbf{k}}^{(b)}\right]. \quad (5.35)$$

Recalling the form of the projector in Eq. (5.14), the first correction due to SOC is at the quadratic level and can be obtained by calculating the following trace,

$$\begin{aligned}&\frac{1}{16}\,\text{Tr}\big[\tau_z\vec{J}\cdot\vec{\sigma}\tau_y\vec{\lambda}_{\mathbf{k}}\cdot\vec{\sigma}\tau_z\vec{J}\cdot\vec{\sigma}\tau_y\vec{\lambda}_{\mathbf{k}}\cdot\vec{\sigma}\big]\\ &= -\frac{1}{4}\Big\{J_x^2(\lambda_{x,\mathbf{k}}^2 - \lambda_{y,\mathbf{k}}^2 - \lambda_{z,\mathbf{k}}^2) + J_y^2(-\lambda_{x,\mathbf{k}}^2 + \lambda_{y,\mathbf{k}}^2 - \lambda_{z,\mathbf{k}}^2) + J_z^2(-\lambda_{x,\mathbf{k}}^2 - \lambda_{y,\mathbf{k}}^2 + \lambda_{z,\mathbf{k}}^2)\\ &\quad + 4(J_xJ_y\lambda_{x,\mathbf{k}}\lambda_{y,\mathbf{k}} + J_xJ_z\lambda_{x,\mathbf{k}}\lambda_{z,\mathbf{k}} + J_yJ_z\lambda_{y,\mathbf{k}}\lambda_{z,\mathbf{k}})\Big\}.\end{aligned} \quad (5.36)$$

In general, due to the symmetry of the SOC in the minimal model (see Eqs. (4.5), (4.55) and (4.61)), the last line in this expression vanishes for all space groups in Tables 5.1-5.2 after performing the $\mathbf{k}$-sum, except for the monoclinic groups in Table 5.1 with point group $P = C_{2h}$.

Focusing on tetragonal systems, the contribution to the free energy in Eq. (5.34) quadratic in $\vec{J}$ simplifies to $\frac{a_{J_x^2}}{2}(J_x^2+J_y^2)+\frac{a_{J_z^2}}{2}J_z^2$. Therefore, including the correction due to SOC from Eq. (5.36), the coefficient in Eq. (5.20) is split into

$$a_{J_x^2} = -2\sum_{\mathbf{k}}\frac{1}{t_{x,\mathbf{k}}^2+t_{z,\mathbf{k}}^2+\vec{\lambda}_{\mathbf{k}}^2}\left\{t_{z,\mathbf{k}}^2\left[\left.\frac{df(\varepsilon)}{d\varepsilon}\right|_{\varepsilon=E_{\mathbf{k}}^{(+)}}+\left.\frac{df(\varepsilon)}{d\varepsilon}\right|_{\varepsilon=E_{\mathbf{k}}^{(-)}}\right]+t_{x,\mathbf{k}}^2\frac{2\left[f\left(E_{\mathbf{k}}^{(-)}\right)-f\left(E_{\mathbf{k}}^{(+)}\right)\right]}{E_{\mathbf{k}}^{(-)}-E_{\mathbf{k}}^{(+)}}\right\}$$
$$-\sum_{\mathbf{k}}\frac{\lambda_{z,\mathbf{k}}^2}{t_{x,\mathbf{k}}^2+t_{z,\mathbf{k}}^2+\vec{\lambda}_{\mathbf{k}}^2}\left\{\left.\frac{df(\varepsilon)}{d\varepsilon}\right|_{\varepsilon=E_{\mathbf{k}}^{(+)}}+\left.\frac{df(\varepsilon)}{d\varepsilon}\right|_{\varepsilon=E_{\mathbf{k}}^{(-)}}-\frac{2\left[f\left(E_{\mathbf{k}}^{(-)}\right)-f\left(E_{\mathbf{k}}^{(+)}\right)\right]}{E_{\mathbf{k}}^{(-)}-E_{\mathbf{k}}^{(+)}}\right\}, \tag{5.37}$$

$$a_{J_z^2} = -2\sum_{\mathbf{k}}\frac{1}{t_{x,\mathbf{k}}^2+t_{z,\mathbf{k}}^2+\vec{\lambda}_{\mathbf{k}}^2}\left\{t_{z,\mathbf{k}}^2\left[\left.\frac{df(\varepsilon)}{d\varepsilon}\right|_{\varepsilon=E_{\mathbf{k}}^{(+)}}+\left.\frac{df(\varepsilon)}{d\varepsilon}\right|_{\varepsilon=E_{\mathbf{k}}^{(-)}}\right]+t_{x,\mathbf{k}}^2\frac{2\left[f\left(E_{\mathbf{k}}^{(-)}\right)-f\left(E_{\mathbf{k}}^{(+)}\right)\right]}{E_{\mathbf{k}}^{(-)}-E_{\mathbf{k}}^{(+)}}\right\}$$
$$-\sum_{\mathbf{k}}\frac{\lambda_{x,\mathbf{k}}^2+\lambda_{y,\mathbf{k}}^2-\lambda_{z,\mathbf{k}}^2}{t_{x,\mathbf{k}}^2+t_{z,\mathbf{k}}^2+\vec{\lambda}_{\mathbf{k}}^2}\left\{\left.\frac{df(\varepsilon)}{d\varepsilon}\right|_{\varepsilon=E_{\mathbf{k}}^{(+)}}+\left.\frac{df(\varepsilon)}{d\varepsilon}\right|_{\varepsilon=E_{\mathbf{k}}^{(-)}}-\frac{2\left[f\left(E_{\mathbf{k}}^{(-)}\right)-f\left(E_{\mathbf{k}}^{(+)}\right)\right]}{E_{\mathbf{k}}^{(-)}-E_{\mathbf{k}}^{(+)}}\right\}. \tag{5.38}$$

To determine the preferred moment orientation, we can examine the following expression,

$$a_{J_x^2}-a_{J_z^2} = 2\sum_{\mathbf{k}}\frac{\lambda_{x,\mathbf{k}}^2-\lambda_{z,\mathbf{k}}^2}{t_{x,\mathbf{k}}^2+t_{z,\mathbf{k}}^2+\vec{\lambda}_{\mathbf{k}}^2}\left\{\left.\frac{df(\varepsilon)}{d\varepsilon}\right|_{\varepsilon=E_{\mathbf{k}}^{(+)}}+\left.\frac{df(\varepsilon)}{d\varepsilon}\right|_{\varepsilon=E_{\mathbf{k}}^{(-)}}-\frac{2\left[f\left(E_{\mathbf{k}}^{(-)}\right)-f\left(E_{\mathbf{k}}^{(+)}\right)\right]}{E_{\mathbf{k}}^{(-)}-E_{\mathbf{k}}^{(+)}}\right\}. \tag{5.39}$$

Here, we have used that $E_{\mathbf{k}}^{(\pm)}$ transforms trivially under the operations of the point group D_{4h}, so that for tetragonal systems $\lambda_{x,\mathbf{k}}^2$ gives the same contribution as $\lambda_{y,\mathbf{k}}^2$ under the integral (see Eq. (4.5)).

As seen from Eq. (4.5), for the particular case of RuO_2 we expect $\lambda > \lambda_z$, since the $\mathbf{k}$-dependence of the SOC term in the z direction is of higher order. To calculate Eq. (5.39), we consider again the one-orbital model relevant for RuO_2 derived in Sec. 4.3 with the band structure shown in Fig. 4.5(a). Using $\lambda > \lambda_z$, we find $a_{J_z^2} > a_{J_x^2}$, and therefore the minimal model predicts an out-of-plane orientation for the altermagnetic moments, in agreement with the experimental observation reported in Ref. [208].

Thus, Eq. (5.35) allows us to predict the preferred direction for the altermagnetic moments from microscopic models. This also applies to hexagonal systems, where $\lambda_{x,\mathbf{k}}$ and $\lambda_{y,\mathbf{k}}$ are related by symmetry, as seen from the SOC form in Eq. (4.61) for the model relevant to CrSb and MnTe. In contrast, for orthorhombic systems, the three coefficients are different, as seen from Eq. (4.55) for the model relevant to $FeSb_2$, resulting in $a_{J_x^2} \neq a_{J_y^2} \neq a_{J_z^2}$.

5.7 Bilinear coupling between magnetization and Néel order

Having introduced the phenomenological expression for the free energy in the presence of SOC in Eq. (5.34), in this section we focus on the bilinear coupling between the magnetization and the Néel order that is now permitted by symmetry. We begin by considering all point groups entering in Tables 5.1-5.2 and obtaining an expression for the free energy invariant when this

term is symmetry allowed. Then, we turn to the minimal model in Eq. (5.7). First, we derive the form of the coupling $\vec{c}_{\text{soc}} \cdot \vec{m} \times \vec{J}$ introduced in Eq. (5.34), and find an analytic expression for the coefficient $\vec{c}_{\text{soc}}$. Secondly, we analyze how this form of the coupling restricts the free energy invariants that are generated from the minimal model. This provides information on the dependence of the induced weak ferromagnetism on the strength of the SOC.

5.7.1 General symmetry arguments

In order to construct the free energy, we must identify the combinations of the two order parameters that transform like invariants, similarly to Sec. 3.2. Hence, the first step is to identify the transformation properties of the order parameters. As seen from Eq. (5.8), the magnetization $\vec{m}$ transforms like the spin degrees of freedom in each point group, and thus belongs to the axial vector irrep Γ_A. In contrast, $\vec{J}$ belongs to the irrep $\Gamma_A \otimes \Gamma_N$, with Γ_N denoting the symmetry of the $t_{z,\mathbf{k}}$ hopping identified in Tables 5.1-5.2, see also Eq. (5.7) and the discussion below it. As discussed in Ref. [253], a bilinear coupling between the two orders exists if the direct product $\Gamma_A \otimes \Gamma_A \otimes \Gamma_N$ contains the irrep transforming trivially under all point group operations. Equivalently, there is a free energy invariant if $\Gamma_A \otimes \Gamma_A$ contains Γ_N.

Let us illustrate this with an example, considering the point group D_{4h}. In this case, $\Gamma_A = E_g \oplus A_{2g}$ (see Table 2.1), and therefore from the product tables we find $\Gamma_A \otimes \Gamma_A = A_{1g} \oplus 2E_g \oplus (E_g \otimes E_g)$. Neither A_{1g} nor E_g belong to Γ_N, as seen from Table 5.2, so the only invariants can come from $E_g \otimes E_g = A_{1g} \oplus A_{2g} \oplus B_{1g} \oplus B_{2g}$. Therefore, for each of $\Gamma_N = A_{2g}, B_{1g}, B_{2g}$ there is an allowed bilinear coupling. In particular, let us focus now on the case $\Gamma_N = B_{2g}$. The magnetization transforms like the spin Pauli matrices, $(m_x, m_y) \sim (\sigma_x, \sigma_y) \sim (k_x k_z, k_y k_z)$, while from Eq. (5.8) we see that for the Néel order $(J_x, J_y) \sim \tau_z(\sigma_x, \sigma_y) \sim (k_y k_z, k_x k_z)$, where we have used that τ_z transforms like $\Gamma_N = B_{2g} \sim k_x k_y$. As a consequence, this shows that the only allowed invariant is given by $m_x J_y + m_y J_x$. Following this procedure, in Table 5.3 we list the invariant for all point groups, using the axial vector irrep detailed in Table 5.4.

Importantly, for the point group D_{6h}, the axial vector corresponds to $\Gamma_A = A_{2g} \oplus E_{1g}$. In contrast to the previous example, now the only invariant can come from $E_{1g} \otimes E_{1g} = A_{1g} \oplus A_{2g} \oplus E_{2g}$, and therefore there is only a bilinear coupling for $\Gamma_N = A_{2g}$. In particular, this result is relevant for the altermagnetic material candidates MnTe and CrSb discussed in Sec. 4.8.3, which belong to space group 194 with Wyckoff position 2a, and thus $\Gamma_N = B_{1g}$ (see Table 5.2). Therefore, for $\Gamma_N = B_{1g}$ only higher-order couplings between $\vec{J}$ and $\vec{m}$ are allowed, in general giving rise to a smaller magnetization when compared to the case $\Gamma_N = A_{2g}$. This result is in agreement with Ref. [244], where the small ferromagnetic moment in MnTe was recently discussed.

Thus, directly from symmetry arguments, we can identify point groups for which the magnetization only couples to $\vec{J}$ through higher-order terms in the SOC. As seen from Table 5.3, they correspond to C_{6h}, O_h, and $\Gamma_N = B_{1g}, B_{2g}$ for D_{6h}, which would generally give rise to a smaller magnetization when compared to the other cases where the bilinear coupling is allowed.

Table 5.3: Free energy invariant for the bilinear coupling between $\vec{m}$ and $\vec{J}$ in the presence of SOC, with P denoting the point group and Γ_N corresponding to the irrep of the spin splitting in each point group. The last column specifies if the coupling is generated from the order parameter $\tau_z \vec{J} \cdot \vec{\sigma}$, otherwise a secondary order parameter is needed to obtain the coupling.

P	Γ_N	Invariant	Coupling generated with $\tau_z \vec{J} \cdot \vec{\sigma}$
C_{2h}	B_g	$\alpha_1 J_x m_z$, $\alpha_2 J_y m_z$ $\alpha_3 J_z m_y$, $\alpha_4 J_z m_x$	✓
D_{2h}	B_{1g}	$\alpha_1 m_x J_y + \alpha_2 m_y J_x$	$\alpha_1 = \alpha_2$: ✘ $\alpha_1 \neq \alpha_2$: ✓
D_{2h}	B_{2g}	$\alpha_1 m_y J_z + \alpha_2 m_z J_y$	$\alpha_1 = \alpha_2$: ✘ $\alpha_1 \neq \alpha_2$: ✓
D_{2h}	B_{3g}	$\alpha_1 m_z J_x + \alpha_2 m_x J_z$	$\alpha_1 = \alpha_2$: ✘ $\alpha_1 \neq \alpha_2$: ✓
C_{4h}	B_g	$m_x J_y + m_y J_x$, $m_x J_x - m_y J_y$	✘
D_{4h}	A_{2g}	$m_x J_y - m_y J_x$	✓
D_{4h}	B_{1g}	$m_x J_x - m_y J_y$	✘
D_{4h}	B_{2g}	$m_x J_y + m_y J_x$	✘
D_{3d}	A_{2g}	$m_x J_y - m_y J_x$	✓
C_{6h}	B_g	-	-
D_{6h}	A_{2g}	$m_x J_y - m_y J_x$	✓
D_{6h}	B_{1g}	-	-
D_{6h}	B_{2g}	-	-
O_h	A_{2g}	-	-

Table 5.4: Axial vector irreducible representation Γ_A and antisymmetric direct product $[\Gamma_A \otimes \Gamma_A]_-$ relevant for Sec. 5.7.2 (see Appendix F) for all point groups considered in Table 5.3.

P	C_{2h}	D_{2h}	C_{4h}	D_{4h}	D_{3d}	C_{6h}	D_{6h}	O_h
Γ_A	$B_g \oplus A_g$	$B_{1g} \oplus B_{2g} \oplus B_{3g}$	$A_g \oplus E_g$	$E_g \oplus A_{2g}$	$A_{2g} \oplus E_g$	$A_g \oplus E_{1g}$	$A_{2g} \oplus E_{1g}$	T_{1g}
$[\Gamma_A \otimes \Gamma_A]_-$	B_g	$B_{1g} \oplus B_{2g} \oplus B_{3g}$	A_g	A_{2g}	A_{2g}	A_g	A_{2g}	T_{1g}

5.7.2 Conclusions from microscopic models

In the previous section, we constructed the free energy invariant for the different point groups, based only on symmetry considerations. Here, we consider again the microscopic model in Eq. (5.7) to investigate whether the previous invariants are indeed generated from this model.

With this purpose, we calculate the lowest-order coupling between the altermagnetic order parameter and the magnetization. Hence, we derive the contribution to the free energy using Eq. (5.10) which contains mixed interactions in $\vec{m}$ and $\vec{J}$,

$$F_{mJ}^{(2)} = \frac{\mathcal{V}}{\beta}\,\mathrm{Tr}\left[\sum_{a,b} G^{(a)}(\mathbf{k}, i\omega_n) G^{(b)}(\mathbf{k}, i\omega_n)\tau_z \vec{J}\cdot\vec{\sigma} P_{\mathbf{k}}^{(a)} \vec{m}\cdot\vec{\sigma} P_{\mathbf{k}}^{(b)}\right]. \tag{5.40}$$

We focus first on calculating the trace with the projector given in Eq. (5.14),

$$\frac{1}{16}\,\mathrm{Tr}\left[\tau_z \vec{J}\cdot\vec{\sigma}\left(\mathbb{1} + \frac{H_1(\mathbf{k})}{E_{1,\mathbf{k}}^{(a)}}\right)\vec{m}\cdot\vec{\sigma}\left(\mathbb{1} + \frac{H_1(\mathbf{k})}{E_{1,\mathbf{k}}^{(b)}}\right)\right]. \tag{5.41}$$

As shown in Eq. (5.23), in the absence of SOC the free energy for the mixed term vanishes. Thus, we focus on the first correction due to SOC from $\tau_y\vec{\lambda}_{\mathbf{k}}\cdot\vec{\sigma}$ entering in $H_1(\mathbf{k})$. The only non-zero contribution is obtained when the previous term is combined with τ_x in the other Hamiltonian, obtaining

$$2i\frac{t_{x,\mathbf{k}}}{16}\,\mathrm{Tr}\big[(\vec{J}\cdot\vec{\sigma})(\vec{\lambda}_{\mathbf{k}}\cdot\vec{\sigma})(\vec{m}\cdot\vec{\sigma})\big] = \frac{t_{x,\mathbf{k}}}{2}\vec{\lambda}_{\mathbf{k}}\cdot(\vec{m}\times\vec{J}). \tag{5.42}$$

With this result, we can write the free energy in Eq. (5.40) as

$$F_{mJ}^{(2)} = \frac{\mathcal{V}}{2\beta}\sum_{i\omega_n,\mathbf{k}}\sum_{a,b}\frac{t_{x,\mathbf{k}}}{E_{1,\mathbf{k}}^{(a)}E_{1,\mathbf{k}}^{(b)}}G^{(a)}(\mathbf{k}, i\omega_n)G^{(b)}(\mathbf{k}, i\omega_n)\vec{\lambda}_{\mathbf{k}}\cdot(\vec{m}\times\vec{J}). \tag{5.43}$$

By comparing with the form $\vec{c}_{\mathrm{soc}}\cdot\vec{m}\times\vec{J}$ in Eq. (5.34), we can identify an expression for the $\vec{c}_{\mathrm{soc}}$ coefficient. Performing the Matsubara sum, it can be written as

$$\vec{c}_{\mathrm{soc}} = 2\sum_{\mathbf{k}}\vec{\lambda}_{\mathbf{k}}\frac{t_{x,\mathbf{k}}}{t_{x,\mathbf{k}}^2 + t_{z,\mathbf{k}}^2 + \vec{\lambda}_{\mathbf{k}}^2}\left\{\left.\frac{df(\varepsilon)}{d\varepsilon}\right|_{\varepsilon=E_{\mathbf{k}}^{(+)}} + \left.\frac{df(\varepsilon)}{d\varepsilon}\right|_{\varepsilon=E_{\mathbf{k}}^{(-)}} - \frac{2\left[f\left(E_{\mathbf{k}}^{(-)}\right) - f\left(E_{\mathbf{k}}^{(+)}\right)\right]}{E_{\mathbf{k}}^{(-)} - E_{\mathbf{k}}^{(+)}}\right\}. \tag{5.44}$$

The form $\vec{m}\times\vec{J}$ entering in the free energy shows that the minimal model only generates invariants with an antisymmetric combination of the two order parameter components. Thus, following the group theory formalism introduced in the previous section, this implies that the microscopic model in Eq. (5.7) only gives an invariant if the antisymmetric direct product of the two axial vectors, $[\Gamma_A\otimes\Gamma_A]_-$, contains Γ_N. The antisymmetric product for all the point groups considered is included in Table 5.4, while Appendix F details the procedure for calculating it.

Let us focus again on the previous example for the point group D_{4h}. As seen from Table 5.3, an invariant can be written for $\Gamma_N = A_{2g}, B_{1g}, B_{2g}$. However, since $[E_g\otimes E_g]_- = A_{2g}$ (see Appendix F), the minimal model only gives a non-vanishing bilinear coupling for $\Gamma_N = A_{2g}$. Table 5.3 shows that this coupling is of the form $\hat{z}\cdot\vec{m}\times\vec{J}$, as expected from Eq. (5.43). Focusing on Eq. (5.44), we can verify that the invariant is not generated for RuO_2, where $\Gamma_N = B_{2g}$. This

is because, as seen from Eq. (4.5), all components of $\vec{\lambda}_{\mathbf{k}}$ transform like a non-trivial irrep of D_{4h}. Therefore, since the other quantities entering in Eq. (5.44) have the full symmetry of the point group, after performing the $\mathbf{k}$ integral the coefficient $\vec{c}_{\text{soc}}$ vanishes, in agreement with the previous argument from the antisymmetric direct product.

Following this procedure and using the results for the antisymmetric direct product listed in Table 5.4, we indicate in Table 5.3 whether the altermagnetic order parameter $\tau_z \vec{J} \cdot \vec{\sigma}$ generates the invariants for the different point groups, which would give rise to an induced weak ferromagnetism that is linear in the strength of the SOC. In the cases where it is not generated, we expect that it will be at least quadratic in the SOC. Given that the effect of SOC is predicted to be small in altermagnets [26], the induced ferromagnetism will be larger when the minimal model gives rise to the invariant.

Interestingly, focusing on orthorhombic materials, with $P = D_{2h}$, Table 5.3 shows that the invariant is always generated from the minimal model when the antisymmetric combination is also obtained, i.e., away from the fine-tuned case $\alpha_1 = \alpha_2$. Thus, the microscopic model predicts a magnetization linear in the SOC strength.

Remarkably, Ref. [257] recently identified two tetragonal altermagnetic material candidates compatible with a g-wave symmetry for the spin splitting, Nb_2FeB_2 and Ta_2FeB_2. These two materials belong to space group 127 and Wyckoff position 2a for the Fe sites, and therefore they correspond to $\Gamma_N = A_{2g}$, as seen from Table 5.2. In this case, Table 5.3 shows that a bilinear coupling between $\vec{m}$ and $\vec{J}$ linear in the SOC is generated from the minimal model. As a consequence, we predict a larger induced magnetization for these two tetragonal materials than in RuO_2.

However, in the presence of the magnetic orders $\vec{J}$ and $\vec{m}$, other secondary order parameters that share the same symmetry are also always induced. For instance, the order parameter $\sin\frac{k_x}{2}\sin\frac{k_y}{2}\cos\frac{k_z}{2}\tau_x\sigma_x$ or the current loop order $\sin\frac{k_x}{2}\cos\frac{k_y}{2}\sin\frac{k_z}{2}\tau_y$ share the same symmetry as m_y and J_x, and thus they coexist. These secondary order parameters may generate the bilinear couplings that are not obtained from $\tau_z \vec{J} \cdot \vec{\sigma}$, but we expect that the coupling through secondary order parameters will in general be of higher order in the SOC, therefore giving smaller magnetizations. The role of secondary order parameters should be investigated in more detail, but we leave it as future work as this is beyond the scope of this Chapter.

5.7.3 Interplay with anomalous Hall effect

Having introduced the general symmetry arguments to derive the form of the invariant for the induced magnetization, and having explored which are generated from the microscopic model in Eq. (5.7), we end this section by briefly discussing the interplay of the magnetization with the anomalous Hall effect. Previous works revealed that the anomalous Hall effect is symmetry enforced to be finite together with a non-zero magnetization [250, 251]. Here, we focus on comparing the size of the two effects and the dependence on the SOC strength.

In Sec. 4.7 we derived a general analytic expression for the Berry curvature which is linear in the SOC, and explicitly demonstrated for RuO_2 that the Berry curvature is large and yields a finite Hall conductivity linear in the SOC, see Figs. 4.12-4.13. In particular, the general

expression for the Berry curvature is given in Eq. (4.50). Due to the non-trivial symmetry of $t_{z,\mathbf{k}}$ and $\lambda_{x,\mathbf{k}}$, only the following term gives rise to a finite Hall conductivity after performing the $\mathbf{k}$ integral (see Eq. (4.51)),

$$\Omega_{ij}^{(\alpha,\beta)} = \frac{1}{\left(E_{\mathbf{k}}^{(\alpha,\beta)}\right)^3} \sum_{m,n=i,j} \varepsilon_{mn} J \partial_m \lambda_{x,\mathbf{k}} \partial_n t_{x,\mathbf{k}}. \tag{5.45}$$

This clearly shows that the Berry curvature is linear in the SOC and does not depend on the hopping $t_{z,\mathbf{k}}$. Hence, when the anomalous Hall effect is symmetry allowed, the minimal model reveals that it is always non-zero and of the same order of magnitude for all Γ_N, as opposed to the magnetization, which may be of higher order in the SOC depending on Γ_N (see Table 5.3).

5.8 Discussion and conclusions

In this Chapter, we have obtained the Landau free energy expansion and the analytic expressions for the coefficients from the minimal models constructed in Chapter 4. With this purpose, we have introduced the magnetization and the altermagnetic order parameters and we have calculated the quadratic and quartic contributions to the free energy expansion. We have focused first on a d-wave altermagnet to derive the coefficients, and we have demonstrated that the lowest-order coupling between m and J is given by the gradient terms in the absence of SOC. The analytic expression for this coefficient showed that the gradient term is non-zero only when the hopping $t_{z,\mathbf{k}}$ is finite. In addition, we have minimized the free energy with respect to the magnetization to find an expression relating m and J, which revealed that the magnetization vanishes linearly with temperature and that its size can be compared to J by using the analytic expressions for the coefficients entering in the free energy expansion.

We have extended the minimal models in Chapter 4 to obtain the symmetry of the spin splitting for all space groups containing inversion symmetry and Wyckoff positions of multiplicity two, which allowed us to provide the phenomenological form of the gradient terms in all these cases. We noticed that the coupling of the magnetization and the altermagnetic order parameter through the gradient terms is dictated by the symmetry of the spin splitting and can be quadratic (as in the d-wave altermagnet case), quartic or even of sixth order, depending on the space group and the Wyckoff position.

Moreover, we have included the role of SOC to investigate how it modifies the free energy, considering three-component order parameters. First, we have focused on the orientation of the altermagnetic moments due to SOC, demonstrating that for tetragonal systems the free energy splits and the in-plane and out-of-plane coefficients become distinct. By applying the expressions to the particular case of RuO_2, we have observed that the preferred orientation for the moments is out-of-plane.

Then, we have focused on the bilinear coupling between the magnetization and the altermagnetic order parameter that is only allowed in the presence of SOC. By using general symmetry arguments, we have constructed the form of the free energy invariant for all relevant point groups, already revealing that in MnTe and CrSb only higher-order couplings between $\vec{m}$ and $\vec{J}$ are allowed. We have derived the form of the bilinear coupling from the microscopic model,

obtaining that only antisymmetric combinations of the two orders are generated. In these cases, the induced weak ferromagnetism is linear in the SOC, and therefore it will be larger, as SOC is expected to have a weak effect on altermagnets [26]. Importantly, in RuO_2 the coupling between the magnetization and the altermagnetic order parameter from the minimal model is at least quadratic in the SOC, and thus we predict a smaller induced magnetization compared to the tetragonal altermagnetic material candidates Nb_2FeB_2 and Ta_2FeB_2 [257] or orthorhombic compounds, where the coupling should be linear in the SOC. Finally, we have investigated the interplay with the anomalous Hall effect, showing that the minimal model gives rise to a large Hall conductivity linear in the SOC, while depending on the symmetry of the spin splitting the induced magnetization may be of higher order in the SOC.

Furthermore, we have also pointed out that secondary order parameters with the same symmetry as the magnetization and altermagnetic orders are also always induced, which may give rise to a bilinear coupling. In this direction, we could construct the free energy for the secondary order parameters and obtain the analytic expressions for the Landau coefficients to determine whether the induced magnetization is linear or of higher order in the SOC. Additionally, we could investigate the new contributions generated to the anomalous Hall effects. Notably, it would be interesting to explore the current loop order $\sin\frac{k_x}{2}\cos\frac{k_y}{2}\sin\frac{k_z}{2}\tau_y$, which shares the same symmetry as the altermagnetic order $\tau_z\sigma_x$ in RuO_2, but does not couple to the spin degree of freedom.

Finally, we have shown that SOC induces weak ferromagnetism by permitting a coupling of the magnetization and altermagnetic order parameter in the free energy. Thus, a natural next step would be to formulate the Landau free energy for the coupling of the induced ferromagnetism to external fields, which may reveal new directions to manipulate altermagnetic domain walls. Similarly, as discussed in Sec. 4.9, strain can also be included in the minimal model to explore the new terms allowed in Landau theory, and to examine the effect on domain walls and the induced magnetization. With the insight from Landau theory, we could solve self-consistently for the order parameters and study the domain walls to determine the magnetization gradient profile and observe how it is modified by external fields.

Conclusions and Outlook

In this thesis, we have explored different topics of current interest in the fields of superconductivity and magnetism. Here, we present a summary of the main results and discuss directions for future research.

In the first part of the thesis, we studied unconventional superconductivity arising from the Hubbard model. First, in Chapter 1 we considered a single-orbital extended Hubbard model and derived the pairing interaction within an RPA spin-fluctuation mechanism approach. We investigated the role of extended Coulomb interactions in the preferred superconducting state, obtaining phase diagrams with many transitions between different symmetries. These rich phase diagrams offer many possibilities to form accidental degeneracies between spin-singlet orders, where the condensate develops a complex order parameter exhibiting time-reversal symmetry breaking. Thus, this suggests that these exotic states may occur in materials where longer-range Coulomb interactions are important, as it has been proposed for Sr_2RuO_4 or the Kagome metals [18, 113], even though these materials require generalizing the approach to describe multiorbital systems.

In Chapter 2, we focused on multiorbital systems to compare on equal footing spin-fluctuation mediated pairing and Hund's pairing. With this purpose, we considered a two-orbital model relevant for iron-based superconductors, which shows almost no nesting, and a three-orbital model relevant for Sr_2RuO_4, where the susceptibility exhibits significant momentum dependence. In the latter case, the spin-fluctuation mechanism dominates over Hund's pairing, giving rise to higher critical temperatures, whereas for the two-orbital model the two pairing mechanisms lead to comparable results. This suggests that, in systems with a strong momentum-dependent susceptibility, the inter-orbital spin-triplet states obtained from Hund's pairing might not be stabilized. The comparison of the two pairing mechanisms could also be applied to other relevant unconventional superconductors where Hund's pairing has been proposed as the mechanism giving rise to superconductivity [122, 124–126, 128–133].

In the second part of the thesis, we explored the superconducting diode effect for a Rashba superconductor. Specifically, in Chapter 3 we compared two configurations inducing the helical phase and the diode effect: an in-plane magnetic field and a uniform out-of-plane magnetization gradient. Notably, we demonstrated for a wide range of parameters that both mechanisms generate comparable diode efficiencies. Hence, magnetization gradients may offer a realistic alternative to experimentally realize the diode effect. Moreover, we analyzed different profiles for the magnetization gradient, although a further optimization of the profile could significantly

enhance the efficiency. In this direction, a natural next step would be to introduce magnetization gradients with a non-vanishing profile, since in this thesis we focused on devices with no net out-of-plane magnetization. Also importantly, by considering arrays of impurities, we observed that bound states close to zero energy might play an important role in enhancing the diode efficiency. This could be further investigated by considering a minimal model with two magnetic impurities and analyzing the current-phase relations for different bound states energies.

In the last part of the thesis, we focused on the emergent field of altermagnetism. In particular, in Chapter 4 we constructed minimal models for altermagnetism, and applied them to altermagnetic material candidates of current interest. The minimal models allowed us to derive analytic expressions for the susceptibilities and the Berry curvature, revealing the role of degeneracies in stabilizing altermagnetism and obtaining a large anomalous Hall response. In addition, we found that nodal planes and lines give rise to a large Berry curvature. Along these lines, it would be interesting to investigate other experimental responses that get enhanced. Moreover, we demonstrated that the minimal models are sufficiently general to describe d-wave, g-wave and i-wave symmetry for the spin splitting. Nonetheless, we restricted to Wyckoff positions of multiplicity two, and hence a natural extension would be to generalize the model to describe materials with more atoms or orbitals per unit cell.

The minimal models provided the setup to derive the Landau free energy in terms of the magnetization and the altermagnetic order parameter. Concretely, in Chapter 5 we obtained expressions for the coefficients in the Landau theory from the minimal models. In addition, we introduced the phenomenological form for the gradient terms coupling the two order parameters at domain walls for all space groups that allow Wyckoff positions of multiplicity two. In the presence of SOC, we have shown that there is a preferred orientation of the altermagnetic moments, which depends on hopping parameters and SOC strength. Moreover, when the effect of SOC is included, there is an allowed bilinear coupling between the magnetization and the altermagnetic order parameter, which may be linear or of higher order in the SOC depending on the irreducible representation for the spin splitting. Finally, investigating the coupling of the induced magnetization to an external field or applied strain using Landau theory may reveal methods to manipulate domain walls, paving the way for experimental detection and applications of altermagnetism.

Appendix A

Fourier transformation of the effective interaction in real space

In this Appendix, we describe how to Fourier transform the effective interaction obtained by summing up the contribution from bubble and ladder diagrams to all orders, as described in Sec. 1.2. To generalize the result, we start from a multiorbital interaction Hamiltonian in momentum space,

$$H_{\text{int}} = \sum_{\mathbf{k},\mathbf{k}',\tilde{\mu}_i} [V(\mathbf{k},\mathbf{k}')]^{\tilde{\mu}_1\tilde{\mu}_2}_{\tilde{\mu}_3\tilde{\mu}_4} c^\dagger_{\mathbf{k}\tilde{\mu}_1} c^\dagger_{-\mathbf{k}\tilde{\mu}_3} c_{-\mathbf{k}'\tilde{\mu}_2} c_{\mathbf{k}'\tilde{\mu}_4}, \tag{A.1}$$

where $\tilde{\mu}_i = \mu_i \sigma_i$ is a combined index including orbital and spin degrees of freedom. We Fourier transform this Hamiltonian to real space,

$$H = \sum_{\mathbf{i},\Delta\mathbf{r}} \sum_{\tilde{\mu}_i} \sum_{\mathbf{k},\mathbf{k}'} [V(\mathbf{k},\mathbf{k}')]^{\tilde{\mu}_1\tilde{\mu}_2}_{\tilde{\mu}_3\tilde{\mu}_4} e^{i(\mathbf{k}-\mathbf{k}')\cdot\Delta\mathbf{r}} c^\dagger_{\mathbf{i}\tilde{\mu}_1} c^\dagger_{\mathbf{i}+\Delta\mathbf{r}\tilde{\mu}_3} c_{\mathbf{i}+\Delta\mathbf{r}\tilde{\mu}_2} c_{\mathbf{i}\tilde{\mu}_4}. \tag{A.2}$$

Hence, the effective interaction in real space is given by

$$[V(\Delta\mathbf{r})]^{\tilde{\mu}_1\tilde{\mu}_2}_{\tilde{\mu}_3\tilde{\mu}_4} = \sum_{\mathbf{k},\mathbf{k}'} [V(\mathbf{k},\mathbf{k}')]^{\tilde{\mu}_1\tilde{\mu}_2}_{\tilde{\mu}_3\tilde{\mu}_4} e^{i(\mathbf{k}-\mathbf{k}')\cdot\Delta\mathbf{r}}. \tag{A.3}$$

However, this expression requires summing over $\mathbf{k}$ and $\mathbf{k}'$ and therefore is numerically costly. Nonetheless, as we will see below, we can simplify the momentum dependence.

For completeness, we repeat here the form of the interactions from bubble and ladder diagrams in Eq. (1.40),

$$\begin{aligned}\Big[V_{\text{eff}}(\mathbf{k},\mathbf{k}')\Big]^{\tilde{\mu}_1\tilde{\mu}_2}_{\tilde{\mu}_3\tilde{\mu}_4} = \sum_{\boldsymbol{\delta},\boldsymbol{\delta}'} & e^{-i\boldsymbol{\delta}\cdot\mathbf{k}} e^{i\boldsymbol{\delta}'\cdot\mathbf{k}'} \Big[W(\mathbf{k}+\mathbf{k}',\boldsymbol{\delta})\chi_{\text{RPA}}(\mathbf{k}+\mathbf{k}',\boldsymbol{\delta},\boldsymbol{\delta}')W(\mathbf{k}+\mathbf{k}',\boldsymbol{\delta}')\Big]^{\tilde{\mu}_1\tilde{\mu}_2}_{\tilde{\mu}_3\tilde{\mu}_4} \\ & - e^{-i\boldsymbol{\delta}\cdot\mathbf{k}} e^{-i\boldsymbol{\delta}'\cdot\mathbf{k}'} \Big[W(\mathbf{k}-\mathbf{k}',\boldsymbol{\delta})\chi_{\text{RPA}}(\mathbf{k}-\mathbf{k}',\boldsymbol{\delta},\boldsymbol{\delta}')W(\mathbf{k}-\mathbf{k}',\boldsymbol{\delta}')\Big]^{\tilde{\mu}_1\tilde{\mu}_4}_{\tilde{\mu}_3\tilde{\mu}_2}.\end{aligned} \tag{A.4}$$

To simplify the notation, we define

$$\Big[W(\mathbf{k}-\mathbf{k}',\boldsymbol{\delta})\chi_{\text{RPA}}(\mathbf{k}-\mathbf{k}',\boldsymbol{\delta},\boldsymbol{\delta}')W(\mathbf{k}-\mathbf{k}',\boldsymbol{\delta}')\Big]^{\tilde{\mu}_1\tilde{\mu}_4}_{\tilde{\mu}_3\tilde{\mu}_2} \equiv [W\chi W]^{\tilde{\mu}_1\tilde{\mu}_4}_{\tilde{\mu}_3\tilde{\mu}_2}(\mathbf{k}-\mathbf{k}',\boldsymbol{\delta},\boldsymbol{\delta}'). \tag{A.5}$$

Thus, focusing on the second line in Eq. (A.4), we can replace this expression in the Fourier transform of the interaction in Eq. (A.3), obtaining

$$\begin{aligned}[V(\Delta\mathbf{r})]^{\tilde{\mu}_1\tilde{\mu}_2}_{\tilde{\mu}_3\tilde{\mu}_4} &= -\sum_{\mathbf{k},\mathbf{k}'}\sum_{\boldsymbol{\delta},\boldsymbol{\delta}'} e^{i(\mathbf{k}-\mathbf{k}')\cdot\Delta\mathbf{r}} e^{-i\boldsymbol{\delta}\cdot\mathbf{k}} e^{-i\boldsymbol{\delta}'\cdot\mathbf{k}'} [W\chi W]^{\tilde{\mu}_1\tilde{\mu}_4}_{\tilde{\mu}_3\tilde{\mu}_2}(\mathbf{k}-\mathbf{k}',\boldsymbol{\delta},\boldsymbol{\delta}') \\ &= -\sum_{\boldsymbol{\delta},\boldsymbol{\delta}'} \underbrace{\sum_{\mathbf{k}'} e^{-i(\boldsymbol{\delta}+\boldsymbol{\delta}')\cdot\mathbf{k}'}}_{\delta_{\boldsymbol{\delta},-\boldsymbol{\delta}'}} \sum_{\mathbf{k}} e^{i\mathbf{k}\cdot\Delta\mathbf{r}} e^{-i\boldsymbol{\delta}\cdot\mathbf{k}} [W\chi W]^{\tilde{\mu}_1\ \tilde{\mu}_4}_{\tilde{\mu}_3\ \tilde{\mu}_2}(\mathbf{k},\boldsymbol{\delta},\boldsymbol{\delta}'), \end{aligned} \tag{A.6}$$

where in the last line we have shifted $\mathbf{k} \to \mathbf{k} + \mathbf{k}'$. Finally,

$$[V(\Delta\mathbf{r})]^{\tilde{\mu}_1\tilde{\mu}_2}_{\tilde{\mu}_3\tilde{\mu}_4} = -\sum_{\mathbf{k}} e^{i\mathbf{k}\cdot\Delta\mathbf{r}} \sum_{\boldsymbol{\delta}} e^{-i\boldsymbol{\delta}\cdot\mathbf{k}} [W\chi W]^{\tilde{\mu}_1\tilde{\mu}_4}_{\tilde{\mu}_3\tilde{\mu}_2}(\mathbf{k},\boldsymbol{\delta},-\boldsymbol{\delta}). \tag{A.7}$$

Therefore, the Fourier transform of the pairing interaction to real space is significantly simplified, since this expression now only contains the $\mathbf{k}$ and the $\boldsymbol{\delta}$ sum. A similar transformation can be done for the first line in Eq. (A.4), so that we obtain the full pairing interaction Fourier transformed to real space. Using this result, we calculate the pairing interaction in real space shown in Fig. 1.6.

Appendix B

Self-consistent Bogoliubov-de Gennes equations

In the first three Chapters of the thesis, we used the Bogoliubov-de Gennes (BdG) transformation to diagonalize the Hamiltonian and solve self-consistently for the order parameter. Thus, in this Appendix we present the details of the method used. In Chapters 1 and 2 we solved for the superconducting order parameter in momentum space, as in homogeneous systems the **k**-space formulations allows us to work with larger systems. However, since in Chapter 3 we introduced inhomogeneous magnetizations, we worked in the real space basis. Similarly, in Chapter 1 we also solved for the superconducting gap in real space when introducing non-magnetic impurities in Sec. 1.8.

In the first section of this Appendix, we focus on a one-band model, relevant for Chapters 1 and 3. In the second section, we consider the momentum-space formulation and introduce a general notation to include also orbital indices, following the notation introduced in Chapter 2 to describe multiorbital systems.

Real space

Let us first consider the case of a single-band model in real space, since this is relevant for Chapters 1 and 3. The mean-field decoupled Hamiltonian in Eq. (3.10) can be written in matrix form as

$$H_{\mathrm{MF}} = \Psi^{\dagger} H_{\mathrm{BdG}} \Psi, \tag{B.1}$$

where the spinor corresponds to $\Psi = (c_{\mathbf{i}\uparrow}, c_{\mathbf{i}\downarrow}, c^{\dagger}_{\mathbf{i}\uparrow}, c^{\dagger}_{\mathbf{i}\downarrow})^{\top}$, with each entry denoting a vector with length N^2 including all lattice sites, and N being the system size in the x and y direction. The $4N^2 \times 4N^2$ BdG Hamiltonian is constructed as

$$H_{\mathrm{BdG}} = \begin{pmatrix} H_{\mathrm{kin}} + H_{\mathrm{soc}} & \Delta \\ \Delta^{\dagger} & -(H_{\mathrm{kin}} + H_{\mathrm{soc}})^{\top} \end{pmatrix}, \tag{B.2}$$

where H_{kin} and H_{soc} denote the kinetic and spin-orbit coupling terms, respectively, while Δ is the matrix in real space corresponding to the superconducting order parameter. To diagonalize

the BdG Hamiltonian, we introduce the general unitary transformation,

$$\begin{cases} c^{\dagger}_{\mathbf{i}\sigma} = \sum_{n=1}^{2N^2} (u^{n*}_{\mathbf{i}\sigma}\gamma^{\dagger}_n + v^{n}_{\mathbf{i}\sigma}\gamma_n), \\ c_{\mathbf{i}\sigma} = \sum_{n=1}^{2N^2} (u^{n}_{\mathbf{i}\sigma}\gamma_n + v^{n*}_{\mathbf{i}\sigma}\gamma^{\dagger}_n), \end{cases} \tag{B.3}$$

where $(u^n_{\mathbf{i}\uparrow}, u^n_{\mathbf{i}\downarrow}, v^n_{\mathbf{i}\uparrow}, v^n_{\mathbf{i}\downarrow})^{\top}$ is the set of eigenvectors that diagonalize the BdG Hamiltonian with eigenvalues E_n, so that the diagonalized Hamiltonian corresponds to $\sum_n E_n\gamma^{\dagger}_n\gamma_n$. The sum over n includes only the positive eigenenergies.

The Bogoliubov operators satisfy $\langle\gamma_n\gamma_{n'}\rangle = \langle\gamma^{\dagger}_n\gamma^{\dagger}_{n'}\rangle = 0$ and $\langle\gamma^{\dagger}_n\gamma_{n'}\rangle = f(E_n)\delta_{n,n'}$, where $f(E_n) = \frac{1}{1+e^{\beta E_n}}$ is the Fermi function and $\beta = 1/(k_BT)$. Therefore, introducing the transformation in Eq. (B.3), the superconducting order parameter in Eq. (3.14) can be rewritten as

$$\begin{aligned} \Delta_{\mathbf{i}} &= V_{\mathrm{SC}}\left(\langle c_{\mathbf{i}\uparrow}c_{\mathbf{i}\downarrow}\rangle - \langle c_{\mathbf{i}\downarrow}c_{\mathbf{i}\uparrow}\rangle\right) \\ &= -V_{\mathrm{SC}}\sum_n (u^n_{\mathbf{i}\uparrow}v^{n\,*}_{\mathbf{i}\downarrow} - u^n_{\mathbf{i}\downarrow}v^{n\,*}_{\mathbf{i}\uparrow})\tanh\frac{\beta E_n}{2}. \end{aligned} \tag{B.4}$$

The electron density is calculated as

$$\langle n\rangle = \frac{1}{N^2}\sum_{\mathbf{i},\mu,\sigma}\langle c^{\dagger}_{\mathbf{i}\mu\sigma}c_{\mathbf{i}\mu\sigma}\rangle = \frac{1}{N^2}\sum_{\mathbf{i},\mu,\sigma,n}\left\{\left|u^n_{\mathbf{i}\mu\sigma}\right|^2 f(E_n) + \left|v^n_{\mathbf{i}\mu\sigma}\right|^2(1-f(E_n))\right\}. \tag{B.5}$$

In the self-consistent approach, we diagonalize the Hamiltonian and calculate the superconducting order parameter and the electron density for many iterations until the desired precision for these quantities is achieved.

We have introduced the unitary transformation that diagonalizes the BdG Hamiltonian to obtain an expression for the superconducting order parameter. As we detail in Appendix C, this transformation can also be used to calculate the current operator. Note that, since in the one-band model considered in Chapter 1 there is no spin-orbit coupling, it is sufficient to solve a reduced $2N^2 \times 2N^2$ Hamiltonian taking the spinor $\Psi = (c_{\mathbf{i}\uparrow}, c^{\dagger}_{\mathbf{i}\downarrow})^{\top}$. Therefore, in this case, we solve only for half of the eigenvectors that diagonalize the BdG Hamiltonian, $(u^n_{\mathbf{i}\uparrow}, v^n_{\mathbf{i}\downarrow})^{\top}$.

Momentum space

In Chapters 1 and 2 we work with homogeneous systems, and thus we can solve the superconducting order parameter in momentum space. To keep the formalism general and include spin indices and multiple orbitals, we follow the notation in Chapter 2 and use the combined index $\tilde{\mu}_i = \mu_i\,\sigma_i$ to denote both orbital and spin indices.

We mean-field decouple the general interacting Hamiltonian in Eq. (2.2), so that the matrix form now corresponds to

$$\mathcal{H}_{\mathrm{MF}} = \sum_{\mathbf{k}}\Psi^{\dagger}_{\mathbf{k}}\mathcal{H}_{\mathrm{BdG}}(\mathbf{k})\Psi_{\mathbf{k}}, \tag{B.6}$$

with the spinor $\Psi_{\mathbf{k}} = (\{c_{\mathbf{k}\tilde{\mu}_i}\}, \{c_{-\mathbf{k}\tilde{\mu}_i}\})$, including the different orbital and spin combinations. For instance, for a two-orbital model the spinor corresponds to $\Psi_{\mathbf{k}} = (c_{\mathbf{k}1\uparrow}, c_{\mathbf{k}1\downarrow}, c_{\mathbf{k}2\uparrow}, c_{\mathbf{k}2\downarrow}, c_{-\mathbf{k}1\uparrow}, c_{-\mathbf{k}1\downarrow},$

$c_{-\mathbf{k}2\uparrow}, c_{-\mathbf{k}2\downarrow}$), with 1 and 2 denoting the two orbitals. The BdG Hamiltonian has dimensions $2n_{\text{spin}}n_{\text{orb}} \times 2n_{\text{spin}}n_{\text{orb}}$, where $n_{\text{spin}} = 2$ corresponds to the spin degree of freedom and n_{orb} is the number of orbitals, and is given by

$$\mathcal{H}_{\text{BdG}}(\mathbf{k}) = \begin{pmatrix} \mathcal{H}_{\text{kin}}(\mathbf{k}) + \mathcal{H}_{\text{soc}}(\mathbf{k}) & \Delta_{\mathbf{k}} \\ \Delta_{\mathbf{k}} & -(\mathcal{H}_{\text{kin}}(\mathbf{k}) + \mathcal{H}_{\text{soc}}(\mathbf{k}))^{\top} \end{pmatrix}, \tag{B.7}$$

where $\mathcal{H}_{\text{kin}}(\mathbf{k})$ and $\mathcal{H}_{\text{soc}}(\mathbf{k})$ are the non-interacting Hamiltonians in momentum space corresponding to the kinetic and the spin-orbit coupling terms, respectively. In addition, $\Delta_{\mathbf{k}}$ is a $n_{\text{spin}}n_{\text{orb}} \times n_{\text{spin}}n_{\text{orb}}$ matrix in orbital and spin space, with the components given by

$$[\Delta_{\mathbf{k}}]^{\tilde{\mu}_i}_{\tilde{\mu}_j} = \sum_{\mathbf{k}',\tilde{\mu}_k,\tilde{\mu}_l} [V(\mathbf{k},\mathbf{k}')]^{\tilde{\mu}_i,\tilde{\mu}_l}_{\tilde{\mu}_j,\tilde{\mu}_k} \langle c_{-\mathbf{k}'\tilde{\mu}_l} c_{\mathbf{k}'\tilde{\mu}_k} \rangle. \tag{B.8}$$

Here, $[V(\mathbf{k},\mathbf{k}')]^{\tilde{\mu}_i,\tilde{\mu}_l}_{\tilde{\mu}_j,\tilde{\mu}_k}$ denotes the effective interaction in orbital and spin space. Similarly to the real-space problem, we introduce the following unitary transformation to diagonalize the BdG Hamiltonian,

$$\begin{cases} c^{\dagger}_{\mathbf{k}\tilde{\mu}_i} = \sum\limits_{n=1}^{2N^2} \left(u^{n*}_{\mathbf{k}\tilde{\mu}_i}\gamma^{\dagger}_{\mathbf{k}n} + v^{n}_{\mathbf{k}\tilde{\mu}_i}\gamma_{-\mathbf{k}n}\right), \\ c_{\mathbf{k}\tilde{\mu}_i} = \sum\limits_{n=1}^{2N^2} \left(u^{n}_{\mathbf{k}\tilde{\mu}_i}\gamma_{\mathbf{k}n} + v^{n*}_{\mathbf{k}\tilde{\mu}_i}\gamma^{\dagger}_{-\mathbf{k}n}\right), \end{cases} \tag{B.9}$$

with $(\{u^{n}_{\mathbf{k}\tilde{\mu}_i}\}, \{v^{n}_{-\mathbf{k}\tilde{\mu}_i}\})^{\top}$ corresponding to the set of eigenvectors that diagonalize the BdG Hamiltonian.

The electron density in momentum space is obtained by summing over all spin and orbital configurations,

$$\langle n \rangle = \frac{1}{N^2}\sum_{\mathbf{k},\mu,\sigma} \langle c^{\dagger}_{\mathbf{k}\mu\sigma} c_{\mathbf{k}\mu\sigma} \rangle = \frac{1}{N^2}\sum_{\mathbf{k},\mu,\sigma,n} \left\{ \left|u^{n}_{\mathbf{k}\mu\sigma}\right|^2 f(E_{\mathbf{k}n}) + \left|v^{n}_{\mathbf{k}\mu\sigma}\right|^2 (1 - f(E_{-\mathbf{k}n})) \right\}. \tag{B.10}$$

Using the unitary transformation in Eq. (B.9), the superconducting order parameter corresponding to the Γ irreducible representation in Eqs. (1.59), (2.14) can be calculated as

$$\begin{aligned} [\Delta_{\Gamma}]^{\tilde{\mu}_i}_{\tilde{\mu}_j} &= \sum_{\mathbf{k}',\tilde{\mu}_k,\tilde{\mu}_l} [V(\boldsymbol{\delta})]^{\tilde{\mu}_i,\tilde{\mu}_l}_{\tilde{\mu}_j,\tilde{\mu}_k} g^{\Gamma}_{\mathbf{k}'} \left\langle c_{-\mathbf{k}'\tilde{\mu}_l} c_{\mathbf{k}'\tilde{\mu}_k} \right\rangle \\ &= -\sum_{\mathbf{k}',\tilde{\mu}_k,\tilde{\mu}_l} [V(\boldsymbol{\delta})]^{\tilde{\mu}_i,\tilde{\mu}_l}_{\tilde{\mu}_j,\tilde{\mu}_k} g^{\Gamma}_{\mathbf{k}'} \sum_{n} u^{n}_{\mathbf{k}'\tilde{\mu}_k} v^{n*}_{-\mathbf{k}\tilde{\mu}_l} \tanh\frac{\beta E_{\mathbf{k}'n}}{2}. \end{aligned} \tag{B.11}$$

Thus, the superconducting order parameter is obtained using the unitary transformation that diagonalizes the Hamiltonian, and the symmetry of the solutions is classified according to the irreducible representations of the point group D_{4h}, as discussed in the first two Chapters.

Appendix C

Derivation of the current operator

In Chapter 3 we investigated the superconducting diode effect arising from different magnetization configurations. Thus, obtaining the currents in the system is crucial to calculate the efficiency of the diode effect and to examine the current patterns in real space. The first step is to solve self-consistently for the superconducting order parameter, as described in Appendix B. Once we have the converged solution, the next step is to calculate the currents, as we detail in this Appendix. This is also used in Chapter 1 to study the current patterns induced by non-magnetic impurities at the coexistence region between two different symmetries, see Sec. 1.8.

To derive the current operator, let us consider a nearest-neighbor hopping Hamiltonian on a square lattice, even though the same derivation can be followed for next-nearest neighbor hoppings (see Eq. (1.60)). With this purpose, we assume a site-dependent vector potential $\mathbf{A}$, so that the hopping term is modified by a phase factor,

$$H_A = -t \sum_{\mathbf{i},\boldsymbol{\delta},\sigma} (c^\dagger_{\mathbf{i}+\boldsymbol{\delta}\sigma} c_{\mathbf{i}\sigma} e^{i\mathbf{A}\cdot\boldsymbol{\delta}} + \text{h.c.}), \tag{C.1}$$

where in the case of nearest neighbors $\boldsymbol{\delta} = \{\hat{\mathbf{x}}, -\hat{\mathbf{x}}, \hat{\mathbf{y}}, -\hat{\mathbf{y}}\}$. The current operator in the $\hat{\mathbf{x}}$ direction is given by the response to the vector potential [258]

$$J_{\mathbf{i},\hat{\mathbf{x}}} = \lim_{A_x \to 0} \left\{ -\frac{\delta H_A}{\delta A_x} \right\}. \tag{C.2}$$

Similarly, an analogous expression can be obtained in the other directions. Therefore, more generally, the current density from site $\mathbf{i}$ to $\boldsymbol{\delta}$ can be written as

$$J_{\mathbf{i},\boldsymbol{\delta}} = it \sum_{\sigma} \left[\left\langle c^\dagger_{\mathbf{i}+\boldsymbol{\delta}\sigma} c_{\mathbf{i}\sigma} \right\rangle - \text{h.c.} \right]. \tag{C.3}$$

Analogously, the same derivation can be followed to calculate the current operator for the Rashba SOC hopping term in Eq. (3.12), obtaining the results in Eqs. (3.17)-(3.18).

Having obtained the expression for the current vector at each lattice site, we calculate this quantity by introducing the unitary transformation in Eq. (B.3) that diagonalizes the Hamiltonian (see Appendix B). Hence, the current response becomes

$$J_{\mathbf{i},\boldsymbol{\delta}} = -2t \sum_{\sigma,n} \text{Im}\left\{ u^{n*}_{\mathbf{i}+\boldsymbol{\delta}\sigma} u^n_{\mathbf{i}\sigma} f(E_n) + v^n_{\mathbf{i}+\boldsymbol{\delta}\sigma} v^{n*}_{\mathbf{i}\sigma} f(-E_n) \right\}, \tag{C.4}$$

with $f(E_n)$ denoting the Fermi function.

As discussed in Appendix B, in the case of a one-band model without spin-orbit coupling, which is relevant for Chapter 1, it is sufficient to solve the reduced eigensystem $2N^2 \times 2N^2$,

$$H_{\mathrm{BdG}} \begin{pmatrix} u^n_{\mathbf{i}\uparrow} \\ v^n_{\mathbf{i}\downarrow} \end{pmatrix} = E_n \begin{pmatrix} u^n_{\mathbf{i}\uparrow} \\ v^n_{\mathbf{i}\downarrow} \end{pmatrix}, \tag{C.5}$$

since the following symmetry holds:

$$\begin{Bmatrix} E_n \\ u^n_{\mathbf{i}\uparrow} \\ v^n_{\mathbf{i}\downarrow} \end{Bmatrix} \longrightarrow \begin{Bmatrix} -E_n \\ v^{n^*}_{\mathbf{i}\uparrow} \\ u^{n^*}_{\mathbf{i}\downarrow} \end{Bmatrix}. \tag{C.6}$$

Thus, to calculate the current we can use this symmetry to rewrite Eq. (C.4) as

$$J_{\mathbf{i},\boldsymbol{\delta}} = -2t \sum_{\text{all}\, n} \mathrm{Im}\Big\{ u^{n^*}_{\mathbf{i}+\boldsymbol{\delta}\uparrow} u^n_{\mathbf{i}\uparrow} f(E_n) + v^n_{\mathbf{i}+\boldsymbol{\delta}\downarrow} v^{n^*}_{\mathbf{i}\downarrow} f(-E_n) \Big\}, \tag{C.7}$$

where now we have to sum over all n, including positive and negative eigenenergies,

Finally, to obtain the total current vector on each lattice site from Eqs. (C.4) and (C.7), we average over the two nearest-neighbor bonds in the $\hat{\mathbf{x}}$ and the $\hat{\mathbf{y}}$ direction in the following way,

$$\mathbf{J}_{\mathbf{i}} = \frac{1}{2} \sum_{\boldsymbol{\delta}} \boldsymbol{\delta} J_{\mathbf{i},\boldsymbol{\delta}} = \frac{1}{2} \Big[\hat{\mathbf{x}} (J_{\mathbf{i},\hat{\mathbf{x}}} - J_{\mathbf{i},-\hat{\mathbf{x}}}) + \hat{\mathbf{y}} (J_{\mathbf{i},\hat{\mathbf{y}}} - J_{\mathbf{i},-\hat{\mathbf{y}}}) \Big]. \tag{C.8}$$

This expression is used in Chapter 3 to obtain the current patterns and the current-phase relation, see for instance Figs. 3.8-3.9. In addition, we also use it to calculate the currents patterns in Chapter 1 at the coexistence region between different symmetries, see Figs. 1.11-1.12.

Appendix D

Matrix basis of the order parameter coupling to odd parity functions

In Section 2.3 we classified in detail the symmetries of the order parameter for matrices coupling to even parity functions ($g^{\Gamma_g}_{-\mathbf{k}} = g^{\Gamma_g}_{\mathbf{k}}$), since these are the stabilized solutions from the self-consistent approach. In this Appendix, we additionally classify the order parameter for the matrices coupling to an odd-parity basis function ($g^{\Gamma_u}_{-\mathbf{k}} = -g^{\Gamma_u}_{\mathbf{k}}$). This case is distinct since Eq. (2.12) reveals that the matrices coupling to odd form factors fulfill $[\Delta_{\Gamma_u}]^{\tilde{\mu}_i}_{\tilde{\mu}_j} = [\Delta_{\Gamma_u}]^{\tilde{\mu}_j}_{\tilde{\mu}_i}$. In the following subsections, we consider the two-orbital and three-orbital models discussed in Chapter 2.

Two-orbital model

We consider a two-orbital model for d_{xz} and d_{yz} orbitals. Since the matrices coupling to odd parity functions satisfy $[\Delta_{\Gamma_u}]^{\tilde{\mu}_i}_{\tilde{\mu}_j} = [\Delta_{\Gamma_u}]^{\tilde{\mu}_j}_{\tilde{\mu}_i}$, we start from the following matrix in orbital and spin space,

$$\hat{\Delta}_{\Gamma_u} = \begin{pmatrix} [\Delta_{\Gamma_u}]^{xz\uparrow}_{xz\uparrow} & [\Delta_{\Gamma_u}]^{xz\uparrow}_{xz\downarrow} & [\Delta_{\Gamma_u}]^{xz\uparrow}_{yz\uparrow} & [\Delta_{\Gamma_u}]^{xz\uparrow}_{yz\downarrow} \\ [\Delta_{\Gamma_u}]^{xz\uparrow}_{xz\downarrow} & [\Delta_{\Gamma_u}]^{xz\downarrow}_{xz\downarrow} & [\Delta_{\Gamma_u}]^{xz\downarrow}_{yz\uparrow} & [\Delta_{\Gamma_u}]^{xz\downarrow}_{yz\downarrow} \\ [\Delta_{\Gamma_u}]^{xz\uparrow}_{yz\uparrow} & [\Delta_{\Gamma_u}]^{xz\downarrow}_{yz\uparrow} & [\Delta_{\Gamma_u}]^{yz\uparrow}_{yz\uparrow} & [\Delta_{\Gamma_u}]^{yz\uparrow}_{yz\downarrow} \\ [\Delta_{\Gamma_u}]^{xz\uparrow}_{yz\downarrow} & [\Delta_{\Gamma_u}]^{xz\downarrow}_{yz\downarrow} & [\Delta_{\Gamma_u}]^{yz\uparrow}_{yz\downarrow} & [\Delta_{\Gamma_u}]^{yz\downarrow}_{yz\downarrow} \end{pmatrix}. \tag{D.1}$$

Following an analogous procedure to Sec. 2.3, we obtain the irreducible representations summarized in Table D.1.

Three-orbital model

We focus on a three-orbital model including d_{xz}, d_{yz} and d_{xy} orbitals. Similarly to the previous section, we start from a 3×3 matrix in orbital and spin space which satisfies $[\Delta_{\Gamma_u}]^{\tilde{\mu}_i}_{\tilde{\mu}_j} = [\Delta_{\Gamma_u}]^{\tilde{\mu}_j}_{\tilde{\mu}_i}$. The classification of the gap symmetries is detailed in Table D.3. In this case, the gap symmetries in Table D.3 transforming like reducible representations can be combined to obtain terms transforming as an irrep of D_{4h}, which are listed in Table D.2.

Table D.1: Classification of the order parameter components that couple to an odd form factor ($g^{\Gamma_u}_{-\mathbf{k}} = -g^{\Gamma_u}_{\mathbf{k}}$) in orbital and spin space, considering a two-orbital model for d_{xz} and d_{yz} orbitals. We include whether each combination corresponds to singlet or triplet in orbital and spin space, and indicate when it is an intra-orbital term. The transformation of the spin and orbital matrices is detailed in Tables 2.1 and 2.2, respectively, which is used to obtain the total irrep for each combination.

$\hat{\Delta}_{\Gamma_u}$	Orbital	$\boldsymbol{\kappa}_i$	Spin	$\boldsymbol{\sigma}_i$	Irrep
$\frac{-i}{2}\left([\Delta_{\Gamma_u}]^{xz\downarrow}_{yz\uparrow} - [\Delta_{\Gamma_u}]^{xz\uparrow}_{yz\downarrow}\right)$	Singlet	κ_y	Singlet	σ_0	A_{2g}
$\frac{-1}{4}\left([\Delta_{\Gamma_u}]^{xz\uparrow}_{xz\uparrow} - [\Delta_{\Gamma_u}]^{xz\downarrow}_{xz\downarrow} + [\Delta_{\Gamma_u}]^{yz\uparrow}_{yz\uparrow} - [\Delta_{\Gamma_u}]^{yz\downarrow}_{yz\downarrow}\right)$	Triplet, Intra	κ_0	Triplet	σ_x	$E^x_g(i)$
$\frac{-i}{4}\left([\Delta_{\Gamma_u}]^{xz\uparrow}_{xz\uparrow} + [\Delta_{\Gamma_u}]^{xz\downarrow}_{xz\downarrow} + [\Delta_{\Gamma_u}]^{yz\uparrow}_{yz\uparrow} + [\Delta_{\Gamma_u}]^{yz\downarrow}_{yz\downarrow}\right)$	Triplet, Intra	κ_0	Triplet	σ_y	$E^y_g(i)$
$\frac{1}{2}\left([\Delta_{\Gamma_u}]^{xz\uparrow}_{xz\downarrow} + [\Delta_{\Gamma_u}]^{yz\uparrow}_{yz\downarrow}\right)$	Triplet, Intra	κ_0	Triplet	σ_z	A_{2g}
$\frac{-1}{4}\left([\Delta_{\Gamma_u}]^{xz\uparrow}_{xz\uparrow} - [\Delta_{\Gamma_u}]^{xz\downarrow}_{xz\downarrow} - [\Delta_{\Gamma_u}]^{yz\uparrow}_{yz\uparrow} + [\Delta_{\Gamma_u}]^{yz\downarrow}_{yz\downarrow}\right)$	Triplet, Intra	κ_z	Triplet	σ_x	$E^x_g(ii)$
$\frac{-i}{4}\left([\Delta_{\Gamma_u}]^{xz\uparrow}_{xz\uparrow} + [\Delta_{\Gamma_u}]^{xz\downarrow}_{xz\downarrow} - [\Delta_{\Gamma_u}]^{yz\uparrow}_{yz\uparrow} - [\Delta_{\Gamma_u}]^{yz\downarrow}_{yz\downarrow}\right)$	Triplet, Intra	κ_z	Triplet	σ_y	$E^y_g(ii)$
$\frac{1}{2}\left([\Delta_{\Gamma_u}]^{xz\uparrow}_{xz\downarrow} - [\Delta_{\Gamma_u}]^{yz\uparrow}_{yz\downarrow}\right)$	Triplet, Intra	κ_z	Triplet	σ_z	B_{2g}
$\frac{-1}{2}\left([\Delta_{\Gamma_u}]^{xz\uparrow}_{yz\uparrow} - [\Delta_{\Gamma_u}]^{xz\downarrow}_{yz\downarrow}\right)$	Triplet	κ_x	Triplet	σ_x	$E^x_g(iii)$
$\frac{-i}{2}\left([\Delta_{\Gamma_u}]^{xz\uparrow}_{yz\uparrow} + [\Delta_{\Gamma_u}]^{xz\downarrow}_{yz\downarrow}\right)$	Triplet	κ_x	Triplet	σ_y	$E^y_g(iii)$
$\frac{1}{2}\left([\Delta_{\Gamma_u}]^{xz\uparrow}_{yz\downarrow} + [\Delta_{\Gamma_u}]^{xz\downarrow}_{yz\uparrow}\right)$	Triplet	κ_x	Triplet	σ_z	B_{1g}

Table D.2: Classification of the order parameter components obtained by combining the reducible representations in Table D.3 for the order parameter matrices coupling to an odd form factor ($g^{\Gamma_u}_{-\mathbf{k}} = -g^{\Gamma_u}_{\mathbf{k}}$) in orbital and spin space, considering a three-orbital model for d_{xz}, d_{yz} and d_{xy} orbitals. We classify the terms in combined orbital and spin space, and indicate the corresponding irrep in each case.

$\hat{\Delta}_{\Gamma_u}$	Combined spin and orbital	Orbital	Spin	Irrep
$\frac{-1}{4}\left(i[\Delta_{\Gamma_u}]^{xz\uparrow}_{xy\uparrow} + i[\Delta_{\Gamma_u}]^{xz\downarrow}_{xy\downarrow} + [\Delta_{\Gamma_u}]^{yz\uparrow}_{xy\uparrow} - [\Delta_{\Gamma_u}]^{yz\downarrow}_{xy\downarrow}\right)$	$\lambda_4\sigma_y + \lambda_6\sigma_x$	Triplet	Triplet	A_{2g}
$\frac{-1}{4}\left(i[\Delta_{\Gamma_u}]^{xz\uparrow}_{xy\uparrow} + i[\Delta_{\Gamma_u}]^{xz\downarrow}_{xy\downarrow} - [\Delta_{\Gamma_u}]^{yz\uparrow}_{xy\uparrow} + [\Delta_{\Gamma_u}]^{yz\downarrow}_{xy\downarrow}\right)$	$\lambda_4\sigma_y - \lambda_6\sigma_x$	Triplet	Triplet	B_{2g}
$\frac{-1}{4}\left([\Delta_{\Gamma_u}]^{xz\uparrow}_{xy\uparrow} - [\Delta_{\Gamma_u}]^{xz\downarrow}_{xy\downarrow}) + i[\Delta_{\Gamma_u}]^{yz\uparrow}_{xy\uparrow} + i[\Delta_{\Gamma_u}]^{yz\downarrow}_{xy\downarrow}\right)$	$\lambda_4\sigma_x + \lambda_6\sigma_y$	Triplet	Triplet	B_{1g}
$\frac{-1}{4}\left([\Delta_{\Gamma_u}]^{xz\uparrow}_{xy\uparrow} - [\Delta_{\Gamma_u}]^{xz\downarrow}_{xy\downarrow}) - i[\Delta_{\Gamma_u}]^{yz\uparrow}_{xy\uparrow} - i[\Delta_{\Gamma_u}]^{yz\downarrow}_{xy\downarrow}\right)$	$\lambda_4\sigma_x - \lambda_6\sigma_y$	Triplet	Triplet	A_{1g}

Table D.3: Classification of the order parameter components that couple to an odd form factor ($g^{\Gamma_u}_{-\mathbf{k}} = -g^{\Gamma_u}_{\mathbf{k}}$) in orbital and spin space, considering a three-orbital model for d_{xz}, d_{yz} and d_{xy} orbitals. We include whether each combination corresponds to singlet or triplet in orbital and spin space, and indicate when it is an intra-orbital term. The transformation of the spin and orbital matrices is detailed in Tables 2.1 and 2.4, respectively, which is used to obtain the total irrep for each combination.

$\hat{\Delta}_{\Gamma_u}$	Orbital	$\boldsymbol{\lambda}_i$	Spin	$\boldsymbol{\sigma}_i$	Irrep
$\frac{i}{2}\left([\Delta_{\Gamma_u}]^{xz\uparrow}_{yz\downarrow} - [\Delta_{\Gamma_u}]^{xz\downarrow}_{yz\uparrow}\right)$	Singlet	$\lambda_y z$	Singlet	σ_0	A_{2g}
$\frac{i}{2}\left([\Delta_{\Gamma_u}]^{xz\uparrow}_{xy\downarrow} - [\Delta_{\Gamma_u}]^{xz\downarrow}_{xy\uparrow}\right)$	Singlet	λ_5	Singlet	σ_0	$E^y_g(i)$
$\frac{i}{2}\left([\Delta_{\Gamma_u}]^{yz\uparrow}_{xy\downarrow} - [\Delta_{\Gamma_u}]^{yz\downarrow}_{xy\uparrow}\right)$	Singlet	λ_7	Singlet	σ_0	$E^x_g(i)$
$\frac{-i}{6}\left([\Delta_{\Gamma_u}]^{xz\uparrow}_{xz\uparrow} + [\Delta_{\Gamma_u}]^{xz\downarrow}_{xz\downarrow} + [\Delta_{\Gamma_u}]^{yz\uparrow}_{yz\uparrow} + [\Delta_{\Gamma_u}]^{yz\downarrow}_{yz\downarrow} + [\Delta_{\Gamma_u}]^{xy\uparrow}_{xy\uparrow} + [\Delta_{\Gamma_u}]^{xy\downarrow}_{xy\downarrow}\right)$	Triplet, Intra	λ_0	Triplet	σ_y	$E^y_g(ii)$
$\frac{1}{3}\left([\Delta_{\Gamma_u}]^{xz\uparrow}_{xz\downarrow} + [\Delta_{\Gamma_u}]^{yz\uparrow}_{yz\downarrow} + [\Delta_{\Gamma_u}]^{xy\uparrow}_{xy\downarrow}\right)$	Triplet, Intra	λ_0	Triplet	σ_z	A_{2g}
$\frac{-1}{6}\left([\Delta_{\Gamma_u}]^{xz\uparrow}_{xz\uparrow} - [\Delta_{\Gamma_u}]^{xz\downarrow}_{xz\downarrow} + [\Delta_{\Gamma_u}]^{yz\uparrow}_{yz\uparrow} - [\Delta_{\Gamma_u}]^{yz\downarrow}_{yz\downarrow} + [\Delta_{\Gamma_u}]^{xy\uparrow}_{xy\uparrow} - [\Delta_{\Gamma_u}]^{xy\downarrow}_{xy\downarrow}\right)$	Triplet, Intra	λ_0	Triplet	σ_x	$E^x_g(ii)$
$\frac{-i}{2}\left([\Delta_{\Gamma_u}]^{xz\uparrow}_{yz\uparrow} + [\Delta_{\Gamma_u}]^{xz\downarrow}_{yz\downarrow}\right)$	Triplet	λ_1	Triplet	σ_y	$E^y_g(iii)$
$\frac{1}{2}\left([\Delta_{\Gamma_u}]^{xz\uparrow}_{yz\downarrow} + [\Delta_{\Gamma_u}]^{xz\downarrow}_{yz\uparrow}\right)$	Triplet	λ_1	Triplet	σ_z	B_{1g}
$\frac{-1}{2}\left([\Delta_{\Gamma_u}]^{xz\uparrow}_{yz\uparrow} - [\Delta_{\Gamma_u}]^{xz\downarrow}_{yz\downarrow}\right)$	Triplet	λ_1	Triplet	σ_x	$E^x_g(iii)$
$\frac{-i}{4}\left([\Delta_{\Gamma_u}]^{xz\uparrow}_{xz\uparrow} + [\Delta_{\Gamma_u}]^{xz\downarrow}_{xz\downarrow} - [\Delta_{\Gamma_u}]^{yz\uparrow}_{yz\uparrow} - [\Delta_{\Gamma_u}]^{yz\downarrow}_{yz\downarrow}\right)$	Triplet, Intra	λ_3	Triplet	σ_y	$E^y_g(iv)$
$\frac{1}{2}\left([\Delta_{\Gamma_u}]^{xz\uparrow}_{xz\downarrow} - [\Delta_{\Gamma_u}]^{yz\uparrow}_{yz\downarrow}\right)$	Triplet, Intra	λ_3	Triplet	σ_z	B_{2g}
$\frac{-1}{4}\left([\Delta_{\Gamma_u}]^{xz\uparrow}_{xz\uparrow} - [\Delta_{\Gamma_u}]^{xz\downarrow}_{xz\downarrow} - [\Delta_{\Gamma_u}]^{yz\uparrow}_{yz\uparrow} + [\Delta_{\Gamma_u}]^{yz\downarrow}_{yz\downarrow}\right)$	Triplet, Intra	λ_3	Triplet	σ_x	$E^x_g(iv)$
$\frac{-i}{2}\left([\Delta_{\Gamma_u}]^{xz\uparrow}_{xy\uparrow} + [\Delta_{\Gamma_u}]^{xz\downarrow}_{xy\downarrow}\right)$	Triplet	λ_4	Triplet	σ_y	Reducible
$\frac{1}{2}\left([\Delta_{\Gamma_u}]^{xz\uparrow}_{xy\downarrow} + [\Delta_{\Gamma_u}]^{xz\downarrow}_{xy\uparrow}\right)$	Triplet	λ_4	Triplet	σ_z	$E^y_g(v)$
$\frac{-1}{2}\left([\Delta_{\Gamma_u}]^{xz\uparrow}_{xy\uparrow} - [\Delta_{\Gamma_u}]^{xz\downarrow}_{xy\downarrow}\right)$	Triplet	λ_4	Triplet	σ_x	Reducible
$\frac{-i}{2}\left([\Delta_{\Gamma_u}]^{yz\uparrow}_{xy\uparrow} + [\Delta_{\Gamma_u}]^{yz\downarrow}_{xy\downarrow}\right)$	Triplet	λ_6	Triplet	σ_y	Reducible
$\frac{1}{2}\left([\Delta_{\Gamma_u}]^{yz\uparrow}_{xy\downarrow} + [\Delta_{\Gamma_u}]^{yz\downarrow}_{xy\uparrow}\right)$	Triplet	λ_6	Triplet	σ_z	$E^x_g(v)$
$\frac{-1}{2}\left([\Delta_{\Gamma_u}]^{yz\uparrow}_{xy\uparrow} - [\Delta_{\Gamma_u}]^{yz\downarrow}_{xy\downarrow}\right)$	Triplet	λ_6	Triplet	σ_x	Reducible
$\frac{-i}{4\sqrt{3}}\left([\Delta_{\Gamma_u}]^{xz\uparrow}_{xz\uparrow} + [\Delta_{\Gamma_u}]^{xz\downarrow}_{xz\downarrow} + [\Delta_{\Gamma_u}]^{yz\uparrow}_{yz\uparrow} + [\Delta_{\Gamma_u}]^{yz\downarrow}_{yz\downarrow} - 2[\Delta_{\Gamma_u}]^{xy\uparrow}_{xy\uparrow} - 2[\Delta_{\Gamma_u}]^{xy\downarrow}_{xy\downarrow}\right)$	Triplet, Intra	λ_8	Triplet	σ_y	$E^y_g(vi)$
$\frac{1}{2\sqrt{3}}\left([\Delta_{\Gamma_u}]^{xz\uparrow}_{xz\downarrow} + [\Delta_{\Gamma_u}]^{yz\uparrow}_{yz\downarrow} - 2[\Delta_{\Gamma_u}]^{xy\uparrow}_{xy\downarrow}\right)$	Triplet, Intra	λ_8	Triplet	σ_z	A_{2g}
$\frac{-1}{4\sqrt{3}}\left([\Delta_{\Gamma_u}]^{xz\uparrow}_{xz\uparrow} - [\Delta_{\Gamma_u}]^{xz\downarrow}_{xz\downarrow} + [\Delta_{\Gamma_u}]^{yz\uparrow}_{yz\uparrow} - [\Delta_{\Gamma_u}]^{yz\downarrow}_{yz\downarrow} - 2[\Delta_{\Gamma_u}]^{xy\uparrow}_{xy\uparrow} + 2[\Delta_{\Gamma_u}]^{xy\downarrow}_{xy\downarrow}\right)$	Triplet, Intra	λ_8	Triplet	σ_x	$E^x_g(vi)$

Appendix E

Two-dimensional minimal model for altermagnetism in a tetragonal system

In Sec. 4.2 we introduced the general minimal model for altermagnetism, as shown in Eq. (4.1), and we derived the specific form for the dispersion and the hoppings in space group 136, relevant for RuO_2 (see Eqs. (4.6)-(4.7)). Motivated by the RuO_2 bands and the case of κ-Cl discussed in Sec. 4.8, here we introduce a minimal model for a two-dimensional tetragonal system and show that it gives rise to a leading altermagnetic instability.

The minimal model for a two-dimensional tetragonal system inspired by RuO_2 is given by

$$H(\mathbf{k}) = t_1(\cos k_x + \cos k_y) + t_2 \cos k_x \cos k_y + t_3 \cos\frac{k_x}{2}\cos\frac{k_y}{2}\tau_x + t_4 \sin k_x \sin k_y \tau_z - \mu, \qquad \text{(E.1)}$$

where we neglect the SOC terms. The hoppings are illustrated in Fig. E.1. In particular, in Figs. E.1(c) and (d) we see that the t_4 hopping is different for the two sublattices, as it couples to τ_z in the minimal model.

Figures E.2(a)-(b) show the normal and altermagnetic band structures, respectively, inspired by the RuO_2 bands shown in Fig. 4.5, and considering that the Fermi level is at the van Hove singularity at the M-point. As seen, there is an altermagnetic spin splitting of the bands along the M-Γ direction. In Fig. E.2(c) we show the Hartree-Fock calculations using this model. The altermagnetic order is stabilized for a smaller interaction U when compared to the ferromagnetic instability, as also verified by the susceptibility calculations (not shown). The order parameter is sensitive to small variations in the filling due to the van Hove singularity, as the critical interaction U rapidly increases.

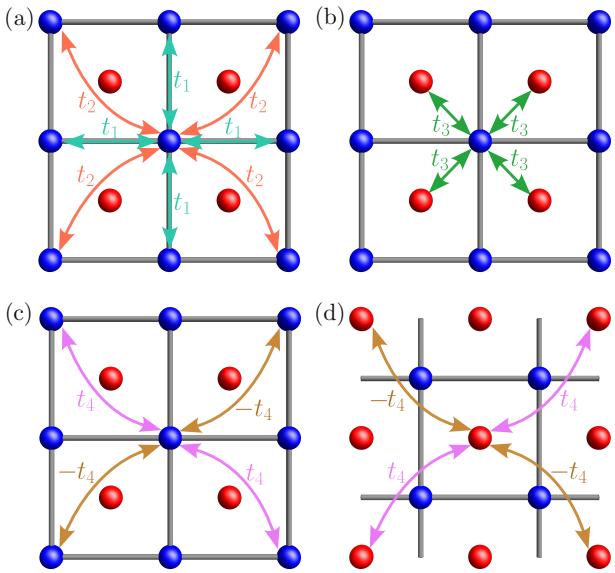

Figure E.1: Illustration of the hoppings in the two-dimensional minimal model introduced in Eq. (E.1). The red and blue dots correspond to the two sublattices.

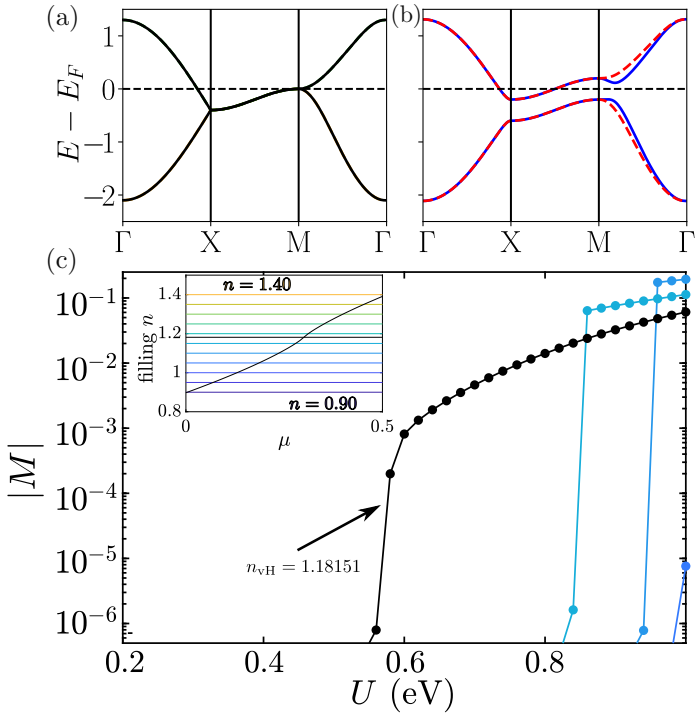

Figure E.2: Band structure for a two-dimensional minimal model inspired by the RuO_2 bands in (a) the normal, and (b) the altermagnetic state, using the minimal model in Eq. (E.1), with the hopping parameters $\{t_1, t_2, t_3, t_4, \mu\} = \{-0.1, 0.1, 1.7, 0.3, 0.3\}$ and $J_z = 0.2$ in (b). (c) Hartree-Fock calculation for the altermagnetic order parameter using the bands in panel (a) and the Hamiltonian in Eq. (E.1), for $k_B T = 10^{-4}$ and $N = 1200^2$.

Appendix F

Antisymmetric direct product of point-group representations

In Sec. 5.7 we introduced the bilinear coupling between the magnetization $\vec{m}$ and the altermagnetic order parameter $\vec{J}$ generated only in the presence of spin-orbit coupling. However, the free energy expansion from the microscopic model in Eq. (5.7) shows that the only generated invariants are of the form $\vec{c}_{\rm soc}\cdot\vec{m}\times\vec{J}$ (see Eq. (5.34)). From the point group theory point of view, this implies that the invariants are induced when the antisymmetric direct product of the two axial vectors $[\Gamma_A\otimes\Gamma_A]_-$ contains Γ_N. In this Appendix, we detail how to calculate this product and focus on two examples.

Following Ref. [259], the direct products of representations can be split into symmetric and antisymmetric parts, which are given by

$$\begin{aligned}\chi^{\rm sym} &= \frac{1}{2}(\chi^2(g)+\chi(g^2)),\\ \chi^{\rm asym} &= \frac{1}{2}(\chi^2(g)-\chi(g^2)),\end{aligned} \tag{F.1}$$

respectively, where $\chi(g)$ is the character for the point group operation g and $\chi(g^2)$ is the character for the same operation squared, which describe how a certain operation affects the basis functions and can be found in the character tables.

Let us focus first on the point group D_{4h}, in particular in the product of representations $E_g\otimes E_g$. Table F.1 lists the characters for the symmetry operations of D_{4h} in the E_g representation, obtained from the Bilbao crystallographic server [224, 225]. Using now Eq. (F.1), we identify the symmetric and antisymmetric character for each operation, as included also in Table F.1. Finally, by using the reduction formula,[1] the symmetric and antisymmetric characters can be identified in terms of the different irreducible representations, obtaining

$$\begin{aligned}[E_g\otimes E_g]_+ &= A_{1g}\oplus B_{1g}\oplus B_{2g},\\ [E_g\otimes E_g]_- &= A_{2g}.\end{aligned} \tag{F.2}$$

[1] This can be checked, for instance, at http://symmetry.jacobs-university.de/.

Table F.1: Character table for the E_g irreducible representation of D_{4h}, including also the character of the operation squared, obtained from the Bilbao crystallographic server [224, 225]. The symmetric and antisymmetric characters are calculated using Eq. (F.1).

E_g	E	C_2	$2C_4$	$2C_2'$	$2C_2''$	$\mathcal{I}$	σ_h	$2S_4$	$2\sigma_v$	$2\sigma_d$
$\chi(g)$	2	-2	0	0	0	2	-2	0	0	0
$\chi(g^2)$	2	2	-2	2	2	2	2	-2	2	2
χ^{sym}	3	3	-1	1	1	3	3	-1	1	1
χ^{asym}	1	1	1	-1	-1	1	1	1	-1	-1

As another example, let us focus now on the point group D_{2h}, specifically in the product of representations $(B_{1g} \oplus B_{2g} \oplus B_{3g}) \otimes (B_{1g} \oplus B_{2g} \oplus B_{3g})$. The characters of this representation for the point group operations of D_{2h} are detailed in Table F.2, as well as the symmetric and antisymmetric characters obtained using Eq. (F.1). The reduction formula gives

$$\begin{aligned} [(B_{1g} \oplus B_{2g} \oplus B_{3g}) \otimes (B_{1g} \oplus B_{2g} \oplus B_{3g})]_+ &= 3A_g \oplus B_{1g} \oplus B_{2g} \oplus B_{3g}, \\ [(B_{1g} \oplus B_{2g} \oplus B_{3g}) \otimes (B_{1g} \oplus B_{2g} \oplus B_{3g})]_- &= B_{1g} \oplus B_{2g} \oplus B_{3g}. \end{aligned} \tag{F.3}$$

Following this procedure, we can analogously calculate the antisymmetric direct product of the two axial vectors $[\Gamma_A \otimes \Gamma_A]_-$ for the the different point groups, as shown in Table 5.4.

Table F.2: Character table for the $B_{1g} \oplus B_{2g} \oplus B_{3g}$ representation of D_{2h}, including also the character of the operation squared, obtained from the Bilbao crystallographic server [224, 225]. The symmetric and antisymmetric characters are calculated using Eq. (F.1).

$(B_{1g} \oplus B_{2g} \oplus B_{3g})$	E	C_2^z	C_2^y	C_2^x	$\mathcal{I}$	σ_{xy}	σ_{xz}	σ_{yz}
$\chi(g)$	3	1	1	1	3	1	1	1
$\chi(g^2)$	3	3	3	3	3	3	3	3
χ^{sym}	6	2	2	2	6	2	2	2
χ^{asym}	3	-1	-1	-1	3	-1	-1	-1

Bibliography

[1] M. Roig, A.T. Rømer, P.J. Hirschfeld and B.M. Andersen, *Revisiting superconductivity in the extended one-band Hubbard model: Pairing via spin and charge fluctuations*, *Phys. Rev. B* **106** (2022) 214530.

[2] M. Roig, A.T. Rømer, A. Kreisel, P.J. Hirschfeld and B.M. Andersen, *Superconductivity in multiorbital systems with repulsive interactions: Hund's pairing versus spin-fluctuation pairing*, *Phys. Rev. B* **106** (2022) L100501.

[3] M. Roig, P. Kotetes and B.M. Andersen, *Superconducting diodes from magnetization gradients*, *Phys. Rev. B* **109** (2024) 144503.

[4] M. Roig, A. Kreisel, Y. Yu, B.M. Andersen and D.F. Agterberg, *Minimal Models for Altermagnetism*, arXiv:2402.15616.

[5] M. Roig, A. Kreisel, Y. Yu, B. Andersen and D. Agterberg, *Landau theory of altermagnetism from microscopic models*, *in preparation* (2024) .

[6] H.S. Røising, G. Wagner, M. Roig, A.T. Rømer and B.M. Andersen, *Heat capacity double transitions in time-reversal symmetry broken superconductors*, *Phys. Rev. B* **106** (2022) 174518.

[7] C.N. Breiø, A. Kreisel, M. Roig, P.J. Hirschfeld and B.M. Andersen, *Time-reversal symmetry breaking from lattice dislocations in superconductors*, *Phys. Rev. B* **109** (2024) 014505.

[8] Y. Yu, H.-G. Suh, M. Roig and D.F. Agterberg, *Altermagnetism from coincident Van Hove singularities: application to κ-Cl*, arXiv:2402.05180.

[9] J. Bardeen, L.N. Cooper and J.R. Schrieffer, *Theory of Superconductivity*, *Phys. Rev.* **108** (1957) 1175.

[10] F. Steglich, J. Aarts, C.D. Bredl, W. Lieke, D. Meschede, W. Franz and H. Schäfer, *Superconductivity in the Presence of Strong Pauli Paramagnetism: $CeCu_2Si_2$*, *Phys. Rev. Lett.* **43** (1979) 1892.

[11] J.G. Bednorz and K.A. Müller, *Possible high T_c superconductivity in the Ba-La-Cu-O system*, *Z. Phys. B: Condens. Matter* **64** (1986) 189.

[12] Y. Maeno, H. Hashimoto, K. Yoshida, S. Nishizaki, T. Fujita, J.G. Bednorz and F. Lichtenberg, *Superconductivity in a layered perovskite without copper*, Nature **372** (1994) 532.

[13] A.P. Mackenzie, T. Scaffidi, C.W. Hicks and Y. Maeno, *Even odder after twenty-three years: the superconducting order parameter puzzle of Sr_2RuO_4*, npj Quantum Mater. **2** (2017) 40.

[14] S.A. Kivelson, A.C. Yuan, B. Ramshaw and R. Thomale, *A proposal for reconciling diverse experiments on the superconducting state in Sr_2RuO_4*, npj Quantum Mater. **5** (2020) 43.

[15] T. Oguchi, *Electronic band structure of the superconductor Sr_2RuO_4*, Phys. Rev. B **51** (1995) 1385.

[16] M.W. Haverkort, I.S. Elfimov, L.H. Tjeng, G.A. Sawatzky and A. Damascelli, *Strong Spin-Orbit Coupling Effects on the Fermi Surface of Sr_2RuO_4 and Sr_2RhO_4*, Phys. Rev. Lett. **101** (2008) 026406.

[17] M. Braden, P. Steffens, Y. Sidis, J. Kulda, P. Bourges, S. Hayden, N. Kikugawa and Y. Maeno, *Anisotropy of the Incommensurate Fluctuations in Sr_2RuO_4: A Study with Polarized Neutrons*, Phys. Rev. Lett. **92** (2004) 097402.

[18] A.T. Rømer, D.D. Scherer, I.M. Eremin, P.J. Hirschfeld and B.M. Andersen, *Knight Shift and Leading Superconducting Instability from Spin Fluctuations in Sr_2RuO_4*, Phys. Rev. Lett. **123** (2019) 247001.

[19] A.T. Rømer, P.J. Hirschfeld and B.M. Andersen, *Superconducting state of Sr_2RuO_4 in the presence of longer-range Coulomb interactions*, Phys. Rev. B **104** (2021) 064507.

[20] C.M. Puetter and H.-Y. Kee, *Identifying spin-triplet pairing in spin-orbit coupled multi-band superconductors*, Europhys. Lett. **98** (2012) 27010.

[21] H.G. Suh, H. Menke, P.M.R. Brydon, C. Timm, A. Ramires and D.F. Agterberg, *Stabilizing even-parity chiral superconductivity in Sr_2RuO_4*, Phys. Rev. Res. **2** (2020) 032023.

[22] F. Ando, Y. Miyasaka, T. Li, J. Ishizuka, T. Arakawa, Y. Shiota, T. Moriyama, Y. Yanase and T. Ono, *Observation of superconducting diode effect*, Nature **584** (2020) 373.

[23] P. Kotetes, H.O.M. Sura and B.M. Andersen, *Anatomy of spin and current generation from magnetization gradients in topological insulators and Rashba metals*, Phys. Rev. B **108** (2023) 155310.

[24] D.F. Agterberg and R.P. Kaur, *Magnetic-field-induced helical and stripe phases in Rashba superconductors*, Phys. Rev. B **75** (2007) 064511.

[25] R.P. Kaur, D.F. Agterberg and M. Sigrist, *Helical Vortex Phase in the Noncentrosymmetric $CePt_3Si$*, Phys. Rev. Lett. **94** (2005) 137002.

[26] L. Šmejkal, J. Sinova and T. Jungwirth, *Beyond Conventional Ferromagnetism and Antiferromagnetism: A Phase with Nonrelativistic Spin and Crystal Rotation Symmetry*, *Phys. Rev. X* **12** (2022) 031042.

[27] L. Šmejkal, J. Sinova and T. Jungwirth, *Emerging Research Landscape of Altermagnetism*, *Phys. Rev. X* **12** (2022) 040501.

[28] W. Kohn and J.M. Luttinger, *New Mechanism for Superconductivity*, *Phys. Rev. Lett.* **15** (1965) 524.

[29] N.F. Berk and J.R. Schrieffer, *Effect of Ferromagnetic Spin Correlations on Superconductivity*, *Phys. Rev. Lett.* **17** (1966) 433.

[30] S. Graser, T.A. Maier, P.J. Hirschfeld and D.J. Scalapino, *Near-degeneracy of several pairing channels in multiorbital models for the Fe pnictides*, *New J. Phys.* **11** (2009) 025016.

[31] D.J. Scalapino, E. Loh and J.E. Hirsch, *d-wave pairing near a spin-density-wave instability*, *Phys. Rev. B* **34** (1986) 8190.

[32] K. Miyake, S. Schmitt-Rink and C.M. Varma, *Spin-fluctuation-mediated even-parity pairing in heavy-fermion superconductors*, *Phys. Rev. B* **34** (1986) 6554.

[33] C. Gros, R. Joynt and T.M. Rice, *Superconducting instability in the large-U limit of the two-dimensional Hubbard model*, *Zeitschrift für Physik B Condensed Matter* **68** (1987) 425.

[34] G. Kotliar and J. Liu, *Superexchange mechanism and d-wave superconductivity*, *Phys. Rev. B* **38** (1988) 5142.

[35] H. Shimahara and S. Takada, *Superconductivity and spin density wave in two dimensional hubbard model*, *J. Phys. Soc. Jpn.* **57** (1988) 1044.

[36] R. Hlubina, *Phase diagram of the weak-coupling two-dimensional $t-t'$ Hubbard model at low and intermediate electron density*, *Phys. Rev. B* **59** (1999) 9600.

[37] A.V. Chubukov and J.P. Lu, *Pairing instabilities in the two-dimensional Hubbard model*, *Phys. Rev. B* **46** (1992) 11163.

[38] D. Zanchi and H.J. Schulz, *Superconducting instabilities of the non-half-filled Hubbard model in two dimensions*, *Phys. Rev. B* **54** (1996) 9509.

[39] T. Maier, M. Jarrell, T. Pruschke and J. Keller, *d-Wave Superconductivity in the Hubbard Model*, *Phys. Rev. Lett.* **85** (2000) 1524.

[40] C.J. Halboth and W. Metzner, *d-Wave Superconductivity and Pomeranchuk Instability in the Two-Dimensional Hubbard Model*, *Phys. Rev. Lett.* **85** (2000) 5162.

[41] A.I. Lichtenstein and M.I. Katsnelson, *Antiferromagnetism and d-wave superconductivity in cuprates: A cluster dynamical mean-field theory*, *Phys. Rev. B* **62** (2000) R9283.

[42] C. Honerkamp and M. Salmhofer, *Magnetic and Superconducting Instabilities of the Hubbard Model at the Van Hove Filling*, Phys. Rev. Lett. **87** (2001) 187004.

[43] F. Guinea, R.S. Markiewicz and M.A.H. Vozmediano, *Superconductivity in electron-doped cuprates: Gap shape change and symmetry crossover with doping*, Phys. Rev. B **69** (2004) 054509.

[44] D. Sénéchal, P.-L. Lavertu, M.-A. Marois and A.-M.S. Tremblay, *Competition between Antiferromagnetism and Superconductivity in High-T_c Cuprates*, Phys. Rev. Lett. **94** (2005) 156404.

[45] S.S. Kancharla, B. Kyung, D. Sénéchal, M. Civelli, M. Capone, G. Kotliar and A.-M.S. Tremblay, *Anomalous superconductivity and its competition with antiferromagnetism in doped Mott insulators*, Phys. Rev. B **77** (2008) 184516.

[46] S. Raghu, S.A. Kivelson and D.J. Scalapino, *Superconductivity in the repulsive Hubbard model: An asymptotically exact weak-coupling solution*, Phys. Rev. B **81** (2010) 224505.

[47] E. Gull, O. Parcollet and A.J. Millis, *Superconductivity and the Pseudogap in the Two-Dimensional Hubbard Model*, Phys. Rev. Lett. **110** (2013) 216405.

[48] P. Staar, T. Maier and T.C. Schulthess, *Two-particle correlations in a dynamic cluster approximation with continuous momentum dependence: Superconductivity in the two-dimensional Hubbard model*, Phys. Rev. B **89** (2014) 195133.

[49] P. Corboz, T.M. Rice and M. Troyer, *Competing States in the t-J Model: Uniform d-Wave State versus Stripe State*, Phys. Rev. Lett. **113** (2014) 046402.

[50] A.T. Rømer, A. Kreisel, I. Eremin, M.A. Malakhov, T.A. Maier, P.J. Hirschfeld and B.M. Andersen, *Pairing symmetry of the one-band Hubbard model in the paramagnetic weak-coupling limit: A numerical RPA study*, Phys. Rev. B **92** (2015) 104505.

[51] X. Chen, J.P.F. LeBlanc and E. Gull, *Superconducting Fluctuations in the Normal State of the Two-Dimensional Hubbard Model*, Phys. Rev. Lett. **115** (2015) 116402.

[52] Y. Deng, E. Kozik, N.V. Prokof'ev and B.V. Svistunov, *Emergent BCS regime of the two-dimensional fermionic Hubbard model: Ground-state phase diagram*, Europhys. Lett. **110** (2015) 57001.

[53] B.-X. Zheng and G.K.-L. Chan, *Ground-state phase diagram of the square lattice Hubbard model from density matrix embedding theory*, Phys. Rev. B **93** (2016) 035126.

[54] F. Šimkovic, X.-W. Liu, Y. Deng and E. Kozik, *Ground-state phase diagram of the repulsive fermionic $t-t'$ Hubbard model on the square lattice from weak coupling*, Phys. Rev. B **94** (2016) 085106.

[55] H.-C. Jiang, Z.-Y. Weng and S.A. Kivelson, *Superconductivity in the doped $t-J$ model: Results for four-leg cylinders*, Phys. Rev. B **98** (2018) 140505.

[56] H.-C. Jiang and T.P. Devereaux, *Superconductivity in the doped Hubbard model and its interplay with next-nearest hopping t'*, *Science* **365** (2019) 1424.

[57] A.T. Rømer, T.A. Maier, A. Kreisel, I. Eremin, P.J. Hirschfeld and B.M. Andersen, *Pairing in the two-dimensional Hubbard model from weak to strong coupling*, *Phys. Rev. Research* **2** (2020) 013108.

[58] M. Qin, C.-M. Chung, H. Shi, E. Vitali, C. Hubig, U. Schollwöck, S.R. White and S. Zhang, *Absence of Superconductivity in the Pure Two-Dimensional Hubbard Model*, *Phys. Rev. X* **10** (2020) 031016.

[59] C.-M. Chung, M. Qin, S. Zhang, U. Schollwöck and S.R. White, *Plaquette versus ordinary d-wave pairing in the t'-Hubbard model on a width-4 cylinder*, *Phys. Rev. B* **102** (2020) 041106.

[60] S. Gong, W. Zhu and D.N. Sheng, *Robust d-Wave Superconductivity in the Square-Lattice $t-J$ Model*, *Phys. Rev. Lett.* **127** (2021) 097003.

[61] A. Kreisel, A.T. Rømer, P.J. Hirschfeld and B.M. Andersen, *Superconducting Phase Diagram of the Paramagnetic One-Band Hubbard Model*, *J. Supercond. Nov. Magn.* **30** (2017) 85.

[62] D.J. Scalapino, E. Loh and J.E. Hirsch, *Fermi-surface instabilities and superconducting d-wave pairing*, *Phys. Rev. B* **35** (1987) 6694.

[63] E. Plekhanov, S. Sorella and M. Fabrizio, *Increasing d-Wave Superconductivity by On-Site Repulsion*, *Phys. Rev. Lett.* **90** (2003) 187004.

[64] S. Onari, R. Arita, K. Kuroki and H. Aoki, *Phase diagram of the two-dimensional extended Hubbard model: Phase transitions between different pairing symmetries when charge and spin fluctuations coexist*, *Phys. Rev. B* **70** (2004) 094523.

[65] S. Onari, R. Arita, K. Kuroki and H. Aoki, *Spin-Triplet Superconductivity Induced by Charge Fluctuations in Extended Hubbard Model*, *J. Phys. Soc. Jpn.* **74** (2005) 2579.

[66] S. Raghu, E. Berg, A.V. Chubukov and S.A. Kivelson, *Effects of longer-range interactions on unconventional superconductivity*, *Phys. Rev. B* **85** (2012) 024516.

[67] D. Sénéchal, A.G.R. Day, V. Bouliane and A.-M.S. Tremblay, *Resilience of d-wave superconductivity to nearest-neighbor repulsion*, *Phys. Rev. B* **87** (2013) 075123.

[68] W.-M. Huang, C.-Y. Lai, C. Shi and S.-W. Tsai, *Unconventional superconducting phases for the two-dimensional extended Hubbard model on a square lattice*, *Phys. Rev. B* **88** (2013) 054504.

[69] N. Plonka, C.J. Jia, Y. Wang, B. Moritz and T.P. Devereaux, *Fidelity study of superconductivity in extended Hubbard models*, *Phys. Rev. B* **92** (2015) 024503.

[70] A. Reymbaut, M. Charlebois, M.F. Asiani, L. Fratino, P. Sémon, G. Sordi and A.-M.S. Tremblay, *Antagonistic effects of nearest-neighbor repulsion on the superconducting pairing dynamics in the doped Mott insulator regime*, *Phys. Rev. B* **94** (2016) 155146.

[71] S. Wolf, T.L. Schmidt and S. Rachel, *Unconventional superconductivity in the extended Hubbard model: Weak-coupling renormalization group*, *Phys. Rev. B* **98** (2018) 174515.

[72] J. Hutchinson and F. Marsiglio, *Mixed temperature-dependent order parameters in the extended Hubbard model*, *J. Phys.: Condens. Matter* **33** (2020) 065603.

[73] M. Jiang, U.R. Hähner, T.C. Schulthess and T.A. Maier, *d-wave superconductivity in the presence of nearest-neighbor Coulomb repulsion*, *Phys. Rev. B* **97** (2018) 184507.

[74] A.T. Rømer, T.A. Maier, A. Kreisel, P.J. Hirschfeld and B.M. Andersen, *Leading superconducting instabilities in three-dimensional models for Sr_2RuO_4*, *Phys. Rev. Research* **4** (2022) 033011.

[75] G.M. Luke, Y. Fudamoto, K.M. Kojima, M.I. Larkin, J. Merrin, B. Nachumi et al., *Time-reversal symmetry-breaking superconductivity in Sr_2RuO_4*, *Nature* **394** (1998) 558.

[76] J. Xia, Y. Maeno, P.T. Beyersdorf, M.M. Fejer and A. Kapitulnik, *High Resolution Polar Kerr Effect Measurements of Sr_2RuO_4: Evidence for Broken Time-Reversal Symmetry in the Superconducting State*, *Phys. Rev. Lett.* **97** (2006) 167002.

[77] S. Benhabib, C. Lupien, I. Paul, L. Berges, M. Dion, M. Nardone, A. Zitouni, Z.Q. Mao, Y. Maeno, A. Georges, L. Taillefer and C. Proust, *Ultrasound evidence for a two-component superconducting order parameter in Sr_2RuO_4*, *Nat. Phys.* **17** (2021) 194.

[78] S. Ghosh, A. Shekhter, F. Jerzembeck, N. Kikugawa, D.A. Sokolov, M. Brando, A.P. Mackenzie, C.W. Hicks and B.J. Ramshaw, *Thermodynamic evidence for a two-component superconducting order parameter in Sr_2RuO_4*, *Nat. Phys.* **17** (2021) 199.

[79] Z. Chen, Y. Wang, S.N. Rebec, T. Jia, M. Hashimoto, D. Lu, B. Moritz, R.G. Moore, T.P. Devereaux and Z.-X. Shen, *Anomalously strong near-neighbor attraction in doped 1D cuprate chains*, *Science* **373** (2021) 1235.

[80] Y. Wang, Z. Chen, T. Shi, B. Moritz, Z.-X. Shen and T.P. Devereaux, *Phonon-Mediated Long-Range Attractive Interaction in One-Dimensional Cuprates*, *Phys. Rev. Lett.* **127** (2021) 197003.

[81] D.-W. Qu, B.-B. Chen, H.-C. Jiang, Y. Wang and W. Li, *Spin-triplet pairing induced by near-neighbor attraction in the extended Hubbard model for cuprate chain*, *Commun. Phys.* **5** (2022) 257.

[82] Z.-B. Huang, S.-C. Fang and H.-Q. Lin, *Superconductivity, nematicity, and charge density wave in high-Tc cuprates: A common thread*, arXiv:2109.05519.

[83] M. Jiang, *Enhancing d-wave superconductivity with nearest-neighbor attraction in the extended Hubbard model*, *Phys. Rev. B* **105** (2022) 024510.

[84] W.-C. Chen, Y. Wang and C.-C. Chen, *Superconducting phases of the square-lattice extended Hubbard model*, *Phys. Rev. B* **108** (2023) 064514.

[85] C. Peng, Y. Wang, J. Wen, Y.S. Lee, T.P. Devereaux and H.-C. Jiang, *Enhanced superconductivity by near-neighbor attraction in the doped extended Hubbard model*, *Phys. Rev. B* **107** (2023) L201102.

[86] A.T. Rømer, *Spin-fluctuation mediated superconductivity and magnetic order in the cuprate* $La_{1.88}Sr_{0.12}CuO_4$, Ph.D. thesis, Niels Bohr Institute, 2015.

[87] D.J. Scalapino, *A common thread: The pairing interaction for unconventional superconductors*, *Rev. Mod. Phys.* **84** (2012) 1383.

[88] Y. Cao, C. Setty, A. Kreisel, L. Fanfarillo and P.J. Hirschfeld, *Spin fluctuations in the ultranodal superconducting state of Fe(Se,S)*, *Phys. Rev. B* **110** (2024) L020503.

[89] G. Esirgen and N.E. Bickers, *Fluctuation-exchange theory for general lattice Hamiltonians*, *Phys. Rev. B* **55** (1997) 2122.

[90] G. Esirgen and N.E. Bickers, *Fluctuation exchange analysis of superconductivity in the standard three-band* CuO_2 *model*, *Phys. Rev. B* **57** (1998) 5376.

[91] W. Marshall and S.W. Lovesey, *Theory of Thermal Neutron Scattering: The Use of Neutrons for the Investigation of Condensed Matter*, International series of monographs on physics, Clarendon Press (1971).

[92] G. Squires, *Introduction to the Theory of Thermal Neutron Scattering*, Cambridge University Press (2012).

[93] A.T. Rømer, I. Eremin, P.J. Hirschfeld and B.M. Andersen, *Superconducting phase diagram of itinerant antiferromagnets*, *Phys. Rev. B* **93** (2016) 174519.

[94] W.-C. Lee, S.-C. Zhang and C. Wu, *Pairing State with a Time-Reversal Symmetry Breaking in FeAs-Based Superconductors*, *Phys. Rev. Lett.* **102** (2009) 217002.

[95] S. Maiti, M. Sigrist and A. Chubukov, *Spontaneous currents in a superconductor with* $s+is$ *symmetry*, *Phys. Rev. B* **91** (2015) 161102.

[96] B. Zinkl and M. Sigrist, *Impurity-induced magnetic ordering in* Sr_2RuO_4, *Phys. Rev. Res.* **3** (2021) 023067.

[97] C.N. Breiø, P.J. Hirschfeld and B.M. Andersen, *Supercurrents and spontaneous time-reversal symmetry breaking by nonmagnetic disorder in unconventional superconductors*, *Phys. Rev. B* **105** (2022) 014504.

[98] S.-Z. Lin, S. Maiti and A. Chubukov, *Distinguishing between $s+id$ and $s+is$ pairing symmetries in multiband superconductors through spontaneous magnetization pattern induced by a defect*, Phys. Rev. B **94** (2016) 064519.

[99] H. Tsuchiura, Y. Tanaka, M. Ogata and S. Kashiwaya, *Local magnetic moments around a nonmagnetic impurity in the two-dimensional $t-J$ model*, Phys. Rev. B **64** (2001) 140501.

[100] Z. Wang and P.A. Lee, *Local Moment Formation in the Superconducting State of a Doped Mott Insulator*, Phys. Rev. Lett. **89** (2002) 217002.

[101] J.-X. Zhu, I. Martin and A.R. Bishop, *Spin and Charge Order around Vortices and Impurities in High-T_c Superconductors*, Phys. Rev. Lett. **89** (2002) 067003.

[102] Y. Chen and C.S. Ting, *States of Local Moment Induced by Nonmagnetic Impurities in Cuprate Superconductors*, Phys. Rev. Lett. **92** (2004) 077203.

[103] B.M. Andersen, P.J. Hirschfeld, A.P. Kampf and M. Schmid, *Disorder-Induced Static Antiferromagnetism in Cuprate Superconductors*, Phys. Rev. Lett. **99** (2007) 147002.

[104] J.W. Harter, B.M. Andersen, J. Bobroff, M. Gabay and P.J. Hirschfeld, *Antiferromagnetic correlations and impurity broadening of NMR linewidths in cuprate superconductors*, Phys. Rev. B **75** (2007) 054520.

[105] B.M. Andersen, S. Graser and P.J. Hirschfeld, *Disorder-Induced Freezing of Dynamical Spin Fluctuations in Underdoped Cuprate Superconductors*, Phys. Rev. Lett. **105** (2010) 147002.

[106] M. Schmid, B.M. Andersen, A.P. Kampf and P.J. Hirschfeld, *d-Wave superconductivity as a catalyst for antiferromagnetism in underdoped cuprates*, New J. Phys. **12** (2010) 053043.

[107] M.N. Gastiasoro, P.J. Hirschfeld and B.M. Andersen, *Impurity states and cooperative magnetic order in Fe-based superconductors*, Phys. Rev. B **88** (2013) 220509.

[108] M.N. Gastiasoro, F. Bernardini and B.M. Andersen, *Unconventional Disorder Effects in Correlated Superconductors*, Phys. Rev. Lett. **117** (2016) 257002.

[109] J.H.J. Martiny, A. Kreisel and B.M. Andersen, *Theoretical study of impurity-induced magnetism in FeSe*, Phys. Rev. B **99** (2019) 014509.

[110] R. Micnas, J. Ranninger and S. Robaszkiewicz, *Superconductivity in narrow-band systems with local nonretarded attractive interactions*, Rev. Mod. Phys. **62** (1990) 113.

[111] S. Nayak and S. Kumar, *Exotic superconducting states in the extended attractive Hubbard model*, J. Phys.: Condens. Matter **30** (2018) 135601.

[112] H. Chen, Q. Niu and A.H. MacDonald, *Anomalous Hall Effect Arising from Noncollinear Antiferromagnetism*, Phys. Rev. Lett. **112** (2014) 017205.

[113] A.T. Rømer, S. Bhattacharyya, R. Valentí, M.H. Christensen and B.M. Andersen, *Superconductivity from repulsive interactions on the kagome lattice*, *Phys. Rev. B* **106** (2022) 174514.

[114] W. Kohn and J.M. Luttinger, *New Mechanism for Superconductivity*, *Phys. Rev. Lett.* **15** (1965) 524.

[115] D. Fay and A. Layzer, *Superfluidity of Low-Density Fermion Systems*, *Phys. Rev. Lett.* **20** (1968) 187.

[116] D.J. Scalapino, E. Loh and J.E. Hirsch, *d-wave pairing near a spin-density-wave instability*, *Phys. Rev. B* **34** (1986) 8190.

[117] D.J. Scalapino, *Superconductivity and Spin Fluctuations*, *J. Low Temp. Phys.* **117** (1999) 179.

[118] K. Miyake, S. Schmitt-Rink and C.M. Varma, *Spin-fluctuation-mediated even-parity pairing in heavy-fermion superconductors*, *Phys. Rev. B* **34** (1986) 6554.

[119] P.J. Hirschfeld, M.M. Korshunov and I.I. Mazin, *Gap symmetry and structure of Fe-based superconductors*, *Rep. Prog. Phys.* **74** (2011) 124508.

[120] A. Chubukov, *Pairing Mechanism in Fe-Based Superconductors*, *Annu. Rev. Condens. Matter Phys.* (2012) 57.

[121] A. Kreisel, P.J. Hirschfeld and B.M. Andersen, *On the Remarkable Superconductivity of FeSe and Its Close Cousins*, *Symmetry* **12** (2020) 1402.

[122] J. Spałek, *Spin-triplet superconducting pairing due to local Hund's rule and Dirac exchange*, *Phys. Rev. B* **63** (2001) 104513.

[123] J.E. Han, *Spin-triplet s-wave local pairing induced by Hund's rule coupling*, *Phys. Rev. B* **70** (2004) 054513.

[124] M. Zegrodnik, J. Bünemann and J. Spałek, *Even-parity spin-triplet pairing by purely repulsive interactions for orbitally degenerate correlated fermions*, *New J. Phys.* **16** (2014) 033001.

[125] S. Hoshino and P. Werner, *Superconductivity from Emerging Magnetic Moments*, *Phys. Rev. Lett.* **115** (2015) 247001.

[126] K. Kubo, *Pairing symmetry in a two-orbital Hubbard model on a square lattice*, *Phys. Rev. B* **75** (2007) 224509.

[127] J. Clepkens, A.W. Lindquist, X. Liu and H.-Y. Kee, *Higher angular momentum pairings in interorbital shadowed-triplet superconductors: Application to* Sr_2RuO_4, *Phys. Rev. B* **104** (2021) 104512.

[128] P.A. Lee and X.-G. Wen, *Spin-triplet p-wave pairing in a three-orbital model for iron pnictide superconductors*, *Phys. Rev. B* **78** (2008) 144517.

[129] X. Dai, Z. Fang, Y. Zhou and F.-C. Zhang, *Even Parity, Orbital Singlet, and Spin Triplet Pairing for Superconducting $LaFeAsO_{1-x}F_x$*, *Phys. Rev. Lett.* **101** (2008) 057008.

[130] O. Vafek and A.V. Chubukov, *Hund Interaction, Spin-Orbit Coupling, and the Mechanism of Superconductivity in Strongly Hole-Doped Iron Pnictides*, *Phys. Rev. Lett.* **118** (2017) 087003.

[131] J. Böker, P.A. Volkov, P.J. Hirschfeld and I. Eremin, *Quasiparticle interference and symmetry of superconducting order parameter in strongly electron-doped iron-based superconductors*, *New J. Phys.* **21** (2019) 083021.

[132] A.K.C. Cheung and D.F. Agterberg, *Superconductivity in the presence of spin-orbit interactions stabilized by Hund coupling*, *Phys. Rev. B* **99** (2019) 024516.

[133] S. Sakai, R. Arita and H. Aoki, *Numerical algorithm for the double-orbital Hubbard model: Hund-coupled pairing symmetry in the doped case*, *Phys. Rev. B* **70** (2004) 172504.

[134] S. Cobo, F. Ahn, I. Eremin and A. Akbari, *Anisotropic spin fluctuations in Sr_2RuO_4: Role of spin-orbit coupling and induced strain*, *Phys. Rev. B* **94** (2016) 224507.

[135] O. Gingras, R. Nourafkan, A.-M.S. Tremblay and M. Côté, *Superconducting Symmetries of Sr_2RuO_4 from First-Principles Electronic Structure*, *Phys. Rev. Lett.* **123** (2019) 217005.

[136] C. Castellani, C.R. Natoli and J. Ranninger, *Magnetic structure of V_2O_3 in the insulating phase*, *Phys. Rev. B* **18** (1978) 4945.

[137] M. Roig, *Theoretical Studies of Superconductivity in Sr_2RuO_4*, Master's thesis, Niels Bohr Institute, 2021.

[138] M. Sigrist and K. Ueda, *Phenomenological theory of unconventional superconductivity*, *Rev. Mod. Phys.* **63** (1991) 239.

[139] M. Sigrist, *Introduction to Unconventional Superconductivity*, *AIP Conf. Proc.* **789** (2005) 165.

[140] A. Ramires and M. Sigrist, *Superconducting order parameter of Sr_2RuO_4: A microscopic perspective*, *Phys. Rev. B* **100** (2019) 104501.

[141] S.-O. Kaba and D. Sénéchal, *Group-theoretical classification of superconducting states of strontium ruthenate*, *Phys. Rev. B* **100** (2019) 214507.

[142] A. Tamai, M. Zingl, E. Rozbicki, E. Cappelli, S. Riccò, A. de la Torre et al., *High-Resolution Photoemission on Sr_2RuO_4 Reveals Correlation-Enhanced Effective Spin-Orbit Coupling and Dominantly Local Self-Energies*, *Phys. Rev. X* **9** (2019) 021048.

[143] A. Damascelli, D.H. Lu, K.M. Shen, N.P. Armitage, F. Ronning, D.L. Feng et al., *Fermi Surface, Surface States, and Surface Reconstruction in Sr_2RuO_4*, *Phys. Rev. Lett.* **85** (2000) 5194.

[144] C. Bergemann, S.R. Julian, A.P. Mackenzie, S. NishiZaki and Y. Maeno, *Detailed Topography of the Fermi Surface of Sr_2RuO_4*, *Phys. Rev. Lett.* **84** (2000) 2662.

[145] C. Bergemann, A.P. Mackenzie, S.R. Julian, D. Forsythe and E. Ohmichi, *Quasi-two-dimensional Fermi liquid properties of the unconventional superconductor Sr_2RuO_4*, *Advances in Physics* **52** (2003) 639.

[146] V.B. Zabolotnyy, D.V. Evtushinsky, A.A. Kordyuk, T.K. Kim, E. Carleschi, B.P. Doyle, R. Fittipaldi, M. Cuoco, A. Vecchione and S.V. Borisenko, *Renormalized band structure of Sr_2RuO_4: A quasiparticle tight-binding approach*, *J. Electron Spectrosc. Relat. Phenom.* **191** (2013) 48.

[147] H.G. Suh, Y. Yu, T. Shishidou, M. Weinert, P.M.R. Brydon and D.F. Agterberg, *Superconductivity of anomalous pseudospin in nonsymmorphic materials*, *Phys. Rev. Res.* **5** (2023) 033204.

[148] J. Mravlje, M. Aichhorn, T. Miyake, K. Haule, G. Kotliar and A. Georges, *Coherence-Incoherence Crossover and the Mass-Renormalization Puzzles in Sr_2RuO_4*, *Phys. Rev. Lett.* **106** (2011) 096401.

[149] L. Vaugier, H. Jiang and S. Biermann, *Hubbard U and Hund exchange J in transition metal oxides: Screening versus localization trends from constrained random phase approximation*, *Phys. Rev. B* **86** (2012) 165105.

[150] H. Wu, Y. Wang, Y. Xu, P.K. Sivakumar, C. Pasco, U. Filippozzi, S.S.P. Parkin, Y.-J. Zeng, T. McQueen and M.N. Ali, *The field-free Josephson diode in a van der Waals heterostructure*, *Nature* **604** (2022) 653.

[151] J. Díez-Mérida, A. Díez-Carlón, S.Y. Yang, Y.-M. Xie, X.-J. Gao, J. Senior et al., *Symmetry-broken Josephson junctions and superconducting diodes in magic-angle twisted bilayer graphene*, *Nat. Commun.* **14** (2023) 2396.

[152] J.-X. Lin, P. Siriviboon, H.D. Scammell, S. Liu, D. Rhodes, K. Watanabe, T. Taniguchi, J. Hone, M.S. Scheurer and J.I.A. Li, *Zero-field superconducting diode effect in small-twist-angle trilayer graphene*, *Nat. Phys.* **18** (2022) 1221.

[153] Y.-Y. Lyu, J. Jiang, Y.-L. Wang, Z.-L. Xiao, S. Dong, Q.-H. Chen et al., *Superconducting diode effect via conformal-mapped nanoholes*, *Nat. Commun.* **12** (2021) 2703.

[154] J. Yun, S. Son, J. Shin, G. Park, K. Zhang, Y.J. Shin, J.-G. Park and D. Kim, *Magnetic proximity-induced superconducting diode effect and infinite magnetoresistance in a van der Waals heterostructure*, *Phys. Rev. Res.* **5** (2023) L022064.

[155] C. Baumgartner, L. Fuchs, A. Costa, S. Reinhardt, S. Gronin, G.C. Gardner et al., *Supercurrent rectification and magnetochiral effects in symmetric Josephson junctions*, *Nat. Nanotechnol.* **17** (2022) 39.

[156] E. Strambini, M. Spies, N. Ligato, S. Ilić, M. Rouco, C. González-Orellana et al., *Superconducting spintronic tunnel diode*, *Nat. Commun.* **13** (2022) 2431.

[157] L. Bauriedl, C. Bäuml, L. Fuchs, C. Baumgartner, N. Paulik, J.M. Bauer et al., *Supercurrent diode effect and magnetochiral anisotropy in few-layer $NbSe_2$*, *Nat. Commun.* **13** (2022) 4266.

[158] Y. Hou, F. Nichele, H. Chi, A. Lodesani, Y. Wu, M.F. Ritter et al., *Ubiquitous Superconducting Diode Effect in Superconductor Thin Films*, *Phys. Rev. Lett.* **131** (2023) 027001.

[159] B. Pal, A. Chakraborty, P.K. Sivakumar, M. Davydova, A.K. Gopi, A.K. Pandeya et al., *Josephson diode effect from Cooper pair momentum in a topological semimetal*, *Nat. Phys.* **18** (2022) 1228.

[160] B. Turini, S. Salimian, M. Carrega, A. Iorio, E. Strambini, F. Giazotto, V. Zannier, L. Sorba and S. Heun, *Josephson Diode Effect in High-Mobility InSb Nanoflags*, *Nano Lett.* **22** (2022) 8502.

[161] W.-S. Du, W. Chen, Y. Zhou, T. Zhou, G. Liu, Z. Zhang et al., *Superconducting Diode Effect and Large Magnetochiral Anisotropy in T_d-$MoTe_2$ Thin Film*, arXiv:2303.09052.

[162] M. Gupta, G.V. Graziano, M. Pendharkar, J.T. Dong, C.P. Dempsey, C. Palmstrøm and V.S. Pribiag, *Gate-tunable superconducting diode effect in a three-terminal Josephson device*, *Nat. Commun.* **14** (2023) 3078.

[163] A. Gutfreund, H. Matsuki, V. Plastovets, A. Noah, L. Gorzawski, N. Fridman et al., *Direct observation of a superconducting vortex diode*, *Nat. Commun.* **14** (2023) 1630.

[164] H. Narita, J. Ishizuka, D. Kan, Y. Shimakawa, Y. Yanase and T. Ono, *Magnetization Control of Zero-Field Intrinsic Superconducting Diode Effect*, *Adv. Mater.* **35** (2023) 2304083.

[165] D. Margineda, A. Crippa, E. Strambini, Y. Fukaya, M.T. Mercaldo, M. Cuoco and F. Giazotto, *Sign reversal diode effect in superconducting Dayem nanobridges*, *Commun. Phys.* **6** (2023) 343.

[166] M. Nadeem, M.S. Fuhrer and X. Wang, *The superconducting diode effect*, *Nat. Rev. Phys.* **5** (2023) 558.

[167] A. Daido, Y. Ikeda and Y. Yanase, *Intrinsic Superconducting Diode Effect*, *Phys. Rev. Lett.* **128** (2022) 037001.

[168] A. Daido and Y. Yanase, *Superconducting diode effect and nonreciprocal transition lines*, *Phys. Rev. B* **106** (2022) 205206.

[169] S. Ilić and F.S. Bergeret, *Theory of the Supercurrent Diode Effect in Rashba Superconductors with Arbitrary Disorder*, *Phys. Rev. Lett.* **128** (2022) 177001.

[170] N.F.Q. Yuan and L. Fu, *Supercurrent diode effect and finite-momentum superconductors*, *Proc. Natl. Acad. Sci.* **119** (2022) e2119548119.

[171] J.J. He, Y. Tanaka and N. Nagaosa, *A phenomenological theory of superconductor diodes*, *New J. Phys.* **24** (2022) 053014.

[172] H.D. Scammell, J.I.A. Li and M.S. Scheurer, *Theory of zero-field superconducting diode effect in twisted trilayer graphene*, *2D Mater.* **9** (2022) 025027.

[173] H.F. Legg, D. Loss and J. Klinovaja, *Superconducting diode effect due to magnetochiral anisotropy in topological insulators and Rashba nanowires*, *Phys. Rev. B* **106** (2022) 104501.

[174] M. Davydova, S. Prembabu and L. Fu, *Universal Josephson diode effect*, *Sci. Adv.* **8** (2022) eabo0309.

[175] T. Karabassov, I.V. Bobkova, A.A. Golubov and A.S. Vasenko, *Hybrid helical state and superconducting diode effect in superconductor/ferromagnet/topological insulator heterostructures*, *Phys. Rev. B* **106** (2022) 224509.

[176] Y. Zhang, Y. Gu, P. Li, J. Hu and K. Jiang, *General Theory of Josephson Diodes*, *Phys. Rev. X* **12** (2022) 041013.

[177] Y. Tanaka, B. Lu and N. Nagaosa, *Theory of giant diode effect in d-wave superconductor junctions on the surface of a topological insulator*, *Phys. Rev. B* **106** (2022) 214524.

[178] D. Kochan, A. Costa, I. Zhumagulov and I. Žutić, *Phenomenological Theory of the Supercurrent Diode Effect: The Lifshitz Invariant*, arXiv:2303.11975.

[179] A. Costa, J. Fabian and D. Kochan, *Microscopic study of the Josephson supercurrent diode effect in Josephson junctions based on two-dimensional electron gas*, *Phys. Rev. B* **108** (2023) 054522.

[180] H. Bruus and K. Flensberg, *Many-body quantum theory in condensed matter physics: an introduction*, OUP Oxford (2004).

[181] S.S. Pershoguba, K. Björnson, A.M. Black-Schaffer and A.V. Balatsky, *Currents Induced by Magnetic Impurities in Superconductors with Spin-Orbit Coupling*, *Phys. Rev. Lett.* **115** (2015) 116602.

[182] V.M. Edelstein, *Characteristics of the Cooper pairing in two-dimensional noncentrosymmetric electron systems*, *Soviet Physics - JETP* **68** (1989) 1244.

[183] V.M. Edelstein, *Magnetoelectric Effect in Polar Superconductors*, *Phys. Rev. Lett.* **75** (1995) 2004.

[184] B.M. Andersen, I.V. Bobkova, P.J. Hirschfeld and Y.S. Barash, *Bound states at the interface between antiferromagnets and superconductors*, *Phys. Rev. B* **72** (2005) 184510.

[185] B.M. Andersen, I.V. Bobkova, P.J. Hirschfeld and Y.S. Barash, $0-\pi$ *Transitions in Josephson Junctions with Antiferromagnetic Interlayers*, *Phys. Rev. Lett.* **96** (2006) 117005.

[186] J. Cayao, N. Nagaosa and Y. Tanaka, *Enhancing the Josephson diode effect with Majorana bound states*, *Phys. Rev. B* **109** (2024) L081405.

[187] C.N. Breiø and B.M. Andersen, *Chern insulator phases and spontaneous spin and valley order in a moiré lattice model for magic-angle twisted bilayer graphene*, *Phys. Rev. B* **107** (2023) 165114.

[188] S. Banerjee and M.S. Scheurer, *Enhanced Superconducting Diode Effect due to Coexisting Phases*, *Phys. Rev. Lett.* **132** (2024) 046003.

[189] S. Hayami, Y. Yanagi and H. Kusunose, *Momentum-Dependent Spin Splitting by Collinear Antiferromagnetic Ordering*, *J. Phys. Soc. Jpn.* **88** (2019) 123702.

[190] K.-H. Ahn, A. Hariki, K.-W. Lee and J. Kuneš, *Antiferromagnetism in RuO_2 as d-wave Pomeranchuk instability*, *Phys. Rev. B* **99** (2019) 184432.

[191] L. Šmejkal, R. González-Hernández, T. Jungwirth and J. Sinova, *Crystal time-reversal symmetry breaking and spontaneous hall effect in collinear antiferromagnets*, *Sci. Adv.* **6** (2020) eaaz8809.

[192] L.-D. Yuan, Z. Wang, J.-W. Luo, E.I. Rashba and A. Zunger, *Giant momentum-dependent spin splitting in centrosymmetric low-Z antiferromagnets*, *Phys. Rev. B* **102** (2020) 014422.

[193] I.I. Mazin, K. Koepernik, M.D. Johannes, R. González-Hernández and L. Šmejkal, *Prediction of unconventional magnetism in doped $FeSb_2$*, *Proc. Natl. Acad. Sci.* **118** (2021) e2108924118.

[194] S. Bhowal and N.A. Spaldin, *Ferroically Ordered Magnetic Octupoles in d-Wave Altermagnets*, *Phys. Rev. X* **14** (2024) 011019.

[195] I. Mazin, *Editorial: Altermagnetism—a new punch line of fundamental magnetism*, *Phys. Rev. X* **12** (2022) 040002.

[196] S.A. Kivelson, I.P. Bindloss, E. Fradkin, V. Oganesyan, J.M. Tranquada, A. Kapitulnik and C. Howald, *How to detect fluctuating stripes in the high-temperature superconductors*, *Rev. Mod. Phys.* **75** (2003) 1201.

[197] V. Oganesyan, S.A. Kivelson and E. Fradkin, *Quantum theory of a nematic Fermi fluid*, *Phys. Rev. B* **64** (2001) 195109.

[198] Y. Guo, H. Liu, O. Janson, I.C. Fulga, J. van den Brink and J.I. Facio, *Spin-split collinear antiferromagnets: A large-scale ab-initio study*, *Materials Today Physics* **32** (2023) 100991.

[199] T. Berlijn, P.C. Snijders, O. Delaire, H.-D. Zhou, T.A. Maier, H.-B. Cao, S.-X. Chi, M. Matsuda, Y. Wang, M.R. Koehler, P.R.C. Kent and H.H. Weitering, *Itinerant Antiferromagnetism in RuO_2*, *Phys. Rev. Lett.* **118** (2017) 077201.

[200] M. Naka, S. Hayami, H. Kusunose, Y. Yanagi, Y. Motome and H. Seo, *Spin current generation in organic antiferromagnets*, *Nat. Commun.* **10** (2019) 4305.

[201] M. Naka, S. Hayami, H. Kusunose, Y. Yanagi, Y. Motome and H. Seo, *Anomalous Hall effect in κ-type organic antiferromagnets*, *Phys. Rev. B* **102** (2020) 075112.

[202] S. Reimers, L. Odenbreit, L. Šmejkal, V.N. Strocov, P. Constantinou, A.B. Hellenes et al., *Direct observation of altermagnetic band splitting in CrSb thin films*, *Nat. Commun.* **15** (2024) 2116.

[203] S. Lee, S. Lee, S. Jung, J. Jung, D. Kim, Y. Lee et al., *Broken Kramers Degeneracy in Altermagnetic MnTe*, *Phys. Rev. Lett.* **132** (2024) 036702.

[204] D.-F. Shao, S.-H. Zhang, M. Li, C.-B. Eom and E.Y. Tsymbal, *Spin-neutral currents for spintronics*, *Nat. Commun.* **12** (2021) 7061.

[205] R. González-Hernández, L. Šmejkal, K. Výborný, Y. Yahagi, J. Sinova, T. Jungwirth and J. Železný, *Efficient Electrical Spin Splitter Based on Nonrelativistic Collinear Antiferromagnetism*, *Phys. Rev. Lett.* **126** (2021) 127701.

[206] L. Šmejkal, A.B. Hellenes, R. González-Hernández, J. Sinova and T. Jungwirth, *Giant and Tunneling Magnetoresistance in Unconventional Collinear Antiferromagnets with Nonrelativistic Spin-Momentum Coupling*, *Phys. Rev. X* **12** (2022) 011028.

[207] L. Šmejkal, A.H. MacDonald, J. Sinova, S. Nakatsuji and T. Jungwirth, *Anomalous Hall antiferromagnets*, *Nat. Rev. Mater.* **7** (2022) 482.

[208] Z. Feng, X. Zhou, L. Šmejkal, L. Wu, Z. Zhu, H. Guo et al., *An anomalous Hall effect in altermagnetic ruthenium dioxide*, *Nat. Electron.* **5** (2022) 735.

[209] R.D. Gonzalez Betancourt, J. Zubáč, R. Gonzalez-Hernandez, K. Geishendorf, Z. Šobáň, G. Springholz et al., *Spontaneous Anomalous Hall Effect Arising from an Unconventional Compensated Magnetic Phase in a Semiconductor*, *Phys. Rev. Lett.* **130** (2023) 036702.

[210] T. Osumi, S. Souma, T. Aoyama, K. Yamauchi, A. Honma, K. Nakayama, T. Takahashi, K. Ohgushi and T. Sato, *Observation of a giant band splitting in altermagnetic MnTe*, *Phys. Rev. B* **109** (2024) 115102.

[211] O. Fedchenko, J. Minár, A. Akashdeep, S.W. D'Souza, D. Vasilyev, O. Tkach et al., *Observation of time-reversal symmetry breaking in the band structure of altermagnetic RuO_2*, *Sci. Adv.* **10** (2024) eadj4883.

[212] J. Krempaský, L. Šmejkal, S.W. D'Souza, M. Hajlaoui, G. Springholz, K. Uhlířová et al., *Altermagnetic lifting of Kramers spin degeneracy*, *Nature* **626** (2024) 517.

[213] Z. Lin, D. Chen, W. Lu, X. Liang, S. Feng, K. Yamagami et al., *Observation of Giant Spin Splitting and d-wave Spin Texture in Room Temperature Altermagnet RuO_2*, arXiv:2402.04995.

[214] A. Bose, N.J. Schreiber, R. Jain, D.-F. Shao, H.P. Nair, J. Sun, X.S. Zhang, D.A. Muller, E.Y. Tsymbal, D.G. Schlom and D.C. Ralph, *Tilted spin current generated by the collinear antiferromagnet ruthenium dioxide*, *Nat. Electron.* **5** (2022) 267.

[215] H. Bai, L. Han, X.Y. Feng, Y.J. Zhou, R.X. Su, Q. Wang, L.Y. Liao, W.X. Zhu, X.Z. Chen, F. Pan, X.L. Fan and C. Song, *Observation of Spin Splitting Torque in a Collinear Antiferromagnet RuO_2*, *Phys. Rev. Lett.* **128** (2022) 197202.

[216] S. Karube, T. Tanaka, D. Sugawara, N. Kadoguchi, M. Kohda and J. Nitta, *Observation of Spin-Splitter Torque in Collinear Antiferromagnetic RuO_2*, *Phys. Rev. Lett.* **129** (2022) 137201.

[217] M. Hiraishi, H. Okabe, A. Koda, R. Kadono, T. Muroi, D. Hirai and Z. Hiroi, *Nonmagnetic Ground State in RuO_2 Revealed by Muon Spin Rotation*, *Phys. Rev. Lett.* **132** (2024) 166702.

[218] P. Keßler, L. Garcia-Gassull, A. Suter, T. Prokscha, Z. Salman, D. Khalyavin, P. Manuel, F. Orlandi, I.I. Mazin, R. Valentí and S. Moser, *Absence of magnetic order in RuO_2: insights from μSR spectroscopy and neutron diffraction*, arXiv:2405.10820.

[219] A.B. Hellenes, T. Jungwirth, R. Jaeschke-Ubiergo, A. Chakraborty, J. Sinova and L. Šmejkal, *P-wave magnets*, *arXiv* (2023) [2309.01607].

[220] R.M. Fernandes, V.S. de Carvalho, T. Birol and R.G. Pereira, *Topological transition from nodal to nodeless Zeeman splitting in altermagnets*, *Phys. Rev. B* **109** (2024) 024404.

[221] Y. Yu, T. Shishidou, S. Sumita, M. Weinert and D.F. Agterberg, *Spin-orbit enabled unconventional Stoner magnetism*, arXiv:2310.00838.

[222] D.S. Antonenko, R.M. Fernandes and J.W.F. Venderbos, *Mirror Chern Bands and Weyl Nodal Loops in Altermagnets*, arXiv:2402.10201.

[223] L. Attias, A. Levchenko and M. Khodas, *Intrinsic anomalous and crystal Hall effects in altermagnets*, arXiv:2402.12115.

[224] M.I. Aroyo, J.M. Perez-Mato, C. Capillas, E. Kroumova, S. Ivantchev, G. Madariaga, A. Kirov and H. Wondratschek, *Bilbao crystallographic server: I. databases and crystallographic computing programs*, *Zeitschrift für Kristallographie - Crystalline Materials* **221** (2006) 15.

[225] M.I. Aroyo, A. Kirov, C. Capillas, J.M. Perez-Mato and H. Wondratschek, *Bilbao Crystallographic Server. II. Representations of crystallographic point groups and space groups*, *Acta Cryst. A* **62** (2006) 115.

[226] H.T. Stokes, B.J. Campbell and R. Cordes, *Tabulation of irreducible representations of the crystallographic space groups and their superspace extensions*, *Acta Cryst. A* **69** (2013) 388.

[227] N.F. Yuan, H. Isobe and L. Fu, *Magic of high-order van Hove singularity*, *Nat. Commun.* **10** (2019) 5769.

[228] J.W. Stout and H.E. Adams, *Magnetism and the Third Law of Thermodynamics. The Heat Capacity of Manganous Fluoride from 13 to 320°K.*, *J. Am. Chem. Soc.* **64** (1942) 1535.

[229] A. Kreisel, B.M. Andersen, P.O. Sprau, A. Kostin, J.C.S. Davis and P.J. Hirschfeld, *Orbital selective pairing and gap structures of iron-based superconductors*, *Phys. Rev. B* **95** (2017) 174504.

[230] T.A. Maier and S. Okamoto, *Weak-coupling theory of neutron scattering as a probe of altermagnetism*, *Phys. Rev. B* **108** (2023) L100402.

[231] Y. Fang, J. Cano and S.A.A. Ghorashi, *Quantum geometry induced nonlinear transport in altermagnets*, arXiv:2310.11489.

[232] A. Graf and F. Piéchon, *Berry curvature and quantum metric in N-band systems: An eigenprojector approach*, *Phys. Rev. B* **104** (2021) 085114.

[233] A.V. Lukoyanov, V.V. Mazurenko, V.I. Anisimov, M. Sigrist and T.M. Rice, *The semiconductor-to-ferromagnetic-metal transition in $FeSb_2$*, *Eur. Phys. J. B* **53** (2006) 205.

[234] S. Sumita, M. Naka and H. Seo, *Fulde-Ferrell-Larkin-Ovchinnikov state induced by antiferromagnetic order in κ-type organic conductors*, *Phys. Rev. Res.* **5** (2023) 043171.

[235] H. Kino and H. Fukuyama, *Phase Diagram of Two-Dimensional Organic Conductors: $(BEDT\text{-}TTF)_2X$*, *J. Phys. Soc. Jpn.* **65** (1996) 2158.

[236] I.J. Park, S. Kwon and R.K. Lake, *Effects of filling, strain, and electric field on the Néel vector in antiferromagnetic CrSb*, *Phys. Rev. B* **102** (2020) 224426.

[237] M. Uchida, T. Nomoto, M. Musashi, R. Arita and M. Kawasaki, *Superconductivity in Uniquely Strained RuO_2 Films*, *Phys. Rev. Lett.* **125** (2020) 147001.

[238] J.P. Ruf, H. Paik, N.J. Schreiber, H.P. Nair, L. Miao, J.K. Kawasaki et al., *Strain-stabilized superconductivity*, *Nat. Commun.* **12** (2021) 59.

[239] C.A. Occhialini, L.G.P. Martins, S. Fan, V. Bisogni, T. Yasunami, M. Musashi, M. Kawasaki, M. Uchida, R. Comin and J. Pelliciari, *Strain-modulated anisotropic electronic structure in superconducting RuO_2 films*, *Phys. Rev. Mater.* **6** (2022) 084802.

[240] O. Gomonay, V.P. Kravchuk, R. Jaeschke-Ubiergo, K.V. Yershov, T. Jungwirth, L. Šmejkal, J. van den Brink and J. Sinova, *Structure, control, and dynamics of altermagnetic textures*, *npj Spintronics* **2** (2024) 35.

[241] I.I. Mazin, *Notes on altermagnetism and superconductivity*, arXiv:2203.05000.

[242] D. Chakraborty and A.M. Black-Schaffer, *Zero-field finite-momentum and field-induced superconductivity in altermagnets*, arXiv:2309.14427.

[243] B. Brekke, A. Brataas and A. Sudbø, *Two-dimensional altermagnets: Superconductivity in a minimal microscopic model*, *Phys. Rev. B* **108** (2023) 224421.

[244] I.I. Mazin, *Origin of the gossamer ferromagnetism in MnTe*, arXiv:2407.14389.

[245] K.P. Kluczyk, K. Gas, M.J. Grzybowski, P. Skupiński, M.A. Borysiewicz, T. Fas et al., *Coexistence of Anomalous Hall Effect and Weak Net Magnetization in Collinear Antiferromagnet MnTe*, arXiv:2310.09134.

[246] M. Milivojević, M. Orozović, S. Picozzi, M. Gmitra and S. Stavrić, *Interplay of altermagnetism and weak ferromagnetism in two-dimensional RuF_4*, *2D Mater.* **11** (2024) 035025.

[247] S.-W. Cheong and F.-T. Huang, *Altermagnetism with non-collinear spins*, *npj Quantum Mater.* **9** (2024) 13.

[248] C. Autieri, R.M. Sattigeri, G. Cuono and A. Fakhredine, *Staggered Dzyaloshinskii-Moriya inducing weak ferromagnetism in centrosymmetric altermagnets and weak ferrimagnetism in noncentrosymmetric altermagnets*, arXiv:2312.07678.

[249] H. Dohnomae, K. Shintaku, N. Nakayama and T. Shinjo, *Structural and magnetic properties of Cr/Sb multilayers*, *Appl. Surf. Sci.* **60-61** (1992) 807.

[250] D.-F. Shao, S.-H. Zhang, G. Gurung, W. Yang and E.Y. Tsymbal, *Nonlinear Anomalous Hall Effect for Néel Vector Detection*, *Phys. Rev. Lett.* **124** (2020) 067203.

[251] H. Chen, T.-C. Wang, D. Xiao, G.-Y. Guo, Q. Niu and A.H. MacDonald, *Manipulating anomalous Hall antiferromagnets with magnetic fields*, *Phys. Rev. B* **101** (2020) 104418.

[252] I.I. Mazin, *Altermagnetism Then and Now*, *Physics* **17** (2024) 4.

[253] P.A. McClarty and J.G. Rau, *Landau Theory of Altermagnetism*, *Phys. Rev. Lett.* **132** (2024) 176702.

[254] P. Coleman, *Introduction to many-body physics*, Cambridge University Press (2015).

[255] A. Altland and B.D. Simons, *Condensed matter field theory*, Cambridge university press (2010).

[256] E.K. Dahl and A. Sudbø, *Derivation of the Ginzburg-Landau equations for a ferromagnetic p-wave superconductor*, *Phys. Rev. B* **75** (2007) 144504.

[257] X.-Y. Hou, H.-C. Yang, Z.-X. Liu, P.-J. Guo and Z.-Y. Lu, *Large intrinsic anomalous Hall effect in both Nb_2FeB_2 and Ta_2FeB_2 with collinear antiferromagnetism*, *Phys. Rev. B* **107** (2023) L161109.

[258] D.J. Scalapino, S.R. White and S. Zhang, *Insulator, metal, or superconductor: The criteria*, *Phys. Rev. B* **47** (1993) 7995.

[259] C. Bradley and A. Cracknell, *The mathematical theory of symmetry in solids: representation theory for point groups and space groups*, Oxford University Press (2009).